This work is protected by copyright and other intellectual property rights and duplication or sale of all or part is not permitted, except that material may be duplicated by you for research, private study, criticism/review or educational purposes. Electronic or print copies are for your own personal, non-commercial use and shall not be passed to any other individual. No quotation may be published without proper acknowledgement. For any other use, or to quote extensively from the work, permission must be obtained from the copyright holder/s.

High-resolution studies of massive young stellar objects in the Magellanic Clouds

Jacob L. Ward

Doctor of Philosophy

Faculty of Natural Sciences, Keele University

June 2017

Abstract

This thesis presents sub-arcsecond resolution observations of massive Young Stellar Objects (YSOs) in two satellite galaxies of the Milky Way, the Magellanic Clouds. With metallicities of $\sim$0.5 and $\sim$0.2 $Z_{\odot}$ for the Large Magellanic Cloud (LMC) and Small Magellanic Cloud (SMC), respectively the Magellanic Clouds present a unique opportunity to study star formation in environments which differ significantly from those of our own Galaxy.

19 targets in the SMC and 3 targets in the H II region LHA 120-N113 in the LMC were observed with the near-infrared integral field spectrograph SINFONI at the VLT. Archival SINFONI data towards 7 targets in the Tarantula nebula in the LMC were also obtained. These observations reveal a wide variety of spatially extended emission line morphologies, indicative of outflows and compact H II regions. Additionally, the most direct indications to date for the presence of discs in massive YSOs in the Magellanic Clouds are presented.

Previously obtained optical spectra towards massive YSOs in the SMC have been analysed, as well as newly obtained spectra using the Robert Stobie Spectrograph (RSS) at the Southern African Large Telescope (SALT). Fabry-Perot interferometric observations obtained with RSS at SALT towards two star forming H II regions in the Magellanic Clouds, are also presented, along with a new Fabry-Perot data reduction pipeline. Through analysis of the optical spectra in the context of the SINFONI data the massive YSOs in the SMC appear to reside in a porous ISM, allowing a large mean-free-path for energetic photons.

Through a comparison of massive YSOs in the Magellanic Clouds and a previously obtained Galactic sample, evidence of significantly enhanced accretion rates towards the YSOs in the Magellanic Clouds is detected. Whilst the underlying mechanism of this enhancement is uncertain, there appears to be a convincing correlation between metallicity and accretion rates in massive YSOs.

Acknowledgements

The work presented in this thesis is based on data obtained from data obtained with the SINFONI at the European Southern Observatory's Very Large Telescope under programme 092.C-0723(A) (PI: Oliveira, J.) and SINFONI data obtained from the ESO archive from programme 090.C-0587(A) (PI: Alves, J.F.). Additional data were obtained with the Southern African Large Telescope under programmes 2014-1-UKSC-003, 2015-2-SCI-014 and 2016-1-SCI-008 as well as observations obtained with the Double Beam Spectrograph (DBS) at the Australia National University Telescope (PI: Wood, P.). The work presented in Chapter 3 has been previously published in Ward et al. (2016) and that presented in Chapters 4 and 5 has been previously published in Ward et al. (2017). The parameters obtained from previous observations presented in Table 3.1 of Chapter 3 are the result of SED fitting analyses provided by Marta Sewiło for Ward et al. (2016). All other original results appearing in these publications and presented in this thesis were produced by myself.

I would like to thank my supervisors Joana Oliveira and Jacco van Loon for their support, guidance and more than a small amount of patience throughout my PhD. I also express my gratitude to the members of the Astrophysics group at Keele University for creating a friendly and comfortable working environment.

I want to thank my fellow students at Keele university for their support both academically and morally and for helping to maintain some degree of sanity through regular trips to the KPA and the pub. On a similar note I would like to thank the current and past members of Leeds University Union Canoe Club for taking me far away from my studies for extended periods of time and without whom my life would be far less interesting.

I would like to thank my parents Peter and Ceinwen and my brother Adam for their constant support throughout my time at Keele and everything leading up to it as well as providing plentiful food and beer on the rare occasions I make it back to Norfolk. Last but certainly not least, I would like to thank my girlfriend Francesca, who has kept me sane and motivated throughout. She has been amazing putting up with me the past few years and without her, writing this thesis would have been impossible.

Contents

List of Tables

List of Figures

1 Introduction

Massive stars extensively shape and ionize their environments through strong winds, fast outflows and intense UV radiation; enriching the interstellar medium (ISM) with heavier elements and they can even trigger or disrupt further star formation. The mechanisms for forming low mass stars have been studied extensively and are now reasonably well understood (as summarised in Shu, Adams & Lizano 1987). However, relatively little is known about massive ($M > 10\,M_{\odot}$) star formation. The vast majority of our understanding of the formation of stars is deduced from near-solar metallicity, Galactic star forming regions. This presents a relatively limited view of star formation in the universe. With the development of ever larger telescopes and more sophisticated instrumentation it is now possible to study cloud scale star formation physics outside of our Galaxy. In our closest neighbouring galaxies, the Magellanic Clouds, star formation can be studied on the scale of individual stars and young stellar objects.

1.1 Molecular clouds: initial conditions for star formation

The initial stages of star formation, the collapse of molecular clouds into dense molecular cores, depends on the ability of gravitational collapse to overcome the various cloud support mechanisms. This balance of energies is described by the virial theorem. The virial theorem is derived here in the same way as that shown in Krumholz (2015), starting with the Eulerian equations of motion excluding viscosity and resistivity:

$$\frac{\partial \rho}{\partial t} = -\nabla \cdot (\rho \mathbf{v}) \tag{1.1}$$

$$\frac{\partial}{\partial t}(\rho \mathbf{v}) = -\nabla \cdot (\rho \mathbf{v}\mathbf{v}) - \nabla P + \frac{1}{4\pi}(\nabla \times \mathbf{B}) \times \mathbf{B} - \rho \nabla \phi \tag{1.2}$$

In these equations ρ is the density, $\mathbf{v}$ is the velocity vector, P is pressure, $\mathbf{B}$ is the vector of magnetic field strength, ϕ is the gravitational potential meaning that the gravitational force per unit volume is given in the final term ($-\rho \nabla \phi$). Equation 1.2 can be expressed using the

tensors $\mathbf{\Pi}$ and $\mathbf{T_M}$ (McKee & Zweibel, 1992):

$$\frac{\partial}{\partial t}(\rho \mathbf{v}) = -\nabla \cdot (\mathbf{\Pi} - \mathbf{T_M}) - \rho \nabla \phi \ , \tag{1.3}$$

where

$$\mathbf{\Pi} = \rho \mathbf{v}\mathbf{v} + P\mathbf{I}, \tag{1.4}$$

$$\mathbf{T_M} = \frac{1}{4\pi}\left(\mathbf{B}\mathbf{B} - \frac{B^2}{2}\mathbf{I}\right), \tag{1.5}$$

and $\mathbf{I}$ is the identity tensor. The substitution of Eqn. 1.5 into Eqn. 1.2 is given in detail in Appendix A.

The moment of inertia, I, about the origin of a system represents the mass distribution over the volume of that system:

$$I = \int_V \rho r^2 dV \ . \tag{1.6}$$

In order to gauge how the mass distribution of the system changes with time, I is differentiated with respect to t:

$$\frac{dI}{dt} = \int_V \frac{\partial \rho}{\partial t} r^2 dV \ . \tag{1.7}$$

Equation 1.1 can then be substituted into Eqn. 1.7 and the r^2 can be moved inside the divergence:

$$\frac{dI}{dt} = \int_V \nabla \cdot (\rho \mathbf{v}) r^2 dV \tag{1.8}$$

$$\frac{dI}{dt} = \int_V \nabla \cdot (\rho \mathbf{v} r^2) dV + 2\int_V \rho \mathbf{v} \cdot \mathbf{r} dV \tag{1.9}$$

Gauss's theorem (divergence theorem) can then be used to equate the volume integral into a surface integral (Spiegel, Lipschutz & Spellman, 2009):

$$\int_V \nabla \cdot (\rho \mathbf{v} r^2) dV = \int_S (\rho \mathbf{v} r^2) dS \tag{1.10}$$

Differentiating with respect to time again yields

$$\frac{d^2 I}{dt^2} = -\int_S r^2 \frac{\partial}{\partial t}(\rho \mathbf{v}) dS + \int_V \frac{\partial}{\partial t}(\rho \mathbf{v}) \cdot \mathbf{r} dV \ . \tag{1.11}$$

Substituting in the momentum equation with the tensors $\mathbf{\Pi}$ and $\mathbf{T_M}$ (Eqn. 1.3):

$$\frac{d^2 I}{dt^2} = -\frac{d}{dt}\int_S r^2 (\rho \mathbf{v}) dS - \int_V \mathbf{r} \cdot [\nabla \cdot (\mathbf{\Pi} - \mathbf{T_M}) + \rho \nabla \phi] dV \tag{1.12}$$

The second order differential with of the moment of inertia respect to time represents the acceleration of the system towards, or away from the origin of the coordinate system. In the case of cloud-scale physics this is generally the centre of the cloud and therefore a negative value of d^2I/dt^2 is indicative of global collapse of the cloud if that cloud is currently at rest (i.e. neither expanding nor contracting).

The term including the two tensors can be simplified significantly using the identity,

$$\int_V \mathbf{r} \cdot \nabla \cdot \mathbf{T} dV = \int_S \mathbf{r}\mathbf{T} \cdot dS - \int_V Tr\mathbf{T} dV \tag{1.13}$$

for an arbitrary tensor $\mathbf{T}$ (see Appendix A for details) where $Tr\mathbf{T} = T_{ij}$ is the trace of tensor $\mathbf{T}$. The traces of the two tensors (Krumholz 2015) used in this derivation are:

$$Tr\mathbf{\Pi} = 3P + \rho v^2 \tag{1.14}$$

$$Tr\mathbf{T_M} = -\frac{B^2}{8\pi} \tag{1.15}$$

Finally, substituting the identities of the tracers into the equation for momentum (Eqn. 1.3) and multiplying by half, the virial theorem is arrived at (Appendix A). Imposing the assumption that no gas crosses the surface of the cloud, the virial theorem is then reduced to:

$$\frac{1}{2}\frac{d^2I}{dt^2} = 2(\mathcal{T} - \mathcal{T}_S) + \mathcal{B} + \mathcal{W} \tag{1.16}$$

where $\mathcal{T}$ is the sum of the kinetic and thermal energy of the cloud, $\mathcal{T}_S$ represents the external pressure applied to the cloud surface, the magnetic pressure gradient between the cloud interior and exterior is given by $\mathcal{B}$ and the gravitational energy of the cloud is represented by $\mathcal{W}$:

$$\mathcal{T} = \int_V \left(\frac{1}{2}\rho v^2\right) dV \tag{1.17}$$

$$\mathcal{T}_S = \int_S \mathbf{r}\mathbf{\Pi} \cdot dS \tag{1.18}$$

$$\mathcal{B} = \frac{1}{8\pi}\int_V B^2 dV + \int_S \mathbf{r} \cdot \mathbf{T_M} dS \tag{1.19}$$

$$\mathcal{W} = -\int_V \rho \mathbf{r} \cdot \nabla\phi dV. \tag{1.20}$$

For a stable cloud, assuming only the effects of gravity and thermal pressure and neglecting the effects of magnetic fields and external pressure , the virial theorem can be expressed simply

as:

$$2U + \Omega = 0 \tag{1.21}$$

where the thermal energy of the cloud is given by U (assuming an ideal monatomic gas),

$$U = \frac{3}{2}PV = \frac{3}{2}NkT \tag{1.22}$$

and the gravitational potential is represented by Ω,

$$\Omega = -\frac{3}{5}\frac{GM^2}{R}. \tag{1.23}$$

By setting $N = \frac{M}{\mu \mathrm{m_H}}$ where μ is the mean molecular weight and $\mathrm{m_H}$ is the mass of a hydrogen atom and expressing the radius R in terms of mass (M) and density (ρ), the condition for collapse can be defined:

$$M > M_J = \left(\frac{5kT}{G\mu \mathrm{m_H}}\right)^{\frac{3}{2}} \left(\frac{3}{4\pi\rho}\right)^{\frac{1}{2}}, \tag{1.24}$$

M_J is the critical mass at which a molecular cloud will undergo collapse, known as the Jeans Mass and obtained from the Jeans criterion introduced in Jeans (1902). Equations 1.22, 1.23 and 1.24 are specific to the simple case of a constant density sphere of radius R.

By substituting $\rho = n\mu m_H$ and the definition of isothermal sound speed along with the mass of a hydrogen atom, the mean molecular mass, the gravitational constant and Boltzmann constant the Jeans mass can be approximated as:

$$M_J \approx \frac{T^{\frac{3}{2}}}{n^{1/2}} M_\odot, \tag{1.25}$$

where n is measured in units of $10^4\,\mathrm{cm}^{-3}$ and T is in units of 10 K (Stahler & Palla, 2004). When applied to typical temperatures and densities ($\sim$20 K & $\sim 10^3\,\mathrm{cm}^{-3}$, Stahler & Palla 2004) of Giant Molecular Clouds (GMCs) this yields Jeans Masses on the order of $\sim 7 \times 10^4\,M_\odot$ (assuming a mean molecular mass of 2), much smaller than the masses of the clouds themselves which would suggest that all GMCs should exist in a state of global collapse. However if molecular clouds and clumps were collapsing on the free-fall time-scale then the star formation rate of the galaxy would have to be far greater than it is observed to be so this cannot be the case (Hennebelle & Falgarone, 2012).

Mechanical turbulence contributes to the term $\mathcal{T}$ in Eqn. 1.16, alongside thermal energy. Turbulent velocities in molecular clouds do appear to approach the values required to

counteract the force of gravity (Shu, Adams & Lizano, 1987). In the absence of a significant magnetic field however, this fluid turbulence dissipates rapidly and perturbations in the cloud would have to be regularly refreshed in order to sustain a turbulence-driven support mechanism (Goldreich & Kwan, 1974). It is therefore clear that more than radiatively driven turbulence is required to support a molecular cloud.

Additional support is provided in the form of magnetic fields. The longevity of magnetic fields compared to the rapidly dissipated fluid turbulence makes them a primary candidate for molecular cloud support. Charged particles are electrostatically bound to the magnetic field permeating the cloud and spiral round the field lines effectively freezing the magnetic field in the cloud so that the magnetic field flux is conserved. A critical mass that is required to counteract the supporting force provided by the magnetic field and allow a cloud with a given magnetic field flux, Φ, to undergo collapse has been derived through detailed modelling (Mouschovias, 1976; Mouschovias & Spitzer, 1976):

$$M_{cr} = 0.13\frac{\Phi}{G^{1/2}} \approx 10^3 M_{\odot} \left(\frac{B}{30\mu G}\right)\left(\frac{R}{2pc}\right)^2. \tag{1.26}$$

It is expected that the ratio of magnetic field energy to gravitational energy should remain approximately constant throughout collapse because the ratio is independent of radius.

Linear polarisation observations have demonstrated the existence of well defined, ordered magnetic fields in molecular clouds (Vrba, Strom & Strom, 1976; Moneti et al., 1984; Schleuning et al., 2000; Sugitani et al., 2010). However, Zeeman splitting OH and CN observations suggest a mean mass-to-flux ratio of $M/\Phi \sim 2$ to $3 \times (M/\Phi)_{crit}$ and no molecular clouds have been observed so far to have a sub-critical M/Φ. Magnetic fields therefore are unlikely to be the dominant support mechanism for molecular clouds (Hennebelle & Falgarone, 2012) but they can certainly make a considerable contribution. The supporting effect of the magnetic field can be summarised as a magnetic field pressure (Eqn. 1.19).

Finally it is important to note that, the problem of molecular cloud support and indeed whether they are supported at all or if they are transient objects remains under active discussion (Dobbs et al., 2014).

1.2 From molecular clouds to stars

The formation of stars first requires the formation and collapse of dense cores within molecular clouds. In order to collapse molecular clouds into dense cores, cloud stability must be lost and

the support mechanisms outlined in the previous section must be overcome. Gravitational instabilities in otherwise quasi-stable molecular clouds can result from external forces such as supernovae or increased gas pressures in active galactic nuclei (e.g Zubovas, Sabulis & Naujalis 2014). Galaxy spiral arms are also suggested to have a non-negligible role in the producing the gravitational stabilities necessary to trigger cloud collapse (e.g. Kim, Ostriker & Stone 2002, Baba, Morokuma-Matsui & Saitoh 2017). An increasingly accepted mechanism of injecting the required turbulent fields into molecular clouds is through cloud-cloud collisions (e.g. Balfour et al. 2015, Haworth et al. 2015, Fukui et al. 2016).

In order to collapse a cloud into dense cores, the supportive force due to magnetic field flux needs to be overcome. Ambipolar diffusion is the favoured mechanism for the removal of magnetic field flux from dense cores, allowing magnetically supported structures to collapse. Magnetic fields only affect particles which have a charge, neutral particles are free to pass through a magnetic field unhindered (assuming they do not interact directly with the charged particles bound to the field), leading to the core having a lower flux than the surrounding cloud. However OH Zeeman measurements by Crutcher, Hakobian & Troland (2009) of dark cloud cores and surrounding envelopes suggest, in direct contrast to what is expected from ambipolar diffusion, that $(M/\Phi)_{core} < (M/\Phi)_{envelope}$. The stability, evolution and collapse of molecular clouds is not yet fully understood (Dobbs et al., 2014); however, a detailed discussion of the stability of molecular clouds falls outside the scope of this thesis.

Treating gravitational collapse as isothermal is often convenient and makes the problem considerably simpler. However it is important to consider if and when this is a sensible assumption to make. In the initial stages of core collapse heating of the molecular cloud is dominated by cosmic ray interactions with material in the cloud. This effect is negligible compared to the energy loss through CO emission that can be expected for the CO(1-0) transition in a typical core (Stahler & Palla, 2004). This cooling rate can then be used to estimate a cooling time-scale based on this mechanism which is significantly lower than the free fall time-scale and therefore it is a sensible assumption that initial core collapse is isothermal.

In an isothermal contraction the temperature remains the same whilst the density increases, meaning that the Jeans Mass must decrease which in turn means that as isothermal collapse continues, smaller cores within the cloud can begin to collapse locally. This process is called fragmentation and will continue for as long as the system is in an isothermal state assuming no external forces. As the density increases however, so does the opacity of the cores

and eventually the cores will become opaque to their own radiation and the dominant cooling mechanisms become inefficient leading to increased temperatures which in turn increases the Jeans Mass, thus halting fragmentation.

This process of gravitational collapse and fragmentation manifests itself in the formation of cold molecular cores (with typical densities of 10^4–$10^6\,\mathrm{cm}^{-3}$, Klessen 2011) within the denser regions/clumps of the molecular clouds. Observationally these appear as over-dense regions in molecular clouds, traced by clumps of CO emission and are often referred to as starless cores or cold cores.

As fragmentation ends, a hydrostatic core remains which can continue to accrete material from its surrounding circumstellar envelope. At the boundary between the core and envelope where the accreted material falls onto the core a shock front is formed where the free fall velocity can be expressed as:

$$v_{ff}(r) = \sqrt{\frac{2GM}{r}}. \tag{1.27}$$

The time-scale for the collapse of a molecular cloud core under gravity with no additional forces applied is the free-fall time-scale:

$$t_{ff} = \left(\frac{3\pi}{32G\rho}\right)^{\frac{1}{2}}. \tag{1.28}$$

The excess kinetic energy of the material being accreted must be dissipated at the shock front. Assuming this takes the form only of the emission of photons from the shocked region, the accretion luminosity can be obtained:

$$L_{acc} \sim \frac{1}{2}\dot{M}v_{ff}^2 \sim \frac{GM\dot{M}}{R_S}, \tag{1.29}$$

where R_S is the radius from the centre to the shock front and $\dot{M}$ is the infall rate. As the temperature exceeds 2000 K contraction is allowed to continue by the dissipation of excess energy through the dissociation of molecular hydrogen, causing a second phase of core contraction which continues until hydrostatic equilibrium is again established at a smaller radius. This marks the end of the first dense core phase and the start of the protostellar phase. A second accretion shock front develops as the protostar continues to accrete material.

Considering an in-falling core of radius R with a global angular velocity Ω which undergoes collapse to a smaller radius, r, angular momentum conservation implies that the angular velocity must increase: $\omega r^2 = \Omega R^2$. A centrifugal force term is produced from the rotation of a molecular cloud which increases with the square of angular velocity, thus providing

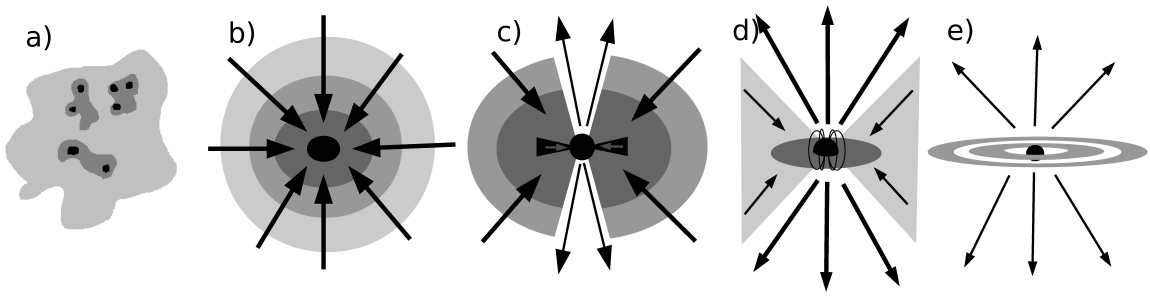

Figure 1.1: Main phases of low mass star formation. a) Dense clumps form within molecular clouds, b) Gravitational collapse into a cold core, c) an embedded protostar accreted material from a disc and forms bipolar outflows, d) a classical T Tauri star accretes material from a disc through magnetospheric accretion generating powerful outflows, e) a pre-main sequence star with a remnant disc.

significant support perpendicular to the rotational axis:

$$F_C = m\omega^2 r. \tag{1.30}$$

In order to conserve angular momentum, ω must be proportional to r^{-2} as a cloud collapses so the centrifugal force is proportional to r^{-3} whereas the force due to gravity is proportional to r^{-2}. Therefore during collapse the centrifugal supporting force increases at a faster rate than the gravitational force thus imposing a limit on collapse in the direction perpendicular to the rotational axis whilst providing no supporting force parallel to the axis of rotation. This process facilitates the formation of disc-like structures. Angular momentum conservation means that without an efficient mechanism to remove angular momentum main sequence stars would be formed with angular velocities far higher than any of those observed. The removal of angular momentum is achieved through three mechanisms; the transfer of angular momentum to a star cluster or planetary system, the outward transfer of angular momentum through a disk and magnetic braking. It has been shown that pre-stellar discs can be formed thousands of years before a stellar core is formed (Bate, 2011).

The formation of a typical solar mass star is summarised by Shu, Adams & Lizano (1987) and Lada & Shu (1990) in 4 distinct stages: dense cores are formed within molecular clouds as magnetic and turbulent support is lost (as described previously); a protostar is formed from the collapsing core; a bipolar outflow is formed along the rotational axis of the star; finally as the infall onto the star halts the star moves onto the main sequence. The observational main stages of low mass star formation are shown schematically in Fig. 1.1.

Newly formed protostars (Class 0 protostars) remain embedded within a warm core of dust

and gas, generally rich in molecular emission line species such as CH_3OH and H_2O (Williams & Viti, 2013). Observationally therefore, they are best studied in the far-infrared, sub-mm and thermal radio regimes (Stahler & Palla, 2004; Schulz, 2005). As accretion continues, protostellar discs and outflows (the effects of outflows are discussed in Section 1.3.4) form and their combined effects aid in the dissipation of much of the circumstellar envelop mass. The result is a Class I protostar which exhibit high levels of accretion from a circumstellar disc with reduced rates of infall onto the disc. Observationally these sources are classified by their spectral index measured between 2 and 20 μm, $\alpha_{\rm IR} = d\log(\lambda F_\lambda)/d\log(\lambda)$ (e.g. Ward-Thompson & Whitworth 2011). Class 0 and I sources are defined as exhibiting a spectral index greater than 0.

The end of infall onto the core marks the beginning of the pre-main sequence phase for low mass stars. This transition is characterised observationally by a decrease in spectral index with Class II sources (classical T Tauri stars) exhibiting $-1.5 < \alpha_{\rm IR} < 0$. At this point much but not all of the circumstellar envelope has been removed through accretion and outflows, making the star visible in the optical, with disc and outflow structures. Class III protostars (weak-lined T Tauri stars) are defined as having a spectral index value of $\alpha_{\rm IR} < -1.5$. They exhibit much weaker line emission than classical T Tauri stars which implies much lower rates of accretion and thus a later evolutionary stage. They have little or no remaining circumstellar envelope but may continue to exhibit a remnant disc (Ward-Thompson & Whitworth, 2011) which could be the site of planet formation.

In order to contract, traversing the pre-main sequence phase and move onto the main sequence, the protostar must radiate away the remaining gravitational potential energy and so a time-scale for the contraction of the protostar, the Kelvin-Helmholz time-scale, can be estimated by dividing the gravitational energy by the luminosity:

$$t_{K-H} \sim \frac{GM^2}{RL}. \tag{1.31}$$

This time-scale is used to measure the time of the contraction until the core enters a phase of full hydrogen burning, establishing thermal equilibrium and marking the transition of the object onto the main sequence.

1.3 Massive Star formation

Whilst much of the process of low mass star formation is understood, the formation of high mass stars is yet to be understood to the same level of detail. The two main problems with massive star formation are first how to collapse a large enough reservoir of material into a dense core to form a massive star and secondly how to overcome radiative pressure in later stages of star formation to accrete material onto the protostar itself.

Increasing the mass of a star necessarily increases its temperature and luminosity. However, the relation between stellar mass and luminosity is not straightforward. For example, Massey & Meyer (2001) find that for solar mass zero-age main sequence stars $L \propto M^{4.7}$ whilst for more massive stars this relation decreases to $L \propto M^{3.1}$ and $L \propto M^{1.6}$ for $10\,M_{\odot}$ and $100\,M_{\odot}$ stars, respectively. Not only does the luminosity increase towards higher masses but so does the radius. For example a $12\,M_{\odot}$ star (representative of a spectral type of B0) has a luminosity of $\sim$10 000 $L_{\odot}$ and a radius of $\sim 4\,R_{\odot}$ (Massey & Meyer, 2001). Applying Eqn. 1.31, to this example we arrive at $t_{K-H} \sim 100\,\mathrm{kyr}$. Given typical accretion rates of $10^{-4}\,M_{\odot}\mathrm{yr}^{-1}$ (Krumholz, 2015), the formation timescale for such a star must be on the order of 100 kyr. Considering that as a protostar (which has not yet finished contracting), the radius must be larger than that of a zero-age main sequence star it is clear that for massive stars the Kelvin-Helmholz timescale is shorter than the formation timescale.

This means that massive stars arrive on the main sequence whilst still accreting. and remain deeply embedded in their natal molecular clouds. As a result there are no direct analogues of Class II or III protostars for massive star formation and all massive Young Stellar Objects (YSOs) therefore exhibit high levels of extinction. This makes the study of most massive protostars using wavelength ranges shorter than the near-infrared J-band problematic, although many larger H II complexes which contain star forming regions are visible in the optical (e.g. LHA 115-N81 in the SMC, see Chapter 5). OB-type stars typically spend $\sim 15\%$ of their lifetime embedded in their natal molecular cloud (Churchwell, 2002).

Radiative pressure from the protostar itself becomes a significant support mechanism in the formation of more massive stars ($M > 10\,M_{\odot}$). The luminosity of a blackbody is given by:

$$L_{*} = 4\pi\sigma_{B}R_{*}^{2}T_{eff}^{4}. \tag{1.32}$$

As the temperature of the object increases with increased mass, the luminosity (and therefore the momentum imparted by radiative pressure) increases proportional to T_{eff}^{4} and therefore

the force from radiative pressure increases disproportionately to the increase in gravitational force. The radiative pressure from a massive young star is therefore large enough to prevent continued spherical accretion onto a protostar (Kahn, 1974). When the powerful jets and outflows produced by a protostar are also taken into account it becomes apparent that there must be an upper limit ($\sim 10\,\mathrm{M}_{\odot}$) on how massive a star can be formed through the mechanism outlined in Shu, Adams & Lizano (1987) for lower mass stars.

It is important to consider the effect of an accretion disc on the formation of massive stars. The dusty discs will be self-shielding against the ultra-violet radiation from the protostars (Kuiper et al., 2010) which means that accretion from the disc will not be prevented by radiative pressure as spherical accretion would be. Indeed it has been shown in Kuiper et al. (2010) that this mechanism of disc accretion can form stars in excess of 150 $\mathrm{M}_{\odot}$ and in the dense region surrounding the protostar gas opacity is sufficient to shield material further (Kuiper & Yorke, 2013). It is therefore clear that whilst in low mass star formation discs are an almost accidental product of the star formation, in massive star formation they are a necessity. The problem remains however, of how to accrete material from a large reservoir without the onset of further fragmentation leading to the formation of a cluster of lower mass stars.

1.3.1 Proposed mechanisms for massive star formation

A number of different mechanisms have been proposed for the formation of high mass stars but the validity of these models can only be assessed through detailed comparison with observations. A range of star formation models (with varying accretion rates) of Galactic protostellar distributions and luminosities have been tested by Davies et al. (2011), including models with accelerating, decreasing and approximately constant accretion rates. Through comparison with data obtained from the Red MSX[1] Source (RMS, Lumsden et al. 2013) survey of galactic massive young stellar objects Davies et al. (2011) found that those models that used accelerating accretion rates best matched the luminosity distribution of the protostellar population of the Milky Way. The most prominent of these accelerating accretion rate models are the turbulent core model and competitive accretion.

The turbulent core model, proposed by McKee & Tan (2003), is based on the principle of using supersonic turbulence and high pressures to support molecular cores which become unstable, exhibiting accelerating accretion rates. The model requires a steep density gradient

[1] *Midcourse Space eXperiment* (Egan et al., 2003)

within the core itself to prevent further fragmentation (which would lead to the formation of larger numbers of lower mass stars), and it also requires high accretion rates to overcome radiative pressure. The star formation rate has been successfully predicted in galactic molecular clouds using the premise that they are supersonically turbulent (Krumholz & McKee, 2005). Additionally, simulations of a cluster with properties similar to those of the Orion nebula cluster have been produced which have an initial mass function (IMF) which is consistent with observations (Krumholz, Klein & McKee, 2012). However, the massive starless cores necessary to this mechanism are predicted to be extremely rare and challenging to detect. Only recently the first very massive starless (potentially $\sim 170\,M_\odot$) core candidate has been detected Kong et al. (2017) using ALMA observations.

Competitive accretion (Bonnell & Bate, 2006) takes a different approach: mass is funnelled from a large reservoir of gas to the inner regions of a molecular cloud through the combined gravitational attraction of lower mass cores. This necessarily creates a system where massive stars are formed in the centre of a molecular cloud with lower mass star formation in the outer regions. This is made possible by the inefficiency of fragmentation (Bonnell et al., 2001), which prevents further fragmentation before mass can be funnelled to the centre of the cluster. The resulting mass segregation (massive stars occupying the centre of the cluster and lower mass stars populating the outer regions) can be observed in Westerlund 1 (Gennaro et al., 2011). However there is significant evidence to suggest that at least in some regions stars with masses $\sim 100\,M_\odot$ appear to not have been formed in over-dense regions and thus could not have been formed via competitive accretion (e.g. Cygnus OB 2; Wright et al. 2014, 2016). Moreover the simulations of Allison et al. (2009) and Spera, Mapelli & Jeffries (2016) predict that star clusters containing massive stars become mass segregated within a few Myr, showing that there is therefore no reason to assume that the massive stars currently observed in clusters formed in a segregated environment. The results of these simulations are reinforced by observational evidence presented in Jaehnig, Da Rio & Tan (2015).

Another mode of massive star formation has been suggested where high mass stars are formed from the merging of lower mass protostars in a tightly bound cluster (Zinnecker & Yorke, 2007). This mechanism of massive star formation was proposed to tackle the radiative pressure problem and explain the tendency for OB stars to be observed in tight clusters. The radiative pressure problem can be avoided by invoking self-shielding dusty discs, and whilst the tightly packed OB clusters issue remains, many massive stars are observed in loosely bound OB associations and it is unclear whether or not tightly bound clusters could

be formed through other mechanisms. Whilst it is physically an apparently valid mechanism for star formation, in practice it would require exceptionally high stellar densities of the order of $10^6\,\mathrm{pc}^{-3}$ (Bonnell & Bate, 2005) and so would be relatively rare as this density is on the order of the highest stellar density measured (Megeath, Wilson & Corbin, 2005).

The high accretion rates required for the massive star formation mechanisms outlined above have been modelled by Hosokawa & Omukai (2009) resulting in 4 distinct evolutionary phases: adiabatic accretion; swelling; Kelvin-Helmholz contraction; main-sequence accretion. The models also set upper mass limits for very high accretion rates ($\dot{M} = 3 \times 10^{-3} M_{\odot}\mathrm{yr}^{-1}$) of $\sim 60 M_{\odot}$ for pre-main sequence stars and $\sim 250 M_{\odot}$ for main sequence stars (at solar metallicity) as the radiative pressure of the protostar and the accretion front inhibits growth. These high accretion rates can therefore account for all stellar masses observed to date.

It has therefore become clear that massive star formation can occur through known physical mechanisms and the radiative pressure problem can be overcome. The exact mechanism for massive star formation remains elusive however, and the observational evidence obtained so far fails to provide a definitive solution to this problem. Both of the two main classes of theory have problems that are yet to be overcome; turbulent core accretion requires a more detailed understanding of the fragmentation properties of magnetised, turbulent gas and the importance of external interactions in crowded clusters whereas competitive accretion faces the challenges of assessing the effect of feedback and explaining the observational evidence of massive starless cores (Tan et al., 2014). It is possible that multiple modes of massive star formation can occur either through the combined effect of different mechanisms, or different mechanisms applying to different initial conditions in a star forming region.

1.3.2 The formation of H II regions

In the later stages of massive star formation, radiative feedback becomes significant through strong stellar winds and hard ionizing radiation fields. Massive stars and protostars emit ionizing photons which strip electrons from atomic hydrogen in the circumstellar environment, creating a volume of ionized plasma surrounding the star known as an H II region. This spherical (for a single massive star) region of ionized gas is also referred to as the Strömgren sphere. The recombination coefficient $\alpha_{\mathrm{rec}}(T)$ is used to describe the rate at which protons and electrons recombine to form neutral hydrogen in the ionized medium. The volumetric

recombination rate is (Stahler & Palla, 2004):

$$\mathcal{R} = n_e n_p \alpha_{\rm rec}(T) \tag{1.33}$$

where n_e and n_p are the number densities of electrons and protons respectively (over any significant volume $n_e = n_p$). Assuming constant electron density and temperature as a function of spatial position, and integrating over a sphere the number of ionizations and subsequent recombinations can be balanced as:

$$\mathcal{N}_* = \frac{4\pi}{3} n_e^2 \alpha'_{\rm rec}(T) R_S^3 \tag{1.34}$$

where $\mathcal{N}_*$ is the rate of ionization events and R_S is then the Strömgren radius which describes the size of the H II region. In this equation $\alpha'_{\rm rec}$ is the combined recombination coefficient for all possible transitions of H I.

After the initial formation of the Strömgren sphere which occurs very quickly, the H II region continues to expand relatively slowly so that a shell-like structure is formed made up of an ionization front, an outer shock front caused by the expansion into the interstellar medium and a fully ionized interior. The process of ionization of a gaseous envelope and subsequent expansion gives rise to ultra-compact H II regions (UCHIIs) and compact H II regions. Whilst the earliest stage UCHIIs have radii <0.1 pc (Churchwell, 1990), the largest H II regions are found when massive stars are formed in large numbers, ionizing very large volumes of gas and can extend over tens or even hundreds of parsecs (e.g. M8, NGC 2244, NGC 3603 and Carina; Kennicutt 1984). Photo-dissociation regions (PDRs) form at the interface between H II regions and the surrounding ISM (Hollenbach & Tielens, 1997, 1999). PDRs result from the interaction from far-UV (6 eV–13.6 eV) photons sourced in young massive stars with the surrounding gas, driving much of the chemistry of star forming regions. These regions are therefore expected in the later stages of massive star formation where densities are significantly lower, allowing for a larger mean-free-path of far-UV photons.

1.3.3 An observational perspective

From an observational point of view the formation of massive stars progresses through four distinct evolutionary phases: the starless/cold core phase, the massive Young Stellar Object (YSO) phase (also known as the hot core phase), the ultra-compact H II region (UCHII) phase and finally the star stops accreting material, expanding the H II region before shedding its

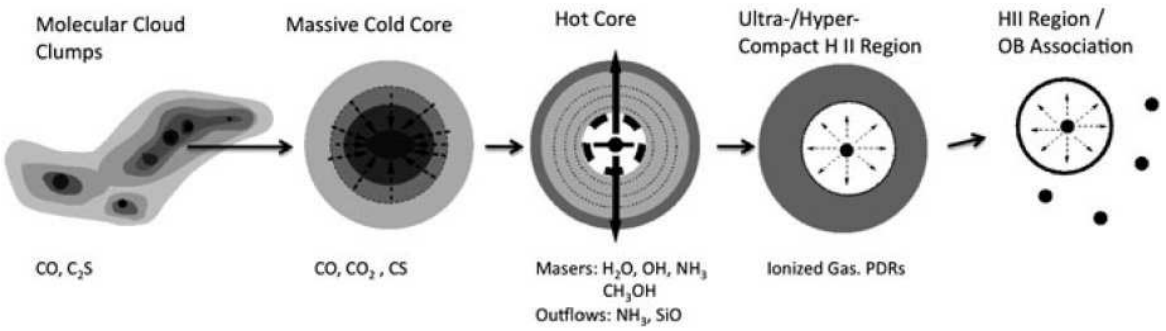

Figure 1.2: A schematic representation of the proposed evolutionary sequence for massive star formation from Schulz (2005).

natal molecular cloud through strong winds (Zinnecker & Yorke, 2007). This sequence is shown schematically in Fig. 1.2 (from Schulz 2005).

Massive YSOs appear as unresolved point sources in mid-infrared imaging with little or no radio continuum emission unless an HII region or an ionised wind is present. Sub-mm line emission observations can be used to trace extended outflows originating from massive protostars including CO (e.g. Ridge & Moore 2001) and SiO (e.g. Gibb, Davis & Moore 2007). Evidence of fast outflows (from H_2 and forbidden [Fe II] lines) and compact discs (from fluorescent Fe II line emission and CO bandhead emission) has been observed using near-infrared long-slit spectroscopy (Porter, Drew & Lumsden, 1998; Lumsden et al., 2012; Cooper et al., 2013). Integral field spectroscopy in the near-infrared of small numbers of Galactic massive YSOs have detected more direct evidence of outflows in the form of Brγ emission and evidence of Keplarian rotating CO gas (Davies et al., 2010; Murakawa et al., 2013). Outflows from massive protostars are revisited in more detail in Section 1.3.4. The high levels of extinction present in galactic massive YSOs mean that typically these objects can not be directly observed in wavelengths shorter than the near-infrared. As a protostar develops into a massive star within the dense natal cloud of gas and dust the continuum emission begins to ionize the surrounding environment to form a UCHII region.

The first major analyses of massive YSOs were made possible using the *Infrared Astronomical Satellite* (IRAS). Wood & Churchwell (1989) applied a two-colour selection criterion to the IRAS point source catalogue, identifying 1646 embedded massive stars in the Galactic plane (along with 71 in the Magellanic Clouds) and through comparison with optically visible O-type stars inferred that massive stars spend 10–20 % of their lifetimes embedded in molecular clouds. Indeed, using data from the *Midcourse Space Experiment* (MSX) massive stars have been estimated to spend 2–4$\times10^5$ yr in the massive YSO phase depending on the

final mass of the star (Davies et al., 2011; Mottram et al., 2011a). This means that despite the high luminosities of massive YSOs they present a challenge to study even in infrared wavelengths because they are intrinsically rare in our Galaxy.

The largest survey of massive YSOs to date is the RMS survey (Lumsden et al., 2013) with an aim to map and study galactic massive YSOs in the region of $10^\circ < l < 350^\circ$. within the flux and colour cuts in the mid-infrared (8, 14 and 24 μm) and the near-infrared (*J-, H-* and *K*-bands) from MSX and 2MASS data defined in Lumsden et al. (2002) it has achieved a completeness greater than 95%. After the initial source selection of $\sim$ 2000 sources, a number of follow up observations have been carried out in the far-infrared and sub-mm (Mottram et al., 2010, 2011b), CO mm line observations (Urquhart et al., 2007b, 2008), in the radio with resolution $\sim 1''$ resolution (Urquhart et al., 2007a, 2009; Hoare et al., 2012; Purcell et al., 2013) and near-infrared *H*- and *K*- band spectroscopy (Cooper et al. 2013; Lumsden et al. in preparation; Ward et al. in preparation). This has lead to the classification of $\sim$ 600 sources as massive YSOs and $\sim$ 500 sources as UCHIIs. The RMS survey therefore provides the most comprehensive catalogue of massive YSOs to compare samples from the Magellanic Clouds with.

The *Spitzer* Galactic Legacy Infrared Mid-Plane Survey Extraordinaire (GLIMPSE; Benjamin et al. 2003, Churchwell et al. 2009) has also contributed valuable data to the massive star formation community through imaging the entire Galactic plane in all four *Spitzer*/IRAC bands (3.6, 4.5, 5.8 and 8.0 μm). Whilst this survey lacks the longer wavelength data of the RMS survey, meaning that it cannot use the same colour/luminosity cuts to select YSO candidates, the significant improvement in spatial resolution has led to a number of more targeted studies of massive star forming regions (e.g. Mercer et al. 2007, Smith et al. 2010). GLIMPSE has also led to the identification of over 300 massive YSOs by utilising the higher spatial resolution to identify extended green objects thought to be associated with protostellar outflows, using the 4.5 μm emission (Cyganowski et al., 2008).

As shown in the previous sections, discs play an indispensable role in our current understanding of massive star formation. However due to the relatively large distances to massive YSOs and their deeply embedded nature the detection of discs around massive protostars has proved problematic (Zhang, 2005) and only a few examples of discs around massive protostars have been detected (e.g. Shepherd & Kurtz 1999; Patel et al. 2005). Interferometric studies have been able to resolve increasing numbers of disc structures in the sub-mm using facilities such as the Sub-mm Array (SMA; e.g. Chen et al. 2016, Ilee et al. 2016). Disc properties

in massive YSOs can also be determined using the near-infrared CO bandhead red-wards of 2.25 μm, revealing emission properties consistent with the presence of Keplarian rotating discs (Ilee et al., 2013). Spatially resolving the velocity profile of discs at shorter wavelengths has only recently become a possibility using adaptive optics modules (e.g. Davies et al. 2010, Murakawa et al. 2013).

Observationally, UCHIIs and compact H II regions appear very similar to massive YSOs in the mid-infrared. The emission peaks in the same $50 - 100\mu$m range as massive YSOs and they display many of the same spectral features in the mid-infrared and near-infrared. Unlike massive YSOs, radio emission is typically strong due to free-free emission in the ionized gas (Hoare, 2005). In addition H II regions do not exhibit the same bipolar outflows observed towards massive YSOs and thus it is expected that the rates of accretion have slowed considerably by the time the UCHII region is formed (Hoare, 2005). In the near-infrared, all of the *H*- and *K*- band Brackett series emission lines are invariably present (e.g Cooper et al. 2013, Ward 2013, Ward et al. in preparation) which is often not the case in massive YSOs (although the entire Brackett series appears to be present in later evolutionary stage massive YSOs which are in the process of forming UCHIIs) and the near-infrared spectra of HII regions tend to appear considerably less red due to a lower dust excess. Formed at the edges of H II regions, PDRs are commonly observed as bright regions of 3.3 μm poly-cyclic aromatic hydrocarbon (PAH) emission, H_2 emission and CO emission as in the Orion Bar (Tielens et al., 1993). Indeed the total H_2 luminosity of molecular clouds is dominated by emission from PDRs, even in clouds exhibiting strong shocks (Luhman et al., 1994; Luhman & Jaffe, 1996).

Maser emission in the radio wavelength regime represents one of the key tracers of massive star formation (Fish, 2007). OH masers are formed through the radiative excitation of molecules by massive stars and are therefore usually associated with bright near-infrared sources and H II regions (Weaver et al., 1965; Ruiz-Velasco et al., 2016). Methanol masers represent another key signpost towards massive star forming regions (Menten, 1991; Walsh et al., 1998; Hill et al., 2005) forming both from the impact of a wind with interstellar gas and the ionizing radiation field of massive stars (Stahler & Palla, 2004). The production of water masers detected towards star forming regions require high densities and energies which are only present at the shock fronts at the interface between powerful outflows and the surrounding ISM. H_2O maser emission is produced when the water molecules dissociated at the shock front reform in the cooler downstream environment (Schulz, 2005). In some cases

water maser emission is also believed to be associated with discs (Seth, Greenhill & Holder, 2002; Gallimore et al., 2003)

1.3.4 Outflows from massive protostars

The accretion process onto massive stars and protostars present an extremely energetic environment. The feedback from massive YSOs is therefore one of the key areas of interest in star formation from both observational and theoretical points of view. As massive protostars are necessarily deeply embedded in their natal molecular clouds, the various forms of feedback often provide some of the best indicators of the physical processes within a massive YSO.

Observationally, outflows from YSOs are commonly observed using molecular tracers in the infrared or sub-mm or alternatively maser emission in the radio regime (see above). *K*-band H_2 1–0S(1) emission (2.1218 μm) sourced in molecular outflows from protostars have been observed as part of the UKIRT Widefield Infrared Survey for H_2 (UWISH2; Froebrich et al. 2011) with outflow lengths ranging from 0.1 to 3 pc with 25% of the sample on scales of 1 pc or larger (Ioannidis & Froebrich, 2012).

One of the most noticeable features of outflows from massive protostars is that they exhibit a wide range of properties from very collimated bipolar outflows (e.g. Forbrich et al. 2009; Davies et al. 2010; Varricatt et al. 2010; Varricatt 2011; Wang et al. 2011) to broad, poorly collimated outflows (e.g Fallscheer et al. 2009; Beuther et al. 2010; Beltrán et al. 2011). The question of why we see such a wide range of morphologies is therefore of particular interest as it is likely strongly related to the accretion/outflow balance in massive YSOs of different ages and/or masses. Recent theoretical works by Kuiper, Yorke & Turner (2015) and Tanaka, Tan & Zhang (2016) have examined the evolution of protostellar outflows as a function of the mass and age of the protostar. Kuiper, Yorke & Turner (2015) find that in early stage YSOs, strongly collimated outflows are expected as a result of kinematic feedback (i.e. feedback from the accretion process) whilst as the protostar evolves, radiative acceleration from the surface of the star becomes increasingly important, broadening the outflow. The study of Tanaka, Tan & Zhang (2016) focuses mainly of the formation of H II regions within the cavities created by and confined within disc wind outflows from massive protostars. They found that in the direction perpendicular to the disc an ionized H II region is formed, confined by the disc wind whilst the outer disc surface (perpendicular to the outflow) is not ionized.

1.4 The role of metallicity in star forming environments

The chemical composition of a star forming environment determines the evolutionary progression of a molecular cloud core through the starless-core and protostellar phases and onto the main sequence. Whilst the ISM is primarily made up of hydrogen and helium ($\sim 98\%$ at solar metallicities, Stahler & Palla 2004), it is the presence of heavier elements, the metals, that drive much of the star formation process. I discuss here how many important ingredients of the star formation process could be affected by low metallicity.

1.4.1 Heating and cooling

In order to develop the dense starless cores necessary for massive star formation heat must be dissipated to prevent support from thermal pressure from inhibiting cloud collapse. Whilst hydrogen and helium make up the majority of mass within a cloud, they are unable to efficiently radiate away an appreciable fraction of the total thermal energy content (Stahler & Palla, 2004). Molecular hydrogen is a relatively inefficient cooling agent through molecular line emission because the energy levels of H_2 molecules are widely spaced due to the light and symmetric nature of the molecule. This issue is compounded by the strongly forbidden nature of odd J to even J transitions in H_2 due to the requirement of a change in nuclear spin to transition between ortho and para states meaning that the first rotational transition accessible is the $J = 2 - 0$ with an energy separation of $\sim$510 K (Klessen & Glover, 2014). Thus H_2 is not an efficient coolant at the low temperatures characteristic of molecular clouds.

Returning to the Jeans mass equations (1.24 and 1.32) it is immediately clear that changing the metallicity will affect the mean molecular mass, but given that metallic species only make up a small proportion of the ISM by mass this effect remains minor. More critical is the effect on the temperature, T. Radiation via the fine-structure lines of carbon and oxygen and the rotational transitions of metallic molecules such as water and CO provide the most efficient cooling mechanisms. In particular ^{12}CO is the dominant cooling agent for molecular clouds in the earliest stages of star formation where densities are relatively low; as the density increases other species (C, O_2 and H_2O) become increasingly important (Tielens, 2005). therefore the reduced cooling rates resulting from low metallicities means that lowering the metallicity of a cloud will necessarily increase the Jeans mass. Temperatures at densities typical of pre-stellar cores ($10^4\,\mathrm{cm}^{-3}$) have been predicted to increase by a factor of 2 over a change from solar metallicity to Z$= 0.1\,Z_\odot$, corresponding to a factor of $\sim$3 increase in the

Jeans mass (Glover & Clark, 2012). It is therefore apparent that if the metallicity of a star forming region is reduced, the efficiency of cooling is likely to be effected which in turn could have a significant effect on the initial isothermal collapse of molecular cloud cores and on continued fragmentation processes.

1.4.2 Radiative pressure, winds and outflows

Radiative pressure plays a key role in the regulation of massive star formation as discussed in the Section 1.3. However, the effects of radiative pressure are highly dependant on the metallicity of the material on which the pressure is acting. Through radiative acceleration of particles, strong stellar and disc winds are formed at the sites of massive star formation. The process is a scattering mechanism in which a photon emitted from the photosphere of the star of frequency $\nu_0(1 + \frac{u}{c})$ is absorbed by a particle with an initial velocity u and later re-emitted. The average increase of energy is $h\nu_0/c$ where ν_0 is the frequency of the photon once redshifted due to the motion of the particle away from the photosphere.

This absorption and re-emission requires an electronic transition to take place within the particle and thus this process is most dominant in common ions of heavier elements such as carbon, oxygen and nitrogen. It can therefore be expected that in low metallicity environments, the effects of radiative pressure are significantly reduced due to the higher gas-to-dust ratio. This in turn could lead to an increase in the observed accretion rates as radiative acceleration cannot act as efficiency as a support mechanism.

Self-shielding dusty discs appear to play an essential role in continued accretion onto protostars allowing stars in excess of $10\,\mathrm{M}_\odot$ to form as described in Section 1.3. Whilst it is possible that gas in discs can provide a significant level of shielding (Kuiper & Yorke, 2013), the densities of gas required to meet the same level of shielding as a dusty disc would have to be significantly higher. The rate of accretion onto a protostar is likely to be significantly increased by weaker effects of radiative acceleration; however, the lower levels of shielding in protostellar discs may hamper accretion and/or lower disc lifetimes.

1.4.3 Disc dispersion

One of the key considerations of massive star formation is the lifetime of the discs from which massive protostars are able to accrete material. A number of mechanisms are proposed for the dispersal of protostellar disks, which must necessarily determine the lifetime of the disk and hence the point at which accretion halts. The effects of metallicity on disc lifetimes are

discussed in De Marchi, Panagia & Romaniello (2010); De Marchi et al. (2011); Spezzi et al. (2012); De Marchi, Beccari & Panagia (2013), primarily focused on lower mass pre-main sequence stars in the Magellanic Clouds in which they found evidence of longer disc lifetimes than for similar Galactic sources. I provide a brief review here of effects which could be considered relevant to studies of massive YSOs in low metallicity environments.

The disc dispersion rate due to viscous accretion via the transfer of angular momentum outwards, allowing material to fall inwards onto the protostar (Hollenbach, Yorke & Johnstone, 2000) is predicted to be lower at low metallicities (Durisen et al., 2007). This should increase not only the lifetime of discs in low metallicity environments but also decrease the rate at which material is accreted from the disc onto the protostar.

Photo-evaporation is the radiative heating of discs due to energetic photons. Theoretical studies suggest that photo-evaporation via X-rays is more efficient than photo-evaporation caused by extreme-UV (EUV) radiation by up to two orders of magnitude (Alexander, Clarke & Pringle, 2006a,b; Owen et al., 2010). Ercolano & Clarke (2010) investigated the relationship between metallicity and the lifetimes of circumstellar discs and found that X-ray wind rates increase as a function of metallicity ($t_{phot} \propto Z^{0.52}$), thus reducing the lifetimes of discs due to photo-evaporation.

As well as internal photo-evaporation of the disc due to the formation of the star itself, external photo-evaporation due to the presence of nearby massive stars is also a possible influence on the disc dispersal time. This effect works primarily via the heating of gas in the outer disk from far-UV photons (Spezzi et al., 2012) and is observed in the proplyds in Orion (Bally, O'Dell & McCaughrean, 2000) and is likely to affect sources in the most active star forming regions in the Magellanic Clouds.

1.4.4 Chemistry

Polycyclic aromatic hydrocarbons (PAHs) are thought to be the cause of a range of mid-infrared emission bands via the bending and stretching modes of C–C and C–H bonds resulting from exposure to UV photons (Sandstrom et al., 2010). PAH emission bands are also typically very bright and have been suggested as a means of tracing star formation up to high redshifts although the production of PAH emission is heavily dependant on metallicity and stellar populations which are not currently forming stars also contribute to the 8 μm emission (Calzetti et al., 2007). PAH emission is also commonly used as a diagnostic of evolutionary state of massive YSOs (e.g. Seale et al. 2009).

One of the key findings in low metallicity galaxies is a relatively low detection rate of PAH bands, possibly due to PAH destruction as a result of the decreased levels of dust shielding in low metallicity environments (Madden et al., 2006). Another explanation for the lack of PAH molecules observed in low metallicity galaxies is that the carriers of PAH emission may not be formed in the lowest metallicity galaxies (Engelbracht et al., 2005).

1.4.5 The structure of the interstellar medium

The metallicity of a region is likely to have a profound effect on the structure and behaviour of the ISM. The lower dust abundances in low metallicity environments mean less shielding to high energy photons and therefore a larger mean free path length for UV photons (Madden et al., 2006). Indeed, detailed models of the low-metallicity ISM of the galaxy NGC 4214 indicate that increased porosity is an intrinsic characteristic of the low-metallicity ISM (Dimaratos et al., 2015). Moreover Cormier et al. (2015) find (using data from the *Herschel* Dwarf Galaxy Survey) that the ionized gas/PDR filling factor is ∼4 times higher in low metallicity dwarf galaxies than in metal-rich galaxies, indicative of a more porous ISM structure in low metallicity dwarfs.

The porosity of the low metallicity ISM allows UV photons to permeate over long distances, creating a harder radiation field (proportionately higher far-UV flux) and ionizing gas which lies farther from the sources of excitation (e.g. Chevance et al. 2016). The ISM of the galaxy NGC 1569, which has a similarly low metallicity to the SMC, appears to be very clumpy (Galliano et al., 2003). This means that the ISM in the low metallicity Magellanic Clouds is expected to be clumpier and more porous than that of our own Galaxy which is likely to have a significant effect on the observed feedback from massive star formation.

1.5 The Magellanic Clouds

The Magellanic Clouds (shown in Fig. 1.3) present a unique opportunity to study star formation in environments that differ significantly from the that of the Milky Way. Both have significantly lower metallicities than the Milky Way (∼0.5 and ∼0.2 $Z_{\odot}$) and are affected by tidal forces due to their interaction with each other and with the Milky Way. The tidal forces may have a profound impact on star formation in the Magellanic Clouds as large scale gravitational forces have the potential to increase the rate of triggered star formation or disrupt star forming regions.

The Large Magellanic Cloud (LMC) is one of the closest neighbouring dwarf galaxies to

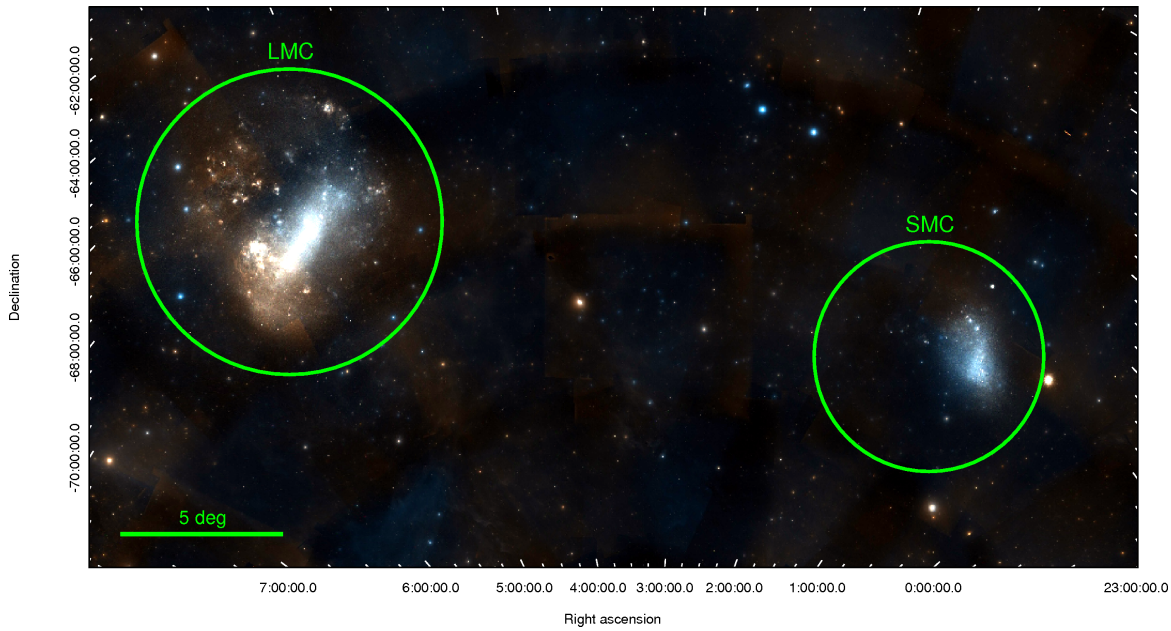

Figure 1.3: Optical three colour image of the Magellanic Clouds system using data from the Digitised Sky Survey (DSS). Red – POSS2 Red, blue – POSS2 Blue, green – average of the red and blue images.

the Milky Way and hosts the most active starburst region in the local group: 30 Doradus (which is revisited in more detail in Chapter 6). Star formation in the LMC appears to be largely limited to clumps, clusters and super-bubbles distributed across the galaxy and it is therefore a possibility that star formation in the LMC propagates through feedback from stellar winds (Meixner et al., 2006). It has been suggested that this same feedback process will ultimately quench the star formation process in the LMC through the dissipation of the ISM (Yamaguchi et al., 2001; Israel et al., 2003).

The Small Magellanic Cloud (SMC) is a highly irregular galaxy which consists of three key regions; the bar, the wing and the tail (which is in fact a high density region of the Magellanic Bridge). The SMC exhibits star formation regions in a highly irregular distribution whereas the older stars are smoothly distributed throughout the galaxy (Gonidakis et al., 2009). This appears to be consistent with the notion that the interaction with the LMC as they pass one another is the main driver of star formation in the SMC.

Unlike studies of star formation in our own galaxy, the Magellanic Clouds present the opportunity to study star formation with little confusion along the line of sight (Meixner et al., 2006) and with less uncertainty in distance measurements. Furthermore it is not possible to accurately characterise star formation as a global process across our entire galaxy as we can only observe our galaxy from within. The Magellanic Clouds provide a unique opportunity to be able to study the star formation process on a galactic scale whilst still

being close enough for us to be able to study individual objects at relatively high spatial resolutions. The LMC has a particularly favourable viewing angle which means that there is only a small variation in distance across the galaxy.

Whilst the SMC is slightly further away and at not as an advantageous angle, the line of sight is rarely so crowded that resolving individual objects is impossible and with its low metallicity and tidally stripped nature, there is much potential in studying star formation in the SMC as an environment which differs significantly from that of our own Galaxy. In addition it should be noted that galaxies in the high redshift universe are extremely metal-poor and thus star formation in the SMC may be able to provide a template for star formation in the early universe.

The composition of the Magellanic Clouds is one of the key reasons that make them an interesting laboratory for the study of star formation. The often quoted metallicities of the Magellanic Clouds are $0.5\,Z_{\odot}$ and $0.2\,Z_{\odot}$ for the LMC and the SMC, respectively (Dufour, Shields & Talbot, 1982; Bernard et al., 2008). This value is based on the abundances of Oxygen in the LMC and SMC compared to solar abundances. Whilst these proportions are roughly valid for the majority of metals, there are some key departures including carbon and nitrogen (Dufour, Shields & Talbot, 1982).

1.5.1 Distances

Distances towards the Magellanic Clouds can be difficult to determine. They are obviously too far away for parallax to be effective and thus the study of light-curves from Cepheid variables and eclipsing binaries are used to determine distances. Groenewegen (2000) made use of the Period-Luminosity relations of Cepheid variables in the LMC to calculate distances of 52.48 ± 2.73 kpc and 51.29 ± 4.18 kpc based on $V+I$ and $K-$band photometry, respectively. Laney, Joner & Pietrzyński (2012) utilised bright red clump stars to determine distances to the LMC of 49.89 ± 1.40 kpc in the H-band and 49.43 ± 0.46 kpc in the K-band which is in agreement with the result from Groenewegen (2000). In this work a distance of 49.4 ± 0.5 kpc will be assumed to the LMC, in line with the K-band observations of Laney, Joner & Pietrzyński (2012).

The SMC does not present as favourable a viewing angle as the LMC and thus it has a greater line of sight depth and greater uncertainty in the distances to individual objects. The most precise distance to the SMC provided by Groenewegen (2000) is 66.82 ± 3.45 kpc. Two more recent studies of eclipsing binaries (Harries, Hilditch & Howarth, 2003; Hilditch,

Howarth & Harries, 2005) and one of bump Cepheids (Keller & Wood, 2006) have found lower distances of 59.98±2.83 kpc, 60.59±0.98 kpc, and 61.77 ±0.68 kpc, respectively. On the other hand one of the most recent studies of eclipsing binaries in the SMC (North et al., 2010) gives a distance of 66.4 ± 0.9 kpc claiming that it is likely this longer distance is the correct one based on better observational data available in the 2010 study than in previous work. As well as the distance, the line of sight depth of the SMC is also important to consider. Assuming a Gaussian distribution of stars, the 2σ depth of the SMC calculated by North et al. (2010) is 7.6 kpc. Given the significant depth of the SMC, a distance of 60±4 kpc is assumed in this thesis.

The systemic velocities of the Magellanic Clouds are $\sim$250 km s^{-1} and $\sim$160 km s^{-1} for the closer LMC and more distant SMC, respectively (Feast, Thackeray & Wesselink, 1961).

1.5.2 Star formation studies in the Magellanic Clouds

As briefly mentioned in Section 1.3.3, IRAS was used to select 71 embedded massive stars in the Magellanic Clouds but due to its relatively poor spatial resolution, IRAS data is of limited use for studies at the distances of the Magellanic Clouds. Whilst highly targeted studies of star formation in the Magellanic Clouds has been possible for some time (e.g. Olsen 1999; Walborn et al. 1999; Gorjian et al. 2004) as well as star formation history studies (e.g. Olsen 1999; Smecker-Hane et al. 2002; Harris & Zaritsky 2004), the *Spitzer* Space Telescope (*Spitzer*; Werner et al. 2004) and the *Herschel* Space Observatory (*Herschel*; Pilbratt et al. 2010) have revolutionised the study of massive star formation in the Magellanic Clouds. *Spitzer* and *Herschel* have allowed the systematic identification and analysis of YSOs on a parsec scale across the whole areas of the LMC and SMC for the first time.

The *Spitzer* SAGE survey

The *Spitzer* Surveying the Agents of Galactic Evolution (SAGE; Meixner et al. 2006) survey observed the whole LMC at wavelengths of 3.6, 4.5, 5.8, 8.0 (IRAC, Fazio et al. 2004), 24, 70 and 160 μm (MIPS, Rieke et al. 2004). The 3.6, 8.0 and 70 μm SAGE mosaics for the entire LMC are shown as a composite image in Fig. 1.4. Over 2000 YSO candidates have been selected using photometry from the *Spitzer*-SAGE point-source catalogue by Whitney et al. (2008), Gruendl & Chu (2009) & Carlson et al. (2012). These studies all utilised colour-magnitude diagrams (CMDs) and colour-colour diagrams to select YSO candidates but the manner in which they determine the cuts in the colour-magnitude space to select candidates

differs significantly.

The Whitney et al. (2008) catalogue used model massive YSO spectral energy distributions (SEDs) to predict the location of massive YSOs in the CMDs and then using catalogues of known contaminants such as planetary nebulae (e.g. Leisy et al. 1997) to determine regions of the CMDs where contaminants dominate the sample. This process yielded a sample of 1197 YSO candidates in the LMC with a conservative upper limit of contamination of 55 % ; however this catalogue is likely to exclude the most massive YSOs and more evolved massive YSOs as these illuminate a large volume and thus do not appear as point sources (Whitney et al., 2008).

Gruendl & Chu (2009) adopted a different approach starting with the 8.0 μm versus (4.5-8.0) CMD to eliminate foreground sources and select YSO candidates, which were then examined individually taking into consideration the morphology, environment and SED for each source. This method yielded a total of 855 definite YSOs along with 317 probable YSOs giving a total of 1172 as well as an additional 213 objects for which a YSO nature could not be definitively excluded. This process of using a single colour selection criteria excludes YSO candidates which are less massive than $\sim$4 $M_{\odot}$ (Carlson et al., 2012).

Finally, the Carlson et al. (2012) photometric study combined SAGE photometry with photometry in the optical and near-infrared from the Magellanic Clouds Photometric Survey (MCPS; Zaritsky, Harris & Thompson 1997) and the InfraRed Survey Facility (IRSF; Kato et al. 2007), respectively. Nine star forming H II regions were targeted in the LMC including LHA 120-N113 and LHA 120-N160 (Henize, 1956) which are discussed in Chapters 3 and 6 of this thesis, respectively. Five mid-infrared colour-magnitude combinations were used to select a sample of YSOs which were then combined with shorter wavelength photometry from 2MASS. The grid of 20 000 YSO SED models and corresponding fitting program of Robitaille et al. (2006, 2007) were then used to determine the candidates which are fit well by the YSO models, whilst sources best fit by model contaminant SEDs (e.g. galaxies, AGB stars etc.) were discarded. The Carlson et al. (2012) catalogue lists 1045 YSO candidates without the lower mass limit of the Gruendl & Chu (2009) catalogue, consisting of 918 new candidates and only 127 previously identified YSO candidates.

A number of spectroscopic studies towards these sources have been carried out by Shimonishi et al. (2008), Seale et al. (2009), Oliveira et al. (2009), Shimonishi et al. (2010), van Loon et al. (2010a) and Woods et al. (2011).

The Shimonishi et al. (2008) and Shimonishi et al. (2010) studies focused on 3.05 μm and

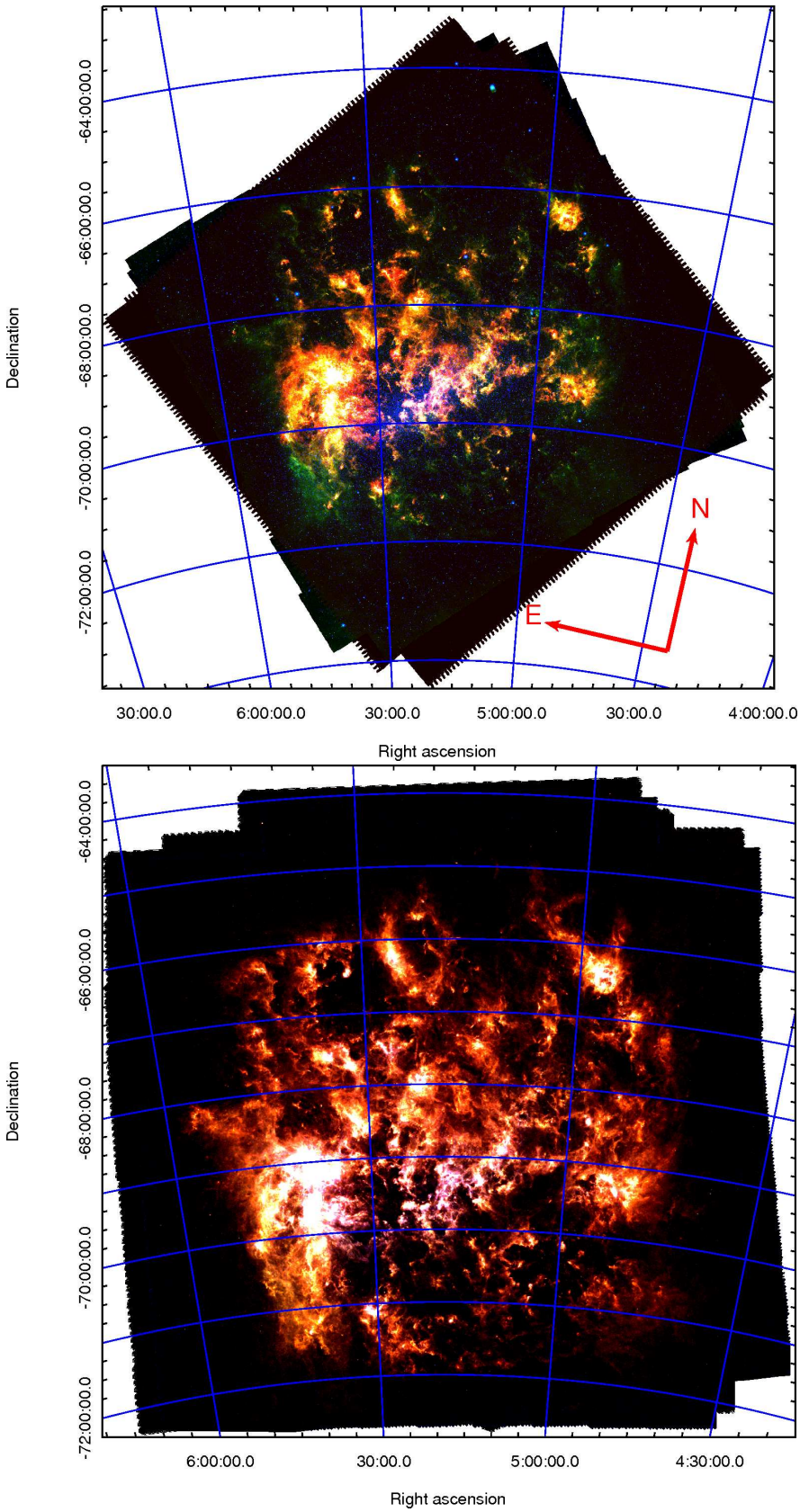

Figure 1.4: Upper panel: *Spitzer*-SAGE three colour image of the LMC; red – 70 μm (MIPS), green – 8.0 μm (IRAC), blue – 3.6 μm (IRAC). Lower panel: *Herschel*-HERITAGE three colour image of the LMC; red – 500 μm (SPIRE), green – 250 μm (SPIRE), blue – 100 mum (PACS).

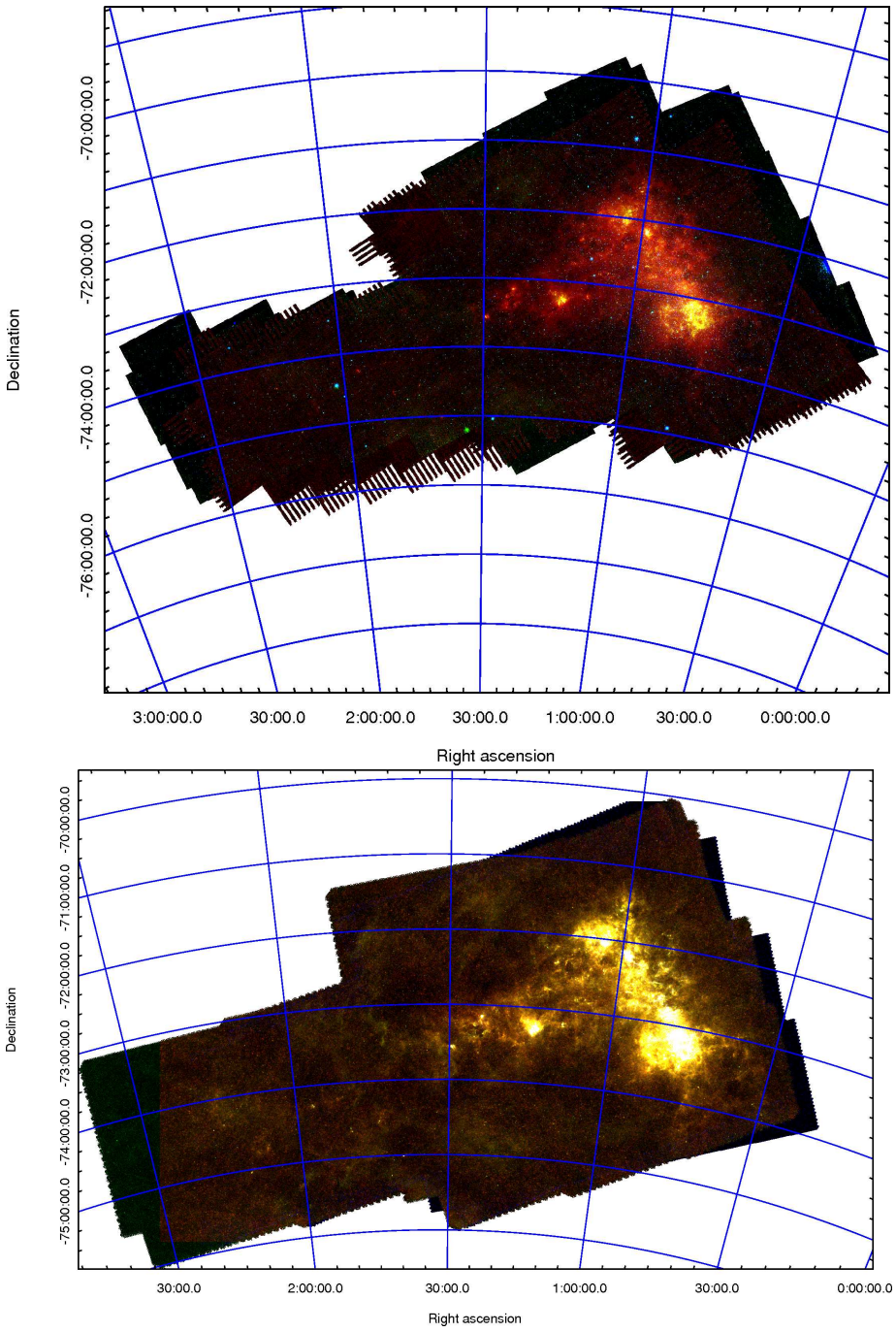

Figure 1.5: Upper panel: *Spitzer*-SAGE-SMC three colour image of the SMC; red – 70 μm (MIPS), green – 8.0 μm (IRAC), blue – 3.6 μm (IRAC). Lower panel: *Herschel*-HERITAGE three colour image of the SMC; red – 500 μm (SPIRE), green – 250 μm (SPIRE), blue – 100 mum (PACS).

4.27 μm H_2O and CO_2 ice features towards 12 YSOs as part of the *AKARI* IRC survey of the LMC (Ita et al., 2008); they found a CO_2/H_2O ice column density ratio significantly higher than that observed in our own Galaxy whilst the CO/H_2O ratio is similar to that of the Milky Way which they attribute to a harder UV radiation field and/or higher dust temperatures in the LMC. Oliveira et al. (2009) also analyses ice features but towards 15 sources as part of the SAGE-Spec legacy program, a follow-up spectroscopic study of SAGE sources using *Spitzer*-IRS (Houck et al., 2004). The 6 μm H_2O and 15 μm CO_2 ice features were observed in Oliveira et al. (2009), again finding an over-abundance of CO_2 ice which is possibly the result of higher dust temperatures leading to increased CO_2 production; Oliveira et al. (2011) find both CO and CO_2 were found to be enhanced in the LMC. The van Loon et al. (2010a) study used *Spitzer*-MIPS data to perform low resolution infrared spectroscopic analysis of 48 compact sources in the LMC of various types. This included six YSOs and seven possible YSOs, detecting [O III] emission towards two YSOs, indicative of the presence of very energetic UCHIIs.

Seale et al. (2009) presented an analysis of 297 YSO candidates in the LMC using *Spitzer*-IRS spectra, confirming 277 sources as YSOs and eliminating 20 contaminants. The YSOs were also classified into types based on the dominant features observed the spectra. The S, P and O types by Seale et al. (2009) indicate spectra dominated by silicate absorption, PAH emission and silicate emission respectively, whilst an E following the primary classification indicates the presence of fine structure emission. Note that the Seale et al. (2009) classification scheme does not consider the presence of ices, which are indicative of shielded colder regions and are thus expected to be found in early stage YSOs.

Similarly Woods et al. (2011) performed a mid-infrared *Spitzer*-IRS spectral classification of point sources in the LMC, including 29 YSOs and two H II regions. The spectral types for YSOs from Woods et al. (2011) are also based on the spectral features detected; ice absorption (G1), silicate absorption (G2), PAH emission (G3) and silicate emission (G4). These classifications are thought to represent an evolutionary sequence from early-stage YSOs (G1) to later-stage YSOs (G3) with G4 sources most likely representing Herbig AeBe stars. This classification scheme is in the process of being applied to all YSOs in the LMC for which IRS spectra are available (Jones et al. in prep).

The S^{3}MC and SAGE-SMC surveys

The "*Spitzer* Survey of the Small Magellanic Cloud" (S^{3}MC; Bolatto et al. 2007) imaged the relatively dense, star forming region of the SMC body at 3.6, 4.5, 5.8, 8.0, 24, 70 and 160 μm. The S^{3}MC survey used strict colour-magnitude criteria to select YSO candidates in order to minimise the number of contaminants in the catalogue which biased the sample towards the brightest YSOs. This yielded a total of around 280 YSO candidates.

The "Surveying the Agents of Galaxy Evolution in the Tidally Stripped, Low Metallicity Small Magellanic Cloud" (SAGE-SMC; Gordon et al. 2011) mapped the full SMC over the same wavelength range as S^{3}MC. RGB images of the SAGE-SMC mosaics are shown in Fig. 1.5. The SAGE-SMC survey culminated in the production of a two epoch, photometric point source catalogue with over 2 000 000 entries for the SMC.

The photometric catalogues of S^{3}MC and SAGE-SMC were used by Sewiło et al. (2013) to identify a sample of 742 high-reliability YSO candidates in the SMC along with 242 possible YSOs based on a similar combination of colour-magnitude cuts, morphologies and SED analysis as for the Gruendl & Chu (2009) catalogue of the LMC. A spectroscopic analysis of 34 of these high probability YSOs was subsequently carried out by Oliveira et al. (2013) with *Spitzer-IRS*. Whilst far from a complete sample, these 34 sources are representative a wide range of mid-infrared colour-colour and colour-magnitude parameter space, likely indicative of a range of ages and masses for masses of at least $\sim$10 $M_\odot$ (Oliveira et al., 2013). These sources are therefore only representative of the $\sim$150 highest mass ($M > 9\,M_\odot$) sources in the Sewiło et al. (2013) sample. Of these, 33 were confirmed to be massive YSOs and they were classified using both the Seale et al. (2009) and Woods et al. (2011) classification schemes, exhibiting a wide range of properties and hence evolutionary states. This study also utilised ancillary optical and radio data to aid in the classification and discussion of the sources. Further details of this study are given in Chapter 4 as it forms the basis of the target selection criteria for the observations presented in that Chapter.

The *Herschel* HERITAGE survey

The *Herschel* HERITAGE ("*Herschel* Inventory of the Agents of Galaxy Evolution"; Meixner et al. 2010, 2013) survey provided coverage over the entire LMC and SMC at wavelengths of 100, 160, 250, 350 and 500 μm (see Figs. 1.4 and 1.5) with the aim of investigating the life cycle of matter in the Magellanic Clouds. HERITAGE therefore maps significantly cooler material than the SAGE surveys and thus is useful for identifying the earliest stage YSOs as

these are deeply embedded, surrounded by cool material and must be associated with a large cool reservoir from which they can accrete material.

The HERITAGE survey was used to obtain integrated dust masses of (7.3±1.7) × 10^5 and (8.3±2.1) × $10^4\,M_\odot$ for the LMC and SMC respectively (Gordon et al., 2014). The gas-to-dust ratios found from the HERITAGE survey were $380^{+350}_{-130} \pm 3$ and $1200^{+1600}_{-420} \pm 120$ (where the uncertainties follow ±systematic uncertainty±random uncertainty) in the LMC and SMC, respectively (Roman-Duval et al., 2014). This is significantly higher that the gas-to-dust ratio computed for our own Galaxy (∼150, Jenkins 2009, Gordon et al. 2014) and consistent with previous measurements of the gas-to-dust ratios by Welty, Xue & Wong (2012) of 450±220 and 900±450 for the LMC and SMC, respectively.

Sewiło et al. (2010) showed that the *Herschel* HERITAGE survey data could be used to fit SEDs of YSOs to obtain physical parameters as well as discover the first stage 0 YSOs in the Magellanic Clouds. One of the sources studied in Sewiło et al. (2010) is re-visited in this work (see Chapter 3). The HERITAGE point source catalogue and subsequent photometric analysis presented in Seale et al. (2014) identifies 2493 *Herschel* YSO candidates in the LMC and 425 in the SMC with approximately 73% and 35% being newly identified in the LMC and SMC, respectively.

Other star formation studies relevant to this work

A method of photometrically identifying PMS stars and determining their accretion rates is presented in De Marchi, Panagia & Romaniello (2010). They then applied this method to a photometric study of a field around SN 1987A near the Tarantula nebula (also known as 30 Doradus) in the LMC (Panagia et al., 2000). Spezzi et al. (2012) performed a study using the same techniques on a sample of ∼1000 PMS stars in the LMC situated between SN 1987A and 30 Doradus with ages in the range 1–14 Myr. Two samples have been similarly studied in two star forming regions NGC 346 and NGC 602 in the SMC, presented in De Marchi et al. (2011) and De Marchi, Beccari & Panagia (2013) respectively. These studies found that PMS stars in the Magellanic Clouds exhibit both higher accretion rates and longer disc lifetimes than their Galactic counterparts and the results are suggestive a strong link between accretion rates and metallicity.

On the other hand Kalari & Vink (2015) performed a spectroscopic analysis of mass accretion rates of PMS stars in the low metallicity Galactic star forming region Sh 2-284 ($Z_{\mathrm{Sh2\text{-}284}}$ ∼0.2 $\mathrm{Z}_\odot$) and find no evidence of a systematic change in the mass accretion rate

with metallicity.

Spitzer data has also been used in addition to complementary optical and near-infrared photometry to study the YSO population of the Magellanic Bridge (Chen et al., 2014), the nearest tidally stripped low metallicity region to our galaxy. They found that in the Magellanic Bridge YSOs were more likely to be associated with optical counterparts than in the LMC. Additionally it was found that the probability of finding a YSO in dense regions (N(H I) $> 2\times10^{20}\,\mathrm{cm}^{-2}$) is three times higher in the LMC than in the Magellanic Bridge, concluding that circumstellar envelopes in the lower metallicity Bridge are more porous and/or clumpy.

Recently significant near-infrared spectroscopic variability has been observed in lower mass YSOs over periods of the order of several hundreds of days (Connelley & Greene, 2014). Young stellar objects in the LMC have been observed to vary photometrically using the Spitzer-SAGE survey data (Vijh et al., 2009) and whilst no spectroscopic variability study has been carried out for a group of confirmed massive YSOs in this wavelength range, it is likely that these too will exhibit similar variability properties. All of the data presented in this thesis both in the LMC and SMC and the Galactic data obtained from literature is single epoch data. Therefore whilst spectroscopic variability of massive YSOs fall outside the scope of this thesis, it remains an an important consideration and in the future multi-epoch spectroscopic studies may have a significant impact on our understanding of massive star formation.

1.6 Project Objectives

The purpose of this study is to gauge the impact of the environment in which massive protostars form on their physical properties and processes which can be inferred through spectral analysis. The main focus will be on massive young stellar objects and H II regions in the relatively low metallicity Magellanic Clouds. There are three approaches implemented in this thesis. The first approach is the use of high spatial resolution integral field spectroscopy in the near-infrared of individual massive YSOs in the Magellanic Clouds. The second is a new analysis of optical spectra towards massive YSOs in the Magellanic Clouds to understand the origin and nature of the exciting objects. Finally the newly commissioned Fabry-Perot interferometry capability of the Southern African Large Telescope (SALT) is applied to assess the relationship between young massive stars and two larger scale H II regions in the Magellanic Clouds.

The high resolution integral field spectroscopy is all based on data obtained with SIN-

FONI at the Very Large Telescope (VLT) at ESO's Paranal observatory. This allows the probing of massive YSOs on sub-parsec scales, revealing significantly extended line emission morphologies and allows the continuum sources to be resolved to a spatial scale of $\sim$0.1 pc. The main aim here is to use the emission line morphologies and the presence of certain emission line species to better understand the physical processes and evolutionary state of each system. The data obtained in this study is then compared to similar observations of massive YSOs in the Milky Way to determine what, if any, physical properties may vary between massive YSOs in the low metallicity Magellanic Clouds and our own Galaxy.

As mentioned in earlier sections, massive stars form in very dense environments and massive protostars remain necessarily deeply embedded in their natal molecular clouds. The presence of optical emission detected towards the majority of massive YSOs presented in Oliveira et al. (2013) is therefore somewhat surprising. These spectra are therefore analysed in more detail in this thesis, specifically with the aim of determining the nature of the emission and the exciting mechanisms and sources present. In addition to the previously obtained spectra, new spectra have also been obtained with SALT and have been analysed in the same way.

Using the Fabry-Perot interferometry capability of SALT it is possible to map both the morphology and kinematics of excited gas over large spatial scales (10s of parsecs) in the Magellanic Clouds. Two H II regions have been targeted with this method which are also observed with both integral field spectroscopy in the near-infrared and optical long-slit spectroscopy. This will allow the relationship between the formation of massive stars on the scale of individual YSOs and the scale of molecular clouds to be assessed in active star forming regions. Of particular interest are the kinematics and extinction maps across these regions compared to those found on smaller scales in the same regions.

From the variations in observed properties of massive YSOs in the Magellanic Clouds from those of our own Galaxy, variations in physical properties and mechanisms can be inferred and thus this may provide an indication of the manner and extent of the effect of metallicity on massive star formation.

2 Observations and data reduction

This chapter describes the various infrared and optical observations and data reduction procedures used to obtain the data used in the analysis described in this thesis in Chapters 3–7.

2.1 Infrared integral Field spectroscopy with VLT/SINFONI

2.1.1 Properties of VLT/SINFONI

SINFONI (Spectrograph for INtegral Field Observations in the Near-Infrared; Eisenhauer et al. 2003) is a Cassegrain focus mounted integral field spectrograph in operation at the European Southern Observatory's (ESO) Very Large Telescope (VLT). The spectrograph operates in the spectral range 1.1–2.45 μm using four gratings (*J, H, K* and *H+K*) with three possible spatial pixel (spaxel) scales: 0.025, 0.1 or 0.25 arcsec. SINFONI is the combination of an adaptive optics module which is a clone of MACAO (Multiple Application Curvature Adaptive Optics; Bonnet et al. 2003) and SPIFFI (SPectrograph for Infrared Faint Field Imaging; Eisenhauer et al. 2000).

The diffraction limited resolution, θ_D, given by $\theta_D = \frac{1.22\lambda}{D}$ for the 8.2 m VLT unit telescopes (UT) at 2.2 μm is 0.068 arcsec; however the diffraction limited resolution is rarely achieved from ground based telescopes due to the effects of atmospheric turbulence. Fried's coherence length, r_0 gives the maximum diameter of a telescope before it is seriously affected by the Earth's atmosphere:

$$r_0 \approx \left(\frac{\lambda \cos z}{550}\right)^{0.6} \text{m (Kitchin, 2003)} \tag{2.1}$$

where z is the angle from the zenith and λ is the observed wavelength. In practice this means that a telescope need only be a few tens of cm in diameter before it suffers significantly from the effects of seeing. In order to overcome the effects of the atmosphere, many observatories now use adaptive optics (AO) systems to compensate for atmospheric turbulence in real time.

AO systems use light diverted from the main operational instrument using a sampling system which is projected onto a wavefront sensor allowing a wavefront correction system to compensate for seeing (Rigaut, 2015). This can be achieved either with a partially reflecting mirror to divert around 10% of the light to the wavefront sensor or by using a dichroic mirror to divert light of a different wavelength to the wavefront sensor. A dichroic mirror is used in SINFONI to reflect visible light onto the wavefront sensor whilst transmitting the near-infrared light to SPIFFI (Eisenhauer et al., 2003). In practice most astronomical AO systems use a natural guide star (NGS) rather than the target itself for the adaptive optics system. The Strehl ratio is used to measure the efficiency of adaptive optics systems, given by the intensity at the centre of the corrected image divided by the intensity at the centre of a perfect diffraction limited image of the same source; the normalised Strehl ratio is the ratio of the corrected image to the uncorrected image.

The isoplanatic area is the area of the sky over which observations will be affected by atmospheric turbulence in a similar manner and is defined by the distance over which the Strehl ratio improvement due to adaptive optics halves. The isoplanatic area is small ($\sim$15 arcsec in the visible and $\sim$80 arcsec in the K-band) and thus only $\sim$1% of the sky can be covered using NGSs even in the near-infrared (Kitchin, 2003). It is therefore becoming increasingly common for observatories to make use of a laser guide star (LGS) system, using a powerful laser to excite sodium atoms in the upper atmosphere ($\sim$90 km) to simulate the presence of a guide star. For the best results the LGS system does need a tip-tilt guide star but this can be situated at a much greater distance on the sky than the distance between an NGS and a target.

The light diverted using the sampling system is projected onto a wavefront sensor. In MACAO, the wavefront sensor is a curvature sensor (introduced by Roddier & Roddier 1988) which detects distortions in the wavefront through comparison of illumination variations across defocused images just inside and outside the focal point using a mirror which vibrates at kilohertz frequencies (Kitchin, 2003). In SINFONI the incoming light from the Cassegrain focus is reflected by two mirrors, creating an image onto the deformable mirror (DM) which is then reflected with two more mirrors towards the SPIFFI focus (Hau & Kaufer, 2015). The visible light is used by the wavefront sensor to calculate the variations in atmospheric turbulence which is in turn used to deform the DM in a closed loop allowing the atmospheric conditions to be accounted for in almost real time. The DM compensates for all atmospheric aberrations up to a 1 arcsec seeing (Hau & Kaufer, 2015).

The integral field spectrograph SPIFFI consists of three key components: the pre-optics, the image slicer and the spectrometer. The characteristics of these components are summarised here but described in detail in Eisenhauer et al. (2000). The pre-optics consist of a fixed collimator, a filter wheel and the optic wheel. The optic wheel is used to select one of three magnifications which produce the three pixel scales available with SINFONI. The image slicer in SPIFFI uses two sets of mirrors known as the small slicer and the large slicer. The incoming light is redirected by the small slicer in different directions depending on the field position, projected towards the large slicer. The large slicer is a larger concave array of plane mirrors which then realigns the beams so that they are parallel but now spatially separated. These "slices" are then projected into the spectrometer, effectively as simultaneous and adjacent long slit observations. The spectrometer itself consists of a collimator, a grating wheel and a camera. The grating wheel houses the four available gratings (*J, H, K* and *H+K*). As discussed earlier, the diffraction limit is 0.068 arcsec for the VLT UTs in the *K*-band which means that with the smallest pixel scale (0.025 arcsec) the camera is diffraction limited. The detector used is a 1k × 1k HAWAII array from Rockwell with a pixel size of 18.5 μm.

2.1.2 Target selection and SINFONI observations

The initial target list for observations of YSOs in the SMC with SINFONI was based on the list of 33 spectroscopically confirmed YSOs from Oliveira et al. (2013) with the additions of candidates in the H II regions LHA 115-N88 A and and LHA 115-N81 (Henize, 1956). Of these initial 33 targets, 19 were observed in the *K*-band with SINFONI which were chosen based on visibility and observing conditions so that the best quality data could be obtained for a wide range of sources. Massive YSOs in the H II region LHA 120-N113 (Henize, 1956) in the LMC were also observed because at the time of the observations the SMC was not visible for the last hour of available time. This time was used to observe three sources in N113 which make up the central dusty lane in the H II region.

The *K*-band integral field spectroscopic observations were carried out for 19 *Spitzer* YSO targets in the SMC and three in the N113 H II region in the LMC using SINFONI at the VLT under program 092.C-0723(A) (PI: Oliveira, J.M.). The list of target coordinates is given in Table 2.1. Each object was observed with four 300 second integrations along with sky offset position observations in an ABBA pattern with jittering. Telluric B-type standard stars were also observed at regular intervals throughout each night in order to provide standard star spectra for telluric correction and flux calibration. Dark, flat lamp, arc lamp and fibre

Table 2.1: J2000 coordinates for all K-band SINOFNI observations presented in Chapters 3 and 4. All targets were observed with four integrations of 300 s.

N113 target #	RA (h:m:s)	Dec (°:′:″)
N113-YSO01	05:13:17.7	-69:22:24.86
N113-YSO03	05:13:25.1	-69:22:44.42
N113-YSO04	05:13:21.6	-69:22:42.19

SMC target #	RA (h:m:s)	Dec (°:′:″)
01	00:43:12.9	-72:59:58.30
02	00:44:51.9	-72:57:34.20
03	00:44:56.4	-73:10:11.28
04	00:45:21.3	-73:12:18.70
06	00:46:24.4	-73:22:07.03
17	00:54:02.3	-73:21:18.60
18	00:54:03.4	-73:19:38.40
20	00:56:06.4	-72:28:27.77
22	00:57:57.1	-72:39:15.40
25	01:01:31.7	-71:50:40.30
26	01:02:48.5	-71:53:18.00
28	01:05:07.3	-71:59:42.70
30	01:06:59.7	-72:50:43.10
31	01:14:39.4	-73:18:29.30
32	00:48:39.6	-73:25:01.00
33	01:05:30.2	-72:49:53.54
34	01:05:49.3	-71:59:48.80
35	01:24:07.9	-73:09:04.00
36	01:09:12.9	-73:11:38.63

Table 2.2: LMC target coordinates and exposure times (ExpT) and number of integrations (N_{int}) for the SINFONI observations presented in Chapter 6.

Target	RA (h:m:s)	Dec (°:′:″)	ExpT s	N_{int}
30DorN	05:38:42.20	−69:06:02.90	30	5
30DorS	05:38:42.00	−69:06:12.90	90	20
S054025.15–694012.1	05:40:24.80	−69:40:13.10	90	20
S053945.94–693839.2	05:39:46.10	−69:38:38.00	90	17
S053943.26–693854.6	05:39:43.20	−69:38:55.50	90	10
S053252.41–694620.1	05:32:52.30	−69:46:19.90	90	20
S053941.89–694612.0	05:39:41.60	−69:46:09.30	180	13

calibration frames were observed during the daytime and linearity lamp frames (which are taken once a week) were obtained from the ESO archive. Observations were carried out with a 0.1×0.05 arcsec spatial scale, yielding a 3.1×3.1 arcmin field-of-view (FOV), for the spectral range 1.95–2.45 μm and with a spectral resolving power of $\lambda/\Delta\lambda = 4000$, yielding a velocity resolution of $\sim$75 km s^{-1} (and therefore allowing the determination of Gaussian centroid positions to $\sim$4 km s^{-1}). Where possible the adaptive optics (AO) module was used. For the SMC sources #17, 18 and 22 and N113-YSO04 we were not able to use AO, yielding a seeing limited spatial resolution for these sources (useful morphological information was still obtained). The target observed with SINFONI are discussed in more detail in Chapters 3 (N113) and 4 (SMC).

The archival LMC *H+K*-band data were obtained using SINFONI under program 090.C-0587(A) (PI: Alves, J.F.). The aim of this program was to target embedded clusters in the LMC; however, three of the seven targets have been classified as PE type YSOs by Seale et al. (2009) and two are classified as embedded sources of an unknown nature as discussed in Chapter 6. The presence of late stage massive YSOs and UCH II regions in at least some of these fields therefore seems likely. The observations were carried out using the 0.25×0.125 arcsec spatial scale (with an 8×8 arcmin FOV) with the *H+K* grating yielding a spectral resolving power of $\lambda/\Delta\lambda = 1500$ and a velocity resolution of $\sim$200 km s^{-1}. Multiple exposures were taken over a relatively wide jittering pattern in order to maximise the field observed. The number of exposures for each of the targets are listed in Table 2.2 along with the corresponding exposure times. The exposure times were typically 90 s with the exceptions of the targets 30DorN and S053941.89-694612.0 which were observed with exposure times of 30 s and 180 s, respectively.

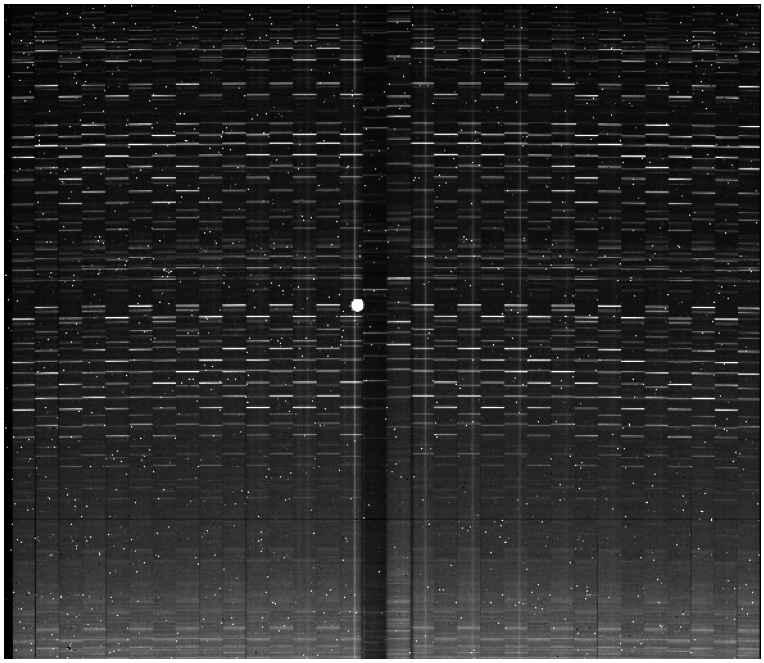

Figure 2.1: One of the raw science frames produced by SINFONI for SMC source #36. Both of the spatial axes are contained along the horizontal of the image while the spectral axis is contained in the vertical. This allows the reconstruction of data cubes with a 0.1 arcsec spatial resolution and 2048 spectral elements. The bright horizontal lines are the sky OH emission lines.

2.1.3 SINFONI initial data reduction

The spectral images produced by SINFONI resemble 32 long slit observations stacked next to each other on the CCD. An example of one of our frames is shown in Fig. 2.1. Each of these is a projection of a single slitlet containing spatial information in the horizontal axis and spectral information in the vertical axis. Stepping horizontally from one slitlet to the next is equivalent to stepping through in the spatial direction orthogonal to that going across each slitlet. Therefore from a single integration onto the CCD a three dimensional data cube can be reconstructed consisting of two spatial dimensions and one spectral dimension.

The raw data were reduced using the standard SINFONI pipeline recipes in GASGANO. Telluric and flux calibration were performed simultaneously for each cube using an IDL[2] script. For each pixel in the target cube, the target spectrum is divided through by the telluric spectrum removing the telluric spectral features. The target spectrum was then multiplied by a blackbody function with a temperature appropriate for the spectral type of the standard star used and scaled to the flux of the standard star. The blackbody spectra

[2]IDL version 8.5.1 (Exelis Visual Information Solutions, Boulder, Colorado).

used in this calibration were generated using PYRAF[3]. This process was looped to apply the same procedure to each spaxel in the cube.

SINFONI is a Cassegrain focus mounted instrument and as such it does suffer from a systematic time-dependent wavelength shift during each night due to flexure. Flexure due to of the motion of opto-mechanical components due to the effect of gravity (i.e. sagging) and the movement of the telescope itself. This effect is always small (less than 3 resolution elements) so it only presents an issue when determining accurate absolute centroid velocity measurements. In order to account for this effect, a second wavelength calibration was performed on the final data cubes using the OH emission lines in the sky data cubes produced in the SINFONI pipeline.

Although sky line subtraction does form part of the standard SINFONI data reduction pipeline, due to the relatively long observing times in this study (up to 8×5 minute exposures plus overheads), the variation in sky line intensities leads to sky line residuals remaining in the final data cubes. The positions of these lines are shown in Fig. D.2. Whilst aesthetically displeasing, the impact of these residuals on the spectral analysis is actually small as none are coincident with any emission lines of interest and the continuum measurements are calculated from models fitted to the continuum so noise and residuals are not an issue.

For SMC source #25 (Chapter 4) the data reduction sequence has yielded a data cube which exhibits negative continuum flux towards the red end of the spectrum. On inspection of the sky cube this appears to be caused by an unusually strong, red continuum in the sky frames most likely caused by contamination from a red continuum source nearby. Whilst this has made continuum flux measurements of source #25 unusable, it is unlikely to have affected the measurements of emission lines towards the source. A number of spectra in the LMC *H+K* grating observations also exhibit significant residual telluric features (see Chapter 6). This should only affect some of the measurements (if any) of the He I 2.0587 μm feature and the H_2 Q-branch emission lines.

2.1.4 SINFONI data enhancement procedure

The relatively low number of spaxels resulting from the initial data reduction procedure can make the results challenging to interpret by eye. Additionally, a small number of artefacts are present in SINFONI data, resulting from the instrument itself. Following the initial reduction of the data I applied a process of re-sampling, Butterworth spatial filtering and instrumental

[3]PyRAF is a product of the Space Telescope Science Institute, which is operated by AURA for NASA.

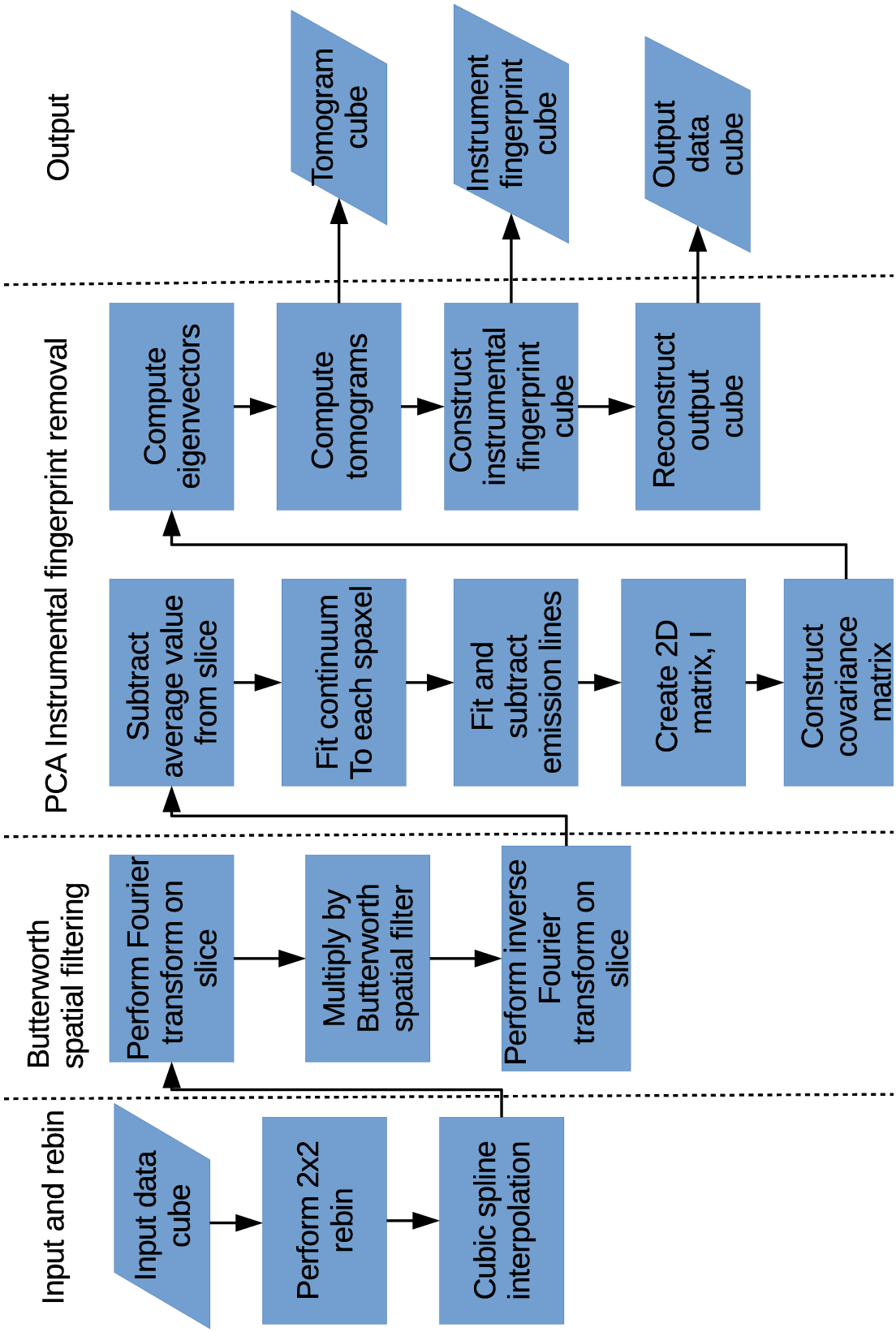

Figure 2.2: Flowchart describing the truncated SINFONI data cube enhancement procedure.

fingerprint removal following the procedure outlined in Menezes, Steiner & Ricci (2014) and Menezes et al. (2015). The procedure is described in detail below and is summarised in Fig. 2.2.

First re-sampling was carried out with a 2×2 rebin (quadrupling the number of spaxels) and a cubic spline interpolation in the two spatial dimensions. This introduces a high spatial-frequency component which can be removed using Butterworth Spatial Filtering (BSF; Gonzalez & Woods 2002) through the following steps.

- Calculation of the Fourier transform of the image, $F(u, \nu)$;
- Multiplication of the Fourier transform by the corresponding Butterworth filter, $H(u, \nu)$;
- Calculation of the inverse Fourier transform of the product $F(u, \nu) \cdot H(u, \nu)$;
- Extraction of the real part of the calculated inverse Fourier transform.

Menezes et al. (2015) determined that a squared circular filter is most appropriate for K-band SINFONI data at 100 mas resolution:

$$H(u,\nu) = \left\{ 1 + \left[\sqrt{\left(\frac{u-u_0}{a} \right)^2 + \left(\frac{\nu-\nu_0}{b} \right)^2} \right]^{2n} \right\}^{-2} \tag{2.2}$$

where n=2 and a=b=0.26 N_y (where N_y is the number of spaxels in the vertical direction). If successful, the high spatial-frequency component introduced in the interpolation step has now been removed.

The final stage of our truncated version of the data treatment procedure of Menezes et al. (2015) is instrumental fingerprint removal using Principal Component Analysis (PCA) as summarised in the following steps.

- All spectral lines are fitted and removed from the input data cube using Gaussian line profiles. The average pixel value for each slice, Q_λ is then subtracted from every pixel in that slice.
- The 3D datacube, D_0 is converted into a two dimensional array, I; $I[\beta, \lambda] = D_0[i, j, \lambda]$ where $\beta_{i,j} = \mu(i-1)+j$ and μ is equal to the number of elements in the first dimension.
- Application of PCA tomography to the 2D matrix as outlined in Steiner et al. (2009).

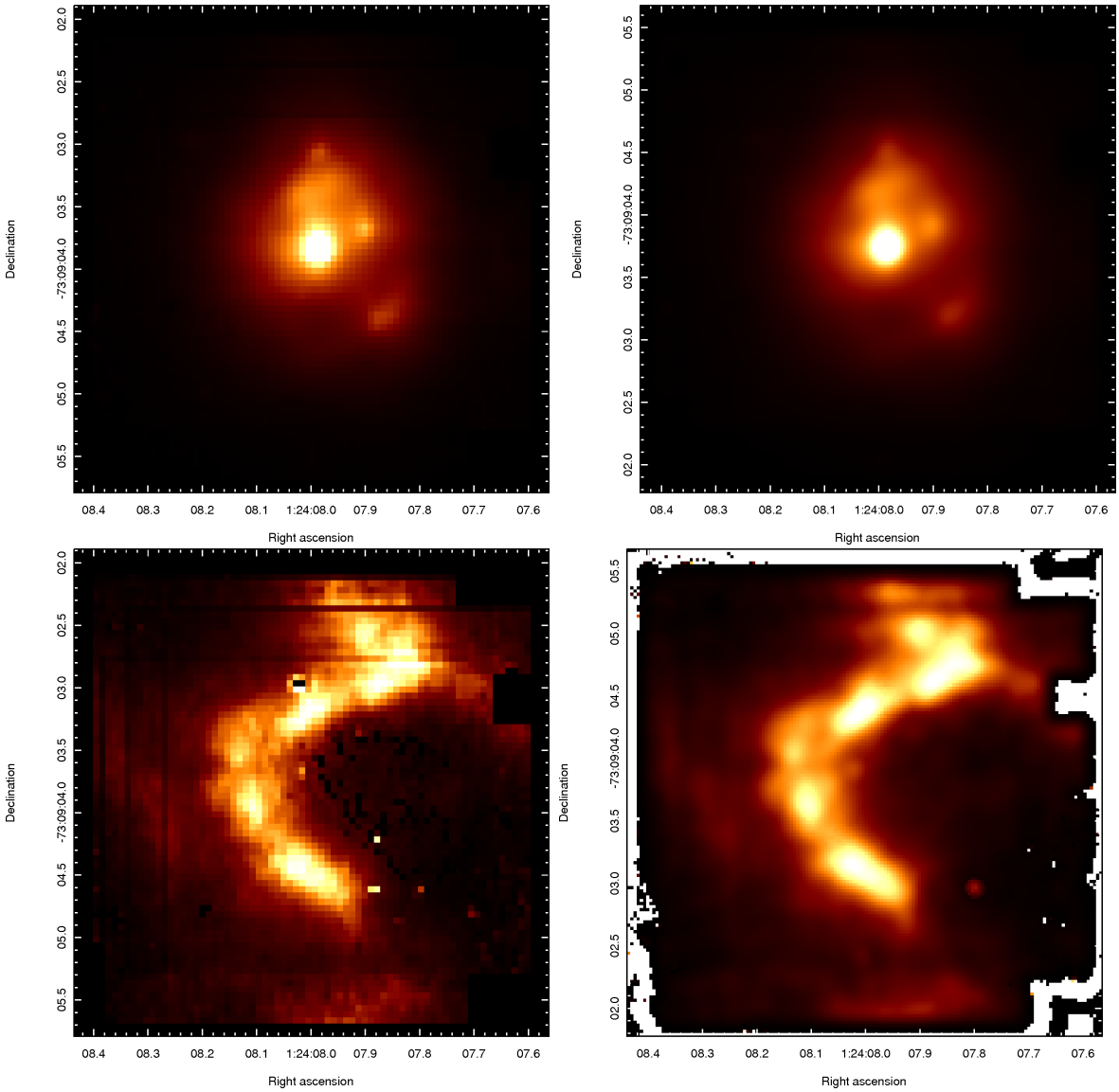

Figure 2.3: Continuum images (upper panels) and H_2 emission line flux images (lower panels) before (left) and after (right) the data treatment procedure outlined in Section 2.1.4 for target #35 in the SMC (see Chapter 4).

- Selection of the eigenvectors related to the instrumental fingerprint. This is done by eye on the basis that the spectral signature will be that of the fingerprint and that the corresponding tomogram must have a spatial morphology including a large horizontal stripe at the bottom of the image (see Menezes et al. 2015 for details).

- Reconstruction of the datacube, excluding the eigenvector and tomogram related to the instrumental fingerprint; $I_{out} = \sum_k T_{\beta,K} \cdot [E_{\lambda,K}]^T$ for $K \neq K_{inst}$.

- The 2D array is converted back into a data cube and the properties subtracted in the first step are now added back in; $D_{out} = I_{i,j,\lambda}$ + emission lines + Q_λ.

Whilst this procedure does not improve the spatial resolution nor change the observed

morphologies and kinematics, it does provide cleaner intensity and velocity maps. As an example, a K-band continuum image and an H_2 emission line flux image have been fitted to a data cube before and after the treatment procedure. These are shown in Fig. 2.3. From these figures it is clear that the treated images are much smoother and easier to interpret. Some bad (poorly fitted) pixels have been smoothed out and the total flux of the cube is the same to within a fraction of a percent. The instrumental fingerprint visible in the H_2 image as straight dark lines has also been significantly reduced and no additional artefacts have been introduced.

2.2 Optical long slit spectroscopy

2.2.1 Properties of SALT/RSS

With a primary mirror diameter of 11 m, the Southern African Large Telescope (SALT; Buckley, Swart & Meiring 2006) is the largest single telescope operating in the visible spectrum in the southern hemisphere. The optical design of SALT is based on the Hobby-Eberly Telescope (HET) at McDonald Observatory in Texas. The design of HET and SALT, unique in large optical telescopes, is characterised by a primary mirror that remains stationary and both the azimuthal and the altitude tracking is accomplished by moving the instrument payload itself across the prime focus. This places altitude restrictions on SALT observations meaning that it can only observe in the altitude range 47°to 59°. Fortunately the Magellanic Clouds lie at J2000 Declinations in the range –65°to –75°which offers some of the longest possible tracking times with SALT. A simple illustration of the setup of SALT is shown in Fig. 2.4.

The Robert Stobie Spectrograph (RSS; Kobulnicky et al. 2003) is the main workhorse instrument of SALT, offering six modes: narrow-band imaging, long-slit spectroscopy, multi-object spectroscopy, Fabry-Perot interferometry and polarimetric imaging/spectroscopy and high speed spectroscopy. The prime focus spectrograph is sensitive to the range 320 nm to 860 nm (with a possible extension to 1.6 μm in the future) and in long-slit mode resolving power of up to ∼9000 can be achieved (Vaisanen, 2015). This section focuses on the long-slit mode of RSS whilst the Fabry-Perot interferometric mode will be discussed in Section 2.3.2.

The camera in RSS can be set to wide range of angles, allowing a choice of wavelength coverages. This is used in combination with six available gratings: pg300, pg900, pg1300, pg1800, pg2300 and pg3000 with resolving power in the ranges 250–600, 600–2000, 1000–3200, 2000–5500, 2200–5500 and 2200–5500, respectively (Vaisanen, 2015). As a spectrograph, it is

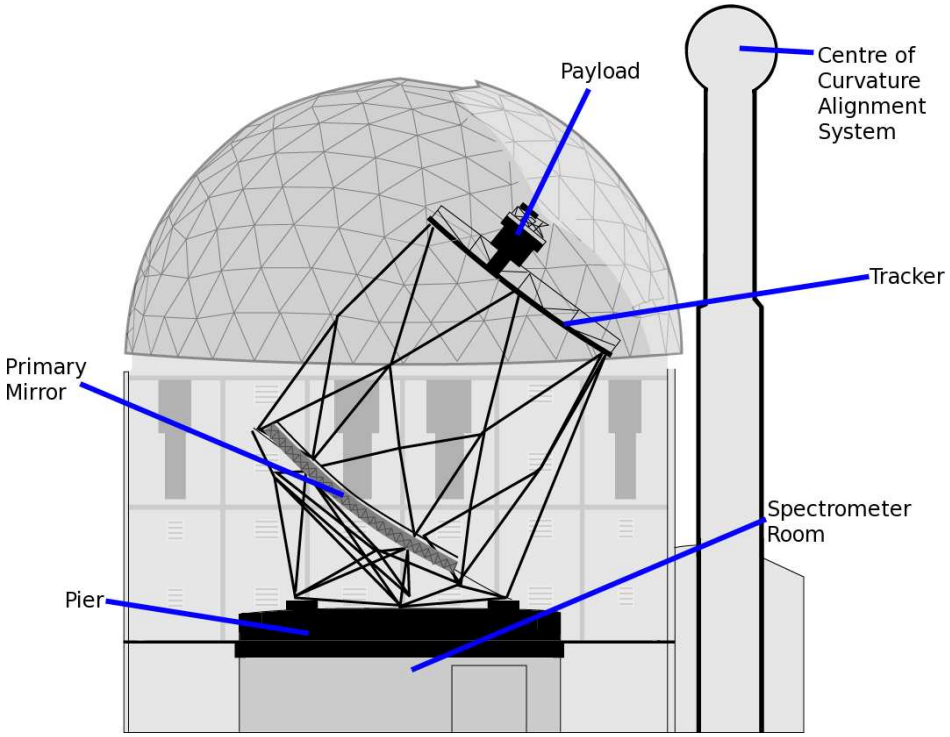

Figure 2.4: Illustration of the SALT setup from http://www.salt.ac.za/wp-content/themes/saao-salt/images/telescope.png.

therefore an extremely versatile instrument which is ideally situated to observe the Magellanic Clouds.

2.2.2 RSS Observations

Spectra were obtained towards the compact H II regions N81 and N88 A in the SMC and towards N113-YSO03 in the LMC, all of which have also been observed with SINFONI. These spectra were obtained using RSS at SALT in long slit mode under program 2014-1-UKSC-003 (PI: Jacob Ward). For all three sources spectra were obtained using the pg900 grating centred at 6318.9 Å to provide broad band low resolution spectra as well as with the pg1800 grating centred on positions of 6597.2 Å (Hα) and 5184.0 Å (closest available to Hβ) to provide medium resolution spectra in these particular areas of interest. A slit width of 1 arcsec was used in all long slit observations with RSS. This made for a total of 9 observations, each consisting of 5 detector iterations with varying exposure times between observations (listed in Table 2.3, along with the spectral ranges observed).

Previous observations (first presented in Oliveira et al. 2013) were obtained using the Double Beam Spectrograph (DBS) at the Australia National University Telescope (PI: Wood, P.) are also analysed in this study. DBS spectra were obtained towards 28 sources including

Table 2.3: List of exposure times for all SALT/RSS long-slit observations.

Target	Grating	spectral range (Å)	exposure time (s)
N81	pg900	4768.8–7804.0	34
N81	pg1800	4454.8–5859.8	200
N81	pg1800	5924.2–7202.2	164
N88	pg900	4768.8–7804.0	30
N88	pg1800	4454.8–5859.8	239
N88	pg1800	5924.2–7202.2	250
N113	pg900	4768.8–7804.0	400
N113	pg1800	4454.8–5859.8	650
N113	pg1800	5924.2–7202.2	571

15 sources which were also observed in the *K*-band with SINFONI (see Chapters 3 and 4). These spectra cover the range 3600–9500 Å with a spectral resolution of ∼4.5 Å and a slit width of 2 arcsec. These spectra are re-analysed along side the new SALT spectra in Chapter 5.

2.2.3 RSS long slit data reduction

The Starlink data reduction package FIGARO was used to reduce the RSS spectra using the following procedure. First the flat field calibration frames for each observation were combined into a master flat field. Next all of the images were cleaned of cosmic rays using the automated BCLEAN function and each of these was then flat fielded by dividing the spectral image by the master flat field frame. Then all of the exposures were stacked to create a summed spectral image and the spectral images were then split up into separate images for each of the three CCDs so that when the spectra are extracted any drift between the detectors can be accounted for. The spectra were then extracted using the FIGARO EXTRACT function for the bright central source in each observation.

The arc lamp observations were similarly split up and spectra were extracted from the central regions of the arc spectral images. Wavelength calibration was carried out using the ARC function with the line lists provided on the SALT website and this wavelength solution was then copied into the science spectra. Standard star spectra were obtained from the SALT database which were observed within one month of the science observations taking place. These spectra were treated in the same way as the science spectra and were then multiplied by the ratio of the exposure times of the science and standard observations. The science spectra were divided by the standard star spectrum and then multiplied by a blackbody function with the same temperature as that of the standard star, and finally multiplied by

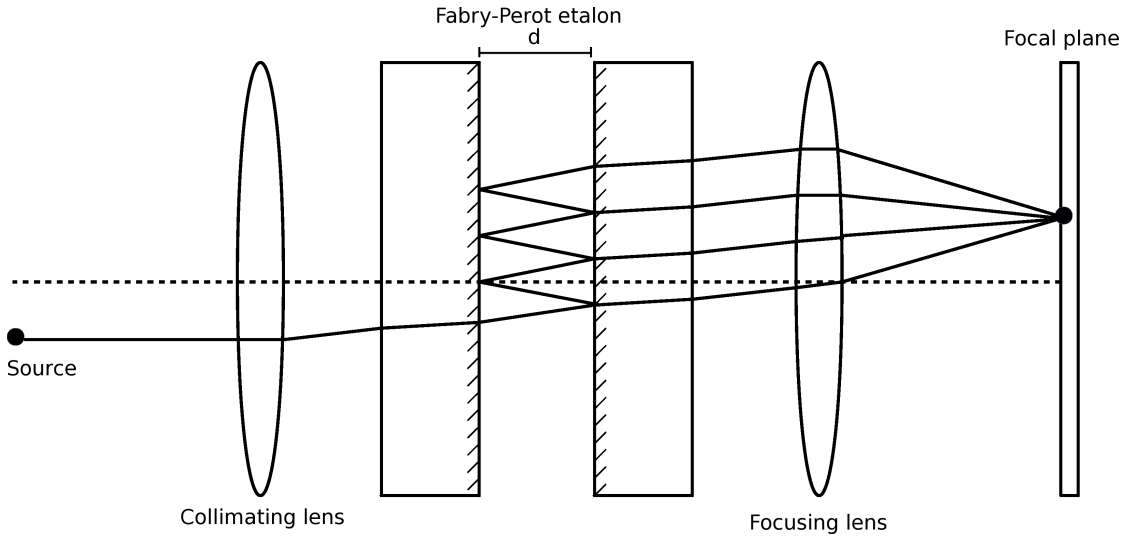

Figure 2.5: A typical Fabry-Perot setup. The etalon properties are described in the text.

the average flux of the standard star to perform the flux calibration.

2.3 Fabry-Perot interferometry

2.3.1 A brief introduction to Fabry-Perot interferometry

Fabry-Perot interferometry provides relatively high resolution, spatially resolved spectroscopy for narrow wavelength ranges. This makes it ideal to map kinematic properties of a small number of extended emission lines.

A typical Fabry-Perot interferometer consists of an interference filter, a collimator lens and the Fabry-Perot etalon. Fig. 2.5 shows a typical example of a Fabry-Perot setup. The Fabry-Perot etalon consists of two parallel glass plates, separated by a small gap with a high reflectivity coating applied to the inner surfaces.

Suppose a monochromatic beam of light passes into the Fabry-Perot etalon it is reflected between the two plates according to its wavelength, creating an interference pattern at the focal plane which has an intensity response governed by the airy function $\mathcal{A}$;

$$\mathcal{A} = \frac{1}{1 + [4R/(1-R)^2]\sin^2(\frac{2\mu d\cos\theta}{\lambda})} \tag{2.3}$$

where R is the surface intensity reflection coefficient of the high-reflectivity coating, d is the length of the etalon gap, μ is the refractive index of the medium in the gap and θ is the incident angle of the beams on the surface from within the interface. The phase lag ϕ is given by $\phi = 2\pi(2\mu d\cos\theta)/\lambda_0$ where λ_0 is the wavelength incident wave in a vacuum. The energy

transmission coefficient, I_t for a pair of reflecting surfaces can be obtained using R, $\mathcal{A}$ and the transmission coefficient of the reflective coating T, where in an ideal Fabry-Perot etalon $R + T = 1$ and the transmitted intensity, $I_T = I_t I_0$:

$$I_t = \left(\frac{T}{1-R}\right)^2 \mathcal{A}(\phi) \tag{2.4}$$

where I_0 is the illumination at the focal plane. In a real Fabry-Perot setup there is some light lost due to scattering and/or absorption in the dielectric coatings of the Fabry-Perot etalon and the glass itself. This introduces the attenuation coefficient A where $R + T + A = 1$.

The resulting interference pattern follows the condition $2d\cos\theta = N\lambda$ where d is the gap between the plates, λ is the wavelength of the light (where $\lambda = \mu\lambda_0$) and N is the order of interference. The wavelength of the light can therefore be changed by altering the refractive index of the medium between the etalon plates through changing the pressure or by mechanical scanning where the gap between the etalon plates is changed.

The gap between two consecutive orders is given by the free spectral range, $\mathrm{FSR} = \lambda^2/2d$ and the sharpness of the fringes can be measured by the ratio of the FSR to the full width at half maximum (FWHM) of the transition profile which for the ideal etalon is governed by R and is termed the reflectance finesse, $\mathcal{F}_R$:

$$\mathcal{F}_R = \frac{\pi}{2}\sqrt{\frac{4R}{(1-R)^2}} \tag{2.5}$$

which yields a theoretical resolving power, $\mathcal{R}$,

$$\mathcal{R} \equiv \frac{\lambda}{\Delta\lambda} = N\mathcal{F}_R \tag{2.6}$$

where $\Delta\lambda$ is the change in wavelength between elements. In a practical Fabry-Perot system the finesse is also affected by the flatness of the plates which, although are highly polished, can never be perfectly flat. This adds a new term, the defect finesse $\mathcal{F}_D$. The total finesse is given by the combination of the reflectivity and defect components:

$$\frac{1}{\mathcal{F}^2} = \frac{1}{\mathcal{F}_R^2} + \frac{1}{\mathcal{F}_D^2} \tag{2.7}$$

where $\mathcal{F}_D$ is the component of the finesse due to defects in the etalon surface.

2.3.2 Fabry-Perot interferometry with SALT/RSS

RSS has been introduced in Section 2.2.1. Three etalons are available for use in RSS with gap sizes of ∼0.6 nm, ∼2.8 nm and ∼13.6 nm referred to as the low resolution (LR), medium resolution (MR) and high resolution (HR) etalons respectively. These etalons can be used in four modes; the tunable filter (TF), low resolution (LR) and medium resolution (MR) single-etalon modes and the high resolution (HR) dual-etalon mode (Vaisanen, 2015). The reflectance of the coatings used is $R = 0.90$, yielding a finesse of $\mathcal{F}_R = 30$ using the above relation and the defect finesse of the etalons due to the surface quality is $\mathcal{F}_D \sim 50$ so the total finesse is $\mathcal{F} \sim 25$ (Rangwala et al., 2008).

RSS utilises mechanical scanning. Along with checking and correcting the parallelism of the etalons, this is achieved using differential capacitance micrometers and piezo-electric actuators in a three-channel configuration. The first two channels control the parallelism whilst the third is used to set and maintain the gap spacing. This system is able to move the etalon plates over a distance of ∼6 μm with a resolution of 0.49 nm. Setting the LR etalon to its smallest gap of 5 μm gives a resolving power $\mathcal{R} \sim 350$, whilst at its largest gap (∼11 μm) it produces the LR mode with $\mathcal{R} \sim 750$. The MR and HR etalons are both operated near their largest gaps of ∼28 μm and ∼136 μm respectively, as the available 6μm range is not sufficient to significantly change the spectral resolution (Rangwala et al., 2008); these therefore yield resolving powers of ∼1500 and ∼8500 respectively.

The LR mode has been consistently available but unfortunately there have been a number of issues with both the MR and HR etalons. The MR etalon was taken off-line halfway through the 2015-1 semester due to degradation of the reflective etalon coatings meaning that whilst a medium resolution observation of Hα in N88 was successfully obtained, it was not possible to do so for Hβ. As a compromise the low resolution mode was utilised to observe Hβ in N88. The HR dual etalon mode has suffered from numerous issues, most importantly significant ghosting effects and later problems with the etalon mounting.

2.3.3 Target Selection and Fabry-Perot observations

For the Fabry-Perot interferometric observations, the H II regions N88 in the SMC and N113 in the LMC have been selected. These H II regions have been studied in both the optical (Chapter 4) and the near-infrared (Chapters 2 and 3 for N113 and N88 respectively) so they are known to be bright and extended in optical emission features with emission line centroid wavelengths which are well constrained making them ideal for Fabry-Perot observations.

Table 2.4: Fabry-Perot observation parameters. The No. steps column indicates the number of steps in wavelength taken to cover the entire spectral range. The ExpT column gives the exposure times for each scan and the Nint is the number of integrations, i.e. dithered positions, taken.

Target	Target line	RA (h:m:s)	Dec (°:′:″)	mode	spectral range (Å)	No. steps	ExpT (s)	Nint
N88	Hα	01:24:27.83	-73:10:12.4	MR	6559–6591	38	9.5	3
N88	Hβ	01:24:27.83	-73:10:12.4	LR	4854–4898	23	58.5	2
N113	Hβ	5:13:32.89	-69:21:42.5	LR	4855.5–4887.5	17	30	2

Whilst the best spectral resolution is always desirable when attempting to map velocities, this reduces the sensitivity of the observations and requires more scans to cover the same wavelength range. The combined effect is to increase both the exposure times and, crucially for Fabry-Perot observations, the overhead time which is always significant. In addition, the HR mode at RSS has had a number of issues since commissioning (see previous section).

MR Hα and LR Hβ observations of N88 A have been conducted in order to map both the velocity structure of the ionized gas as well as create an extinction map using the Hα/Hβ line flux ratio. A LR Hβ observation of N113 has been carried out. HR Hα observations of both regions are planned.

In all Fabry-Perot setups a shift in wavelength is introduced as a function of the radius of a point from the centre of the optical path. In RSS this means that at the edge of the 4 arcmin radius field, the transmitted wavelength is 24 Å bluer than that at the centre of the optical path. The wavelength range observed therefore must take this into account, meaning that to image the entire field, one would have to add enough scans to cover an additional 24 Å redwards. This wavelength shift goes as a function of radius squared and as such becomes more extreme the further from the centre of the optical path the regions of interest in the observation are. Additionally there are two 20 arcsec detector gaps in the field so multiple dithered positions are required in order to image the entire field. The wavelength ranges observed, the number of steps taken and the number of dithered positions are given in Table 2.4 for each Fabry-Perot observation.

2.3.4 Fabry-Perot Data reduction

The data obtained by RSS passes through an initial data reduction pipeline at the site in South Africa before being released. Data is delivered to the PI in the form of a set of images where each image corresponds to a single etalon configuration. Due to the radial wavelength shift described in section 2.3.3, these images do not in fact represent a single wavelength but

rather a range of wavelengths dependent on the etalon position and the radial wavelength solution. In order to arrive at meaningful science products the produced Fabry-Perot data must be subjected to a further reduction process. I have created a dedicated pipeline of data treatments using IDL. The full data reduction pipeline is summarised in Fig 2.6 and I describe each step in the process here.

Input files, values and cleaning

The file names of the input science images are ingested as a list within an ascii text file and the arc lamp image file name is a single raw input. The user is asked to input the values of the rest wavelength of the target emission line and the rest wavelength of the emission line observed in the arc image. For guidance, the program reads the arc file and outputs the lamp type and the etalon position to the user to help determine the rest wavelength of the arc lamp emission line. If an image suitable for checking the astrometry of the SALT observations is available, the file name of this image is also read at this point.

In order to remove the effects of cosmic rays from the science images they are cleaned using the BCLEAN automated cleaning routine from the FIGARO data reduction package. To use this package the files must first be converted into ndf format from the original fits format using the Starlink CONVERT package. These steps are implemented by writing temporary executable shell scripts into the current directory, processes to execute these scripts are spawned and finally the temporary scripts are deleted. The files are converted from fits to ndf format, then they are cleaned, and finally they are converted back into fits files. Once the cleaning process is completed, the two headers stored in separate extensions of the original fits files are then combined into a single header and written to the new fits files.

At this point a rough astrometry calculation is carried out using the header information from the input images. Using the position angle, reference coordinates and the reference pixel information, a transformation matrix is calculated. This simply defines the step taken in right ascension (RA) and declination (Dec) for each step in the X-direction and each step in the Y-direction of the image in pixels. This is then written into the new header along with reference coordinate information. Whilst the calculations carried out here are correct for the header information supplied, the pointing accuracy of SALT is not perfect and thus a later manual astrometry correction is recommended and a step has been included later using the astrometry reference image.

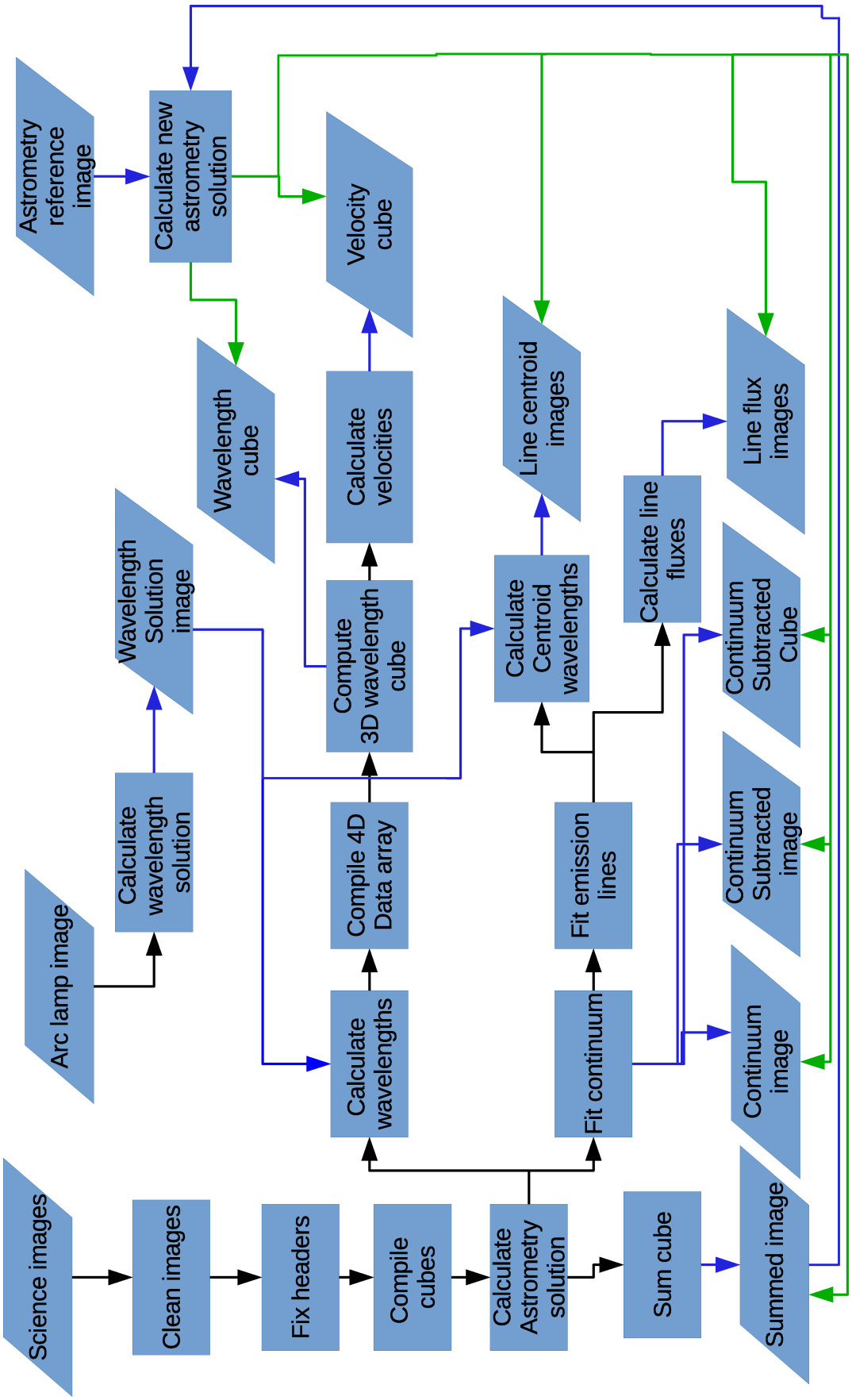

Figure 2.6: Outline of SALT/RSS Fabry-Perot data reduction pipeline. Black arrows show the progression of the pipeline, blue arrows indicates input/output of files and the green arrows show the optional application of the updated astrometry solution.

Radial wavelength solution

The radial wavelength shift from the centre of the optical path (not necessarily the centre of the fits image) must now be characterised. Based on the estimated shift of 24 Å from the centre of the optical path to the edge of the FOV an "ideal" wavelength solution can be calculated. The actual wavelength solution calculated depends on the pixel scale of the observations which with RSS can be varied by varying the pre-binned pixels (anywhere between a 1×1 configuration to a 9×9 configuration) and this calculation must therefore be carried out for each observation individually. Additionally, the exact solution and optical path may vary between observations so it is good practice to carry it out for every observing block.

The first step is to determine the centre of the optical path. This is accomplished by extracting intensity profiles across the centre of the image. These profiles are then split into two halves, either side of the centre pixels of the image and fit with a Gaussian function. These profiles and the fits are displayed and the user is given the option to either use the fit centroid or to simply use the maximum position of the profiles. These positions are then used to determine the centre by taking the difference between the radii of each halve of a profile from the image centre which gives a shift in centre position of the image and the centre position of the optical path.

Next the average arc maximum radius, $\bar{\mathrm{R}}^2$, in pixels is taken. The wavelength shift between the etalon position and the transmitted wavelength at the position where the arc emission line is observed is calculated, $\Delta\lambda$. This is then used to calculate the wavelength shift coefficient, F, where

$$\mathrm{F} = \frac{\Delta\lambda}{\bar{\mathrm{R}}^2}. \tag{2.8}$$

A radial wavelength solution image is now calculated for each spatial element where the wavelength shift at the position (i, j) $(\Delta\lambda_{i,j})$ is given by:

$$\Delta\lambda_{i,j} = \mathrm{F} \times \mathrm{R}_{i,j} \tag{2.9}$$

where $\mathrm{R}_{i,j}$ is the radius from the centre of the optical path to that position. The user is also given the option of using an ideal wavelength solution if for any reason they suspect an issue with the arc lamp observation.

Cube compilation and continuum fitting

For each pointing (dithering position), a data cube is compiled from the individual cleaned science images. The cubes for different dithering positions cannot be combined at this point due to the radial wavelength shift. The etalon position is read in Angstroms from the header of each image and stored as a list in a text file which will be used later to calculate wavelengths. At this point the data cubes are normalised by slice and by a standard star in the field. This is achieved first by taking the mean value of each slice and dividing every spaxel in the slice by that value. Next a star is identified in the field which should have a flat spectrum for the required narrow wavelength range. The spectrum of the standard star is extracted and the entire cube is divided by this standard spectrum. For our observations, massive stars are not suitable standards due to the presence of H I absorption features. If the flux of the standard is known, then the data cube can be flux calibrated at this point by multiplying every element in the cube by this flux value.

The continuum is then fitted to the cube using simply a straight line appropriate for the narrow spectral ranges typically observed in Fabry-Perot mode. Because the Fabry-Perot observations are by their nature dominated by a single emission line, only a small number of the spectral elements are used to fit the continuum, the positions of which depend on the setup of the observation. A 3D continuum cube (containing the fitted continuum function for each spaxel) is created alongside a 2D continuum image and both are written to fits files. The 2D continuum image is a summation along the z-axis of the 3D continuum cube.

Spectral cubes and channel maps

Using the previously compiled cubes for each dithering position, the list of etalon wavelengths and the radial wavelength shift solution it is possible to create data cubes where the spectral direction represents the wavelength rather than a function of the etalon position and the wavelength solution. This is necessary for creating channel maps from the observations.

A four dimensional array is created and populated where the first two dimensions are the X and Y pixels (corrected for the dithering pattern), the third dimension is the stack of the total number of slices from all of the data cubes. The fourth dimension is used to contain two values for each voxel in the three dimensional data cube; the flux and the wavelength. The flux value is simply copied in whilst the wavelength value is calculated at each point using the wavelength list (where the wavelengths are taken from the etalon positions) and the radial wavelength solution. This allows both the dithering position and the radial wavelength shift

to be accounted for simultaneously. Once this is done, a 3D array is created in which the spectral direction is made up of elements of the same width as the difference between etalon positions. This is because any oversampling will lead to rings of missing data at each slice in the output cubes. The flux data is then arranged into this new data cube using the corresponding wavelengths, taking the average flux where more multiple values correspond to the same point in the cube. Finally any remaining gaps between two values in the spectral direction are interpolated over, leading to a complete cone-shaped data structure.

The velocity cube is created by simply converting the wavelength information in the header of the fits cube into equivalent velocity information. Channel maps are then plotted from the final data cubes.

Centroid wavelength and flux maps

Whilst the channel maps are useful, because the process of creating them necessarily rebin the data into arbitrary wavelength elements, they cannot give the most accurate line centroid wavelength available. Instead the emission lines are fitted at every spaxel in each of the individual pointings (i.e. dithered positions).

The emission lines are fitted automatically for each spaxel by selecting the maximum value in each spectrum and using that minus an estimate of the continuum level as the peak of the line and using the index of the line as the estimated centroid. This is then fitted with a Gaussian function over which the program integrates to infinity to obtain a flux. At this point the integrated flux is in arbitrary flux units. To obtain a calibrated integrated flux, this value must be multiplied by the change in wavelength per pixel.

From these fits a central line position in spectral pixels is obtained which, using the (X,Y) position of the spaxel, the radial wavelength solution and the etalon wavelength list, is converted into a centroid wavelength in Angstroms. This is then output to a 2D fits image file and a similar image is created for centroid velocities as well.

Astrometry correction

In general, the actual images output from RSS Fabry-Perot images are linearly offset from the astrometry listed in the header. Using a previously obtained reference image (e.g. an MCELS Hα image or a DSS image) of the region the offset between the Fabry-Perot data and the reference image can be measured directly. This is measured manually by the user and the pipeline will then correct the images by a linear shift in RA and Dec. The updated

RA and Dec values replace those in the image header. These new header keyword values are then copied into all of the data products of the data reduction procedure.

3 Integral field spectroscopy of massive YSOs in LHA 120-N113

The majority of the work presented in this chapter has already been published in Ward et al. (2016). Since publication the images in Figs. 3.2, 3.3 & 3.5 have been updated using the SINFONI data treatment procedure described in Section 2.1.4. This does not affect the results of the study and the original images as displayed in Ward et al. (2016) are given in Appendix B.

3.1 Introduction

LHA 120-N113 (hereafter N113, Henize 1956) is an active star forming region within the LMC which contains a number of *Spitzer* and *Herschel* YSO candidate sources (see Fig. 3.1). We present K-band observations of three of the brightest *Spitzer* massive YSOs in N113 obtained with SINFONI (described in Section 2.1.1) at the European Southern Observatory (ESO) Very Large Telescope (VLT), with spectral and spatial resolutions of 4000 and $0\farcs1$ respectively. Sewiło et al. (2010) discussed two *Herschel* sources in N113 (YSO-1 and YSO-2, shown in Fig. 3.1) and two other YSOs (YSO-3 and YSO-4) in other regions of the LMC. To avoid confusion, the source numbers for YSO-1 and YSO-2 from Sewiło et al. (2010) will be retained but the prefix N113- will be added (N113-YSO01 and N113-YSO02) and two additional YSOs in N113 will be discussed (N113-YSO03 and N113-YSO04).

Whilst *Spitzer* and *Herschel* observations provide a valuable insight into star formation in the Magellanic Clouds, shorter wavelength studies in the near-infrared using large ground based telescopes allow us to resolve individual hot cores and compact H II regions at the distance of the LMC. These new observations provide the highest resolution imaging of these objects to date and the first K-band spectroscopy of massive YSOs in this region.

All three target regions (N113-YSO01, N113-YSO03 and N113-YSO04) are associated with bright knots in Hα emission and have been previously studied using *Spitzer* photometry

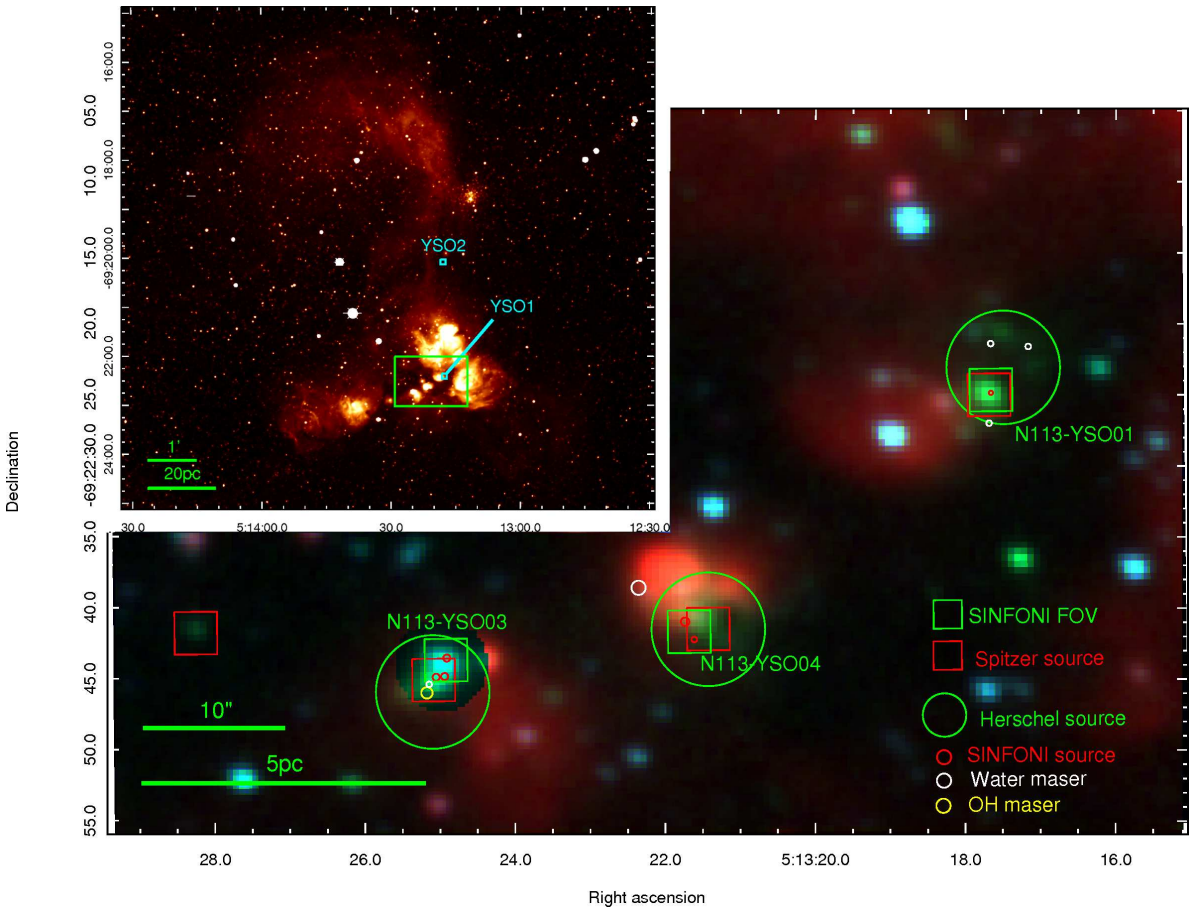

Figure 3.1: Top left panel: wide field Hα image[4] of N113 with positions of YSOs from Sewiło et al. (2010) (*cyan squares*) and the region shown in the main image marked (*green rectangle*). Main image: three colour Hα (red), IRSF *Ks*-band (green) and IRSF *H*-band (blue) (Kato et al., 2007) composite showing positions of the observed N113 SINFONI FOVs (*green squares*) and YSO candidates identified in this work (*red circles*). Also included are the spectroscopically confirmed *Spitzer* YSOs (*red squares*), the *Herschel* YSO candidates (*green circles*; Seale et al. 2014), the water maser positions (*white circles*) and the position of the OH maser (*yellow circle*). The SINFONI *red circles* represent the region from which a spectrum was extracted for each continuum source whilst all other symbol sizes are representative of the spatial accuracy of the data.

Table 3.1: Properties of *Spitzer* YSOs analysed in this paper. YSO02 has been included for completeness using the values from Sewiło et al. (2010). The value for envelope mass is not included in Sewiło et al. (2010). The S09 group refers to the YSO classifications by Seale et al. (2009; S09) where P type sources show prominent PAH emission, PE sources show strong PAH and fine-structure emission. All three of the targets observed in this work have been classed as definite YSOs by Gruendl & Chu (2009) and by Carlson et al. (2012). The bolometric luminosities and masses for N113-YSO01, N113-YSO03 and N113-YSO04 are from new SED fits using existing photometry (see text for full details).

Target	*Spitzer* Source	S09 group	$\log(L_{bol}/L_{\odot})$	Central Mass ($M_{\odot}$)	Envelope Mass ($M_{\odot}$)	Associated Maser emission
N113-YSO02			$4.51^{+0.29}_{-0.30}$	13±2		
N113-YSO01	Y051317.69−692225.0	PE	$5.18^{+0.18}_{-0.08}$	$32.3^{+0.3}_{-0.7}$	$1.8^{+6.3}_{-0.2} \times 10^2$	H_2O
N113-YSO03	Y051325.09−692245.1	P	$5.27^{+0.28}_{-0.27}$	$35.3^{+12.8}_{-0.9}$	$1.6^{+2.3}_{-1.1} \times 10^2$	H_2O, OH
N113-YSO04	Y051321.43−692241.5	PE	$5.24^{+0.31}_{-0.51}$	$34.3^{+13.9}_{-15.8}$	$1.2^{+33.3}_{-0.6} \times 10^2$	H_2O

(Gruendl & Chu, 2009; Carlson et al., 2012), *Spitzer* IRS spectroscopy (Seale et al., 2009), *Herschel* photometry (Sewiło et al., 2010) and *Herschel* spectroscopy (Oliveira et al., in prep.), confirming the YSO classification. Additionally, the region contains a number of water masers including the most intense in the Magellanic Clouds (Lazendic et al., 2002; Oliveira et al., 2006; Imai et al., 2013) and an OH maser (Brooks & Whiteoak, 1997). None of the targets in this paper appear in the YSO catalogue of Whitney et al. (2008) because they do not satisfy the strict point source criterion of the original SAGE point source catalogue of Meixner et al. (2006); since the sources are absent from the SAGE catalogue they are not part of the YSO selection. This is most likely due to their slightly irregular morphologies and the issue is discussed in detail in Chen et al. (2009a).

The following spectroscopic properties are common to all three targets: H_2 emission, PAH emission and fine structure emission (from *Spitzer*-IRS spectra, Seale et al. 2009), and [C II] emission, [O I] emission, and CO emission (from *Herschel* PACS and SPIRE spectroscopy, Oliveira et al. in prep.) whilst evidence of ices has not been observed in any of the targets. HCN and HCO^+ are also detected towards all three sources, indicating high densities (HCN and HCO^+) and photo-dissociation of molecular clouds (HCO^+), both of which are associated with massive star formation (Seale et al., 2012).

Additional properties, including results of Spectral Energy Distribution (SED) fitting using the models of Robitaille et al. (2006), are summarised in Table 3.1. The SED fits for N113-YSO01, N113-YSO03 and N113-YSO04 are performed excluding the *Herschel* photometry and setting the *Spitzer* 70 μm data as upper limits because the spatial regions from which those data are extracted are too large to be directly useful when analysing individual YSOs on the scales relevant for SINFONI observations. Physical parameters are estimated by averaging parameters of all models that fit a source's SED with normalised χ^2 per data point (χ^2/pt) in a range between $(\chi^2/pt)_{\rm best}$ for the best-fitting model and $(\chi^2/pt)_{\rm best} + 3$ (see e.g. Sewiło et al. 2013 for further details). The luminosity and mass of N113-YSO01 are consistent within the quoted uncertainties with those presented in Sewiło et al. (2010), fitted using all available photometry for $\lambda < 50$ μm. Using the calibration from Martins, Schaerer & Hillier (2005) the estimated luminosities for the 3 sources would correspond to O4–O9 stars on the main-sequence; however such estimates cannot be taken at face value since at least two sources are actually resolved into multiple components in the K-band in this work. Whilst all three of the targets of this paper appear similar based on *Spitzer* and *Herschel*

[4]MOSAIC Hα image of N113 from "Magellanic Cloud Emission Line Survey 2" (PI: You-Hua Chu, http://adsabs.harvard.edu/abs/2011noao.prop..537C).

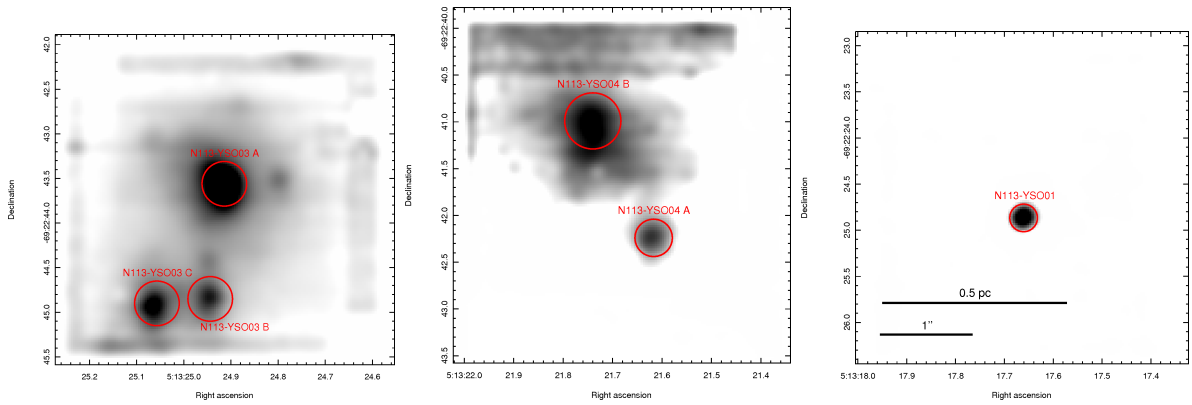

Figure 3.2: SINFONI K-band continuum emission maps. Left to right: N113-YSO03, N113-YSO04, N113-YSO01. Marked regions show the identified continuum sources and the regions from which spectra were extracted.

data (hence similar IRS-based spectral classifications), the K-band observations presented in this work reveal a wide range of sources with different spectral properties.

3.2 Results

3.2.1 Continuum emission and photometry

For each spaxel in the final flux calibrated cubes, the continuum was fitted using a 3rd order polynomial and summed for the spectral range spanning 2.028–2.290 μm to produce continuum flux maps without any contribution from line emission. The resulting images are shown in Fig. 3.2. Multiple continuum sources have been identified using these images; N113-YSO01 contains a single continuum source while N113-YSO03 and N113-YSO4 are resolved into three and two continuum sources, respectively. The positions of each continuum source are given in Table 3.2 and marked in Fig. 3.2 and the red circles show the regions from which 1D spectra were extracted from the cubes using the *sinfo_utl_cube2spectrum* recipe from the SINFONI data reduction pipeline (see Fig. C.1 for extracted spectra). The K-band continuum magnitude for each object, integrated over the same wavelength interval, is given in Table 3.3.

3.2.2 Extinction

In order to impose constraints on the physical properties of the observed YSOs, extinction corrections must be applied to the measurements. Additionally extinction towards an object can provide an assessment of how embedded the source of the emission is. We employed two methods of estimating the extinction towards each source. The first using *JHKs* photometry

Table 3.2: J2000 positions of each of the K-band continuum sources resolved for the first time in this paper.

Object	RA (h:m:s)	Dec (°:′:″)
N113-YSO01	05:13:17.666	−69:22:24.86
N113-YSO03 A	05:13:24.915	−69:22:43.55
N113-YSO03 B	05:13:24.944	−69:22:44.85
N113-YSO03 C	05:13:25.057	−69:22:44.90
N113-YSO04 A	05:13:21.617	−69:22:42.24
N113-YSO04 B	05:13:21.740	−69:22:40.99

from the IRSF (Kato et al., 2007) and the same technique employed in Cooper et al. (2013). The difference in extinctions between two wavelengths can be defined as

$$A_{\lambda 1} - A_{\lambda 2} = m_1 - m_2 + x_i \tag{3.1}$$

where m_1 and m_2 are the shorter wavelength and longer wavelength magnitudes respectively, and x_{int} is the intrinsic colour. Cooper et al. (2013) then arrive at an extinction calculation using the extinction law of Draine & Lee (1984), $A_\lambda = A_V(0.55/\lambda)^{1.75}$, and substituting this into Eqn. 3.1:

$$A_V = \frac{m_1 - m_2 + x_{int}}{0.55^{1.75}(\lambda_1^{-1.75} - \lambda_2^{-1.75})} \tag{3.2}$$

Intrinsic colours of a B0 type star of −0.12 mag and −0.05 mag are assumed for J–H and H–K, respectively (Koornneef, 1983).

The second method is that used in Davis et al. (2011) which utilises the H_2 line fluxes measured from the spectra themselves to estimate extinction. All of the H_2 emission lines analysed in this thesis are ro-vibrational and as such the ro-vibrational notation for H_2 line transitions. This takes the form $\nu_0 - \nu_1\Delta\mathrm{J}(\mathrm{J})$ where ν is the vibrational quantum number, ΔJ is the change in rotational quantum number and J is the rotational quantum number of the final state. The emission lines analysed here only concern two values of ΔJ: the S-branch is the set of transitions where $\Delta\mathrm{J} = -2$ and the Q-branch is where $\Delta\mathrm{J}=0$. Therefore the 1–0S(1) emission line is produced by a transition from $\nu = 1$ to $\nu = 0$ with a change in J of −2 and a final value of J= 1. It is apparent that the two relatively strong H_2 emission lines in the spectral range observed in this work, 1–0S(1) and 1–0Q(3) originate from the same energy level ($\nu_0 = 1$ and $\mathrm{J}_0 = 3$) and therefore the intrinsic ratio between these lines is insensitive to temperature variations. Along with the relatively large wavelength baseline between these two lines this makes them useful for calculating extinction.

Starting with the defining extinction as the difference between the attenuated magnitude and the intrinsic magnitude,

$$A_\lambda = m_a - m_i = -2.5 \log \left(\frac{I_a}{I_i} \right) \tag{3.3}$$

the difference between extinction at two different wavelengths can be arrived at through rearranging the logarithms:

$$A_{\lambda(\mathrm{S}(1))} - A_{\lambda(\mathrm{Q}(3))} = -2.5 \left(\log \left[\frac{\mathrm{S}(1)_a}{\mathrm{S}(1)_i} \right] - \log \left[\frac{\mathrm{Q}(3)_a}{\mathrm{Q}(3)_i} \right] \right) \tag{3.4}$$

$$A_{\lambda(\mathrm{S}(1))} - A_{\lambda(\mathrm{Q}(3))} = -2.5 \left(\log \left[\frac{\mathrm{S}(1)_a}{\mathrm{Q}(3)_a} \right] + \log \left[\frac{\mathrm{Q}(3)_i}{\mathrm{S}(1)_i} \right] \right) \tag{3.5}$$

Using the extinction law, $A_\lambda = (0.55/\lambda)^{1.6}$ (Prato, Greene & Simon, 2003), the relation between A_V and the difference between two extinctions is:

$$A_V = \frac{A_{\lambda 1} - A_{\lambda 2}}{\left(\frac{0.55}{\lambda_1}\right)^{1.6} - \left(\frac{0.55}{\lambda_2}\right)^{1.6}} \tag{3.6}$$

Finally substituting Eqn. 3.5 into Eqn. 3.6 and using the wavelengths $\lambda_{\mathrm{S}(1)} = 2.122$ and $\lambda_{\mathrm{Q}(3)} = 2.42$, along with the intrinsic ratio $I_{Q3}/I_{S1} = 0.704$ (Wolniewicz, Simbotin & Dalgarno, 1998), A_V is calculated as:

$$A_V = -114 \log(0.704[I_{S1}/I_{Q3}]) \tag{3.7}$$

where I_{S1} and I_{Q3} are the measured fluxes of the H_2 1–0S(1) and 1–0Q(3) emission lines, respectively. All the resulting extinction estimates are shown in Table 3.3.

The extinction estimates using the IRSF colours are inconsistent between *J*–*H* and *H*–*K* colours for the same source and for nearby objects in the same FOV. Additionally the technique using IRSF photometry has yielded negative values, likely caused by source confusion and unreliable photometry in the relatively low resolution IRSF data, or by the assumption of source spectral type. Henceforth wherever extinction corrections are applied to the N113 SINFONI observations, the values calculated using the H_2 lines are used as this technique makes no assumptions of intrinsic spectral type and it is available for all six sources. Unfortunately, whilst self-consistent within regions and available for every source, this extinction estimate is accompanied by a large degree of uncertainty as a result of the poor atmospheric transmission at the wavelengths of the Q-branch H_2 lines. Using the Galactic mean R_V

Table 3.3: Measured K-band magnitudes and extinction estimates (calculated using both methods discussed in Section 3.3.2) for all observed continuum sources. The average for each SINFONI FOV is given in the last column. For N113-YSO04 only one IRSF source is detected and it is unclear which of the sources in this work this corresponds to.

Target	K-band mag	A_V (J–H)	A_V (H–Ks)	A_V (H_2 1-0 S(1)/Q(3))	FOV average
N113-YSO01	16.27 ± 0.01	10.7 ± 1.2	16.1 ± 1.1	24.1 ± 17.3	24.1 ± 17.3
N113-YSO03 A	14.60 ± 0.03	−6.1 ± 2.4	−1.6 ± 3.3	13.5 ± 8.5	15.0 ± 0.8
N113-YSO03 B	15.45 ± 0.03	1.8 ± 1.3	11.8 ± 1.0	15.7 ± 5.4	15.0 ± 0.8
N113-YSO03 C	15.20 ± 0.01	8.9 ± 1.4		15.8 ± 3.9	15.0 ± 0.8
N113-YSO04 A	17.67 ± 0.03		11.6 ± 1.6	37.8 ± 8.9	32.4 ± 5.5
N113-YSO04 B	16.53 ± 0.06		11.6 ± 1.6	26.9 ± 6.5	32.4 ± 5.5

dependent extinction law;

$$[A(\lambda)/A_V] = a(x) + b(x)/R_V, \tag{3.8}$$

where $a(x) = 0.574x^{1.61}$ and $b(x) = -0.527x^{1.61}$ for the K-band (Cardelli, Clayton & Mathis, 1989), extinction corrections have been calculated for all measured emission lines. This extinction law was empirically derived by Cardelli, Clayton & Mathis (1989) based on observations in the UV, optical and near-infrared towards well-studied O- and B-type stars. The R_V value adopted is the same as that of the Milky Way extinction curve ($R_V = 3.1$). Although the average value in the LMC has been found to be $R_V = 3.41 \pm 0.06$ (Gordon et al., 2003), in the K-band the effect of a small variation in R_V is negligible when compared to the effect of the line measurement uncertainties.

3.2.3 Emission features

Emission line mapping was achieved by fitting Gaussian profiles to the spectral axis in the final data cubes to calculate a line flux for each spaxel using an IDL script written for this task. The resulting images are shown in Fig. 3.3. Spectra were extracted from the regions shown in Fig. 3.2 of the flux calibrated data cubes using the *sinfo_utl_cube2spectrum* recipe from the SINFONI data reduction pipeline. Emission lines in the extracted 1D spectra for each continuum source were measured by Gaussian fitting within the Starlink software package SPLAT. The measured emission line fluxes (without extinction correction) are given in Table E.1. The flux values obtained from the spectra were converted to line luminosities using a distance of 49.4±0.5 kpc (Laney, Joner & Pietrzyński, 2012).

H I emission

The strongest detected H I emission line in this sample, Brγ, is most commonly associated with accretion in star formation studies. For intermediate mass YSOs the empirically derived

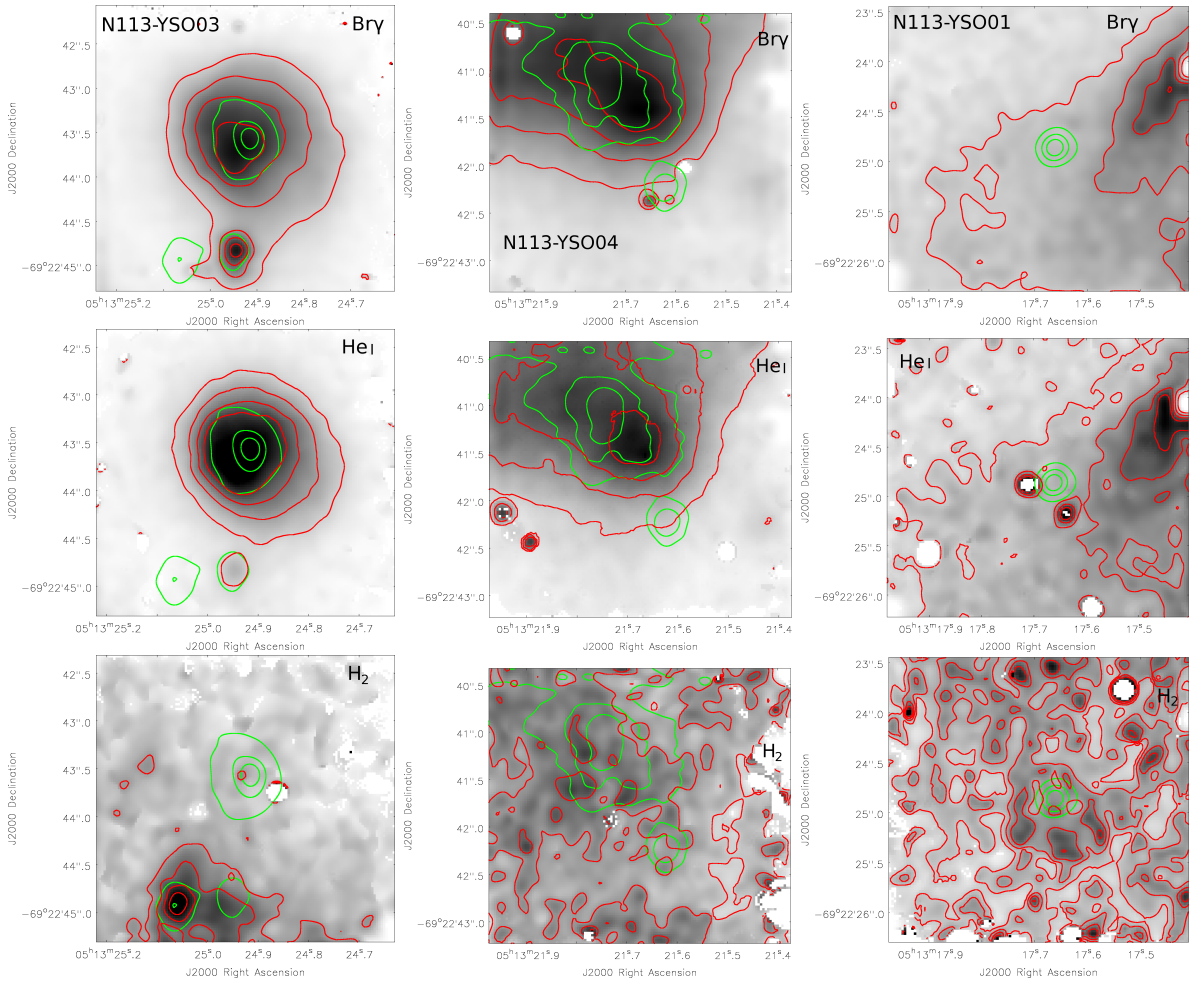

Figure 3.3: Emission line maps with contours overlaid. Red contours - line emission [0.2, 0.4, 0.6, 0.8]×peak, green contours - continuum emission [0.25, 0.5, 0.75]×peak. Left to right - N113-YSO03, N113-YSO04, N113-YSO01. Top to bottom - Brγ, He I, H_2 1-0(S1).

relation from Calvet et al. (2004) can be used to estimate the accretion luminosity from Brγ luminosity:

$$\log(L_{acc}) = -0.7 + 0.9(\log(L_{Br\gamma}) + 4) \tag{3.9}$$

Whilst this relation holds true for Herbig A stars, the higher mass Herbig B type stars have been observed in some cases to exhibit a Brγ emission excess (Donehew & Brittain, 2011; Mendigutía et al., 2011), most likely due to an additional emission component originating from the strong winds driven by stellar UV photons emitted from hot stars. It is likely therefore that a similar effect is present in the more massive YSOs during the later phases of their evolution. For the purposes of comparing this sample with a Galactic sample however, the above relation can be applied to gain an equivalent accretion luminosity assuming that both samples cover the same range of evolutionary states and YSO masses. Additionally the impact that metallicity may have on this relation should be considered. Whilst it is the case that the momentum and mass loss rates of stellar winds are strongly affected by metallicity (Puls, Springmann & Lennon, 2000; Vink, de Koter & Lamers, 1999, 2001; Kudritzki, 2002; Krtička, 2006), it is the number of photons produced which are able to ionize hydrogen that is significant when measuring Brγ emission. Kudritzki (2002) predicts that the number of photons capable of ionising hydrogen is barely affected by a change in metallicity. This suggests that the above relationship between Brγ and accretion luminosity should hold for studies in lower metallicity environments.

Whilst bolometric luminosities have been obtained for each target using existing *Spitzer* data (see Table 3.1), two out of three target fields contain multiple continuum sources and the third exhibits emission that appears to originate from outside the FOV. Without higher resolution mid-infrared studies it will not be possible to accurately determine bolometric luminosities for each of the sources. Therefore the equivalent accretion luminosity is plotted against K-band magnitude in Fig. 3.4 rather than bolometric luminosity. A distance of 49.4$\pm$0.5 kpc (Laney, Joner & Pietrzyński, 2012) was assumed to the LMC and distances to Galactic sources were obtained from the RMS survey database[5]. From Fig. 3.4 it can be ascertained that the Brγ luminosities observed towards all six sources fall within a range consistent with that observed towards the Galactic sources. The sources for which we believe that the emission is associated with that source exhibit a higher Brγ / K-band continuum emission ratio than the remaining sources. The Brγ emission luminosities of the YSOs in this study, while consistent with those of Galactic YSOs but appear to be at the high end of

[5]http://rms.leeds.ac.uk/cgi-bin/public/RMS_DATABASE.cgi

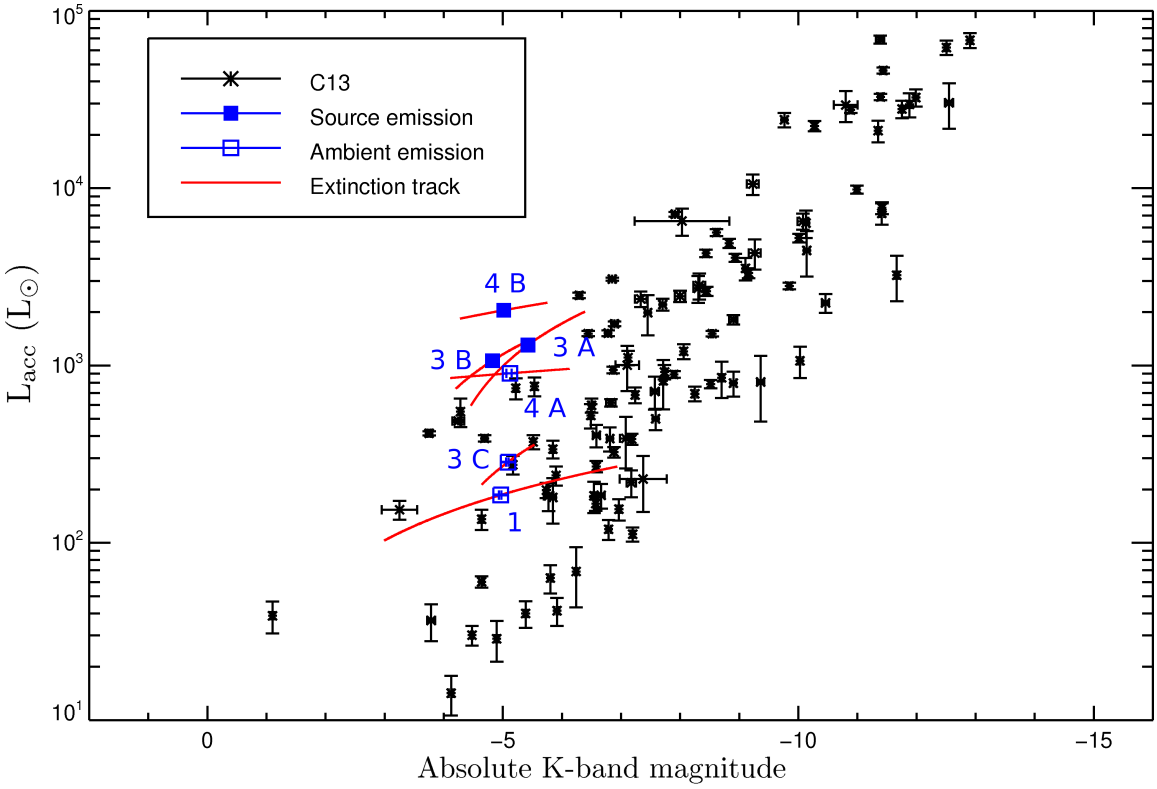

Figure 3.4: Equivalent accretion luminosity against absolute K-band magnitudes. A distance to the LMC of 49.4±0.5 kpc is assumed. Extinction correction has been applied using A_V values described in Section 4.2 for the N113 data and A_V values from Cooper et al. (2013) for the Galactic data. Slit losses have not been taken into account for the Galactic data. The range of possible values allowed by the uncertainty in extinction for each N113 source is shown as a red extinction track. For clarity the N113-YSO prefixes have been omitted. Source emission (*filled squares*) and ambient emission (*open squares*) are discussed in the main text.

the Galactic distribution, possibly indicative of high accretion rates.

The spatial extent of the Brγ emission is mapped in the top row of Fig. 3.3. Where the Brγ emission is significantly spatially extended beyond the continuum source, it is possible that the contribution of non-accretion emission is significant. This appears to be the case in N113-YSO03 A and N113-YSO04 B. The Brγ emission is compact in N113-YSO03 B whilst in the remaining three continuum sources (N113-YSO01, N113-YSO03 C and N113-YSO04 A) the Brγ emission appears to be ambient or produced from other sources in the FOV. The dominant source of Brγ emission in N113-YSO01 peaks outside of the FOV.

In addition to mapping the Brγ emission flux around these sources, centroid velocities have also been mapped relative to the centroid at the westernmost continuum source in each field (N113-YSO01, N113-YSO03 A, N113-YSO04 A), shown in Fig. 3.5. Spaxels where the uncertainty in relative velocity exceeds the imposed limits (5 km s^{-1} in YSO03 and 10 km s^{-1} in YSO01 and YSO04) have been masked. Figure C.1 shows emission line velocity maps obtained from the sky cube for N113-YSO03, showing that there are no significant

systematic velocity gradients. The two sources which exhibit extended Brγ emission (N113-YSO03 A and N113-YSO04 B) exhibit clear velocity gradients ($\pm$10km s^{-1} and $\pm$5km s^{-1} respectively) centred on the continuum source, suggesting the expansion of excited gas around these objects. The off-source Brγ emission in the N113-YSO01 FOV appears to be slightly blueshifted with respect to the central continuum source.

The Pfund series is detected towards three of the six sources resolved in this work; N113-YSO03 A, N113-YSO03 B and N113-YSO04 B. Unfortunately the K-band Pfund series lies in an area of poor atmospheric transmission so it is not easy to obtain accurate measurements of their flux. The positions of the detected Pfund series emission lines are shown in Fig. D.3 and the measured line fluxes are listed in Table E.1. Using the Pfund series emission and the Brγ emission it may be possible to obtain temperatures from the ratios of hydrogen recombination lines if the density is well constrained.

Using the photo-ionization code CLOUDY a grid of 10200 sets of model emission line fluxes were generated with varying densities and temperatures (of the exciting source). As an example the Pfund series 19–5 / Brγ flux ratio is shown for all models allowed by the measured line ratio in Fig. 3.6 where only the masked regions are disallowed temperature/density combinations, demonstrating the scale of the degeneracy. Whilst the measured line ratios are certainly consistent with the presence of massive OB-type stars, no further constraints on these physical parameters were obtained from our data, due the low S/N ratio in the Pfund series measurements, the large reddening uncertainties, and the strong dependence on density that is poorly constrained.

He I emission

The primary production mechanism for the He I emission line is the ionization and subsequent recombination of helium which becomes significant at the ionization boundary and potentially in the collision with surrounding medium (Porter, Drew & Lumsden, 1998). Whilst the He I / Brγ ratio is sensitive to the temperature of the emitting regions, its heavy dependence on density means that it cannot be used as a robust diagnostic of temperature (Shields, 1993).

The 2.0587 μm He I emission line is detected at the position of all six of the continuum sources and extended He I emission is measured around two sources (N113-YSO03 A and N113-YSO04 B; see Fig. 3.3, middle row). The two sources which exhibit the extended He I emission are the strongest He I emitters and those with the first and third highest Brγ fluxes, respectively. The He I doublet at 2.113 μm was detected but not resolved towards

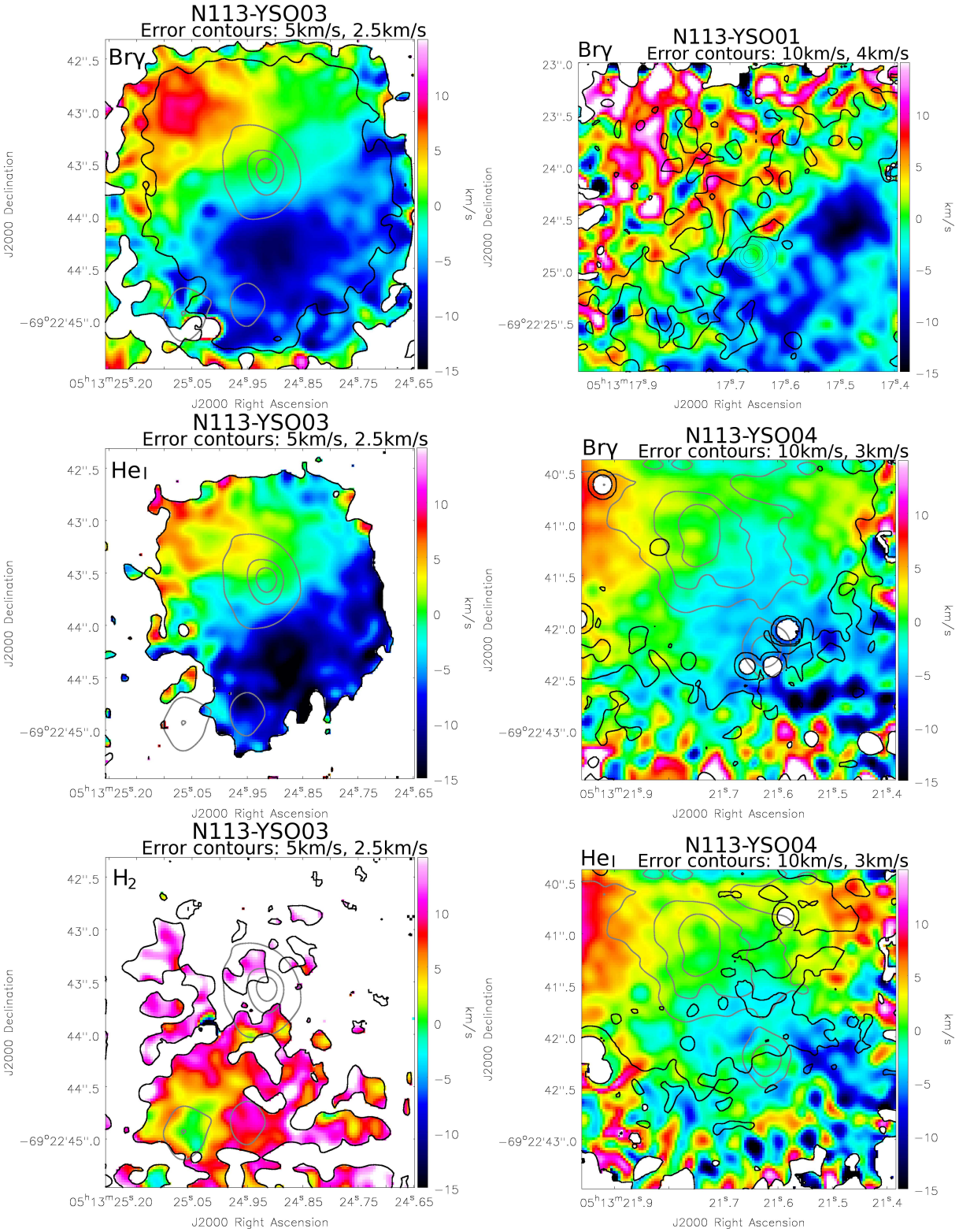

Figure 3.5: Left: Brγ, He I and H_2 2.1218μm centroid velocity maps for N113-YSO03. Right: Brγ centroid velocity map for N113-YSO01 (top) and Brγ and He I velocity maps for N113-YSO04 (middle and bottom). Black contours represent the uncertainties; the outer (left) and inner (right) contour values are indicated in each image. The continuum contour levels are [0.25, 0.5, 0.75]×peak (grey).

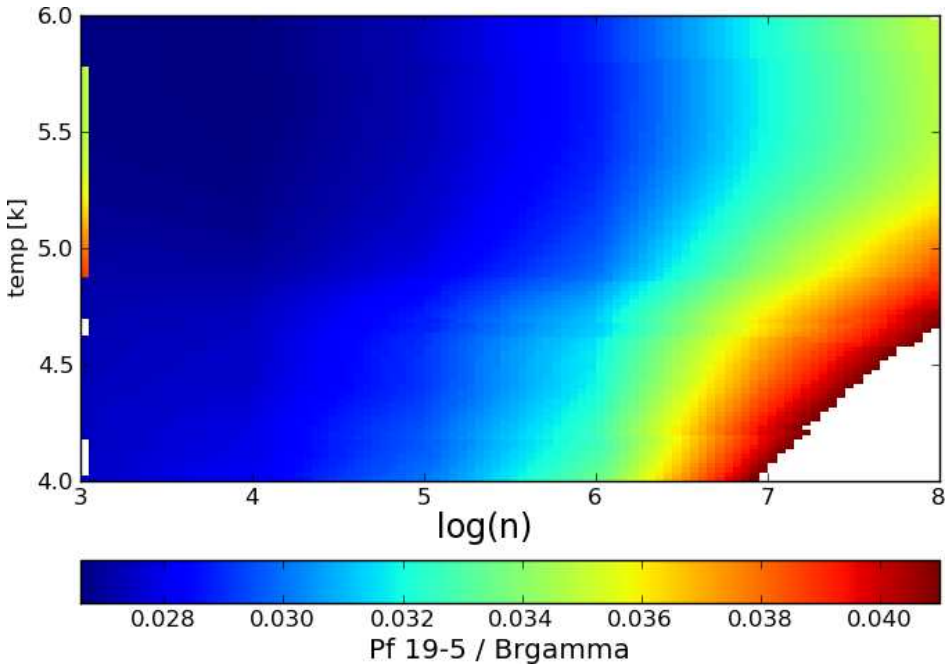

Figure 3.6: Pf 19–5 / Brγ emission line ratios at the temperatures and densities allowed by the measured emission line ratio. The masked area is where the model ratios are inconsistent with the measured ratio.

three sources (N113-YSO03 A, N113-YSO04 A and N113-YSO04 B) indicating a collisional excitation component in regions of high density (Lumsden, Puxley & Hoare, 2001). The flux of the 2.113μm doublet is typically significantly lower than the 2.058 μm line (Table E.1) and the S/N for the doublet in our sample prevents further analysis. No He II emission has been detected towards any of the sources in this work.

Spatially, the He I emission tends to trace the same structures as the Brγ emission, although with weaker and slightly more compact emission. This is to be expected in sources where the central source is hot enough to excite a large volume of surrounding gas as in a compact H II region. In N113-YSO03 C and N113-YSO04 A, the detected He I emission appears to be ambient to the region, possibly originating from N113-YSO03 A and N113-YSO04 B, respectively. The He I emission in N113-YSO01 traces the morphology of the Brγ emission, also appearing to originate outside of the FOV.

Figure 3.7 plots the He I 2.0587 μm emission line luminosity against the Brγ luminosity for all N113 continuum sources and those from Cooper et al. (2013) for which both line measurements are available. It appears that the same trend and range of values is observed in N113 as in the Milky Way. The off source emission in N113-YSO01 (indicated by "1 ext") appears to have a comparable He I/Brγ ratio to N113-YSO03 A and N113-YSO04 B, suggesting that it presents a relatively energetic environment.

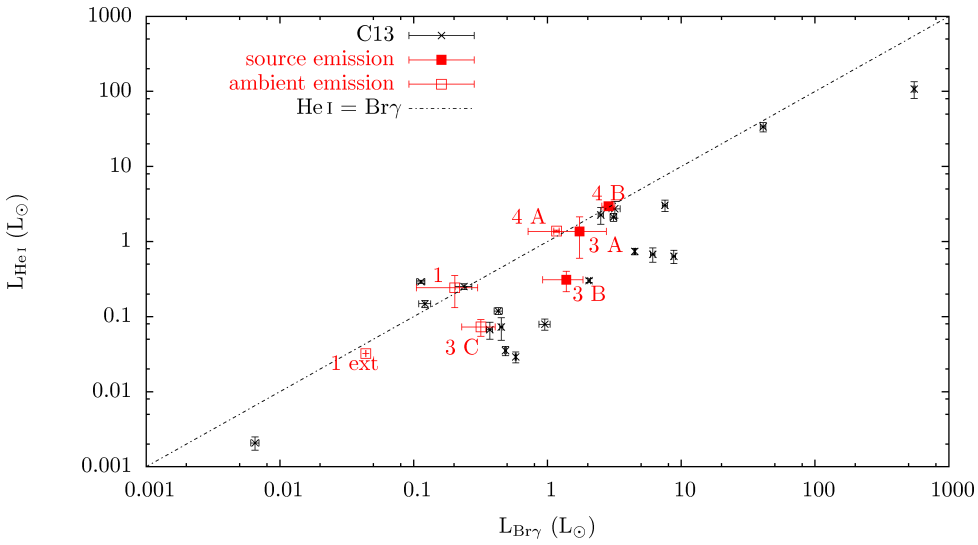

Figure 3.7: He I luminosity plotted against Brγ luminosity for all continuum sources. 1 ext denotes the extended emission in the N113-YSO01 cube (not corrected for extinction). For clarity the N113-YSO prefixes have been omitted.

As well as tracing the same morphological structures, where extended He I emission is present it exhibits the same velocity fields as the Brγ emission, as demonstrated in Fig. 3.5 for N113-YSO03 and N113-YSO04. This is further evidence that the extended Brγ emission and extended He I emission originate from the same strong radiation field.

H_2 emission

The H_2 lines detected in our spectra are identified in Fig. D.1. Although the H_2 emission has been spatially mapped (see Fig. 3.3), the signal-to-noise per spaxel in N113-YSO01 and N113-YSO04 for the H_2 lines is poor and very little morphological information can be obtained. Additionally it appears likely that the H_2 emission in N113-YSO01 and N113-YSO04 is consistent with uniform ambient H_2 emission, unrelated to the discrete YSOs. In N113-YSO03 the H_2 emission is relatively compact and peaks at the position of source C. The H_2 emission measured in source B may have a significant component originating from source C. Whilst N113-YSO03 A does not show significant H_2 emission in Fig. 3.3, on inspection of the extracted spectrum (Fig. D.1) it does exhibit relatively weak H_2 emission which is likely to be ambient, as is the case for N113-YSO01 and N113-YSO04. In summary only N113-YSO03 C is a significant source of H_2 emission.

The H_2 2.1218 μm emission luminosity is plotted against the Brγ luminosity for each of the continuum sources in Fig. 3.8. Little correlation can be seen on this diagram, suggesting that the emitting regions of the lines are unrelated. N113-YSO03 C clearly falls above the

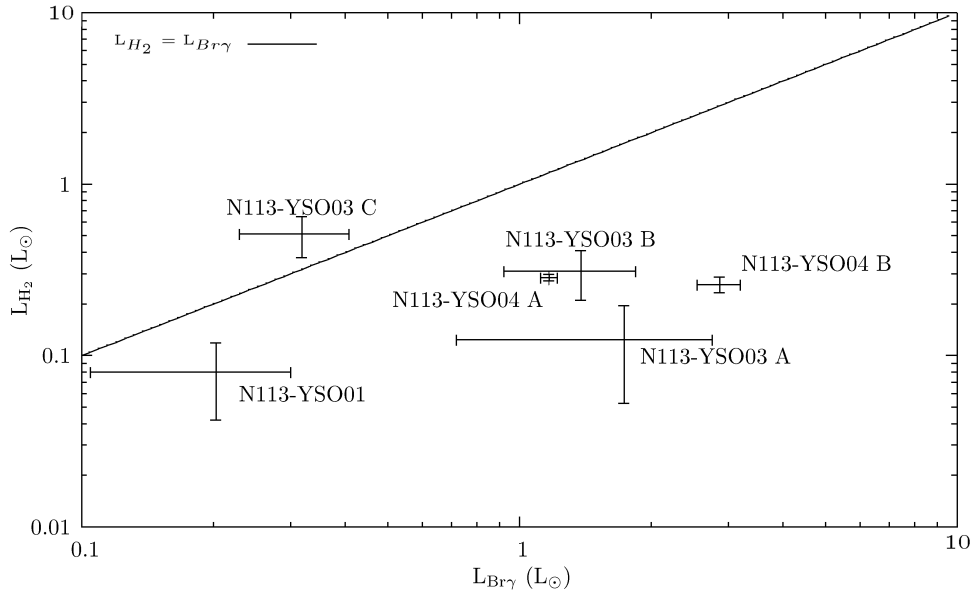

Figure 3.8: H_2 2.1218μm emission against Brγ emission for all observed continuum sources.

Table 3.4: Extinction corrected H_2 emission line ratios with respect to the 1-0S(1) emission line for all objects. Also included are the expected H_2 line ratios for photo-excitation (Black & van Dishoeck, 1987) and shocked emission (Shull & Hollenbach, 1978).

Object	1-0S(0) 2.2235 μm	1-0S(2) 2.0338 μm	1-0S(3) 1.9576 μm	2-1S(1) 2.2477 μm	2-1S(2) 2.1542 μm	2-1S(3) 2.0735 μm
N113-YSO01	0.31±0.35	0.68±0.57		0.39±0.27	0.18±0.12	
N113-YSO03 A	0.41±0.34	0.36±0.28	0.44±0.35	0.30±0.25	0.15±0.12	0.34±0.27
N113-YSO03 B	0.37±0.18	0.30±0.13	0.24±0.10	0.17±0.08	0.06±0.03	0.21±0.09
N113-YSO03 C	0.28±0.11	0.34±0.12	0.45±0.16	0.15±0.06	0.06±0.02	0.17±0.06
N113-YSO04 A	0.26±0.02	0.46±0.04		0.20±0.02	0.15±0.02	0.23±0.02
N113-YSO04 B	0.26±0.04	0.53±0.09		0.34±0.06	0.19±0.03	0.40±0.06
Photo-excitation	0.4–0.7	0.4–0.6		0.5–0.6	0.2–0.4	0.2–0.3
1000 K shock	0.27	0.27	0.51	0.005	0.001	0.003
2000 K shock	0.21	0.37	1.02	0.083	0.031	0.084
3000 K shock	0.19	0.42	1.29	0.21	0.086	0.27
4000 K shock	0.19	0.44	1.45	0.33	0.14	0.47

H_2 = Brγ line whereas Brγ > H_2 for all of the other sources, indicating that N113-YSO03 C is dominated by H_2 emission whilst the remaining sources are dominated by atomic Brγ emission, consistent with the view that the H_2 emission in N113-YSO01, N113-YSO04 and possibly N113-YSO03 A is mostly ambient.

The ratios of K-band H_2 line fluxes have the potential to be used to constrain whether the source of the emission is photo-excited or shock-excited. The extinction corrected flux ratios for all of the observed H_2 lines with respect to the 1–0S(1) line are shown in Table 3.4, with the expected ratios based on models of photo-excited emission and interstellar shocks in molecular clouds at various temperatures given in the lower part of Table 3.4. Whilst it is likely that all targets have contributions from both shocked and a Photo-Dissociation Region

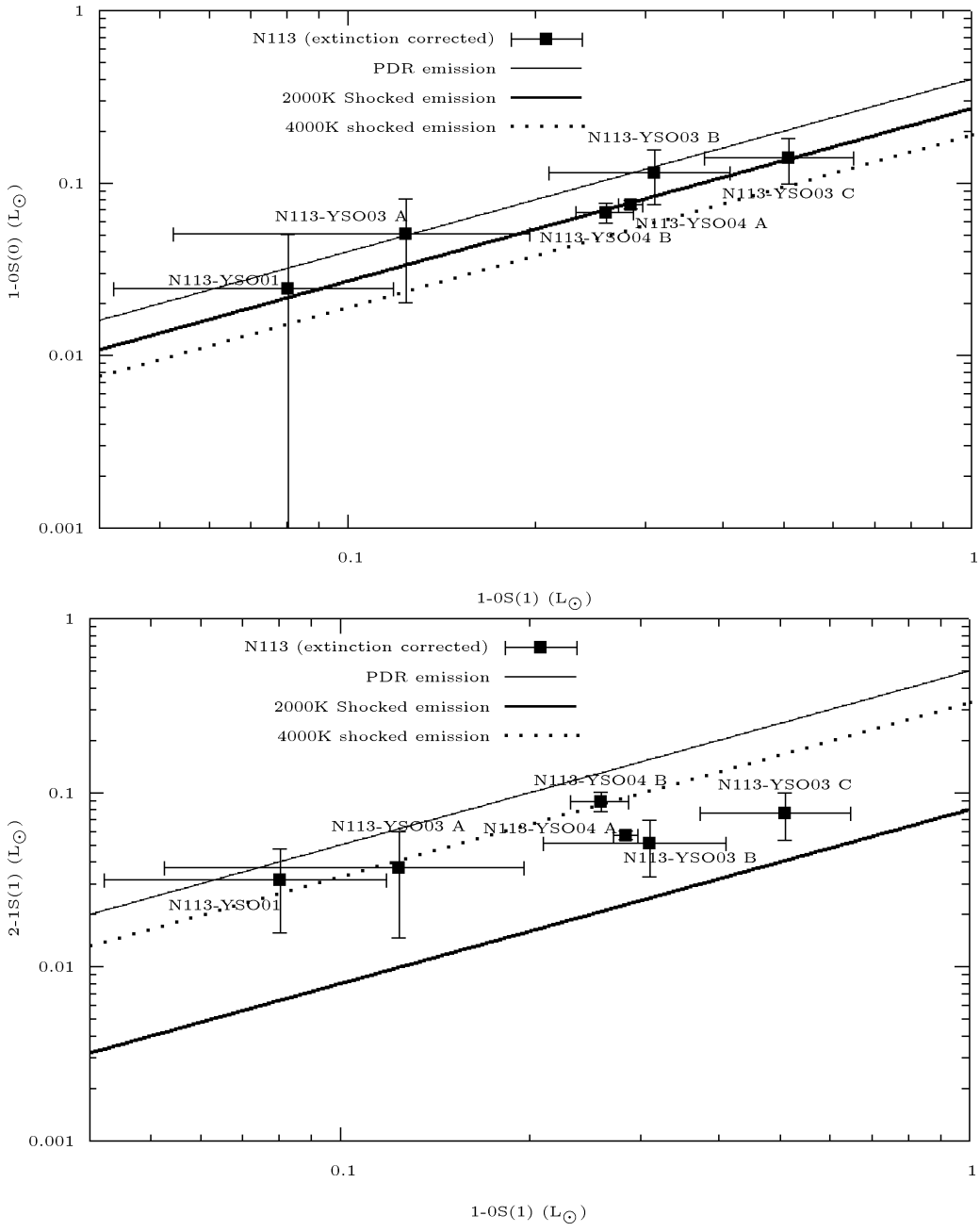

Figure 3.9: Top: H_2 1-0(S0) 2.2235 μm emission against H_2 1-0(S1) 2.1218 μm emission for all observed continuum sources. Bottom: H_2 2-1(S1) 2.2477 μm emission against H_2 1-0(S1) 2.1218 μm emission for all observed continuum sources. Lines shown are for photo-dissociation emission and shocked emission at 2000 K and 4000 K as indicated in the legend.

(PDR), these values can be used to determine which excitation mechanism of H_2 emission is dominant. In the radiative excitation scenario, the ratios with respect to the 2.1218 μm 1-0(S1) line should fall in the range 0.5 to 0.6 and 0.4 to 0.7 for the 2-1(S1) and 1-0(S0) lines (at 2.2477 μm and 2.2235 μm), respectively (Black & van Dishoeck, 1987). Adopting $T = 2000$ K, shock-excitation should give values of 0.08 and 0.21, respectively for the same emission line ratios (Shull & Hollenbach, 1978). Together, these two line ratios have the potential to be used as a diagnostic tool as the 2-1(S1) line ratio has a significant shock temperature dependence whereas the 1-0(S0) ratio exhibits a large gap between predicted PDRs and shocks and, crucially, an inverse dependence on shock temperature.

In Fig. 3.9 the observed 1-0(S0) and 2-1(S1) ratios relative to the 1-0(S1) line are compared to those expected from photo-excitation, and shocked emission at 2000 K and 4000 K. In the upper panel three sources appear highly likely to be shock emission dominated (N113-YSO03 C, N113-YSO04 A, N113-YSO04 B) and two sources could be PDR emission dominated (N113-YSO03 A, N113-YSO03 B) but the uncertainties are large. For the final source (N113-YSO01), the uncertainty in the 1-0(S0) flux is such that no conclusions can be drawn on the origin of the emission. In the lower panel of Fig. 3.9, all of the sources appear to fall within the shocked emission zone, with two of the sources (N113-YSO01, N113-YSO03 A) within 1σ of PDR emission. From this it is concluded that for N113-YSO03C (the only source for which H2 emission is not ambient) the emission is possibly shock-dominated. The H_2 emission from sources A and B in N113-YSO03 may have contribution from both shock excitation and photo-dissociation whilst towards both sources in N113-YSO04 the emission appear to be shock dominated. Due to low S/N no conclusion can be drawn for the source of the H_2 emission in N113-YSO01. The emission line ratios expected for shocked excitation of H_2 lines in this case assume a high density environment of $n = 3.0 \times 10^5\,\mathrm{cm}^{-1}$ and lowering in the density by an order of magnitude can alter the expected ratios by up to around 30% for the some of the emission lines used here. It is therefore doubtful that any of the emission line ratios presented here can alone offer a concrete classification of shocked emission or photo-excited emission but rather offer an indication of the likely nature of the emission.

N113-YSO03 was the only source for which the H_2 centroid velocity field was able to be mapped (Fig. 3.5) and over the relatively small spatial range where this was possible, there appears to be a small velocity gradient towards the red in the emission west of source C.

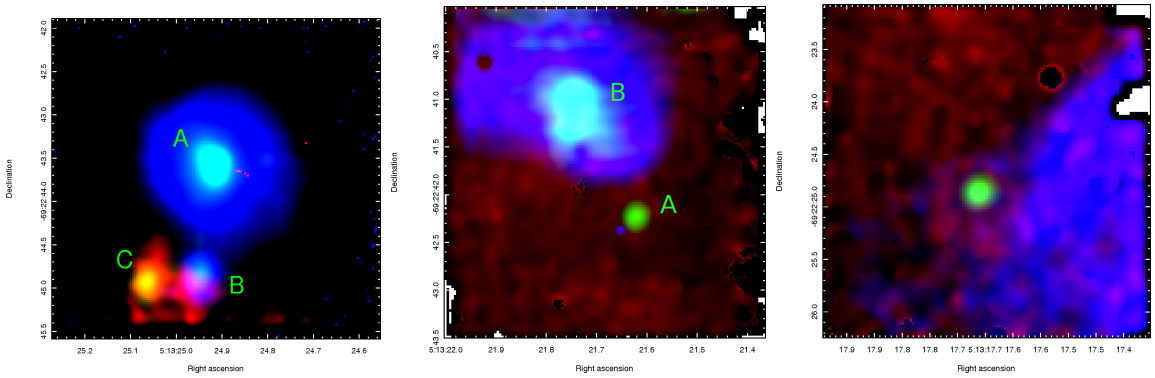

Figure 3.10: Three colour images of all three targets observed with SINFONI in N113. Left to right: N113-YSO03, N113-YSO04, N113-YSO01. Red – H_2 2.1218 μm emission, green – continuum emission, blue – Brγ emission.

3.3 Discussion

Figure 3.10 shows the three colour images of all three targets studied in this chapter, demonstrating the striking differences in emission line morphologies observed despite the remarkably similar properties when observed at lower spatial resolutions (see Table 3.1). In this section each *Spitzer* selected target is discussed in turn.

3.3.1 N113-YSO01

The N113-YSO01 FOV contains a single VLT/SINFONI K-band continuum source to a resolution of $0\farcs2$. *Spitzer* resolution at the shortest wavelengths is $\sim 2''$ so whilst the bolometric luminosity ($1.5^{+0.8}_{-0.3} \times 10^5$ L$_\odot$) for this source is likely to be more robust than most, the emission lines from the spatially unresolved studies will likely be contaminated by the off-source emission seen in Fig. 3.3. Both the Brγ emission and the He I emission peak approximately $1\farcs3$ ($\sim$0.31 pc) away from the continuum source; thus it appears that all of the measured line emission towards this object is ambient or extremely weak. In the top panel of Fig. 3.1, two large Hα bubbles can be seen in close proximity to N113-YSO01. Thus it is possible that the line emission detected towards N113-YSO01 is associated with these larger scale structures.

Figure 3.1 shows the positions of three maser sources that are close to N113-YSO01, however spectroscopically N113-YSO01 does not exhibit any indicators of strong outflows which could stimulate the maser emission. Additionally the distances (0.52 pc – 1.01 pc) between these masers and the N113-YSO01 infrared source suggests that the masers may be in fact associated with other, weaker K-band sources just visible in Fig. 3.1. The maser sources also do not appear to coincide with the prominent *Spitzer* source targeted by these observations.

Massive YSOs without any significant K-band emission lines are not common in the Galactic data set but they have been observed (e.g. G103.8744+01.8558, Cooper et al. 2013). Longer wavelength data available for those Galactic sources makes the YSO identification credible. It is possible that such sources represent the youngest hot core objects or they are simply weakly emitting YSOs. However, the possibility that the source observed in the N113-YSO01 FOV is not in fact a YSO cannot be excluded by this work. At this stage the origin of the line emission in the K-band and *Spitzer*-IRS spectra cannot be constrained.

3.3.2 N113-YSO03

The line morphologies observed in the N113-YSO03 FOV suggest that the three continuum sources represent three different stages of star formation, likely reflecting a range of masses. N113-YSO03 A is the brightest of all the observed sources in the K-band with strong, extended and expanding Brγ emission and He I emission, implying that it is a relatively evolved compact H II region. It also has the strongest He I emission, likely caused by the strong winds associated with an emerging massive star.

N113-YSO03 B also exhibits strong Brγ emission but it is compact and the He I emission is much weaker, suggesting a considerably lower contribution to the Brγ emission from an H II region and thus a cooler and likely earlier stage (younger or less massive) object than N113-YSO03 A, possibly dominated by accretion emission.

N113-YSO03 C exhibits very weak or absent Brγ and He I emission, and prominent H_2 emission. In addition, the H_2 line ratios are consistent with emission that is very heavily dominated by shocked emission but this conclusion assumes a high density ($\sim 3\times10^5\,\mathrm{cm}^{-3}$). It is therefore likely that N113-YSO03 C is the least evolved of the three sources, representing an early stage YSO with strong bipolar outflows. This is also consistent with the much redder continuum slope for its spectrum. The highest intensity water maser source in the Magellanic Clouds was identified at a distance of 0.36±0.07 pc ($1\farcs5\pm0\farcs3$) of source N113-YSO03 C (Lazendic et al., 2002; Oliveira et al., 2006; Carlson et al., 2012). This maser could therefore be associated with source C given that this source appears to be a young source driving an outflow, consistent with water maser emission. Of the three sources resolved in this FOV, N113-YSO03 A is the most massive, having evolved to the point of shaping its environment in the form of a compact H II region, while N113-YSO03 C is the least evolved and thus the least massive.

3.3.3 N113-YSO04

N113-YSO04 exhibits two continuum sources, one compact and one extended and more diffuse. It is likely that most if not all of the H_2 emission detected in the FOV is ambient emission.

As in N113-YSO01, all of the emission in N113-YSO04 A appears to be either ambient emission (H_2 emission) or contaminating emission (Brγ and He I) from N113-YSO04 B. Therefore the possibility that N113-YSO04 A is not a YSO cannot be excluded based on currently available data. N113-YSO04 A exhibits a considerably redder continuum than N113-YSO04 B (see Fig. C.1) and a significantly higher A_V, indicating a more embedded object.

The extended source (N113-YSO04 B) shows strong Brγ and He I emission which is slightly offset from the continuum source. The underlying cause for the offset in the extended line emission is unclear but it is likely to be a result of the geometry of the central source and its projection onto the sky. Indeed, this offset is reminiscent of SINFONI observations of two massive YSOs in the SMC presented in Chapter 4 although those sources differ in that they are also sources of H_2 emission (see Section 4.3.2 for a detailed discussion). It also exhibits a similar expanding velocity profile for the Brγ and He I emission as N113-YSO03 A, implying that strong winds are present around both of these sources and that N113-YSO04 B is in a similar evolutionary state to N113-YSO03 A. The detection of the He I 2.113 μm doublet towards both sources is also consistent with an energetic, high density region such as a compact H II region.

An H_2O maser has been previously identified to the North East of this region (See Fig. 1; Imai et al. 2013) however it has a relatively large separation of $9\farcs6\pm0\farcs5$ (2.3 ± 0.1 pc) which may indicate that this maser is not likely to be associated with either of the N113-YSO04 sources. Without higher resolution imaging in the mid-infrared to sub-mm wavelength range it is not possible to determine the source of this maser emission.

3.4 Chapter summary

Using the SINFONI integral field spectrograph at the VLT, a sample of three *Spitzer* selected YSOs situated in the bright dusty lane in N113 has been observed. The three targets look very similar at longer wavelengths: all are classified as P- or PE-type sources (*Spitzer*/IRS spectrum rich in PAH emission and fine structure emission; Seale et al. 2009). When the sources

are observed at higher spatial resolution in the K-band, a wide variety of morphological and spectral features is revealed. The results of this study are summarised below:

i Of the three *Spitzer* sources, six distinct K-band continuum sources have been resolved. N113-YSO01 contains only a single continuum source, N113-YSO03 contains three and N113-YSO04 contains two.

ii Two sources (N113-YSO03 A, N113-YSO04 B) exhibit strong, extended wind features and are therefore likely to be compact H II regions, i.e. massive objects in the final stages of star formation. The presence of the 2.113 μm He I emission suggests that these are indeed compact H II regions since in the Cooper et al. (2013) Galactic sample this doublet is only found towards H II regions. The velocity fields of extended gas structures around the two continuum sources (N113-YSO03 A and N113-YSO04 B). These measurements imply stellar feedback in the form of stellar winds from newly formed massive stars at the centre of compact H II regions, driving expansion.

iii N113-YSO03 C is dominated by H_2 emission, which is likely to occur in the collimated outflows driven by the youngest hot core phase objects.

iv N113-YSO03 B appears to be a fairly typical, later stage massive YSO: a point source with strong Brγ emission and weaker He I emission.

v The remaining sources, N113-YSO01 and N113-YSO04 A, are compact and do not appear to have any emission lines associated with the continuum source (all observed line emission appears to be ambient). For N113-YSO04 A this emission is likely to be sourced from the extended source N113-YSO04 B whereas in N113-YSO01 the source of the line emission appears to be outside the FOV. Without additional data it is unclear where either of these sources would fall in an evolutionary context: these objects could be featureless YSOs (as observed in the Galaxy) but the possibility of a non-YSO classification cannot be excluded.

vi Levels of extinction have been found to be typically lower than those within our Galaxy. The average extinction, A_V and standard deviation of the N113 sample is 22.3±9.3 mag compared with the values of Cooper et al. (2013) of 45.7±17.6 mag. The average extinction towards massive YSOs in N113 is approximately half that of the Milky Way, consistent with the lower dust-to-gas ratio observed in the LMC (Bernard et al., 2008) and an LMC metallicity of approximately half solar metallicity.

vii A number of interstellar H_2O masers and a single OH maser have previously been detected in the region; however many of these in fact fall at a significant distance from the continuum sources (> 0.5 pc) and are therefore unlikely to be excited by the sources resolved here. The one exception is N113-YSO03 C which is likely to be the excitation source of the water maser to the South East and also possibly the OH maser.

viii The equivalent accretion luminosities calculated are consistent with the Galactic distribution but appear to be high for their K-band magnitudes. The approach used here however does neglect any effects of metallicity K-band continuum emission. Brγ emission and accretion rates are discussed at length and with the addition of sources in the SMC in Section 4.3.1.

ix The CO bandhead, often associated with accretion discs in YSOs, is not detected towards any of the sources presented in this chapter. Even though the disc geometry can have a significant impact on the detection of CO (Kraus et al., 2000; Barbosa et al., 2003) and the sample is small, the lack of CO bandhead emission could be due to CO destruction in the harder radiation fields associated with lower metallicity environments.

Through high spatial resolution characterisation of three similar *Spitzer* sources, a wide range of morphological and spectral properties have been revealed. Two out of the three *Spitzer* sources in this study contain multiple continuum sources and it is likely that this is not an uncommon occurrence in the Magellanic Clouds. Crucially, it has been shown that whilst *Spitzer* and *Herschel* observations provide valuable insights into the star formation process in the Magellanic Clouds, higher spatial resolution is required in order to develop a full understanding of the YSOs in question, especially when comparing them to Galactic samples. These SINFONI observations of YSOs in N113 have provided a useful pilot study for the techniques applied to a larger set of massive YSOs presented in the next chapter as well as a point for comparison between the Milky Way and the SMC.

4 Integral field spectroscopy of massive young stellar objects in the Small Magellanic Cloud

The contents of this Chapter have been published in Ward et al. (2017) and have been reformatted to form a thesis chapter.

4.1 Introduction and previous observations

As described in Chapter 1, the SMC provides a unique laboratory in which to study star formation in an environment which differs significantly from that of our own Galaxy. In this chapter I describe the integral field spectroscopic observations obtained with SINFONI towards 19 spectroscopically confirmed massive YSOs in the SMC.

The majority of the *Spitzer* sources presented in this chapter are a subset of the sample presented in Oliveira et al. (2013). They used the S^{3}MC catalogue (Bolatto et al., 2007) and colour and flux cuts to select YSO candidates yielding 31 YSO candidates. Also added to the sample of Oliveira et al. (2013) were three YSOs identified serendipitously by van Loon et al. (2008) providing a total sample of 34 YSO candidates, all but one of which were spectroscopically confirmed as YSOs based on properties of *Spitzer* InfraRed Spectrograph (IRS) spectra.

A simplified and truncated version of Table 3 from Oliveira et al. (2013) is given in Table 4.1, showing only those *Spitzer* YSOs for which SINFONI data were obtained. This table includes identified emission and absorption features based on *Spitzer* and ground-based data including ice absorption features as well as types based on the classification systems applied to LMC YSOs of Seale et al. (2009) and Woods et al. (2011), explained in Section 1.5.2. Also included in Table 4.1 are the bolometric luminosities of the *Spitzer* sources obtained from SED fitting and whether or not radio emission is detected towards the source. Optical types are also given in Table 4.1 based on the identification of emission lines in the optical spectra presented in Oliveira et al. (2013); type evolution I to V represents an increase in the number

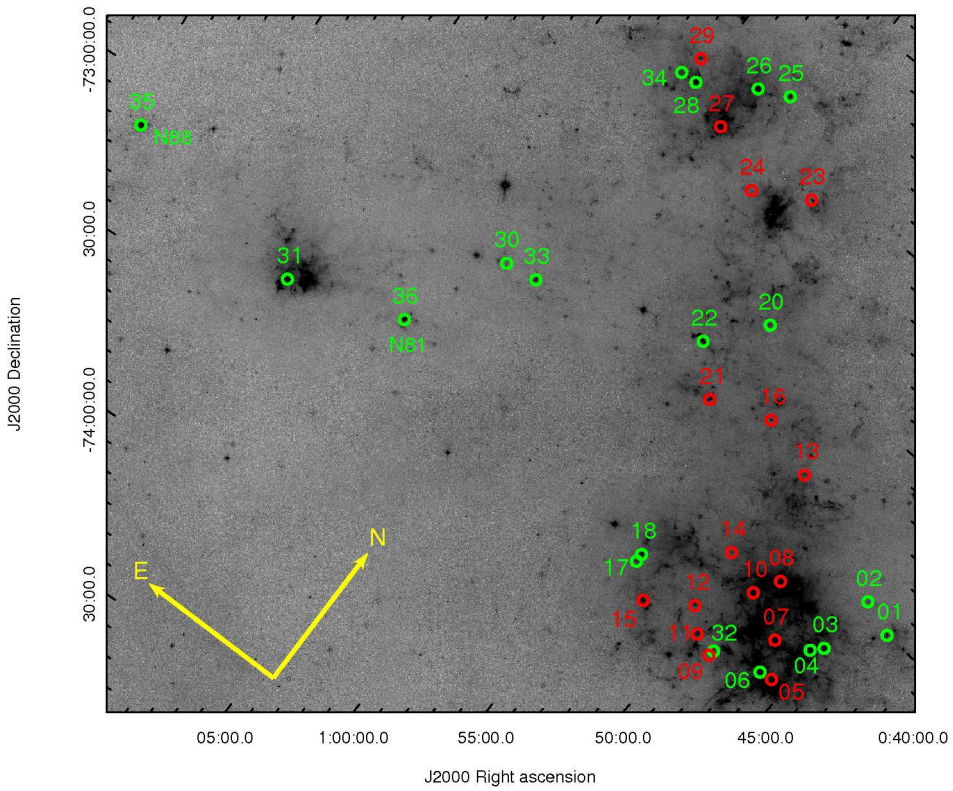

Figure 4.1: SAGE-SMC 8.0 μm mosaic of the Small Magellanic Cloud (Gordon et al., 2011) showing the positions of all 33 spectroscopic massive YSOs presented in Oliveira et al. (2013) with the addition of sources #35 and 36. The sources observed with SINFONI are in green with the remaining sources marked in red. The H II regions N81 (#36) and N88 (#35) are also labelled.

of high excitation energy transitions detected.

Point source catalogues (Wong et al., 2011b, 2012) and high-resolution radio 20, 6 and 3 cm continuum images (Wong et al., 2011a; Crawford et al., 2011) of the SMC have shown that 11 of the 33 YSOs in Oliveira et al. (2013) exhibit radio continuum emission. Radio free–free emission is commonly detected towards UCHIIs (e.g. Hoare et al. 2007) which are formed in the later stages of massive star formation. Of these 11 YSOs associated with radio emission, 7 are discussed in this work.

A subset of 17 spectroscopically confirmed YSOs from Oliveira et al. (2013) has been selected to form a sample of reasonable size which includes a wide variety of *Spitzer* classifications (Seale et al., 2009; Woods et al., 2011) in order to create a representative and relatively unbiased sample. In addition to the 17 confirmed YSOs, two sources are included in the sample which lie within the compact H II regions LHA 115-N81 and LHA 115-N88 A (Henize 1956; assigned the numbers 36 and 35, respectively in Table 4.1). Both of these regions have been previously studied and are known to be associated with young massive main sequence stars and massive star formation. The locations of all of the sources discussed in Oliveira et al. (2013) with the addition of sources #35 and 36 are marked on an 8.0 μm mosaic of the SMC in Fig. 4.1. Although the complete sample of Oliveira et al. (2013) has not been observed with SINFONI, the sources for which observations are available cover the complete range of optical and infrared spectral classifications and cover a wide range of luminosities.

N81, located in the Wing of the SMC was found by Koornneef & Israel (1985) to be relatively free of dust and excited primarily by a central bright star of spectral type O6. Heydari-Malayeri, Le Bertre & Magain (1988) characterised N81 as a young, compact H II "blob" with an extinction of $A_V = 1.4$ mag. N81 has been studied in the Far-UV (Heydari-Malayeri et al., 2002), confirming the presence of very young O-type stars in the H II region and with *JHK* imaging (Heydari-Malayeri et al., 2003) resolving the central region into two sources (which is now resolved into five individual components; Section 4.3.2).

Since its identification by Testor & Pakull (1985) as a high-excitation compact H II region, N88 A has become one of the best studied objects in the SMC and has been the subject of numerous imaging and spectroscopic studies (Roche, Aitken & Smith, 1987; Kurt et al., 1999; Heydari-Malayeri et al., 1999; Testor, Lemaire & Field, 2003; Testor et al., 2005, 2010; Martín-Hernández, Peeters & Tielens, 2008). N88 A is a compact H II region ionized by four central stars with an H_2 emission shell approximately 3 arcsec in diameter. All four of these sources exhibit near-infrared colours consistent with massive YSOs, but could also be

Table 4.1: Previously known properties of YSOs in the SMC from Oliveira et al. (2013), truncated to show only the YSOs observed with SINFONI. The presence or absence of a feature is indicated by ✓and ✗, ? indicating doubt. Silicate emission is identified with ∧. For H_2 emission, ✓? indicates objects for which only two emission lines were detected in the *Spitzer*-IRS range, rather than three to five. Also shown are the detections of either H_2O or CO_2 ice features at 3 μm and 15.2 μm, respectively. The optical ionization classes are defined according to the emission lines present in the spectrum: Type I objects exhibit Balmer, Paschen and O I, Type II objects show hydrogen, O I, [N II], [O II] and [S II] emission, Type III objects show the same lines plus [O III], Type IV objects further add [S III] and finally Type V objects show all these lines plus He I emission. Some objects exhibit a stellar absorption spectrum and others only Hα in emission (see Oliveira et al. 2013 for discussion). The following column indicates whether the object has been detected at radio wavelengths; * signals an extended source. The sources are classified using features in their IRS spectrum, according to two classification schemes previously applied to samples of LMC YSOs (Seale et al., 2009; Woods et al., 2011). The last column provides the luminosities determined from the SED fits. See the main text for further information.

#	PAH emission	Silicate	H_2 emission	H_2O/CO_2 ice 3 μm / 15.2 μm	Optical type	Radio source	YSO class. S09	W11	L (10^3 $L_\odot$)
01	✓	✗	✓	✗	IV/V	Y	PE	G3	16
02	✓	✓	✓	✓	Only Hα emission	Y	S	G1	19
03	✓	✓	✓?	✓	V	Y	S	G1	61
04	✓	✗	✓	✗	II	N	P	G3	2.3
06	✓	✓	✓	✓	Absorption lines	N	S	G1	5.8
17	✓	✓	✓?	✓	Only Hα emission	N	S	G1	22
18	✗	✓	✗	✓	Only Hα emission	N	S	G1	28
20	✓	∧	✓?	✗	I	N	O	G4	1.5
22	✓	✗	✓	✓	IV/V	N	PE	G1	9.1
25	✓	✗	✓	✗	IV	Y	P	G3	17
26	✓	✗	✓	✗	V	Y	PE	G3	12
28	✓	✓	✓?	✗	IV/V	Y	S	G2	140
30	✓	✓?	✓	✓	I	N	P	G1	7.9
31	✓	✗	✓?	✗	No spectrum	Y*	PE	G3	6.7
32	✓	✓	✓	✓	I/II	N	S	G1	3.5
33	✓	✓	✓?	✗	I/II	N	S	G2	26
34	✓	✓	✓?	✓	Only Hα emission	N	S	G1	23

consistent with reddened massive main sequence stars (Testor et al., 2010). N88 A appears to be an exceptionally bright high-excitation blob in the SMC and would rival many of the H II regions in the LMC in this respect (Charmandaris, Heydari-Malayeri & Chatzopoulos, 2008).

As discussed in Section 1.3.3, masers are one of the key phenomena associated with massive star formation; however, relatively few masers have been discovered in the SMC. Of particular interest are water masers, associated with outflows as observed in the earliest stage YSOs, and OH masers which are strongly associated with H II regions. Methanol masers also are one of the key tracers of massive star forming regions (Ellingsen, 2006). To date six interstellar water masers have been detected towards the SMC (Scalise & Braz, 1982; Oliveira et al., 2006; Breen et al., 2013), only one of which lies close enough to one of the sources from Oliveira et al. (2013), source #03, to possibly be associated with it. To date, no OH or

Table 4.2: Positions of each of the K-band continuum sources as determined from the SINFONI continuum images, and the K-band apparent magnitude for each source with the visual extinction value determined from the ratio between the 1-0Q(3) and 1-0S(1) H_2 emission lines.

	J2000			
Source	RA (h:m:s)	Dec (°:′:″)	K (mag)	A_V (mag)
01	00:43:12.885	–72:59:58.18	16.1 ± 0.01	2.6 ± 10.9
02 A	00:44:51.878	–72:57:33.81	15.14 ± 0.01	9.3 ± 8.7
02 B	00:44:52.094	–72:57:34.06	15.75 ± 0.01	4.3 ± 24.4
03	00:44:56.571	–73:10:14.37	13.51 ± 0.01	13.7 ± 10.8
04	00:45:21.283	–73:12:18.39	14.52 ± 0.01	
06	00:46:24.348	–73:22:06.47	17.51 ± 0.02	7.2 ± 6.4
17	00:54:02.269	–73:21:19.02	15.87 ± 0.01	47.5 ± 10.0
18	00:54:03.277	–73:19:39.12	15.88 ± 0.01	18.7 ± 10.1
20	00:56:06.411	–72:28:27.62	15.96 ± 0.01	24.1 ± 13.2
22 A	00:57:56.959	–72:39:16.14	15.96 ± 0.01	9.9 ± 6.4
22 B	00:57:57.182	–72:39:15.54	17.6 ± 0.01	22.5 ± 16.6
25	01:01:31.678	–71:50:38.48		<12.0
26	01:02:48.441	–71:53:17.15	16.68 ± 0.03	14.2 ± 16.6
28 A	01:05:07.229	–71:59:42.54	14.98 ± 0.01	19.5 ± 9.3
28 B	01:05:07.315	–71:59:41.85	17.63 ± 0.01	25.2 ± 12.5
30	01:06:59.656	–72:50:42.82	14.22 ± 0.01	13^{+55}_{-25}
31	01:14:39.284	–73:18:28.21	15.08 ± 0.02	1.5 ± 7.9
32	00:48:39.662	–73:25:00.69	14.66 ± 0.01	22.2 ± 22.1
33	01:05:30.015	–72:49:51.90	11.5 ± 0.01	<5.0
34	01:05:49.349	–71:59:48.59	14.12 ± 0.01	16.0 ± 8.0
35 A	01:24:07.982	–73:09:03.81	13.47 ± 0.04	1.2 ± 17.0
35 B	01:24:07.901	–73:09:03.66	14.65 ± 0.06	<22.5
35 C	01:24:07.867	–73:09:04.36	14.85 ± 0.08	<10.1
35 D	01:24:07.982	–73:09:03.06	14.91 ± 0.06	$1.8^{+12.0}_{-15.8}$
36 A	01:09:12.912	–73:11:38.53	14.93 ± 0.01	<32.5
36 B	01:09:12.889	–73:11:38.28	15.48 ± 0.01	13.3 ± 12.8
36 C	01:09:13.212	–73:11:38.68	16.08 ± 0.01	21.6 ± 32.5
36 D	01:09:13.131	–73:11:38.68	16.54 ± 0.01	35.3 ± 23.3
36 E	01:09:12.693	–73:11:38.58	16.56 ± 0.02	19.9 ± 21.1

methanol masers have been detected in the SMC (van Loon, 2012).

4.2 Results

4.2.1 Continuum emission and *K*-band photometry

For each spaxel in the final flux calibrated cubes, the continuum was fitted and summed for the spectral region spanning 2.028–2.290 μm to produce continuum flux maps without any contribution from line emission. The J2000 RA and Dec positions of each K-band continuum source resolved in this work are given in Table 4.2. The positions of each continuum source are marked in Fig. C.2, the green circles show the regions from which 1D spectra were extracted from the cubes. Values for the K-band apparent magnitude (using the CIT photometric system where the K-band zero point is at 620 Jy) of each of the sources were determined by fitting a polynomial to the continuum of the 1D spectrum for each source and summing the total flux of the fitted continuum (Table 4.2).

Out of 19 observed sources, 14 consist of a single continuum source at the resolution obtained with this study (0.1–0.2 arcsec with AO and ∼0.6 arcsec seeing limited), whilst

the remaining five targets consist of multiple continuum sources. Sources #02, 22 and 28 are resolved into two components whilst sources #35 and 36 are resolved into four and five K-band continuum components, respectively (see Table 4.2 & Fig. C.2).

4.2.2 Extinction

In order to calculate values of extinction towards our sources, the H_2 lines in the extracted spectra were used as described in detail in Chapter 3. The 1-0S(1) / 1-0Q(3) flux ratio (I_{S1}/I_{Q3} in Eqn. 4.1) is used due to its insensitivity to temperature and relatively large wavelength separation (e.g., Davis et al. 2011). Visual extinction is given by:

$$A_V = -114 \times \log(0.704[I_{S1}/I_{Q3}]) \tag{4.1}$$

Extinction corrections were calculated for each emission line individually using the Galactic mean R_V dependent extinction law:

$$[A(\lambda)/A(V)] = a(x) + b(x)/R_V \tag{4.2}$$

where $x = 1/\lambda$, $a(x) = 0.574x^{1.61}$ and $b(x) = -0.527x^{1.61}$ for the K-band (Cardelli, Clayton & Mathis, 1989). An R_V value of 3.1 has been adopted although R_V has been found to range from 2.05±0.17 to 3.30±0.38 in the SMC (Gordon et al., 2003).

The calculated extinction values using this method are given in the final column of Table 4.2. The mean extinction value towards the SMC sources (excluding limits and null values) presented here is A_V = 15.8±3.3 mag, significantly lower than the average towards 139 Galactic massive YSOs obtained from *HK* photometry (45.7±1.5 mag; Cooper et al. 2013) and that of N113 in the LMC (22.3±3.8 mag; Chapter 3 and Ward et al. 2016). Furthermore, the median values for extinction are A_V = 43.8, 20.0 and 14.2 mag for the Galactic sample, the N113 sample and the SMC sample, respectively. This is consistent with the lower dust to gas ratio in the SMC and suggests that extinction scales with metallicity. It should be noted that N113 may not be representative of the LMC (see Chapter 3 and Ward et al. 2016).

4.2.3 *K*-band emission features

H I emission

Brγ emission (2.166 μm) is most commonly associated with accretion in star formation studies. For intermediate mass YSOs the relation from Calvet et al. (2004) can be used to estimate

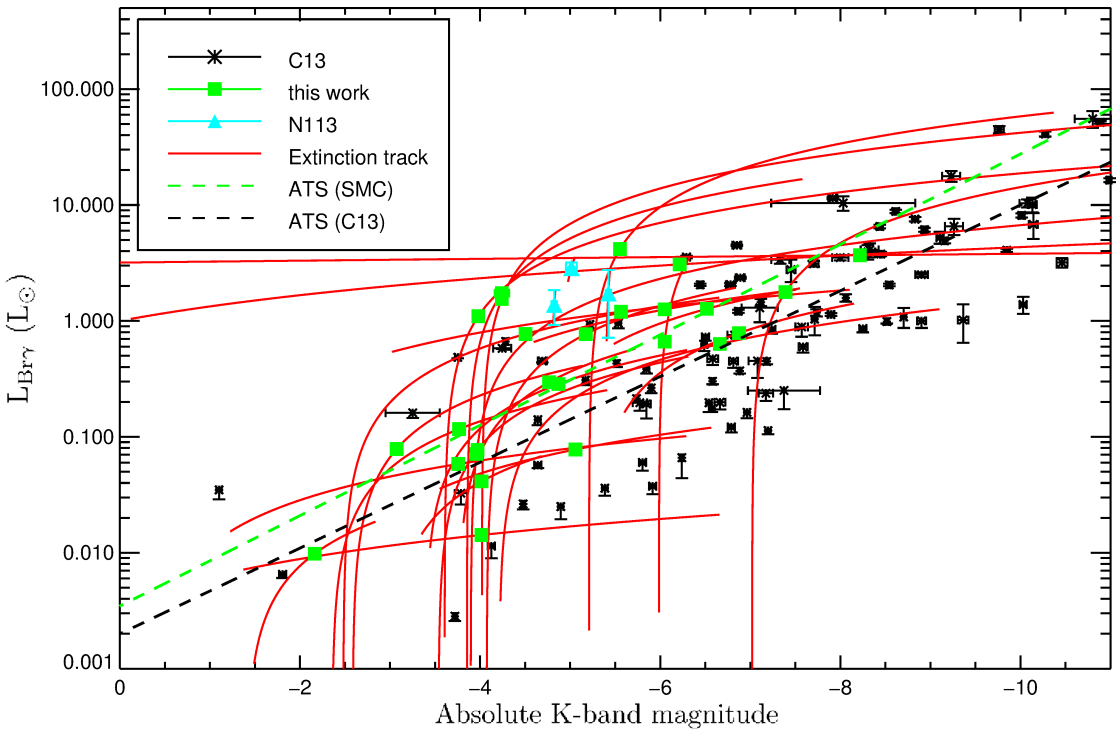

Figure 4.2: Brγ luminosity against absolute K-band magnitude. Data from Cooper et al. (2013) and Ward et al. (2016) are also included for comparison, labelled as C13 and N113, respectively. The red extinction tracks are representative of the uncertainty due to the extinction correction (Table 4.2). The green and black dashed lines indicate the ATS regressions fitted to the SMC and the Cooper et al. (2013) sources respectively.

the accretion luminosity from Brγ luminosity:

$$\log(L_{\rm acc}) = -0.7 + 0.9(\log(L_{\rm Br\gamma}) + 4) \tag{4.3}$$

It is possible that this relation breaks down for massive stars due to an additional emission component originating from the strong stellar winds associated with hot stars. Furthermore, Herbig Be stars do not appear to be modelled successfully through magnetospheric accretion, suggesting a change of accretion mechanism at high masses (e.g., Fairlamb et al. 2015). For the purposes of comparing our sample with a Galactic sample, however, the above relation can be applied to gain an equivalent accretion luminosity assuming that both samples cover the same range of evolutionary states and YSO masses. The models of Kudritzki (2002) make the prediction that the effect of metallicity on the production of photons capable of ionizing hydrogen is almost negligible due to the cancelling effect of metal line blocking and metal line blanketing, and thus the lower metallicity of the SMC should not affect this relationship.

Brγ emission is detected towards 28 of the 29 SINFONI K-band sources observed in this work, making it the most common spectral feature in the data set. Only the spectrum towards

source #02 B does not exhibit Brγ emission. Figure 4.2 shows the extinction corrected Brγ luminosities plotted against absolute K–band magnitude for all sources where Brγ was detected. Also included in this plot are the results of Cooper et al. (2013) and Ward et al. (2016) for YSOs in the Milky Way and N113 in the LMC, respectively, along with extinction tracks which show the allowed positions of sources in the diagram based on the uncertainty of the extinction correction (see Table 4.2).

Akritas-Theil-Sen (ATS; Akritas, Murphy & Lavalley 1995) regressions were fitted to the SMC sample and the Galactic sample and have been used throughout this work in place of a simple linear least-squares fitting routine. ATS regressions are based on the Theil-Sen estimator which is the median of slopes between pairs of points in a 2-dimensional space with non-equal x-coordinates (Theil, 1950; Sen, 1968). The Theil-Sen estimator is that for which the Kendall's τ coefficient for the residuals is approximately zero (Sen, 1968). Kendall's τ is a measurement of rank correlation defined as the difference between the number of concordant pairs of data and the number of discordant pairs of data divided by $n(n-1)/2$ (Kendall, 1938). The statistical significance of the resulting value of τ can be expressed as a p-value which represents the likelihood of a null result based on the uncertainty calculation given in Kendall (1938).

The ATS regressions and Kendall's τ values were computed in the R-project statistics package using the CENKEN function from the NADA library (Helsel, 2005). The primary reason for this was to follow an analysis strategy consistent with that of Cooper et al. (2013), with which the emission line luminosity data obtained in this work is compared. ATS regressions are also more robust against outliers than simple least squares fitting (Sen, 1968; Rousseeuw & M., 1987). This is potentially useful in data sets such as those presented in this work consisting of data with high uncertainties such as those presented here.

In order to calculate uncertainties in the ATS regressions fitted in this work 1000 model data sets were generated for each fit. Each model data set consists of the same number of data points as the observed data where each data point has random x and y values assuming a normal distribution using the measured value as the mean and the 1σ uncertainty as the σ of the Gaussian profile. A new ATS regression is then fitted to each model data set in order to represent the plausible range that the true linear regression could occupy based on the uncertainties in the observed data. The standard deviations are then calculated for the slope and y-intercept using the distribution of the model ATS regressions.

The ATS regression fit takes the form $y = 10^{ax+b}$; we compute the values of $a_{SMC} =$

-0.39 ± 0.05 and $b_{SMC} = -2.5 \pm 0.3$ for the SMC sample whilst the Galactic sample yielded values of $a_{MW} = -0.37 \pm 0.01$ and $b_{MW} = -2.69 \pm 0.03$. The associated Kendall's τ values are $\tau_{SMC} = -0.5$ and $\tau_{MW} = -0.70$ for the SMC and the Cooper et al. (2013) samples respectively, indicating a stronger correlation for the Galactic sample than for the SMC sample. The p values, which represent the likelihood of there being no correlation between $L_{\mathrm{Br}\gamma}$ and K-band magnitude, are 0.0004 and $<1\times10^{-8}$ for the SMC and Galactic samples respectively, indicative of a definite correlation for both sets of data.

Whilst consistent with the Galactic sample, our sample of SMC sources exhibit Brγ emission luminosities that are high for their absolute K-band magnitudes compared with the Cooper et al. (2013) data. Not accounting for any difference in the K-band continuum emission or additional sources of excitation, assuming that Eqn. 4.3 holds true this suggests that YSOs in the SMC exhibit higher accretion rates than their counterparts in the Milky Way causing higher levels of Brγ emission. This is discussed in detail in Section 4.3.1.

In the majority of sources, the Brγ emission is compact but in 7 of the 19 FOVs there is evidence of extended H I emission as shown in Fig. 4.3. In sources #01, 28 and 35 (N88 A) it extends roughly symmetrically from a central continuum source whilst in sources #03 and 31 it is extended over a significant area and offset to one side of a continuum source. Source #28 also exhibits weak elongated Brγ emission extending to the south of the continuum source (Fig. 4.3, red contour). Source #02 exhibits relatively compact and collimated extended Brγ emission in one direction from the continuum source. Finally for source #36 (N81), there appears to be relatively high levels of ambient Brγ emission which is unsurprising given the nature of the N81 H II region (see Section 4.1). The extended Brγ emission to the west most likely originates outside the FOV as the peak of the emission is at the edge of the observed region whilst that in the east appears to be associated with (or have a component associated with) source #36 C and possibly #36 D.

In addition to analysing Brγ emission morphologies and fluxes, the centroid velocity of the emission has also been calculated using the centroid of the Gaussian profile fitted to the emission line at every spaxel to create velocity maps. Figure 4.4 shows the Brγ centroid velocity maps for sources #01, 02, 03, 28, 35 and 36 relative to the brightest K-band continuum source in each field. Sources #02 and 28 exhibit similar velocity fields surrounding the continuum source with no clear gradient in Brγ emission velocity; to the south of source #28 the weak, elongated Brγ component (red contour in Fig. 4.3 and black contour in Fig. 4.4) appears to be red-shifted with respect to the continuum source by 5–10 km s^{-1}. For

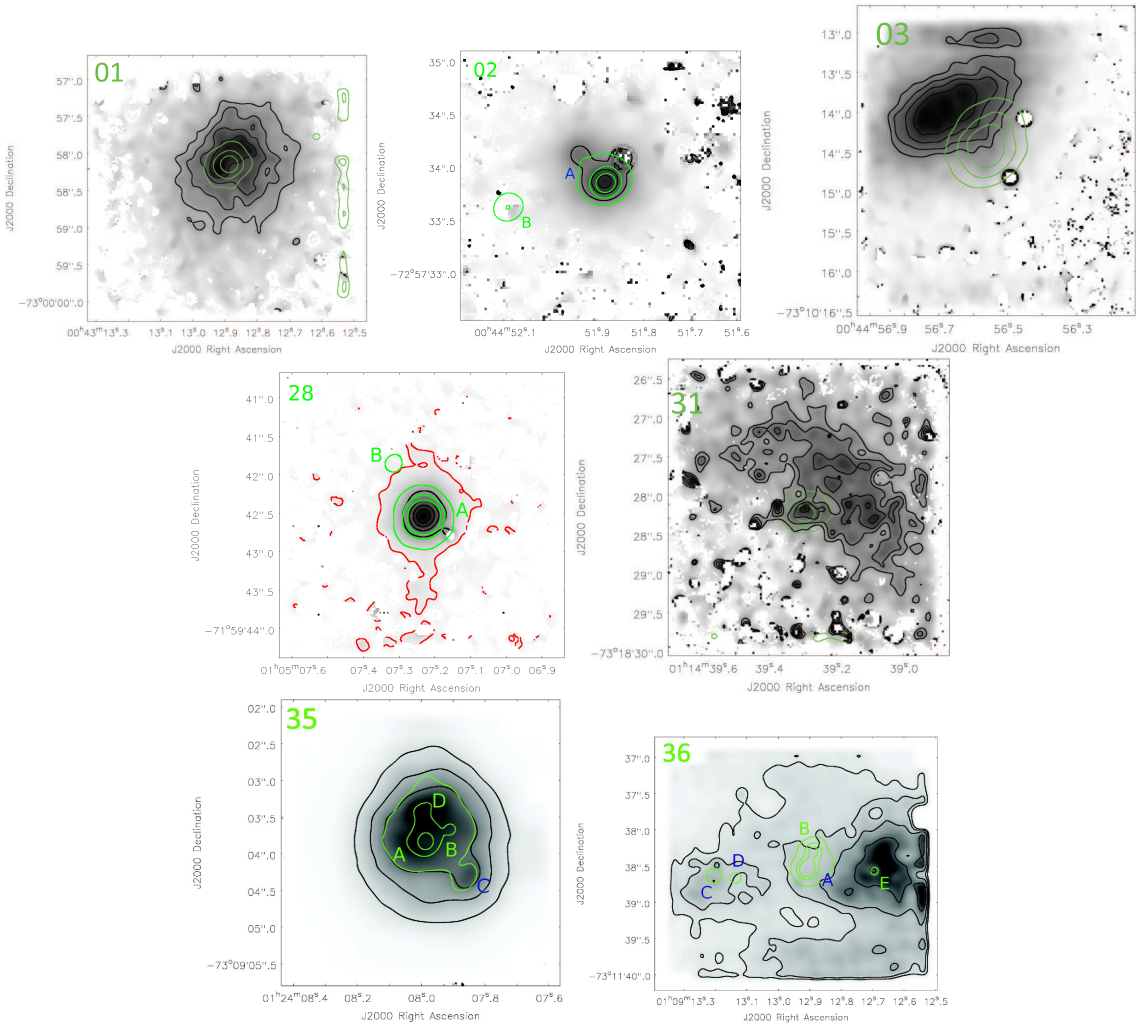

Figure 4.3: Extended Brγ emission line morphologies for sources #01, 02, 03, 28, 31, 35 (N88 A) and 36 (N81). Black contours - [0.2,0.4,0.6,0.8] $\times$ maximum Brγ 2.1661 μm integrated flux, green contours - [0.25, 0.5, 0.75] $\times$ maximum continuum integrated flux. The red contours in source #28 indicate significantly weaker (4×10^{-22} Wm^{-2}/spaxel), more extended Brγ emission.

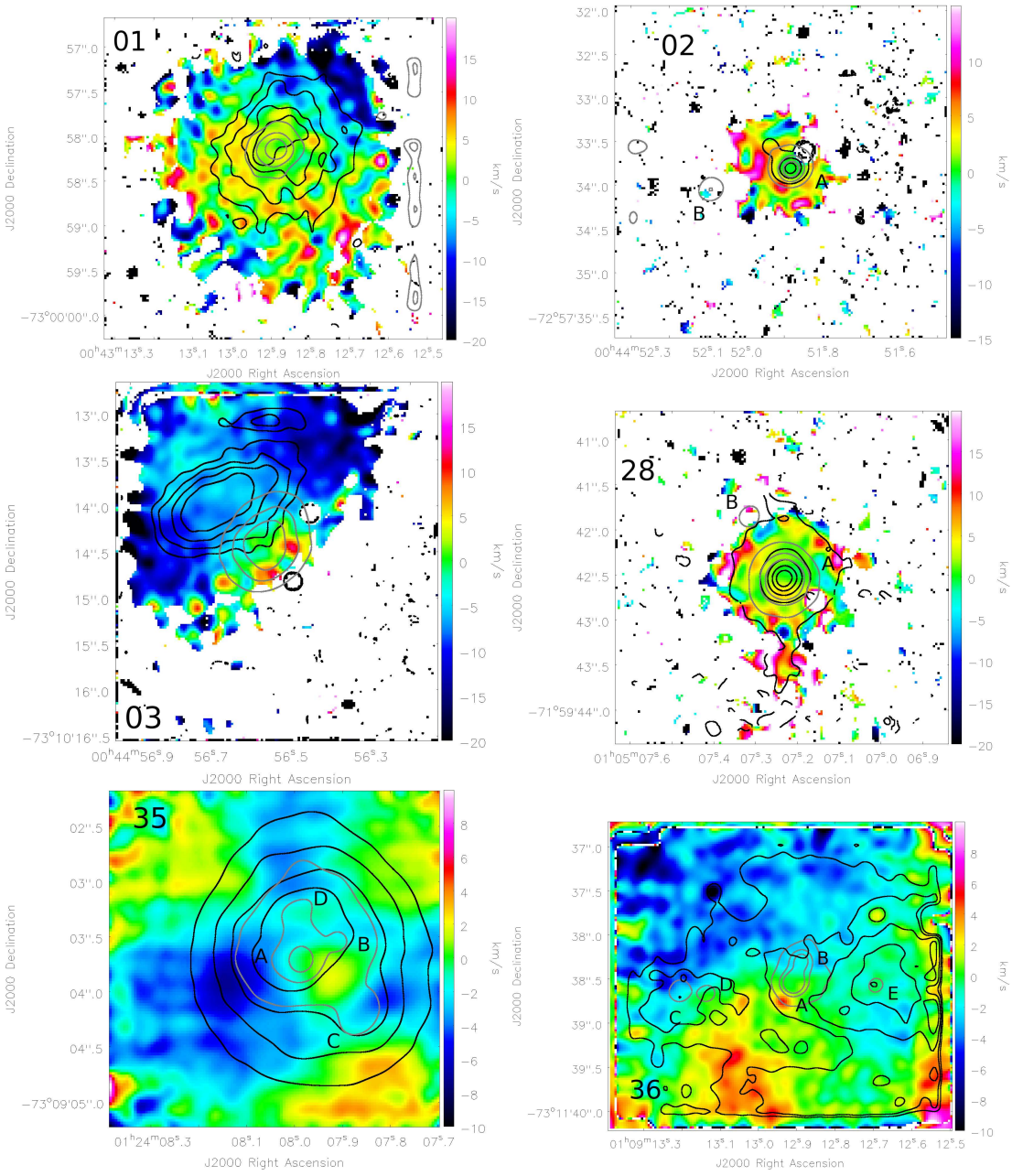

Figure 4.4: Brγ centroid velocity maps for sources #01, 02, 03, 28, 35 and 36. Black contours - Brγ 2.1661 μm integrated flux, grey contours - continuum flux (see Fig. 4.3). The black contours in source #28 trace the same emission as the black and the red contours in Fig. 4.3. Velocities are relative to that measured towards the brightest continuum source in the FOV.

sources #01 and 35 the velocity maps show velocity gradients of 5–10 km s^{-1} which are consistent with an expanding ionized medium surrounding the continuum sources. Source #03 exhibits a wide extended and blue shifted region of Brγ emission. The map of source #36 shows a significant velocity gradient across the FOV; however, it remains unclear whether this is directly influenced by the continuum sources or whether it is more representative of larger scale motions of ionized gas in the region. Sources #36 C and 36 B appear in regions of Brγ emission which are slightly blue shifted with respect to the emission towards 36 A. Although Brγ emission is extended in source #31, the signal-to-noise ratio is not sufficient to map the velocity field of the emitting gas.

The Pfund series (between 2.37 μm and 2.44 μm) has only been detected and measured towards sources in #35, the compact H II region N88 A. However (as in the previous Chapter) due to the relatively large uncertainties in extinction towards N88 A and the poor signal-to-noise (S/N) in this region, physical properties cannot be determined from the Pfund emission.

He I emission

He I emission is produced from the ionization and subsequent recombination of helium atoms, a significant process at the ionization boundary of H II regions and potentially also in areas of collisional excitation (Porter, Drew & Lumsden, 1998). The strongest and most commonly detected helium emission line in the K-band towards massive YSOs is the 2.059 μm line produced by the 2^1P^0–2^1S transition. This emission line has been detected towards 15 of our K-band continuum sources, nine of which lie in the FOVs of targets #35 and 36 (N88 A and N81, respectively).

Figure 4.5 plots the He I 2.059 μm emission line luminosity against the absolute K-band luminosity, analogous with Fig. 4.2. Also included are the results for Galactic sources from Cooper et al. (2013) and those for sources in N113 in the LMC from Chapter 3 (Ward et al. 2016). Despite the large uncertainties originating in the extinction calculation, it certainly appears that all of the He I fluxes fall within the range observed in the Milky Way and in N113 in the LMC. This suggests that the mechanism causing the increased Brγ emission in the SMC does not appear to affect the He I emission in the same way. Furthermore the ATS regressions fitted to these data also suggest no significant increase is seen in the He I fluxes towards the SMC compared to the Galactic sample. Using the form $y = 10^{ax+b}$, we find values of $a_{\rm SMC} = -0.41 \pm 0.10$ and $b_{\rm SMC} = -3.25 \pm 0.60$ for the SMC data and $a_{\rm MW} = -0.40 \pm 0.02$ and $b_{\rm MW} = -3.19 \pm 0.08$ for the sample of Cooper et al. (2013).

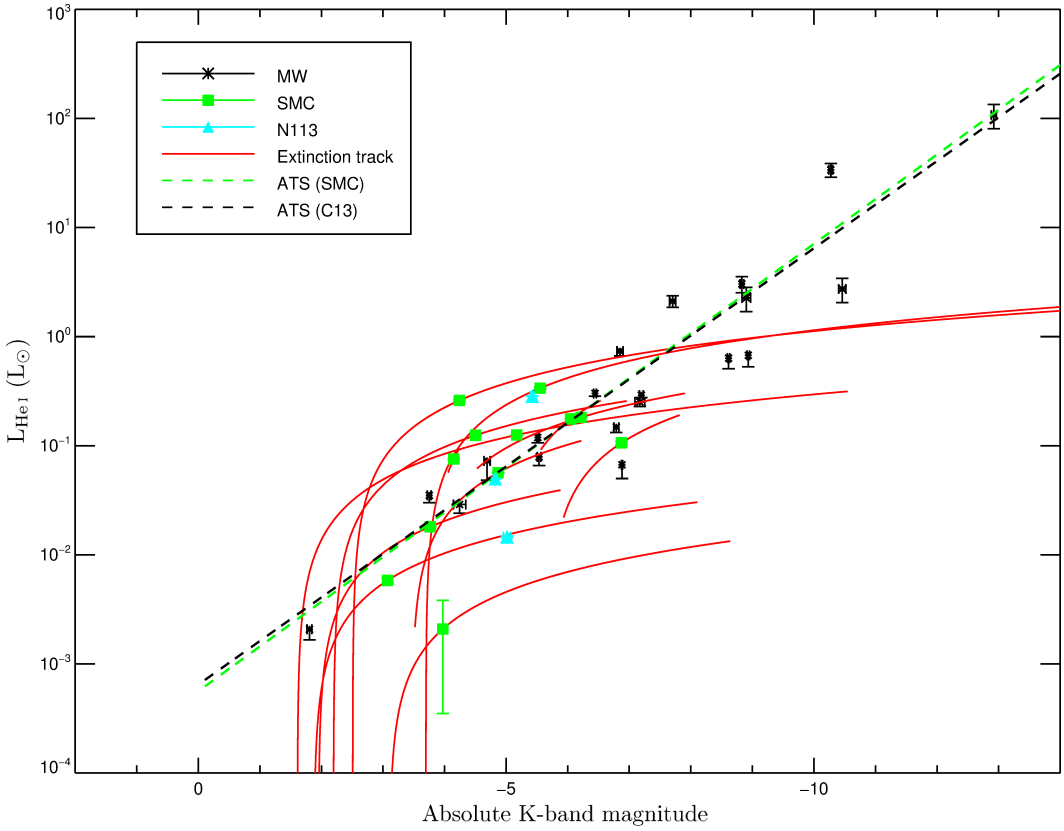

Figure 4.5: He I luminosity versus absolute K-band magnitude. See also caption for Fig.4.2.

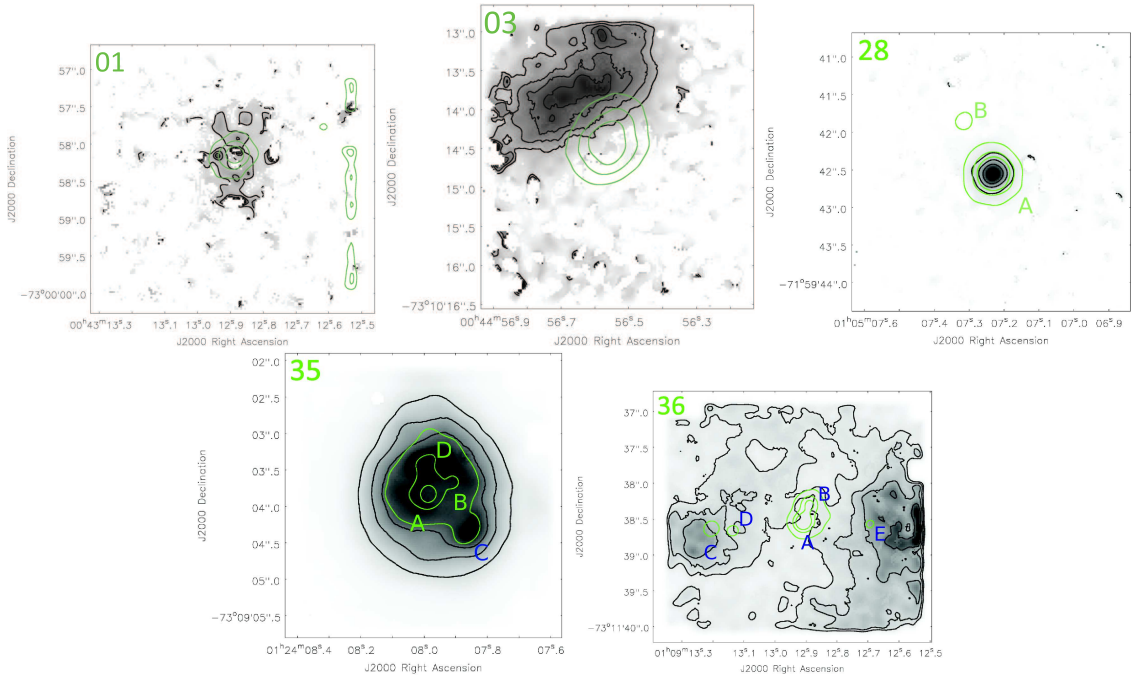

Figure 4.6: He I emission line morphologies for sources #01, 03, 28, 35 and 36. Black contours - [0.2,0.4,0.6,0.8] × maximum He I 2.059μm integrated flux, green contours - continuum flux. The continuum contour levels are as in Fig. 4.3.

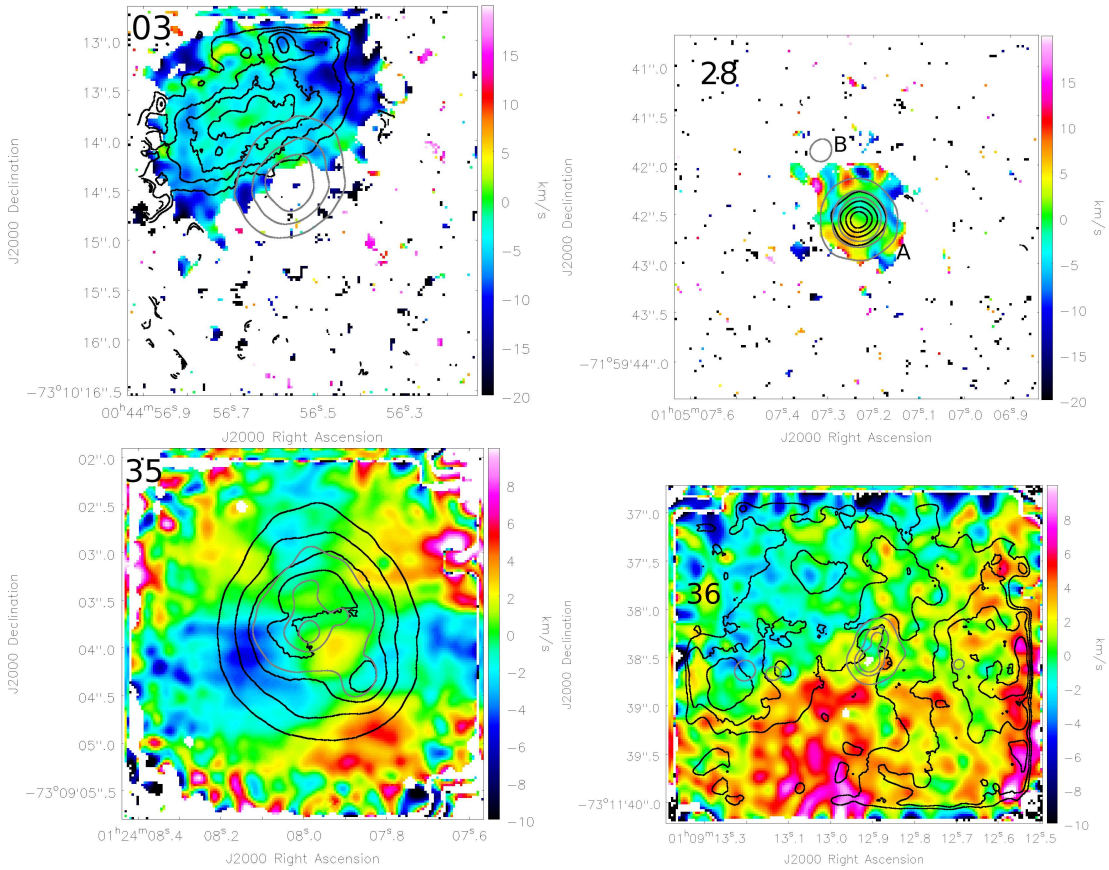

Figure 4.7: He I centroid velocity maps for sources #03, 28, 35 and 36. Black contours - He I 2.059 μm integrated flux, grey contours - continuum flux. See also the caption of Fig. 4.4. Velocities are relative to that measured towards the brightest continuum source in the FOV.

Again, we find a stronger correlation for the Galactic sources than the SMC sources with $\tau_{\rm SMC} = -0.48$ whilst $\tau_{\rm MW} = -0.78$. Similarly the probability of a correlation is higher in the Galactic sample with values of $p_{\rm SMC} = 0.03$ and $p_{\rm MW} = 9 \times 10^{-7}$, indicating probabilities that the magnitude and He I luminosities are correlated of 97% and >99% for the SMC and the Milky Way, respectively.

The morphology and kinematics of the He I 2.059 μm emission has been mapped for five sources for which the S/N was adequate to do so (Figs. 4.6 and 4.7). For the most part the He I emission traces the same morphological structures as the Brγ emission. For sources where line velocities could be reliably measured (#03, 28, 35, 36), the He I velocity maps trace the same velocity structures as the Brγ maps. Both the morphologies and kinematics measured support a common physical origin of Brγ and He I emission for these four sources. The exception is source #28 A which does not exhibit the same southwards narrow jet-like structure in He I emission as in the Brγ emission.

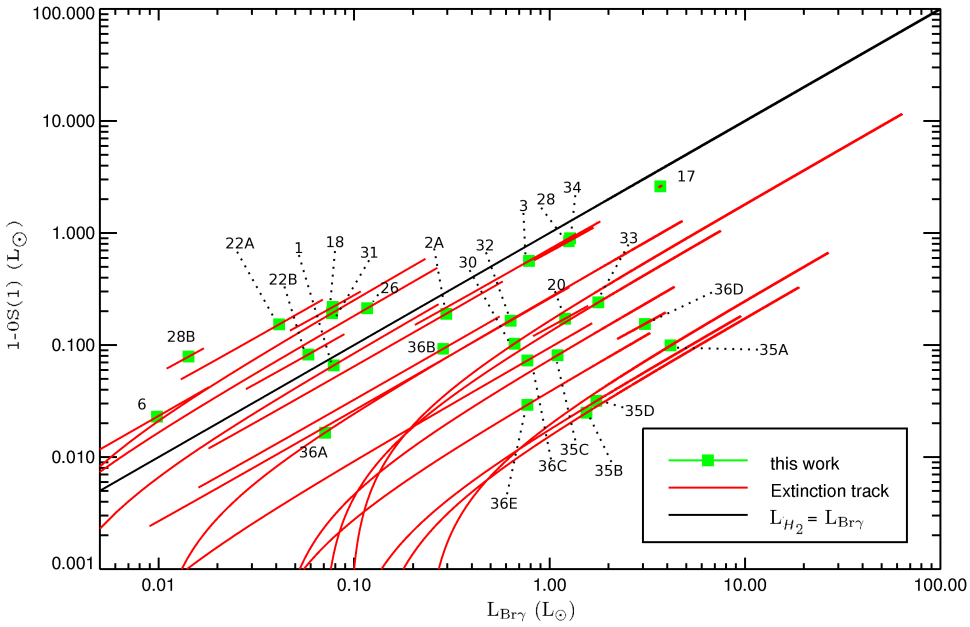

Figure 4.8: H_2 2.1218 μm emission vs Brγ emission. The solid black line shows where the Brγ emission line luminosity and the H_2 emission line luminosity are equal. See also the caption of Fig. 4.2.

H_2 emission

Molecular hydrogen emission lines in the K-band are a commonly used tracer of both shocked emission from outflows and of photo-dissociation regions (PDRs, see Section 1.3.3). We detect the H_2 1-0S(1) and 1-0Q(3) emission lines towards all but one of our sources (#04) whilst the remaining detected H_2 emission lines (1-0S(0), 1-0S(2), 1-0S(3), 2-1S(0), 2-1S(1), 2-1S(2), 1-0Q(1), 1-0Q(2); wavelengths are listed in Table 4.3) have lower rates of detection. The full list of H_2 emission line fluxes is given in Table E.1, and in Fig. 4.8 we have plotted H_2 2.1218 μm luminosity against that of Brγ emission. We find that the H_2 emission dominates (significantly exceeds the Brγ luminosity, $H_2/\mathrm{Br}\gamma > 1.3$) in seven of our sources (#06, 18, 22 A, 22 B, 26, 28 B, 31) and that six sources lie close to the H_2 = Brγ line ($H_2/\mathrm{Br}\gamma > 0.6$; #01, 02 A, 03, 17, 28 A, 34). The remaining sources for which we measure both H_2 emission and Brγ emission appear to be dominated by Brγ emission ($H_2/\mathrm{Br}\gamma < 0.35$).

Through comparison with grids of models simulating H_2 emission from both shock excitation and photo-excitation, it may be possible to distinguish between these excitation mechanisms using the flux ratios between different emission lines (as discussed in the previous Chapter). Table 4.3 shows the extinction corrected intensity ratios of all of the measured H_2 emission lines relative to the 1-0S(1) line with the exception of the Q-branch emission lines. Also included are the model line ratios for photo-excitation (Black & van Dishoeck, 1987) and shocked emission (Shull & Hollenbach, 1978) for comparison. Particularly useful

are the 1–0S(0)/1–0S(1) and 2–1S(1)/1–0S(1) emission line ratios due to the relatively high fluxes of these lines and clear distinctions between the photo-excited and shock-excited ratios (see Table 4.3).

Using the 1-0S(0) / 1-0S(1) and 2-1S(1) / 1-0S(1) emission line ratios, sources #03, 06, 18, 26 and 34 consistently appear to exhibit emission dominated by collisional excitation with ratio ranges of 0.14–0.27 and 0.11–0.25, respectively. Source #25 is the only source which is clearly photo-excited whilst all other sources appear to exhibit contributions from both photo-excitation and shocked excitation. For instance, whilst none of the 2-1S(1) / 1-0S(1) ratios fall within the photo-excitation range, sources #02 B, 28 B, 36 B and 36 E all have 1-0S(0) / 1-0S(1) ratios consistent with photo-excited gas (0.38–0.55) and 2-1S(1) / 1-0S(1) inconsistent with collisional excitation (0.33–0.46). It is likely that the majority of measured H_2 emission has contributions from both photo-excitation and collisional excitation as reflected in the low 2-1S(1) line strength compared to 1-0S(0) line strength which implies that the 2-1S(1) emission is primarily sourced from shocked excitation whilst the 1-0S(0) emission has a larger contribution from photo-excitation.

Again, as stated in Chapter 3, the shocked emission models used are for a density of $n = 3.0 \times 10^5\,\mathrm{cm}^{-3}$ and large deviations from this density lead to significant variations in the expected line ratios. Coupled with the high uncertainties in many of the measured ratios, none of the conclusions drawn from this analysis can be considered definitive, but rather an indication of a likely scenario.

Half of our YSO targets exhibit extended H_2 emission; the morphologies of the 2.1218 μm 1–0S(1) emission line are shown in Fig. 4.9. Comparing Figs. 4.3 and 4.9, it is clear that the Brγ and H_2 emission morphologies are very different. Sources #01, 02 A, 28 A and 30 exhibit H_2 morphologies extended along a single axis, asymmetric with respect to the continuum source. Source #28 A exhibits a v-shape morphology, indicative of a cone like physical structure. Source #06 exhibits two knots of H_2 emission separated from the continuum source (0.6 arcsec and 1.4 arcsec for the southern and north-western knots, respectively), although the weaker north-western knot appears to be linked by a tenuous tail of emission to the continuum source. Sources #03 and 31 both exhibit irregular elongated emission across the continuum source with offset Brγ emission. Bipolar extended emission is observed centred on sources #22 A and 36 B although that of 36 B appears to be slightly off-centre. Finally source #35 exhibits an arc of H_2 emission as previously studied in Testor et al. (2010), tracing the edge of the compact H II region shown in the Brγ emission. The morphologies of the different

Table 4.3: Extinction corrected H_2 emission line ratios with respect to the 1-0S(1) emission line for all continuum sources. Also included are the expected H_2 line ratios for photo-excitation (Black & van Dishoeck, 1987) and shocked emission (Shull & Hollenbach, 1978). The final column gives the origin of the emission for those sources for which we are confident of the diagnosis based on the H_2 emission line ratios.

Source	1-0S(0)	1-0S(2)	1-0S(3)	2-1S(1)	2-1S(2)	2-1S(3)	Origin
	2.2235 μm	2.0338 μm	1.9576 μm	2.2477 μm	2.1542 μm	2.0735 μm	
01	$0.49\ ^{+0.01}_{-0.02}$	$0.44\ ^{+0.05}_{-0.02}$	$0.57\ ^{+0.13}_{-0.06}$	$0.193\ ^{+0.005}_{-0.011}$	$0.158\ ^{+0.005}_{-0.002}$	$0.35\ ^{+0.03}_{-0.01}$	
02 A	$0.36\ ^{+0.01}_{-0.03}$	$0.39\ ^{+0.07}_{-0.01}$	$2.09\ ^{+0.22}_{-0.01}$	$0.115\ ^{+0.010}_{-0.001}$		$0.19\ ^{+0.21}_{-0.01}$	
02 B	$0.55\ ^{+0.02}_{-0.07}$	$0.35\ ^{+0.07}_{-0.05}$	$1.6\ ^{+0.7}_{-0.5}$		$0.168\ ^{+0.010}_{-0.008}$		
03	0.23 ± 0.01	$0.25\ ^{+0.05}_{-0.01}$	$2.23\ ^{+0.17}_{-0.03}$	$0.245\ ^{+0.003}_{-0.019}$	$0.104\ ^{+0.017}_{-0.003}$	$0.229\ ^{+0.025}_{-0.004}$	shock
04							
06	0.14 ± 0.01	$0.37\ ^{+0.11}_{-0.01}$	$1.69\ ^{+0.01}_{-0.22}$	$0.113\ ^{+0.001}_{-0.010}$		$0.089\ ^{+0.075}_{-0.003}$	shock
17		$0.48\ ^{+0.21}_{-0.16}$	$4.12\ ^{+0.18}_{-0.14}$	0.138 ± 0.001			
18	0.25 ± 0.01	$0.38\ ^{+0.03}_{-0.01}$	1.09 ± 0.01	$0.175\ ^{+0.004}_{-0.010}$	$0.070\ ^{+0.004}_{-0.002}$		shock
20	0.23 ± 0.01	$0.45\ ^{+0.02}_{-0.01}$	$1.09\ ^{+0.22}_{-0.11}$				
22 A	$0.38\ ^{+0.01}_{-0.02}$	0.40 ± 0.01	$0.74\ ^{+0.01}_{-0.08}$	$0.182\ ^{+0.003}_{-0.013}$	$0.129\ ^{+0.010}_{-0.002}$	$0.117\ ^{+0.002}_{-0.001}$	
22 B	$0.59\ ^{+0.01}_{-0.03}$	$0.37\ ^{+0.03}_{-0.01}$	$1.87\ ^{+0.04}_{-0.13}$	$0.281\ ^{+0.006}_{-0.018}$	$0.265\ ^{+0.018}_{-0.006}$	$0.218\ ^{+0.038}_{-0.012}$	
25	$0.44\ ^{+0.01}_{-0.03}$			$0.463\ ^{+0.001}_{-0.041}$			photo
26	$0.22\ ^{+0.03}_{-0.01}$	$0.31\ ^{+0.01}_{-0.10}$	$1.14\ ^{+0.21}_{-0.03}$	$0.251\ ^{+0.038}_{-0.003}$	$0.103\ ^{+0.002}_{-0.001}$	$0.189\ ^{+0.001}_{-0.011}$	shock
28 A	0.30 ± 0.01	0.35 ± 0.01	$0.56\ ^{+0.01}_{-0.03}$	$0.151\ ^{+0.004}_{-0.008}$	0.048 ± 0.001	$0.126\ ^{+0.007}_{-0.003}$	
28 B	$0.48\ ^{+0.01}_{-0.02}$	$0.54\ ^{+0.13}_{-0.07}$	$1.02\ ^{+0.18}_{-0.11}$	$0.375\ ^{+0.010}_{-0.016}$		$0.308\ ^{+0.013}_{-0.008}$	
30	$0.31\ ^{+0.03}_{-0.09}$	0.39 ± 0.15	1.2 ± 1.1				
31	$0.50\ ^{+0.01}_{-0.02}$	$0.48\ ^{+0.02}_{-0.05}$	$1.12\ ^{+0.08}_{-0.24}$	$0.242\ ^{+0.004}_{-0.010}$	$0.136\ ^{+0.003}_{-0.001}$	$0.296\ ^{+0.006}_{-0.018}$	
32	$0.29\ ^{+0.01}_{-0.02}$	<1.2		$0.337\ ^{+0.001}_{-0.030}$			
33	$0.30\ ^{+0.01}_{-0.02}$	$0.23\ ^{+0.02}_{-0.03}$		$0.270\ ^{+0.001}_{-0.021}$			
34	0.27 ± 0.01	0.37 ± 0.01	$0.85\ ^{+0.02}_{-0.05}$	$0.112\ ^{+0.003}_{-0.006}$	$0.099\ ^{+0.016}_{-0.006}$		shock
35 A	$0.37\ ^{+0.01}_{-0.04}$	$0.30\ ^{+0.03}_{-0.05}$	$0.92\ ^{+0.22}_{-0.31}$	$0.332\ ^{+0.004}_{-0.041}$	$0.116\ ^{+0.006}_{-0.004}$	$0.195\ ^{+0.012}_{-0.016}$	
35 B	$0.34\ ^{+0.01}_{-0.05}$	$0.23\ ^{+0.04}_{-0.05}$	$0.90\ ^{+0.34}_{-0.41}$	$0.318\ ^{+0.001}_{-0.058}$	$0.081\ ^{+0.005}_{-0.004}$		
35 C	$0.39\ ^{+0.01}_{-0.03}$	$0.44\ ^{+0.04}_{-0.07}$	$1.25\ ^{+0.25}_{-0.38}$	$0.334\ ^{+0.006}_{-0.035}$	$0.095\ ^{+0.004}_{-0.003}$	$0.306\ ^{+0.016}_{-0.024}$	
35 D	$0.37\ ^{+0.01}_{-0.02}$	$0.28\ ^{+0.02}_{-0.03}$	$0.8\ ^{+0.1}_{-0.2}$	$0.173\ ^{+0.001}_{-0.012}$	$0.060\ ^{+0.002}_{-0.001}$	$0.125\ ^{+0.004}_{-0.008}$	
36 A	$0.29\ ^{+0.01}_{-0.08}$	$0.37\ ^{+0.13}_{-0.14}$	$1.2\ ^{+0.9}_{-1.0}$	$0.400\ ^{+0.001}_{-0.126}$			
36 B	$0.41\ ^{+0.01}_{-0.03}$	$0.16\ ^{+0.08}_{-0.01}$	$1.04\ ^{+0.43}_{-0.01}$	$0.388\ ^{+0.001}_{-0.034}$	$0.138\ ^{+0.087}_{-0.002}$	$0.337\ ^{+0.051}_{-0.001}$	
36 C						$0.64\ ^{+0.02}_{-0.04}$	
36 D			$2.44\ ^{+0.04}_{-0.02}$				
36 E	$0.38\ ^{+0.07}_{-0.01}$		$1.13\ ^{+0.03}_{-0.49}$	$0.333\ ^{+0.072}_{-0.002}$			
Photo-excitation	0.4–0.7	0.4–0.6		0.5–0.6	0.2–0.4	0.2–0.3	
1000 K shock	0.27	0.27	0.51	0.005	0.001	0.003	
2000 K shock	0.21	0.37	1.02	0.083	0.031	0.084	
3000 K shock	0.19	0.42	1.29	0.21	0.086	0.27	
4000 K shock	0.19	0.44	1.45	0.33	0.14	0.47	

emission lines are discussed further in Section 4.3.2.

The centroid velocity fields of the extended H_2 emission are shown in Fig. 4.10 with the exception of source #31 for which the S/N was not sufficient to measure the centroid position at each spaxel. The H_2 emission detected towards sources #01, 03 and 28 all appears to be slightly red-shifted with respect to the continuum source whilst source #02 appears to exhibit no significant velocity gradient. The H_2 emission in sources #06 and 30 appear to be blue shifted relative to the continuum source. Sources #22 A and 36 B both appear to be at the centre of bipolar outflow structures and the velocity gradients across the length of the structures certainly support this. Finally in source #35 (N88 A) there appears to be a small velocity gradient from south to north.

CO bandhead emission/absorption

The CO bandhead emission red-wards of 2.29 μm in the K-band is widely associated with accretion discs in YSOs (e.g. Davies et al. 2010; Wheelwright et al. 2010). Towards our targets in the SMC, only source #03 exhibits detectable CO bandhead emission as shown in Fig. 4.11. This emission is weak even for the v = 2–0 transition at $\sim$2.295 μm which is not contaminated by low-J CO absorption lines between 2.32 and 2.38 μm. Whilst the detection of CO bandhead emission originating in discs is strongly dependent on geometry (Kraus et al., 2000; Barbosa et al., 2003), the detection rate towards the SMC sources presented in this work is significantly lower than the 17% of Cooper et al. (2013) and is therefore suggestive of a physical difference between this sample and that of Cooper et al. (2013).

When the comparison is restricted to only the range of bolometric luminosities of our SMC targets (1.5×10^3–1.7×10^5 $L_\odot$) and exclude any sources from Cooper et al. (2013) which exhibit P-cygni line profiles (as we have not observed any in the SMC), the CO bandhead detection rate of Cooper et al. (2013) drops to 15%. However this is still significantly higher than the detection rate found towards sources in the SMC (5%).

The spectrum of source #02 B appears to exhibit CO in absorption (see lower panel of Fig. 4.11). Whilst uncommon in massive YSOs, CO absorption is commonly associated with lower mass YSOs (e.g. Casali & Eiroa 1996). Although the S/N is very poor, using the blue edge of the v=2–0 bandhead, we estimate that the measured velocity towards the CO bandhead falls in the range 60–200 km s^{-1}. This is consistent with the velocity measurements made towards source #02 A (see Section 4.4 and Table 4.4). This detection is discussed in more detail in Section 4.3.2.

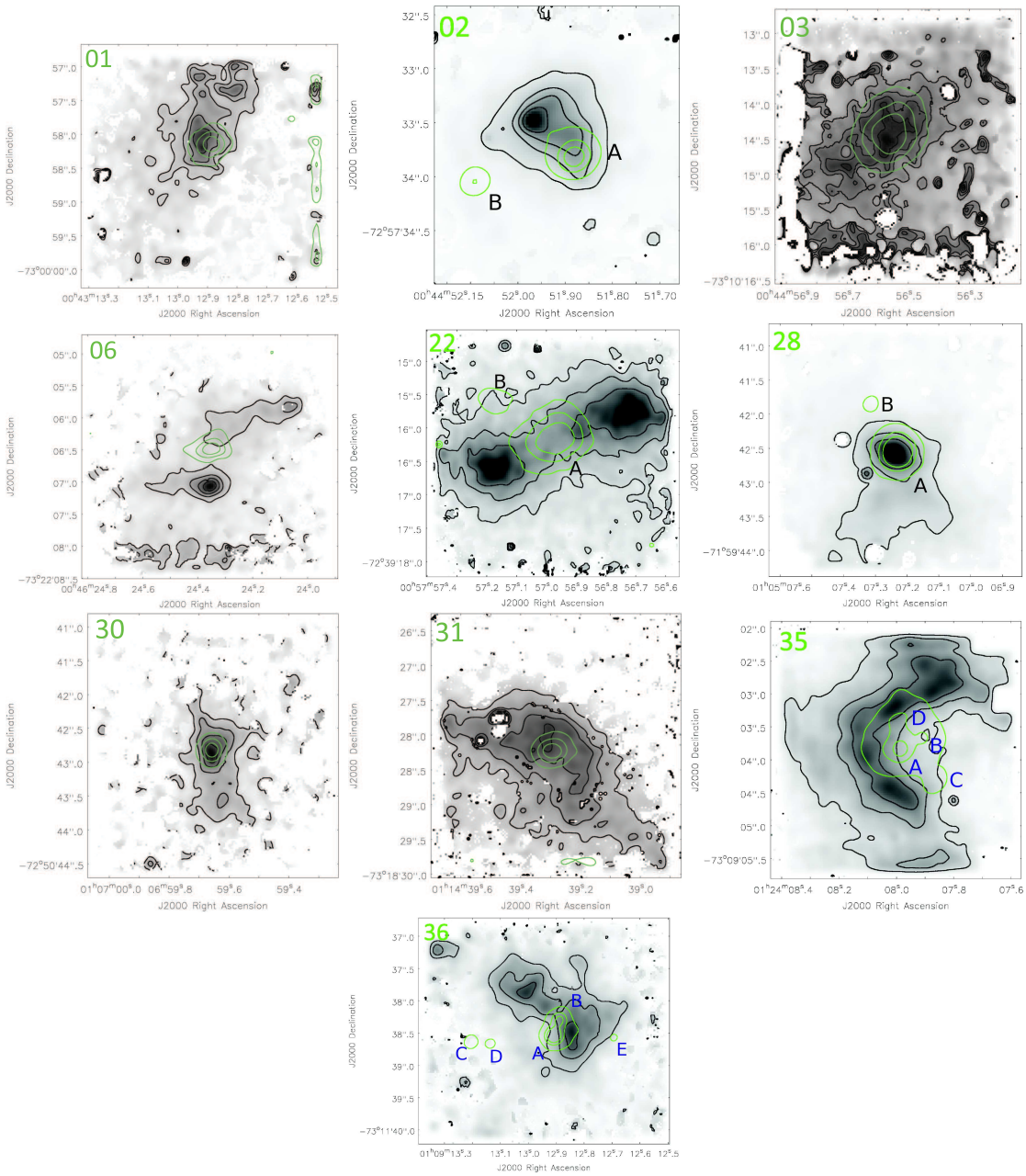

Figure 4.9: H_2 emission line morphologies for sources: #01, 02, 03, 06, 22, 28, 30, 31, 35 and 36. Black contours - [0.2,0.4,0.6,0.8] × maximum H_2 2.1218 μm integrated flux, green contours - continuum flux. The continuum contour levels are as in Fig. 4.3.

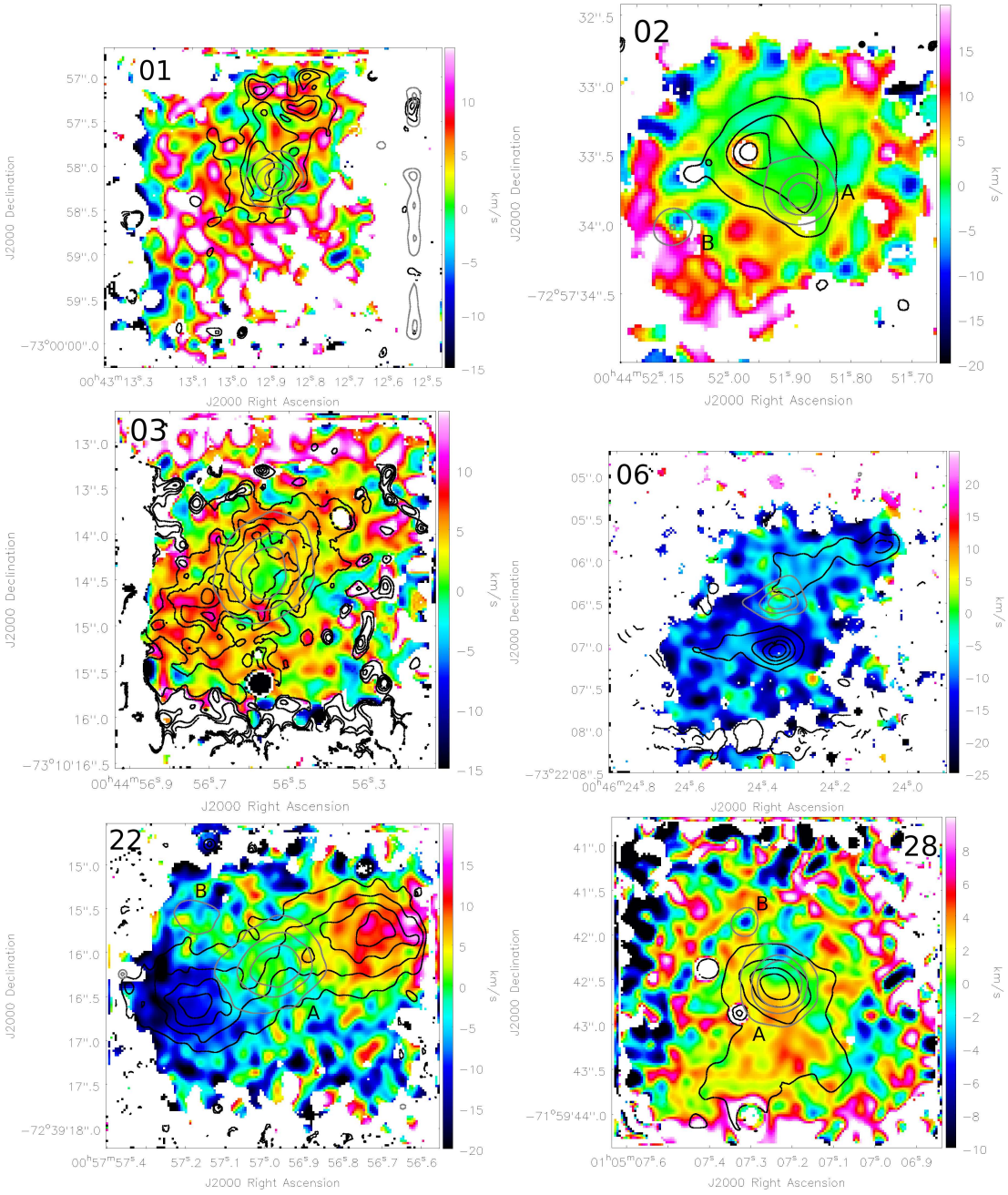

Figure 4.10: H_2 emission line velocity maps for sources #01, 02, 03, 06, 22, 28. Black contours - [0.2,0.4,0.6,0.8] × maximum H_2 2.1218 μm integrated flux, grey contours - [0.25,0.5,0.75] × maximum continuum flux.

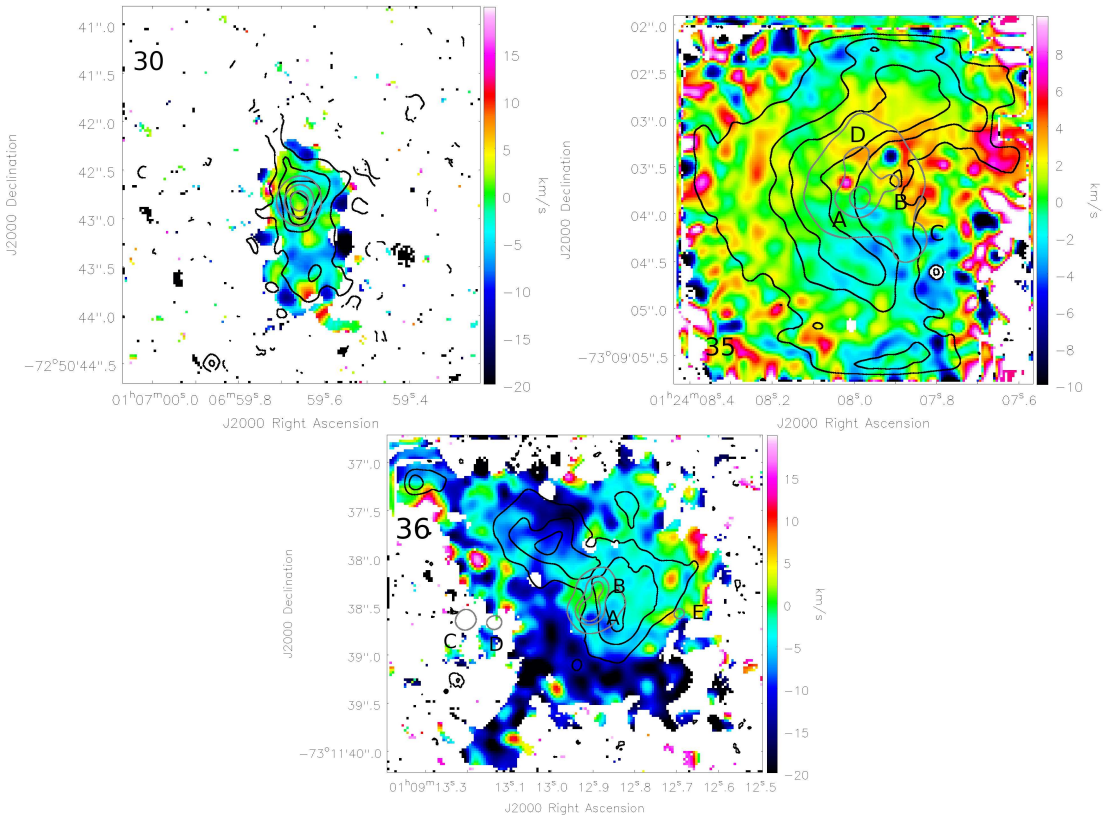

Fig 10 cont. H_2 emission line velocity maps for sources #30, 35, 36.

4.2.4 Kinematics of molecular, atomic and excited hydrogen emission

The Gaussian profiles used to fit the emission lines towards the continuum sources in this work yield centroid wavelengths which are converted into velocities. The heliocentric centroid velocities of the measured Brγ and H_2 2.1218 μm emission lines (with the flexure wavelength shift component subtracted; see Chapter 2) are shown in Table 4.4. Also shown in Table 4.4 are the most likely corresponding heliocentric velocities measured from the H I column density data cube of the SMC (Stanimirovic et al., 1999). Apertures of 2 arcmin radius centred on the coordinates of each of the *Spitzer* YSOs were used to measure the H I 21 cm velocity towards each source.

Figure 4.12 shows the Brγ velocity plotted against H I 21 cm velocity and H_2 2.1218 μm velocity against Brγ velocity. For all but five cases (sources #01, 03, 22 B, 26 and 33) the atomic hydrogen emission velocities agree within 1σ uncertainty. All but two of the H_2 emission velocities are consistent with the Brγ velocities within 2σ; however, on the whole the H_2 emission does appear to be slightly red-shifted with respect to the Brγ emission. The linear fits to the data have the equations $v_{Br\gamma} = 1.04 \pm 0.08 v_{21cm} - 6 \pm 13$ km s^{-1} and $v_{H_2} = 1.2 \pm 0.1 v_{Br\gamma} - 24 \pm 23$ km s^{-1}. This indicates a strong correlation of both the excited atomic gas velocities and the molecular gas velocities with the bulk motions of atomic gas in

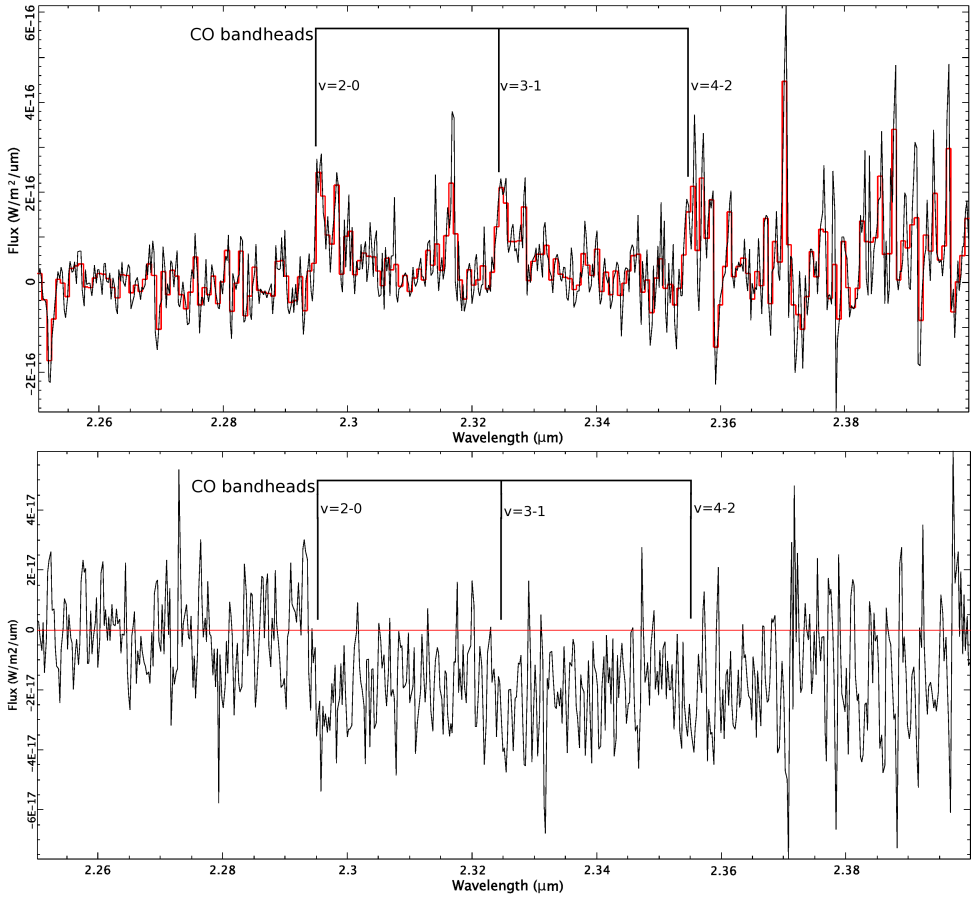

Figure 4.11: Upper panel: The region of the continuum subtracted spectrum of source #03 which contains CO bandhead emission. The 3-1 and 4-2 bandheads appear to be contaminated by CO absorption lines. Lower panel: Continuum subtracted spectrum of source #02 B exhibiting CO absorption features. The positions of the CO bandheads are marked on both spectra.

Table 4.4: Emission line centroid velocities for Brγ and H_2 2.1218 μm emission. Also included are the local H I 21 cm line velocities closest to those velocities measured with SINFONI. Where it is unclear which 21 cm velocity component is associated with the K-band emission, the closest two components are listed. The H I 21 cm data is from Stanimirovic et al. (1999), measured from a radius of 2′ surrounding the YSO source.

	Centroid velocity (km s^{-1})		
#	Brγ	H_2 2.12 μm	H I 21 cm
01	139±8	133±8	130±1
02 A	152±7	162±7	151.3±0.2
02 B		166±7	151.3±0.2
03	156±5	143±5	167.7±0.1
04	137±5		133.4±0.1
06	124±13	152±6	130.4±0.6, 159.6±0.4
17	171±6	179±5	172.0±0.1
18	170±10	183±8	171.1±0.2
20	165±6	168±7	170.0±0.3
22 A	182±8	187±6	175.2±0.3
22 B	191±8	182±6	175.2±0.3
25	167±8	174±7	166.8±0.6
26	184±8	174±8	175.7±0.7
28 A	190±7	202±7	186.9±0.1
28 B	189±10	200±6	186.9±0.1
30	185±7	186±7	179.8±0.5
31	185±7	189±7	182.0±0.3
32	136±8	145±8	140.8±0.1
33	177±4	171±3	165.0±0.1, 196.2±0.3
34	205±8	205±7	196.9±0.4
35 A	156±7	166±8	161.0±0.4
35 B	155±7	168±9	161.0±0.4
35 C	153±7	162±8	161.0±0.4
35 D	154±7	167±8	161.0±0.4
36 A	167±8	180±9	170.0±0.3
36 B	166±8	180±9	170.0±0.3
36 C	166±8	219±13	170.0±0.3
36 D	167±8	184±9	170.0±0.3
36 E	167±9	183±8	170.0±0.3

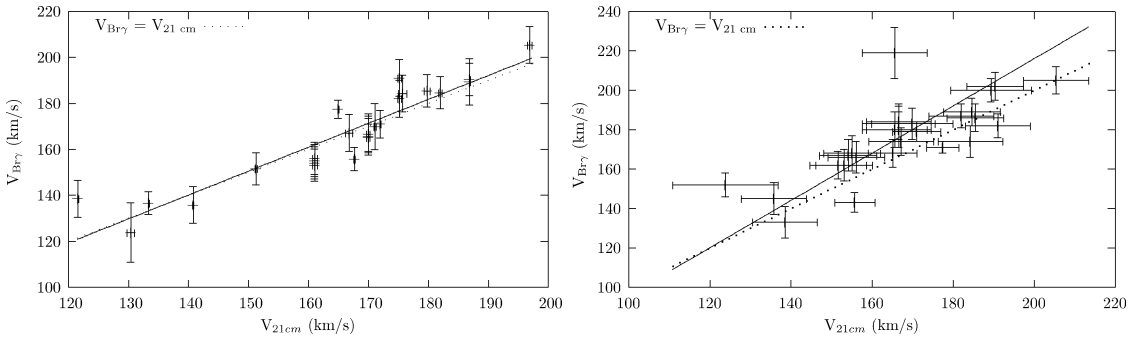

Figure 4.12: Left: Brγ centroid velocity against H I velocities as measured in data cube from Stanimirovic et al. (1999). H I 21 cm centroid velocity taken from an aperture of 2 arcmin centred on the YSO position. Right: H_2 2.1218 μm emission centroid velocity against Brγ centroid velocity for all sources for which both can be measured. The solid lines represent a linear fit to the data whilst the dotted lines show equal velocities.

the ISM of the SMC.

4.3 Discussion

SINFONI IFU observations have revealed a total of 29 K-band sources (with obtained resolutions ranging from $\sim$0.″2 to $\sim$1.″0) within 19 *Spitzer* YSO candidates in the SMC. Of these $\sim$50% exhibit line emission which extends beyond the full-width-half-maximum (FWHM) of the continuum emission. The emission line properties are summarised in Table 4.5.

4.3.1 Brγ emission and accretion rates

In Section 4.2.3 it was shown that the Brγ emission line fluxes for the sample of SMC sources are typically higher than those of Galactic massive YSOs with comparable K-band magnitudes. The ATS regressions fitted to the SMC and Galactic data sets yield the following relations between K-band magnitude and Brγ emission line luminosity.

$$\log(L_{Br\gamma(SMC)}) = (-0.39 \pm 0.05)K - (2.5 \pm 0.3) \tag{4.4}$$

$$\log(L_{Br\gamma(MW)}) = (-0.37 \pm 0.01)K - (2.69 \pm 0.03) \tag{4.5}$$

If we assume that the same empirically derived relation between Brγ emission and accretion luminosity (Eqn. 4.3) holds true for both data sets and take, for example, a massive YSO of -6 mag then we arrive at accretion luminosities of $\sim$620 $L_\odot$ and $\sim$300 $L_\odot$ for the SMC and Milky Way, respectively. Assuming these hypothetical sources are of the same mass and evolutionary state this suggests an accretion rate in the SMC which is double that of an

equivalent object in the Milky Way. Similarly, for the range of absolute K-band magnitudes from 0 to –12 the L_{acc} ratio between the SMC and the Milky Way ranges from 1.6 to 2.6. The Brγ emission measurements towards sources in N113 in the LMC (Z_{SMC} $\sim$0.4 $Z_{\odot}$, Bernard et al. 2008) are on average even higher than those of the SMC sample. However, at least two of the three N113 sources exhibit compact H II regions surrounding the continuum source, contributing significant levels of Brγ emission, likely produced by stellar photons rather than as a result of the accretion shock.

It should be noted that the K-band magnitude for massive YSOs may not be the same in the SMC as in the Milky Way for a given mass and age. Additionally the uncertainties resulting from the extinction corrections for the SMC sources are large (see Fig. 4.2). Nevertheless the results of this chapter appear to be consistent with observations of $\sim$1000 Pre-Main-Sequence (PMS) stars in the LMC by Spezzi et al. (2012) and 680 PMS stars in NGC 346 in the SMC by De Marchi et al. (2011) which suggest significantly higher accretion rates in PMS stars in the lower metallicity Magellanic Clouds. However, Kalari & Vink (2015) analyse the mass accretion rates of PMS stars in the low metallicity Galactic star forming region Sh 2-284 ($Z_{Sh2\text{-}284}$ $\sim$0.2 $Z_{\odot}$) and find no evidence of a systematic change in the mass accretion rate with metallicity. It has been suggested that both detection issues towards the Magellanic Clouds sample and physical factors can contribute towards this discrepancy.

Whilst the results in this work allude to higher accretion rates in massive YSOs in the SMC, it is far from certain whether this effect is the result of the lower metallicity environment presented by the SMC. Addressing the question of how accretion is affected by elemental composition will require significantly improved evolutionary models for low metallicity stars for a wide variety of elemental abundances, masses and ages, as well as more extensive Galactic and Magellanic Clouds observations.

4.3.2 Properties of massive YSOs in the SMC

Notwithstanding resolution effects we expect the K-band emission features to reflect the spectral classifications outlined in Woods et al. (2011), loosely describing an evolutionary sequence. The ice-feature rich G1 type sources are predicted to be the earliest stage YSOs and as such are expected to be dominated by H_2 emission produced in the shock fronts of strongly collimated outflows. The G2 (silicate absorption) sources are expected to exhibit significant Brγ and H_2 emission resulting from UV photons originating at the accretion shock front and outflows, respectively. The later stage YSOs and compact H II regions are

expected to be strong PAH emitters, falling into the G3 type. They are also both expected to exhibit strong Brγ and He I emission as a result of the strongly ionizing radiation field of the young massive star (and the shock front of any still ongoing accretion). Consistently the H_2 emission is expected to be largely photo-excited due to the broadening of outflows into lower velocity, uncollimated stellar winds and higher fluxes of energetic photons from the star itself. Compact H II regions may be distinguished by the presence of free–free radio emission produced by the large volume of ionized gas. Shock excited H_2 emission may also be present at the boundaries of compact H II regions during the expansion of the Strömgren sphere. Finally, G4 type sources are dominated by silicate emission which is observed in a number of Galactic Herbig AeBe stars (e.g. Hanner, Brooke & Tokunaga 1998; Siebenmorgen et al. 2000; Acke & van den Ancker 2004; Ciardi et al. 2005) and could be expected in lower mass, later evolutionary stage objects.

Of the nine sources in the sample that exhibit infrared ice absorption features (G1 type; Woods et al. 2011), all nine exhibit H_2 emission, indicative of outflows in early stage YSOs, with extended H_2 emission in five cases. Two G1 type sources show significant He I emission and only two exhibit free-free radio emission, more commonly found in later stage YSOs and H II regions. Nevertheless our results are largely consistent with the G1 classification representing younger sources. Likewise, of the five G3 type sources (PAH emission), four exhibit radio emission and all of them exhibit He I emission, indicating that these are indeed the more evolved sources. The two G2 type sources (silicate absorption) both exhibit H_2 emission and Brγ emission. The following equivalence can be established between Seale et al. (2009) and Woods et al. (2011): S and SE types are equivalent to G2 types, P and PE types are equivalent to G3 types and O types are equivalent to G4 types. G1 type sources from the Woods et al. (2011) scheme do not have an analogue in the Seale et al. (2009) classifications.

It must be noted that the spatial scales probed by the *Spitzer*-IRS spectra and the radio data differ significantly from the observations presented in this work. The radio emission column in Table 4.1 indicates that such emission is present within a distance of 4 arcsec from the source and thus in reality may be not be directly associated with the K-band continuum sources discussed here. Additionally the slit width of *Spitzer*-IRS varies from 3.6–11.1 arcsec depending on the spectral range, sampling a large area in complex star forming environments and making it difficult to separate the contributions of the YSO and its environment to the measured flux. It should also be noted that some of the IRS sources are resolved into multiple components in this study, demonstrating the obvious limitations of a classification scheme

Table 4.5: Observed spectral properties of all sources. For sources marked with an "E" the relevant line emission is extended beyond the FWHM of the continuum emission. "A" signifies that the emission measured is likely to be ambient whilst ? is indicative of a high degree of uncertainty in either the measurement or the source of the emission. Also included are the mid-IR classifications (W11 type; Woods et al. 2011) and whether radio emission is detected towards the sources. The 9th column gives the optical spectrum type for each source (see Table 4.1) where Hα indicates that only Hα emission is detected. The final column is a type based on the *K*-band morphology observed in this study for each source. Compact sources (C) are discussed in the first part of Section 4.3.2, followed by extended outflow sources (O). The outflow sources #03 and 31 (O*) in which the Brγ and He I emission line morphologies are distinctly offset from the continuum and H_2 emission are then discussed separately. The H II morphological classification indicates that the source is the major ionizing source of a compact H II region. The compact H II region N88 A and N81 are discussed in the final two parts of Section 4.3.2.

Source	H_2 emission	Maser emission	Brγ emission	He I emission	CO bandhead	W11 type	Radio emission	Optical type	Morphological type
01	✓E		✓E	✓E		G3	Y	IV/V	O
02 A	✓E		✓			G1	Y	Hα	O
02 B	✓								C
03	✓E	H_2O	✓E	✓E	✓	G1	Y	V	O*
04			✓	✓		G3	N	II	C
06	✓E		✓	?		G1	N		O
17	✓		✓			G1	N	Hα	C
18	✓		✓	✓		G1	N	Hα	C
20	✓		✓			G4	N	I	C
22 A	✓E		✓			G1	N	IV/V	O
22 B	✓		✓						C
25	✓?		✓?	?		G3	Y	IV	
26	✓		✓	✓		G3	Y	V	C
28 A	✓E		✓E	✓		G2	Y	IV/V	O
28 B	✓			✓					C
30	✓E		✓			G1	N	I	O
31	✓E		✓E	✓		G3	Y*		O*
32	✓		✓			G1	N	I/II	C
33	✓		✓			G2	N	I/II	C
34	✓		✓			G1	N	Hα	C
35 A	✓E		✓E	✓E				V	C/H II
35 B	✓		✓A	✓A					C
35 C	✓		✓A	✓A					C
35 D	✓		✓A	✓A					C
36 A	✓A		✓A	✓A				V	C
36 B	✓E		✓A	✓A					O
36 C			✓A	✓A					C
36 D			✓A	✓A					C
36 E	✓A		✓A	✓A					C

based on low spatial resolution observations.

Compact *K*-band sources

The majority (19/29) of the *K*-band continuum sources identified in this chapter fall within the ultra-compact regime (diameter $\leq$0.1 pc) with little or no line emission extending beyond the FWHM of the continuum source. In this section we discuss these ultra-compact sources with the exception of those in the N88 A (#35) and N81 (#36) fields which are discussed in detail later. In the remaining FOVs 11 sources are classified as compact: #02 B, 04, 17, 18, 20, 22 B, 26, 28 B, 32, 33 and 34.

The five compact sources classified as Seale et al. (2009) S-type (silicate absorption

dominated), #17, 18, 32, 33 and 34, all exhibit either Hα only in the optical spectrum or type I/II optical spectra. None are sources of radio emission, nor do they exhibit He I emission, indicating that these are early stage massive YSOs. Furthermore all but one of these sources (#33, a G2 type) are G1 types, exhibiting ice absorption features indicative of early-stage YSOs. Two of these sources (#18 and 34) exhibit H_2 emission line ratios consistent with shocked excitation linked to outflows whilst none exhibit photo-excitation dominated H_2 emission. They exhibit a wide range of luminosities, K-band magnitudes and extinctions, suggesting a wide range of physical conditions and/or masses but what seems apparent is that these make up the embedded, early stage massive YSOs.

Source #04 is a compact P-type/G3-type (Table 4.1) source, exhibiting a bright K-band continuum despite a relatively low luminosity. Brγ and He I emission are detected towards the source but no H_2 emission, so it is unlikely to be a very early stage YSO due to the lack of outflow indicators. On the other hand, there is no radio emission detected towards this source so identification as an ultra-compact HII region is unlikely. With a spectral type of B0 determined from the CLOUDY optimization (see Chapter 5), this source is likely to fall at the lower end of the mass range.

The only compact PE type (dominated by PAH emission with fine-structure emission), source #26, is also a G3 Woods et al. (2011) type exhibiting a fairly high luminosity (1.2×10^4 $L_\odot$). It has a type V optical spectrum with a log([O III]/Hβ) value comparable to that of N88 A (see Chapter 5, Fig. 5.1) and exhibits Brγ, He I and H_2 emission in the K-band, indicative of a strongly ionizing source. It also exhibits free–free radio emission, typical of an UCHII but the H_2 emission in the K-band appears to be more consistent with shocked emission than photo-excitation although as discussed in Chapter 3 determine the nature of the emission in this way is highly uncertain. Nevertheless it is therefore possible that the H_2 emission originates in a shock front of an expanding UCHII region.

Source #20 is the only YSO in this work that exhibits silicate emission (O type and G4 type classifications of Seale et al. (2009) and Woods et al. (2011) respectively). It is therefore likely to be lower mass than the majority of sources in this study and possibly in a later evolutionary state. The bolometric luminosity is low (1.5×10^3 $L_\odot$), consistent with a Herbig Be type object and the optical type of the star (I) suggests relatively low levels of ionizing radiation. The extinction appears to be unusually high (24$\pm$13 mag; c.f. Fairlamb et al. 2015) suggesting that it is more embedded than would be expected for a Herbig Be star. The high level of extinction measured in the K-band could be a geometric effect, for example

an edge on dusty disc; however, because the object is unresolved this is only speculation.

Source #02 B exhibits a spectrum which is featureless except for H_2 emission which appears to be largely ambient (see Fig. 9) and CO absorption red-wards of 2.9 μm. CO in absorption is not a common feature of massive YSOs but it has been detected towards two high confidence massive YSOs in the Milky Way (G023.6566−00.1273 and G032.0518−00.0902; Cooper et al. 2013). CO absorption is commonplace in lower mass YSOs (e.g., Casali & Eiroa 1996); however, source #02 B is relatively bright ($K = 15.75 \pm 0.1$ mag) and it is therefore unlikely to be a low mass star. The velocity range estimated for the CO absorption towards source #02 B is consistent with the line centroid measurements towards the massive YSO #02 A meaning it cannot be dismissed as an unrelated background source.

The remaining compact sources (#22 B and 28 B) exist in close proximity to a brighter K-band source and are unlikely to be the dominant source of the spectral properties examined by Oliveira et al. (2013). The line emission towards each of these sources appears to be ambient (see Figs 4.2, 4.6 and 4.9) and as such the nature of these sources remains unclear; if they are YSOs then they could be early stage and/or low mass objects.

Extended outflow sources

Seven sources exhibit extended H_2 emission morphologies indicative of molecular outflows: #01, 02A, 06, 22A, 28 A, 30 and 36 B. Two of these sources (#22 A and 36 B) exhibit clear bipolar, relatively collimated structures with a blue- and a red-shifted component (see Figs. 4.9 & 4.10) consistent with a bipolar outflow perpendicular to a disc. Source #22 A exhibits weak, compact Brγ emission whilst the Brγ emission detected towards source #36 B appears to be largely ambient to the region. Source #28 A (see Fig. 4.13) exhibits a slightly red-shifted v-shaped region of H_2 emission to the south, most likely tracing cone shaped shocked and PDR emission at the edges of an outflow. In the centre of the outflow, a low density region is formed allowing the gas there to be ionized which causes the Brγ recombination emission (see Fig. 4.13). Sources #01, 02 A and 30 exhibit extended H_2 emission in a single direction from the continuum source. The last of the outflow-like morphology sources, source #06 exhibits a knot of H_2 emission to the south and a more extended emission structure to the north west. Both of these structures appear slightly blue shifted with respect to the continuum source.

A single source appears to exhibit a 1-0S(0) / 1-0S(1) emission line ratio consistent with purely shocked emission with the majority of sources exhibiting ratios which lie between the

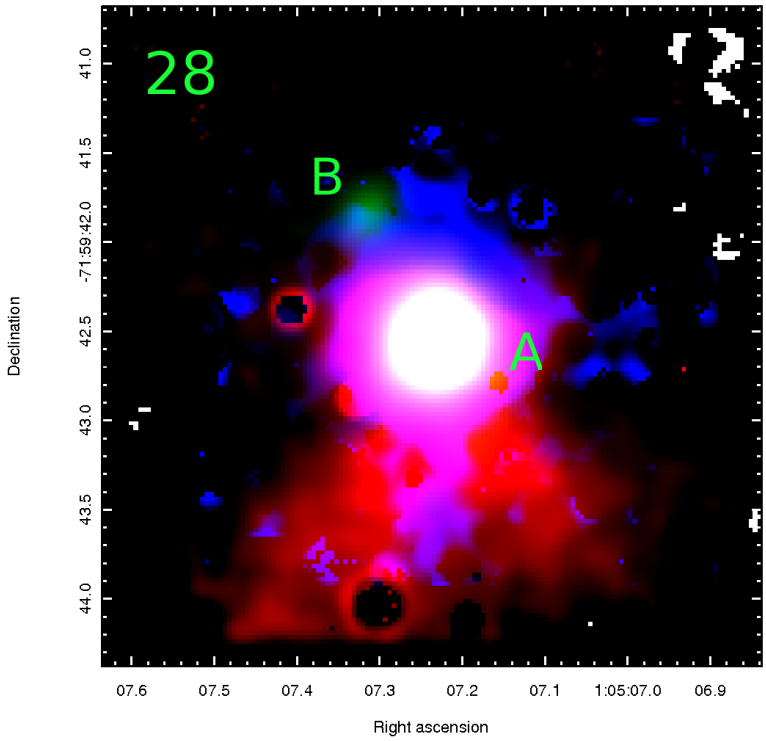

Figure 4.13: Three colour image of source #28. Red - H_2 1-0S(1) emission, green - K-band continuum emission, blue - Brγ emission.

expected ranges for shocked and photo-excited emission. On the other hand all but one 2-1S(1) / 1-0S(1) ratios (where the 2-1S(1) line is measured) are consistent with a shock excitation mechanism. We deduce therefore that, since the upper energy level of the 2-1S(1) transition (12 550 K) is almost double that of the 1-0S(0) transition (6471 K), the 1-0S H_2 transitions may be stimulated by a combination of photo-excitation from the central protostar and shocks from outflows/winds whilst 2-1S transitions are dominated by shocked excitation from outflows.

As discussed previously, the observed ice features towards sources #02, 06, 22 and 30 are consistent with early-stage YSOs (sources #02 and 22 are both resolved into multiple components in the K-band so the origin of the ice absorption in these fields remains uncertain). Source #02 also exhibits radio emission but the difference in spatial resolution means that the radio emission may not originate from the K-band sources detected in this work. Source #01 is dominated by PAH emission indicating a later stage massive YSO whilst source #28 is dominated by silicate absorption and likely is at an evolutionary state between the ice feature dominated sources and source #01.

Target #28 (see Fig. 4.13) is by far the most luminous of our targets with a bolometric luminosity of $1.4{\times}10^5$ $L_\odot$ and source #28 A is the dominant source of K-band emission in

the field. Source #28 A also exhibits relatively high level of extinction in the K-band (for the SMC) and a low level of extinction in the optical. The results of the CLOUDY optimization for the optical spectrum of source #28 indicates excitation consistent with an O9.5 type star (see Chapter 5).

Sources #03 and 31

Although the H_2 emission line morphologies of sources #03 and 31 are consistent with the extended outflow sources, the Brγ and He I morphologies (see Figs. 4.3 and 4.6) clearly distinguish them from the rest of the sources so they are discussed separately in this section. In both cases the atomic emission line structures are offset significantly from both the continuum emission and the H_2 emission.

Originally classified as a planetary nebula by Lindsay (1961) and reclassified as a YSO by van Loon et al. (2010b), source #03 presents a challenging morphology to interpret. A three colour image of source #03 is given in Fig. 4.14, showing the displacement of the Brγ emission (shown in blue) with respect to both the continuum source and the H_2 emission (in green and red, respectively). As this is the only source to exhibit CO bandhead emission, the presence of a disc is probable. The most likely origin of the extended H_2 emission and offset extended Brγ emission is a wide, relatively uncollimated outflow which is bound by the presence of a disc and has created a low density cavity along the axis of rotation in which the remaining gas is ionized. The broadening of outflows in massive YSOs leading to a low density ionized region in the centre of the outflow is predicted and modelled by Kuiper, Yorke & Turner (2015) and Tanaka, Tan & Zhang (2016), caused by continued accretion onto the central protostar in a YSO environment over time. It is therefore possible that this source represents a slightly more evolved state than that of source #28 A (Fig. 4.13).

A comparison of H_2 emission line ratios for the continuum source and the nearby off-source emission indicates that source #03 is dominated by shocked emission towards the continuum source itself with a much lower contribution of shocked excitation further from the continuum source. This is consistent with a photo-excitation region bordering an H II region which is ultimately powered by a broad, uncollimated outflow in the inner regions of the YSO. The kinematics of source #03 (see Table 4.4) indicate that the H_2 emission towards the continuum source is blue-shifted with respect to the Brγ emission and both the extended Brγ emission and He I emission are blue-shifted with respect to the continuum source (see Figs. 4.4 & 4.7)

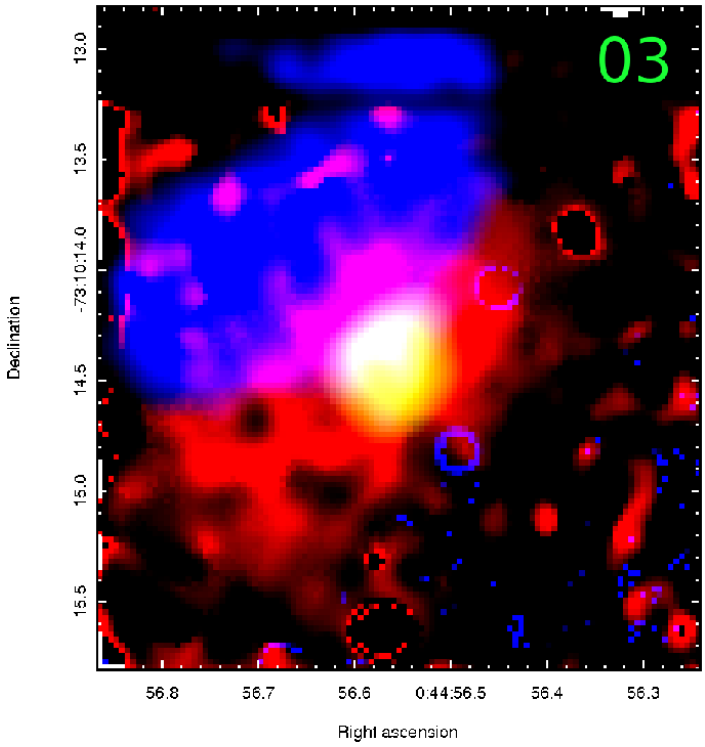

Figure 4.14: Three colour image of source #03. Red - H_2 1-0S(1), green - K-band continuum, blue - Brγ.

Finally, source #03 lies closer to previously detected H_2O maser emission (Breen et al., 2013) than any other source within our sample. The velocity of the maser falls within the range 136.4–143.0 km s^{-1} which is consistent with the velocities we have measured towards the K-band source. This emission is detected approximately 3.7±0.5 arcsec (1.1±0.1 pc) to the south of the position of the continuum source #03, outside the SINFONI FOV. Therefore the maser emission may not in fact associated with source #03. Still if the Brγ emission represents an ionized cavity as the result of powerful outflows from the source then it is conceivable that associated maser emission may be detected at relatively large distances from the continuum source.

Source #31 exhibits similar Brγ and H_2 emission morphologies to source #03. However, the properties of these objects as determined by Oliveira et al. (2013) differ significantly. The Seale et al. (2009) classification of source #03 is an S type and that of the Woods et al. (2011) scheme is G1 whilst for source #31 they are PE and G3. Additionally source #31 has a bolometric luminosity around a tenth that of source #03 indicative of an object with a significantly lower mass. Contrary to source #03, the H_2 1-01S(0) / 1-0S(1) emission line ratio towards source #31 is consistent with a PDR. Source #31, although apparently similar morphologically, possibly represents a much lower mass than source #03.

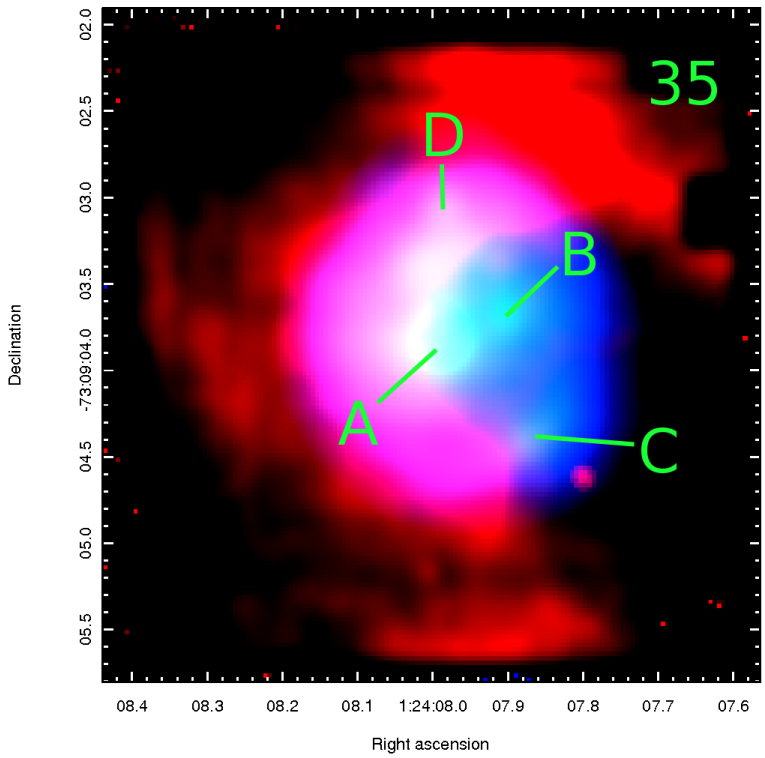

Figure 4.15: Three colour image of source #35 (N88 A). Red - H_2 1-0S(1), green - K-band continuum, blue - Brγ.

Source #35 (N88 A)

The observations presented in this chapter towards N88 A (source #35; Fig. 4.15) are consistent with those by Testor et al. (2010), with the dominant source of ionization being the central bright star (star #41 in Testor et al. 2010). All four bright stars in N88 A appear brighter in this work than Testor et al. (2010) in K-band continuum magnitude. This is most likely because the high levels of background nebulous emission are not taken into account. The measured absolute K-band magnitude of source #35 A is consistent with a ZAMS star with a temperature in excess of 50 000 K, consistent with a star which is more massive than an O3 spectral type object (Hanson, Howarth & Conti, 1997). This is likely to be an overestimate of the mass of the star because the effects of any warm dust excess and nebulous emission are neglected. The resulting best fitting solution using CLOUDY is for an exciting source of spectral type O6 (see Chapter 5).

Source #35 A exhibits strong Brγ emission and He I emission with some ambient H_2 emission originating in the H_2 emission arc (see Fig. 4.15). The remaining sources in N88 A are affected significantly by ambient emission originating from the central bright star #35 A. Peaks in both Brγ emission and He I emission also occur at the positions of sources #35 C and 35 D, which suggests that there is an additional component originating from these sources.

None of the continuum sources appear to be significant sources of H_2 emission, implying that they are not early-stage YSOs. Source #35 B does not appear to exhibit any intrinsic emission but weak emission cannot be ruled out due to its proximity to source #35 A.

Towards the H_2 emission line arc the measured H_2 emission line ratios suggest a combination of collisional excitation and photo-excitation where the emission from 1-0 transitions have a significantly higher contribution from photo-excitation compared to the 2-1 transitions. The collisional component is most likely caused by the impact of the expanding ionized gas on the surrounding molecular cloud, forming the H_2 emission arc observed in the east of N88 A; an additional photo-excited component is sourced from the massive stars in the centre of the region.

Rather than showing an association with the H I gas component at 134±9 km s^{-1} (Testor et al., 2010), both the SINFONI velocity measurements for H I and H_2 emission and the radio H I velocities obtained from the data of Stanimirovic et al. (1999) are significantly higher than this. The H_2 velocities we measure towards the continuum sources in N88 A range from 162 to 167 km s^{-1} with a typical uncertainty of 8 km s^{-1}, consistent with the measured 21 cm peak at 161.1±0.4 km s^{-1}. It therefore appears most likely that N88 A is associated with the SMC gas component at 167±8 km s^{-1} (McGee & Newton, 1981). The Brγ emission velocities range from 153 to 156 km s^{-1} with a typical uncertainty of 7 km s^{-1}, blue-shifted with respect to the bulk motion of the gas. This is consistent with a compact H II region in which the ionized gas is expanding outwards due to radiation pressure at a velocity of ∼10 km s^{-1}, comparable to the compact H II regions observed in LHA 120-N113 in the LMC (Ward et al., 2016).

Source #36 (N81)

The central region of N81 has been resolved into 5 distinct K-band continuum sources, a significant improvement on the previous highest resolution seeing limited imaging available (Heydari-Malayeri et al., 2003) which resolved only two sources. The most distinctive newly resolved feature of N81 is the bipolar H_2 emission centred on (or near to) source #36 B (Fig. 4.16). This bipolar morphology and the observed velocity gradient indicate a bipolar outflow centred on source #36 B, suggestive of an early stage massive YSO.

The majority of the Brγ emission towards this region appears to be ambient and is likely common to the whole N81 H II region. There may be an additional component from one or both of the fainter (and probably lower mass) sources #36 C and 36 E. A similar morphology

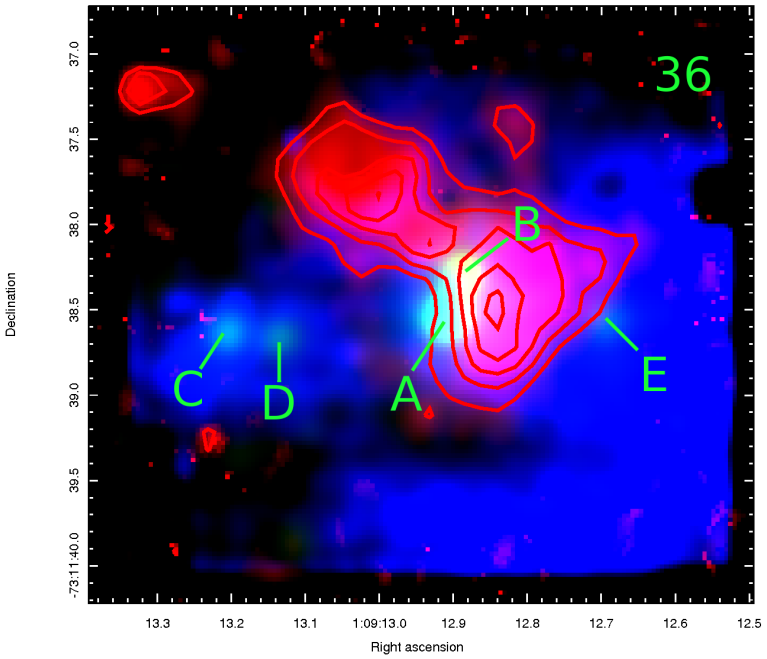

Figure 4.16: Three colour image of source #36 (N81). Red - H_2 1-0S(1), green - K-band continuum, blue - Brγ. For clarity the red contours trace the H_2 emission.

is observed in the He I emission. Although it is the brightest continuum source in the region, emission detected towards source #36 A appears to be entirely ambient.

The velocities we have determined towards sources in N81 from Brγ emission range from 166 to 167 km s^{-1} with uncertainties of $\sim$9 km s^{-1}. These are consistent with both the results of Heydari-Malayeri et al. (1988) determined from Hβ emission and the velocity determined from the radio observations (see Section 4.2.4) indicating a common bulk motion of the atomic and ionized gas. The H_2 2.1218 μm emission towards the same sources has been measured to be consistently red-shifted with respect to the Brγ emission.

4.4 Chapter Summary

In this chapter K-band SINFONI observations have been presented for 17 of the 33 massive YSOs in the SMC presented in Oliveira et al. (2013), as well as two additional targets in N81 and N88 A, revealing a wide range of spectroscopic properties. The conclusions of this chapter are summarised below.

i 14 of the 17 *Spitzer* YSOs in the SMC observed with SINFONI have been resolved into single K-band continuum sources whilst three have been resolved into multiple components in the K-band. Source #35 (N88 A) has been resolved into the previously known 4 continuum components. N81 (#36), previously resolved into two components by Heydari-

Malayeri et al. (2003), has now been resolved into five K-band continuum sources.

ii Visual extinctions have been calculated towards all K-band sources except source #04. A median visual extinction towards the SMC sources of $A_V = 14$ mag is found. The median for the Galactic sources from Cooper et al. (2013) is 44 mag and that for the three YSOs in N113 in the LMC is 20 mag (Ward et al., 2016). This seems to suggest that there is a correlation between extinction towards YSOs and metallicity as $Z_{\rm LMC} \sim 0.5$ $Z_\odot$ and $Z_{\rm SMC} \sim 0.2$ $Z_\odot$.

iii Whilst consistent with the Cooper et al. (2013) sample, Brγ luminosities are high compared with those in the Milky Way, suggesting accretion rates which are on average higher than for the Galaxy.

iv Average velocities have been measured towards the *Spitzer* YSO sources of 169±5 km s^{-1} and 173±4 km s^{-1} for Brγ emission and H_2 emission, respectively. The Brγ emission line velocities are consistent with those of the H I radio observations, indicating that the average motions of the YSOs are bound to the bulk motions of the ISM.

v The majority of the K-band continuum sources (11/20; excluding observations towards the H II regions N81 and N88 A) fall within the unresolved, ultra-compact regime. These sources exhibit a variety of spectral properties and include one probable UCHII region (#26), a possible Herbig Be star (#20) along with spectroscopically typical massive YSOs and two apparently featureless continuum sources (#22 B and 28 B) which may not actually be YSOs exhibiting red continuua with H_2 and/or Brγ and He I emission features.

vi Seven sources with extended H_2 emission morphologies indicative of outflows have been identified, with velocity gradients measured towards four of these. Sources #22 A and 36 B exhibit striking examples of bipolar outflow morphologies. These observations of the well-studied H II region N81 are the first to identify the bipolar outflow originating from source #36 B.

vii Source #28 A exhibits Brγ and H_2 emission line morphologies indicative of an ionized cavity in the centre of the outflow. Source #03 appears to be an extremely broadened (and possibly more evolved) example of the same structure. These structures are possibly the result of the broadening of outflows in massive YSOs predicted by the models of Kuiper, Yorke & Turner (2015) and Tanaka, Tan & Zhang (2016).

viii CO bandhead emission (commonly used as a tracer of discs) has only been detected towards one source (#03), a detection rate of around one third of that towards massive YSOs in the Milky Way (Cooper et al., 2013) for the same range of luminosities. This could be due to either the low gas-phase CO abundance of the SMC (Leroy et al., 2007), or conditions within protostellar discs which differ significantly (such as higher temperatures or less shielding from dust) from those in the Milky Way, leading to a higher rate of CO destruction. CO absorption is somewhat tentatively observed towards one source (#02 B) which could be indicative of a dusty circumstellar environment and possibly suggests a continuum source completely obscured by an edge–on disc.

To conclude, the results presented this chapter represent the first study of massive YSOs in the SMC using integral field spectroscopy, resolving a number of the YSOs into multiple sources for the first time. This study has revealed the presence of multiple large, extended outflow structures and has provided tentative evidence of both a strong dependence of extinction on metallicity and higher accretion rates in massive YSOs in lower metallicity environments.

5 Optical spectroscopy towards sites of massive star formation in the Magellanic Clouds

The majority of the work presented in this chapter has been previously published in Ward et al. (2017). The main exceptions are the optical spectrum towards N113-YSO03 and the Lyman continuum analysis in Section 5.1.3.

In this chapter optical spectra observed towards massive star forming regions in the Magellanic Clouds are presented and studied. The focus of this chapter is primarily on optical spectroscopy towards massive YSOs in the SMC (a subset of which was observed with SINFONI and analysed in Chapter 4) but a spectrum towards N113-YSO03 in the LMC (SINFONI observations discussed in Chapter 3) was also obtained and is presented here. The spectra obtained using RSS at SALT are shown in Figs. D.5, D.6 and D.7.

5.1 Results

5.1.1 Extinction towards optical emission

Although extinction significantly impacts optical observations, it also gives an indication of where the emission originates. This is a particularly important consideration for massive YSOs because they are embedded objects and it is therefore unexpected for them to be observable in the optical regime.

Values of extinction are calculated using H I Balmer series emission lines comparing the attenuated ratio $[H_\alpha/H_\beta]_a$, with the expected intrinsic ratio, $[H_\alpha/H_\beta]_i$;

$$E(B-V) = \frac{\log[H_\alpha/H_\beta]_a - \log[H_\alpha/H_\beta]_i}{0.4(K_{H\beta} - K_{H\alpha})} \tag{5.1}$$

where $K_{H\alpha}$ and $K_{H\beta}$ are 2.535 and 3.609, respectively (Calzetti, 2001). The derivation of this calculation follows the same principles as those used in Chapter 3. The Case B recombination intrinsic line ratio is normally $H_\alpha/H_\beta \approx 2.87$ at 10 000 K; however, this ratio

Table 5.1: extinction values calculated from HI line ratios

source	A_V (optical)	A_V (K-band)
1	1.51±0.05	2.6±10.9
3	0.98±0.18	13.7±10.8
4	3.10±0.18	
7	1.95±0.57	
8	1.15±0.21	
9	0.54±0.13	
12	0.91±0.99	
13	2.65±0.28	
15	0.86±0.19	
20	2.47±1.16	24.1±13.2
22	<0.24	9.9±6.4
25	0.47±0.18	<12
26	<0.30	14.2±16.6
28	0.81±0.35	19.5±9.3
30	2.61±0.34	<67.7
35	<0.09	1.2±17.0
36	<0.08	13.3±12.8
mean	1.5±0.4	12.3±2.7

can vary by 5–10% over a temperature range of 5000–20 000 K (Osterbrock & Ferland, 2006). For Case A recombination the ratio is 2.86 at 10 000 K (Osterbrock & Ferland, 2006) with a similar temperature dependent variance making this ratio largely independent of whether the emission is optically thick or thin. Assuming a Milky Way-like extinction curve with R=3.1, the extinction estimates shown in Table 5.1 are obtained. These extinction values are significantly lower than those calculated from the K-band emission (see Section 4.2) although we are only able to calculate extinction values using both methods for 9 of the targets. For these 9 targets, the mean extinction values are $A_V = 12.4\pm2.4$ mag in the K-band whilst only $A_V = 1.0\pm0.3$ mag in the optical emission. The median values for extinction obtained for these 9 sources are $A_V = 13.3$ and 0.81 mag for the K-band and optical measurements, respectively. Upper limits are used as A_V values in the optical to provide an adequate sample of extinctions derived from optical emission whilst excluding sources with limits in the K-band. The disparity between the extinction values calculated for the optical and near-infrared emission suggests that the optical emission is in fact sampled in a much shallower region of the YSO environment rather than at the YSOs themselves and most likely close to the outer edges of the molecular clouds.

For N113-YSO03 an Hα / Hβ ratio of 1.7±0.3 was determined, apparently inconsistent with either optically thick or thin emission. It is likely that the flux of the Hα emission feature is underestimated in both N113-YSO03 and source #35 in the SMC due to the extremely

broad nature of these features which makes them challenging to fit even with a combination of a Gaussian function and a Lorentz function. It is also possible that there is another systematic effect at work making the spectrum appear bluer than it should; however, this effect would have to be extreme to produce the negative extinction result recorded here. Finally it could be an intrinsic property of the nebulous emission due to scattering within the H II region which is known to cause a negative reddening effect (e.g. Osterbrock & Ferland 2006). Nevertheless it appears from this result that the extinction towards the optical emission in N113 is most likely significantly lower than the value of A_V=15.0±0.8 mag measured towards the near-infrared continuum sources (see Chapter 3).

5.1.2 Nature of emission

An important consideration in the analysis of the measured optical emission lines is the physical process driving the emission, in particular whether the emission is photo-excited or shock excited. In order to constrain this the ratios of emission lines measured in the data are compared with those predicted by models. To investigate the source of the optical emission the MAPPINGS III pre-run photo-ionization grids (Kewley et al., 2001) and shock grids (Allen et al., 2008) are used to constrain the source of the emission. In Fig. 5.1 log([O III]/Hβ) is plotted against log([S II]/Hα) (upper panel) and log([O III]/Hβ) against log([N II]/Hα) (lower panel) for all of the sources for which these emission lines could be measured, as well as predictions from the photo-ionization and collisional excitation grids. Also shown in both panels is the maximum starburst line from Kewley et al. (2001), a theoretical limit above which photo-ionization alone is not sufficient to produce the observed emission.

On inspection of Fig. 5.1 it becomes apparent that the optical emission is not consistent with shocked excitation towards any of the sources in the SMC or in N113-YSO03. The majority of the sources fall close to the photo-ionization models with some scatter. It seems reasonable to assert that, as the emission is caused by photo-excitation and the optical extinctions are significantly lower than those measured in the K-band, the optical emission arises at a significant distance from the SINFONI continuum sources, in a region closer to the surface of the molecular cloud. It is therefore also reasonable to assume that the optical emission may have contributions from stars which are outside of the SINFONI FOVs.

The model photo-ionization grids which have been used in this section also vary significantly with metallicity and as such grids with metallicities of 0.2 $Z_\odot$ and 0.4 $Z_\odot$ (matching

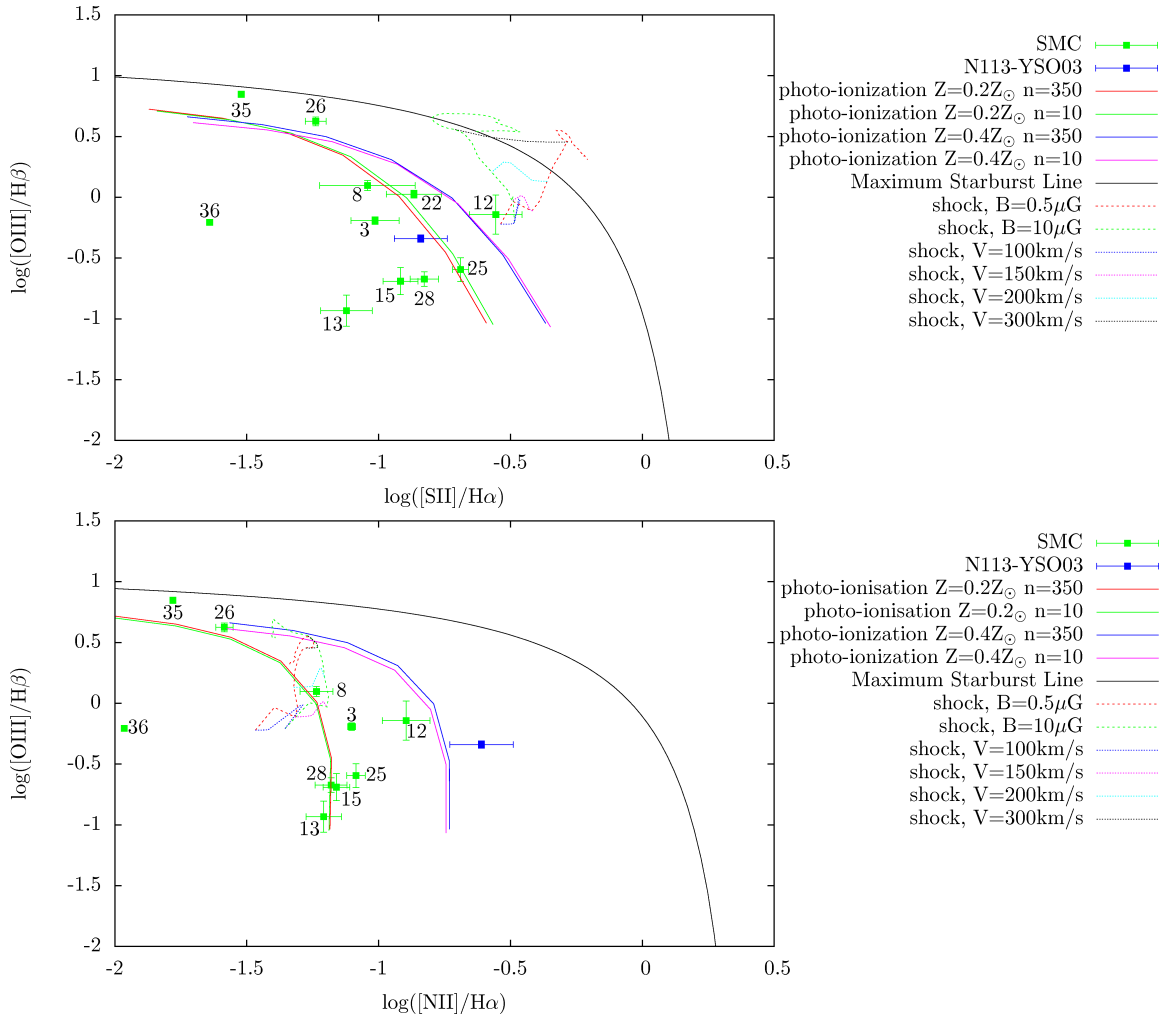

Figure 5.1: Upper: log([O III]/Hβ) vs log([S II]/Hα) Lower: log([O III/Hβ) vs log([N II]/Hα). Also shown are the pre-run MAPPINGS III pre-run STARBURST99 photo-ionization grids (Kewley et al., 2001) and shock excitation grids (Allen et al., 2008) with the Maximum Starburst Line (MSL) from the PEGASE grids.

those of the SMC and LMC, respectively) are shown in Fig. 5.1. Source #12 in the SMC falls closer to the $0.4\,Z_{\odot}$ photo-ionization curves than the $0.2\,Z_{\odot}$ grids in both the upper and lower panels. N113-YSO03 on the other hand lies closer to the $0.2\,Z_{\odot}$ line in the upper panel and closer to the $0.4\,Z_{\odot}$ line in the lower panel, indicating that it is unlikely that this type of analysis can be used to determine reliable estimates of metallicity.

5.1.3 Lyman continuum

The majority of spectra obtained in this sample exhibit strong Hα emission at 6562.8 Å (with the exception of sources 5, 6, 24, 29, 31) which can be used to estimate Lyman continuum flux using the relation from Devereux & Scowen (1994) and estimate a spectral type based on the Lyman continuum.

$$N_{LyC} = 0.83 \times 10^{62} F_{H\alpha} D^2 \tag{5.2}$$

The Hα flux used is in $erg\,s^{-1}\,cm^{-2}$ and the distance is in Mpc. These values are then compared to those of ZAMS stars from Panagia (1973) to obtain a range of spectral types associated with the Lyman continua. The results are shown in Table 5.2.

With the exception of the bright H II regions N88 A (35) and N81 (36), all of our sources have Lyman continua consistent with those of ZAMS early B-type stars. However as mentioned in Section 5.1.2, it is unlikely in most cases that the YSO in question is the only exciting source of the optical emission. Additionally in all but the most evolved compact H II regions and ZAMS stars the majority of the Lyman continuum photons will be absorbed by circumstellar and interstellar dust in the dense star forming environments. It is likely therefore that the mass estimates based on Hα measurements significantly underestimate the masses of the exciting sources.

5.1.4 Cloudy optimization

Where multiple emission lines were detected in the optical spectra I have used the CLOUDY photo-ionization code to fit parameters using the Tlusty grid of OB-type stellar atmosphere models and assuming abundances of Dufour (1984) where available and a metallicity of 0.2 $Z_{\odot}$ for species where measured abundances are not available. When interpreting these results it should be noted that the elemental abundances of the cloud used in the CLOUDY line optimisation process have a significant impact on the results of the analysis. For the N113-YSO03 analysis a metallicity of $0.4\,Z_{\odot}$ was used for both the star and the cloud, consistent with measurements towards the LMC.

Table 5.2: Lyman continuum based on Hα measurements. ! denotes a measurement which has not been corrected for extinction. The last column indicates the corresponding ZAMS spectral type associated with the determined Lyman continuum from Panagia (1973)

Source	Lyman Continuum $\log(F_{LyC})$	ZAMS Spectral type
1	47.22 ± 0.02	B0
2	45.33 ± 0.02 !	B1
3	47.69 ± 0.06	O9.5/B0
4	47.76 ± 0.06	O9.5
7	46.44 ± 0.19	B0.5
8	46.64 ± 0.07	B0/0.5
9	47.29 ± 0.04	B0
10	45.17 ± 0.09 !	B1
11	45.3 ± 0.2 !	B1
12	45.93 ± 0.32	B0.5/1
13	47.36 ± 0.09	B0
14	45.92 ± 0.07 !	B0.5
15	46.71 ± 0.06	B0/0.5
16	45.79 ± 0.04 !	B1
17	45.05 ± 0.06 !	B2
18	45.3 ± 0.1 !	B1
20	47.53 ± 0.38	O9.5/B0
21	47.04 ± 0.12	B0/0.5
22	46.18 ± 0.11	B0.5
23	45.21 ± 0.05 !	B1
25	46.70 ± 0.06	B0/0.5
26	47.26 ± 0.02 !	B0
27	45.32 ± 0.06 !	B1
28	46.70 ± 0.12	B0/0.5
30	46.03 ± 0.02 !	B0.5
32	45.79 ± 0.09 !	B1
33	45.8 ± 0.2 !	B1
34	45.39 ± 0.04 !	B1
35	48.53 ± 0.03 !	O7.5
36	47.76 ± 0.02 !	O9.5
N113-YSO03	47.22±0.08 !	B0

Table 5.3: Results of the CLOUDY emission line optimization for optical spectra based on the Tlusty grid of OB star model atmospheres (Lanz & Hubeny, 2003, 2007). Shown are the emission lines used as inputs and the output stellar temperature and cloud density. Also shown are values representing the variation between the model emission line fluxes and the observed fluxes and the average line flux for each source ('avg |mod–obs|' and 'avg flux', respectively), both expressed as multiples of the uncertainty (σ). The final column gives the spectral type based on ZAMS stars of equivalent effective temperature from Hanson, Howarth & Conti (1997). Sources #07–21 were not observed with SINFONI.

Source	emission lines used	$\log(T_{\rm eff})$ (K)	$\log(n_{\rm H})$ ($\rm cm^{-3}$)	avg |mod–obs| (σ)	avg flux (σ)	Spectral type
01	Hα, Hβ, [S II]6716,6731, [N II]6548,6584	4.511	3.286	1.921	11.736	B0
03	Hα, Hβ, [S II]6716,6731, [N II]6548,6584, [O III]4959,5007	4.505	3.162	2.234	3.329	B0
04	Hα, Hβ, [S II]6716,6731	4.495	2.670	0.540	3.425	B0
07	Hα, Hβ, [S II]6716,6731, [N II]6584	4.517	2.586	0.143	0.964	B0 / O9.5
08	Hα, Hβ, [S II]6716,6731, [N II]6548,6584, [O III]4959,5007	4.539	2.369	0.575	2.477	O9.5
09	Hα, Hβ, [S II]6716,6731, [N II]6548,6584	4.513	3.029	0.958	4.631	B0
12	Hα, Hβ, [S II]6716,6731, [N II]6584, [O III]4959,5007	4.740	1.343	0.104	0.419	<O3
13	Hα, Hβ, [S II]6716,6731, [N II]6548,6584, [O III]4959,5007	4.521	0.106	0.544	1.981	B0 / O9.5
15	Hα, Hβ, [S II]6716,6731, [N II]6548,6584, [O III]4959,5007	4.533	0.998	0.658	2.829	O9.5
21	Hα, Hβ, [S II]6716,6731	4.457	3.125	0.069	1.701	B0.5
22	Hα, Hβ, [S II]6716,6731, [O III]4959,5007	4.585	2.368	0.062	1.724	O8
25	Hα, Hβ, [S II]6716,6731, [N II]6548,6584, [O III]4959,5007	4.534	0.009	0.991	3.263	O9.5
26	Hα, Hβ, [S II]6716,6731, [N II]6584, [O III]4959,5007	4.551	1.171	0.445	1.935	O9
28	Hα, Hβ, [S II]6716,6731, [N II]6548,6584, [O III]4959,5007	4.531	2.098	0.407	1.665	O9.5
35 (N88 A)	Hβ, [O III]4959,5007	4.63	0.46	0.015	8.854	O6
35 (N88 A)	Hα, [S II]6716,6731, [N II]6548,6584	4.54	2.82	2.833	24.52	O9.5
36 (N81)	Hβ, [O III]4959,5007	4.58	2.96	0.670	43.167	O8
36 (N81)	Hα, [S II]6716,6731, [N II]6548,6584	4.56	2.64	1.417	29.0	O8.5
N113-YSO03	Hβ, [O III]4959,5007	4.52	4.42	0.269	22.2	O9.5
N113-YSO03	Hα, [S II]6716,6731, [N II]6548,6584	4.44	3.04	19.5	772	B0.5

For the SALT spectra the red and blue spectral regions have been treated separately, using the pg1800 grating observations for N88 A and N113-YSO03 in order to resolve the [N II] emission lines at 6548 Å and 6584 Å which are blended with the broad Hα emission line in the pg900 grating spectrum. The resulting stellar temperatures and hydrogen densities of the CLOUDY line optimization are shown in Table 5.3. Also given are the values of the average deviation between the observed extinction corrected line flux relative to Hβ (or Hα where Hβ is not used as an input) and the model line flux. This is expressed as a multiple of the uncertainty in the observed relative line flux and thus a number significantly less than one is desirable. The penultimate column shows the average line flux as a multiple of the uncertainty in that line flux and hence values greater than three represent 3σ measurements.

The effective temperatures obtained using CLOUDY for the majority of sources are consistent with late O-/early B-type stars. For sources #07 and 12, the uncertainties in the line flux ratios exceed the values themselves and thus these results are highly uncertain. The fits for sources #01, 03, 09 and 25 are poor: the average difference between the observed and model line fluxes is close to (#09, 25) or greater than (#01, 03) the average uncertainty in the measured line fluxes despite having relatively well constrained emission line fluxes available. This may be an indication that multiple unresolved sources contribute to the excitation of

the optical lines. The red sections of the spectra for sources #35, 36 and N113-YSO03 have proven particularly challenging to fit with CLOUDY. For these spectra multiple bright sources of differing spectral types fall within the 1 arcsec width of the slit. It is therefore unsurprising that it is challenging to fit a single star model to these spectra. Nevertheless these fits are consistent with excitation by massive stars as expected.

5.2 Discussion

Whilst it remains evident that deeply embedded massive YSOs themselves are unlikely to be detected at optical wavelengths, optical emission lines are detected towards a significant number of massive YSOs in the SMC. From our analysis of the Hα and Hβ emission lines we determine values of visual extinction towards the optical emission which are significantly lower than the extinction values calculated from the K-band emission features. Through comparison with model sets of emission line ratios it has been determined that, without exception, the optical emission we have measured is dominated by photo-excitation rather than shocked emission. These findings indicate that the optical emission is sourced in a much shallower region of the molecular cloud and that it is produced via the interaction of UV photons with the gas in the outer regions of the cloud. This therefore implies a large mean free path of UV photons which in turn is likely caused by a porous, possibly clumpy ISM which is consistent with the findings of Madden et al. (2006), Cormier et al. (2015) and Dimaratos et al. (2015).

Using the flux of the Hα emission line it is possible to estimate the Lyman continuum and thus obtain an equivalent spectral type. Because this flux is measured from the surface of the molecular cloud rather than from the YSO itself, it contains a contribution from all of the stars within that region of the cloud. In most cases however it is likely that the massive YSO targeted in this work is the dominant source of the exciting radiation field. Where it is present, the Hα emission towards the targets of this work are consistent with early B-type stars except for sources 35 and 36 where it is consistent with O-type stars. It should be noted however that these are not ZAMS stars and that in most cases the majority of the Lyman continuum emission from the central source may be absorbed by circumstellar and interstellar material and would therefore not contribute to the Lyman continuum flux determined. It is also a possibility that when measuring the Hα emission we are in fact measuring emission caused by lower mass and hence less embedded sources than the dominant K-band source. Of those SMC *Spitzer* YSOs for which we have been unable to obtain Hα measurements only

sources 6 and 31 have been observed with SINFONI.

Using the photo-ionization code CLOUDY, it has been possible to determine densities and exciting source temperatures for the majority of the optical spectra based on the assumption that the gas is excited by a single OB star. The majority of optical spectra are consistent with late-O/early-B type zero-age-main sequence (ZAMS) stars, indicating mass ranges of 10–30 $M_{\odot}$ (Hanson, Howarth & Conti, 1997). However, the objects in question are not straightforward systems comprising of a single ZAMS star illuminating a molecular cloud and the accretion process produces a significant amount of ionizing photons as well. As previously mentioned it is possible that multiple objects contribute to the optical emission (although the emission is still likely to be dominated by the most massive star).

From the medium resolution spectra of N88A, N81 and N113-YSO03 (Fig. D.6 and Fig. D.7) it can be seen that in both cases the profiles of the Hα and Hβ lines are broad and that in N88 A the majority of line profiles are noticeably broadened. The Hα emission towards N88 A has a line width of 2.74$\pm$0.05 Å which corresponds to a velocity dispersion of 125$\pm$2 km s^{-1}. These high velocity dispersions are most likely to be a result of a highly turbulent medium in the high-excitation blob (Chapter 4).

5.3 Chapter summary

The results of this chapter can be summarised in three key points as follows:

i All optical emission measured exhibits lower levels of extinction that the near-infrared emission measured towards the same sources, indicating that it must originate from a shallower region of the cloud.

ii All of the measured optical emission is consistent with photo-excitation which when taken into account along side lower levels of extinction, implies that that there is a large mean-free-path for UV photons in these regions. This in turn implies an interstellar medium which is porous and/or clumpy, as expected in low metallicity environments.

iii The measured optical emission line fluxes are consistent with the presence of one or more massive stars and/or protostars in all cases.

When combined with the results of the near-infrared observations presented in the previous two chapters, a picture emerges of the formation of massive stars within a relatively a porous ISM which in turn significantly shape their environments through strong ionizing

radiation fields, stellar winds and large scale bipolar outflows which leave ionized cavities in their wake.

6 *H+K* integral field spectroscopy of embedded clusters in the Large Magellanic Cloud

In this Chapter a set of archival SINFONI observations towards embedded cluster candidates in the LMC are analysed and discussed. These archival observations are outlined in Section 2.1.

6.1 Introduction

The formation of massive stars culminates in the emergence of clusters and associations of OB stars. The behaviour of and interactions between stars and gas in young clusters of massive stars therefore offer valuable insights into the process of star formation. Due to the embedded nature of the clusters discussed in this chapter they are also good candidates for hosts of massive YSOs and compact H II regions.

Seven fields were observed in the region surrounding the Tarantula nebula in the LMC: two in the 30 Doradus starburst region, one near LHA 120-N159, three near LHA 120-N160 and one to the south west of the region as shown in Fig. 6.1. Also shown in Fig. 6.1 are the positions of H II regions (Henize, 1956) and the field observed with ALMA by Indebetouw et al. (2013). The targets which were observed are summarised in Table 6.1 along with their classifications from the previous studies of Gruendl & Chu (2009) and Seale et al. (2009). The penultimate column gives the identification of any 20 cm radio emission source within 5 arcsec of the target from the Marx, Dickey & Mebold (1997) catalogue. The final column (AT20G source) shows whether or not a source was detected in the Australia Telescope 20 GHz Survey (AT20G; Murphy et al. 2010) within 4 arcsec. For simplicity short names are also assigned to each of the fields (first column of Table 6.1) which are used throughout this chapter.

Four out of the seven targets are classified as definite YSOs in the Gruendl & Chu (2009) catalogue and five appear in the Seale et al. (2009) spectroscopic study of massive YSOs in the LMC. Of the five in the Seale et al. (2009) sample, three spectra are dominated by PAH

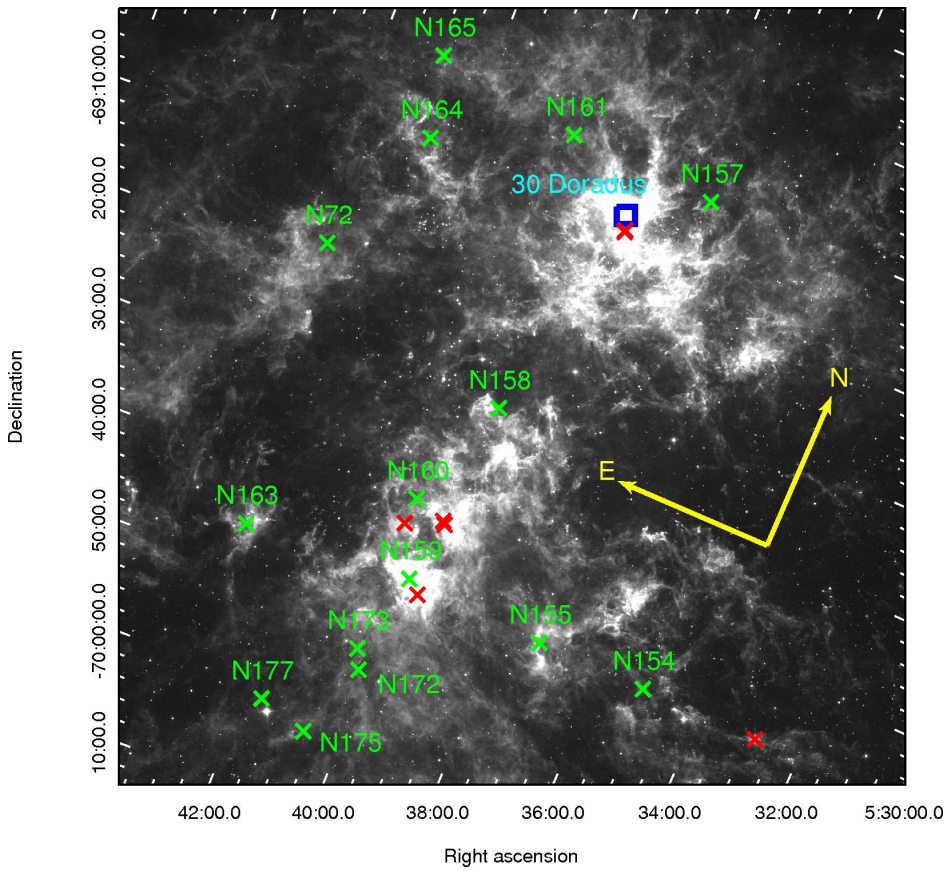

Figure 6.1: *Spitzer*-IRAC 8.0μm image of the region of interest in the LMC, including 30 Doradus and surrounding H II regions. The pointings of the SINFONI observations described here are shown as red crosses. The green crosses show the positions of H II regions (Henize, 1956) and the blue square indicated the approximate FOV observed with ALMA by Indebetouw et al. (2013).

Table 6.1: Target properties. The first column gives a short name for each target used only in this work. A ✓ in the Gruendl & Chu (2009) GC08 column indicates the source is classified as a definite YSO whilst an ✗ means that no nearby source is present in the catalogue. The 20 cm column gives the identification of any 20 cm radio emission source within 5 arcsec of the target from the Marx, Dickey & Mebold (1997) catalogue. The AT20G column indicates whether the source was detected in the Australia Telescope 20 GHz Survey (AT20G; Murphy et al. 2010) within 4 arcsec.

Short name	*Spitzer* name	RA h:m:s	Dec °:′:″	Class GC08	Class S09	20 cm source	AT20G source
30DorN	30 Doradus North	05:38:42.20	-69:06:02.90	✗	✗	✗	✗
30DorS	30 Doradus South	05:38:42.00	-69:06:12.90	✗	✗	✗	✗
LMC01	J054025.15–694012.1	05:40:24.80	-69:40:13.10	✗	PE	✗	✓
LMC02	J053945.94–693839.2	05:39:46.10	-69:38:38.00	✓	U	MDM 75	✓
LMC03	J053943.26–693854.6	05:39:43.20	-69:38:55.50	✓	U	✗	✗
LMC04	J053252.41–694220.1	05:32:52.30	-69:46:19.90	✓	PE	MDM 51	✗
LMC05	J053941.89–694612.0	05:39:41.60	-69:46:09.30	✓	PE	✗	✗

emission and also exhibit fine-structure emission (PE types, as described in Chapter 1) whilst the remaining two are classified as being of unknown nature but are still classed as definite YSOs by Gruendl & Chu (2009). This means that apart from the two fields in 30 Doradus, all of the targets in this data set are likely to contain YSOs.

6.2 Results

6.2.1 Continuum images and point source identification

Using the same procedure introduced in Chapters 3 and 4, polynomial functions were fitted to the spectrum at every spaxel in the data cubes to create continuum images. Separate images were created for the *H*-band and *K*-band with spectral ranges of 1.5365–1.7875 μm and 2.028–2.295 μm, respectively, matching the 2MASS photometric bands. The continuum images are shown in Fig. 6.2.

It is clear that the 30 Doradus South field is by far the most densely populated region, with the other FOVs exhibiting lower numbers of sources. All of the FOVs exhibit multiple continuum sources, which is expected given the original aim of the observations to study clusters of young stars and the extreme recent star formation activity of the region.

Point source identification

Point source identification was carried out using the IDL point source finding script *find.pro* from the IDLPHOT IDL adaptation of the FORTRAN aperture photometry package DAOPHOT. This was applied to the *K*-band continuum images as the main sources of interest in this work are typically brighter in the *K*-band than in the *H*-band. A total of 50 point sources have been selected in the seven $8'' \times 8''$ fields, 19 of which reside in 30DorS. Once the point sources were found, 2D Gaussian functions were fitted to them and an extraction radius was calculated as the FWHM of the Gaussian multiplied by 1.5. Spectra were then automatically extracted from all point sources using the standard SINFONI data reduction recipes with ESO's ESOREX data reduction software. The J2000 coordinates of all of the point sources are given in Table 6.2 and the positions and extracted regions for all sources are marked on the continuum images in Fig. 6.2. Note that some sources very near the edge of the fields (e.g. in the east of 30DorS) have not been extracted because the quality of the data is poor.

Some of the continuum images exhibit continuum emission other than the point sources listed in Table 6.2. These have been rejected based on either the roundness or the sharpness

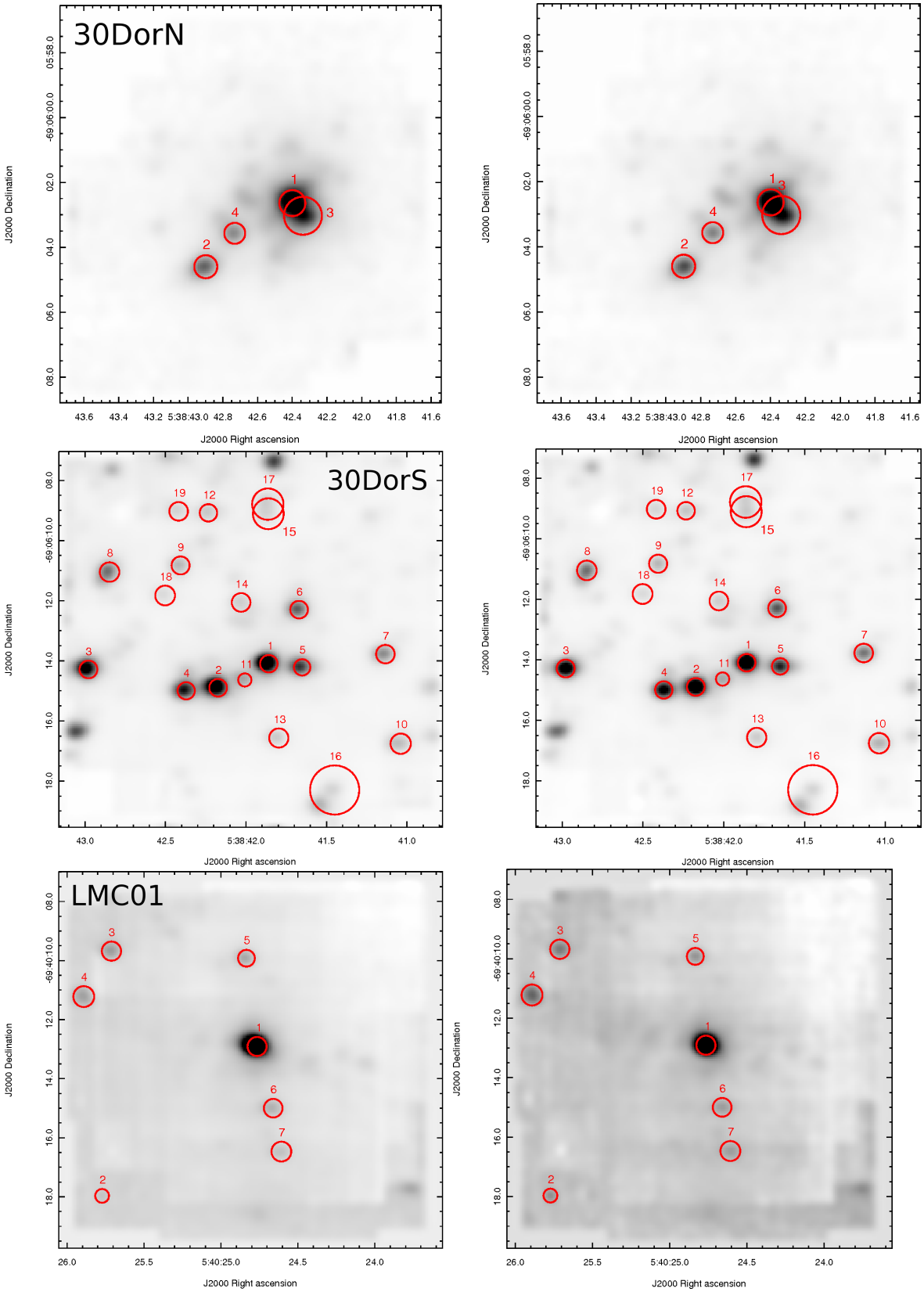

Figure 6.2: *H*-band (left) and *K*-band (right) continuum images for the fields 30DorN, 30DorS and LMC01.

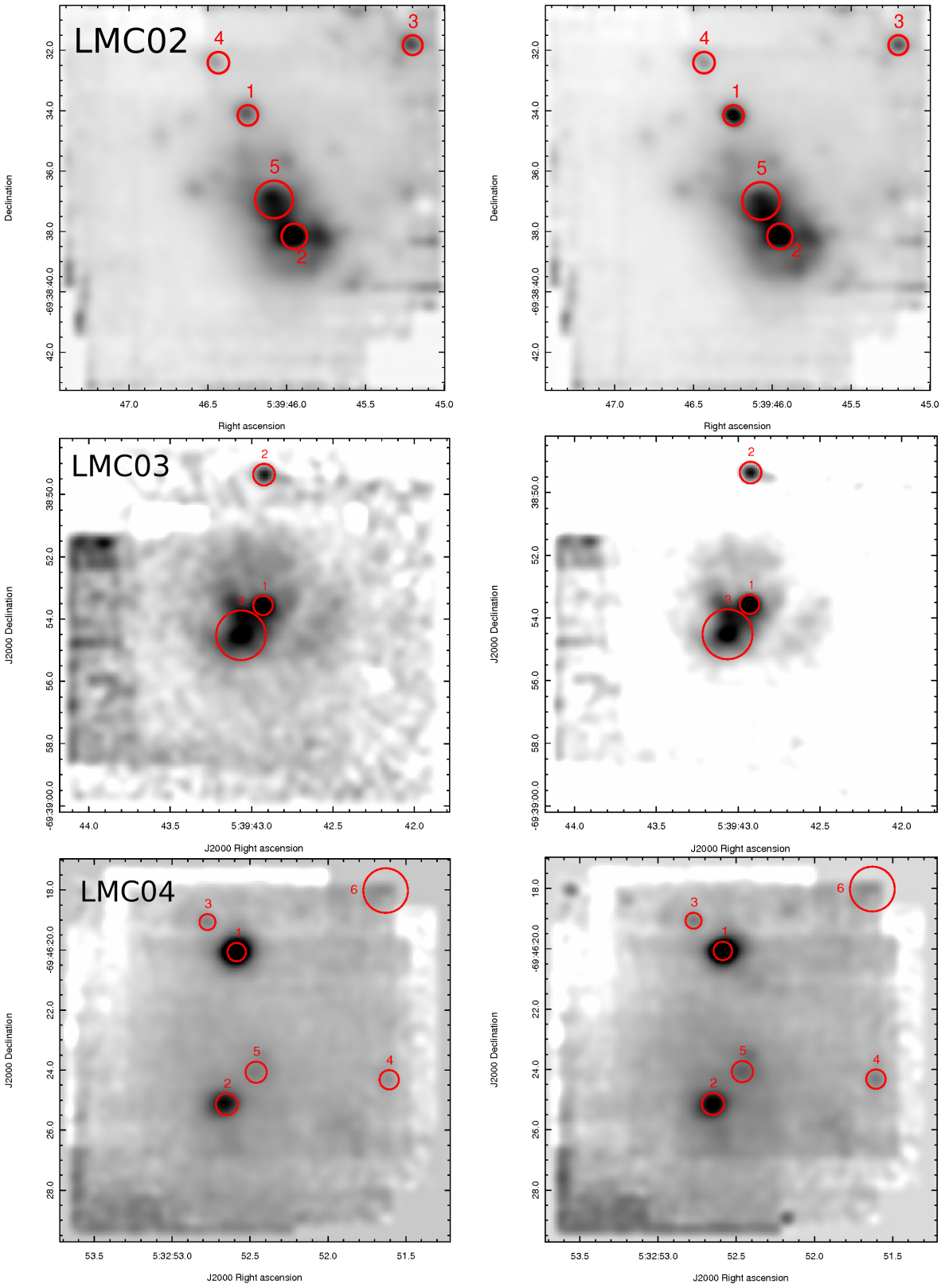

Fig. 6.2 cont. *H*-band (left) and *K*-band (right) continuum images for the fields LMC02, LMC03 and LMC04.

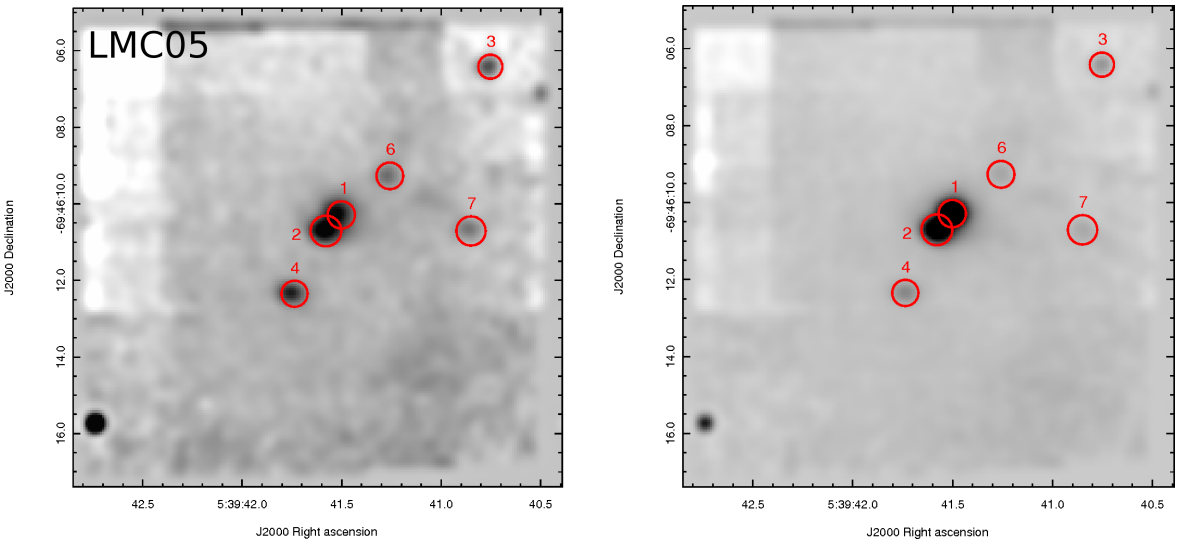

Fig. 6.2 cont. *H*-band (left) and *K*-band (right) continuum images for the field LMC05.

criteria in the IDLPHOT package. For the most part this emission appears to be the result of strong line emission in the regions causing a polynomial to be fitted where there is little or no continuum emission. As such only the sources listed in Table 6.2 will be treated as real continuum sources.

6.2.2 Extinction

Two methods are used to estimate the visual extinction towards the sources. The first is that used in Chapters 3 and 4 using the H_2 emission lines in the *K*-band,

$$A_V = -114 \log(0.704[I_{S1}/I_{Q3}]). \tag{6.1}$$

As discussed in Chapter 4, whilst largely insensitive to variations in temperature and density, this method utilises emission lines which lie in a region of relatively poor atmospheric transmission, increasing the uncertainty in observations with relatively low S/N. This method is dependent on strong H_2 emission which makes it ideal for early stage massive YSOs which exhibit strong bipolar outflows but impossible where no H_2 emission is present, for example in fully ionized environments.

The detection rate of H_2 emission towards this sample is low compared to that of the N113 sample and the SMC sample (Chapters 3 and 4 respectively). Moreover, where present, H_2 emission in this sample tends to be relatively weak towards continuum sources and using the lower resolution *H+K* grating, the Q-branch H_2 lines fall closer to the detector edge than when using the *K*-band grating. This has lead to an incomplete sample of extinctions towards continuum sources with large uncertainties using this method.

An alternative method for the calculation of extinctions is using the observed $H-K$ colours and imposing the assumption that the intrinsic colour of the source is that of an OB type star. The difference between the attenuated colour and the intrinsic colour can be used to calculate the extinction as in Cooper et al. (2013):

$$A_V = \frac{m_1 - m_2 + x_{int}}{0.55^{1.75}(\lambda_1^{-1.75} - \lambda_2^{-1.75})} \tag{6.2}$$

m_1 and m_2 are the apparent magnitudes at the wavelengths λ_1 and λ_2, respectively. The intrinsic colour, x_{int}, is assumed to be that of a B0 type star of H–K = –0.05 (Koornneef & Israel, 1985). Whilst this method was found to be unreliable using the IRSF photometry in Chapter 3 (due to the relatively low resolution of IRSF compared to that of SINFONI), the H+K grating on SINFONI allows the simultaneous acquisition of both the H- and K-band fluxes at the required spatial resolution. H- and K-band fluxes were measured for all sources from the extracted spectra and these were converted into magnitudes according to the CIT photometric system where the K-band zero point is at 620 Jy and for the H-band the zero point is 980 Jy.

Using this photometric method extinction estimates can be calculated towards every detected point source. Although this method assumes an intrinsic colour of a B0-type star, the $H-K$ colours of massive stars do not vary greatly: between an A0V type star and an O3V types the variation is only ±0.05 around the colour of a B0V type star (Cox, 2000), similar to the uncertainties in most of the measured colours.

The results of both extinction calculations are presented in Table 6.2. The mean extinction towards sources in the 30 Doradus regions is 6.7±0.3 mag with a median of 6.6 mag whilst in the other observed fields the mean is 14±2 and the median is 10.9. This implies that the majority of the sources in the 30 Doradus clusters are significantly less deeply embedded than those in the other regions, possibly indicative of more evolved clusters which have expelled much of the material surrounding the young stars.

6.2.3 Colour-magnitude diagram

Using the magnitudes presented in Table 6.2, the distance corrected magnitude (set to 10 pc) and the H–K colours were calculated for all sources and plotted in a colour-magnitude diagram shown in Fig. 6.3. Also shown are the colour-magnitude positions of massive YSOs from Cooper et al. (2013), Herbig AeBe candidates in the Magellanic Bridge from Nishiyama et al. (2007), pre-main sequence stars and YSOs in the star forming regions Sh2–152 and

Table 6.2: Positions of all continuum sources resolved with the LMC *H+K* SINFONI data as well as the *H*- and *K*-band magnitudes and extinctions calculated towards all continuum sources. The penultimate column gives the extinctions calculated with the photometric method whilst the final column gives the extinctions calculated using the *K*-band H_2 emission line ratio.

Field	Source	RA	Dec	H (mag)	K (mag)	$A_V(H–K)$	$A_V(H_2)$
30DorN	1	05:38:42.55	–69:06:02.1	11.20±0.01	10.77±0.02	6.6±0.4	
30DorN	2	05:38:42.73	–69:06:00.1	12.96±0.01	12.32±0.02	10.2±0.4	
30DorN	3	05:38:42.53	–69:06:01.7	11.11±0.01	10.66±0.02	6.9±0.4	
30DorN	4	05:38:42.67	–69:06:01.1	13.25±0.01	12.77±0.01	7.4±0.2	
30DorN	Avg					7.8±0.8	
30DorS	1	05:38:41.92	–69:06:12.5	13.72±0.02	13.39±0.01	4.8±0.4	
30DorS	2	05:38:42.04	–69:06:11.7	14.08±0.01	13.56±0.03	8.1±0.5	
30DorS	3	05:38:42.32	–69:06:12.3	14.10±0.02	13.67±0.02	6.6±0.5	
30DorS	4	05:38:42.11	–69:06:11.6	14.32±0.03	13.86±0.02	7.1±0.6	
30DorS	5	05:38:41.85	–69:06:12.4	14.53±0.03	14.14±0.04	5.9±0.9	
30DorS	6	05:38:41.86	–69:06:14.3	14.81±0.01	14.44±0.02	5.5±0.4	
30DorS	7	05:38:41.67	–69:06:12.8	15.24±0.01	14.68±0.03	8.8±0.5	
30DorS	8	05:38:42.28	–69:06:15.5	14.98±0.02	14.59±0.02	5.9±0.5	
30DorS	9	05:38:42.12	–69:06:15.8	15.79±0.02	15.40±0.04	5.9±0.8	
30DorS	10	05:38:41.63	–69:06:09.8	15.84±0.02	15.35±0.03	7.6±0.6	
30DorS	11	05:38:41.98	–69:06:11.9	16.46±0.02	15.96±0.03	7.8±0.6	
30DorS	12	05:38:42.06	–69:06:17.5	15.97±0.02	15.58±0.04	5.9±0.8	
30DorS	13	05:38:41.90	–69:06:10.0	16.20±0.02	15.77±0.03	6.6±0.6	38±16
30DorS	14	05:38:41.98	–69:06:14.5	16.10±0.02	15.77±0.03	4.8±0.6	
30DorS	15	05:38:41.93	–69:06:17.5	15.01±0.01	14.53±0.03	7.4±0.5	
30DorS	16	05:38:41.78	–69:06:08.3	14.55±0.02	14.21±0.05	5.0±0.9	
30DorS	17	05:38:41.93	–69:06:17.8	14.92±0.02	14.52±0.02	6.1±0.5	
30DorS	18	05:38:42.15	–69:06:14.8	16.59±0.02	16.13±0.05	7.1±0.9	
30DorS	19	05:38:42.12	–69:06:17.6	16.31±0.03	15.93±0.04	5.7±0.9	
30DorS	Avg					6.5±0.3	
LMC01	1	05:40:24.79	–69:40:13.8	14.42±0.01	14.10±0.03	4.7±0.6	<27
LMC01	2	05:40:25.14	–69:40:08.8	20.42±0.50	19.68±1.64	12±30	
LMC01	3	05:40:25.12	–69:40:17.0	16.95±0.05	16.56±0.10	5.9±1.9	13±12
LMC01	4	05:40:25.18	–69:40:15.5	17.35±0.08	15.88±0.08	24.6±2.0	<12.4
LMC01	5	05:40:24.82	–69:40:16.8	16.97±0.04	16.52±0.07	6.9±1.4	<45
LMC01	6	05:40:24.76	–69:40:11.7	17.14±0.03	16.78±0.06	5.4±1.2	
LMC01	7	05:40:24.74	–69:40:10.3	17.80±0.05	16.85±0.10	15.6±1.9	
LMC01	Avg					10.7±2.8	
LMC02	1	05:39:46.24	–69:38:39.4	16.40±0.04	14.76±0.03	27.5±0.9	<22
LMC02	2	05:39:46.13	–69:38:35.4	14.64±0.02	13.90±0.02	11.9±0.5	<8
LMC02	3	05:39:45.87	–69:38:41.7	16.56±0.07	15.54±0.06	16.8±1.6	
LMC02	4	05:39:46.30	–69:38:41.1	17.52±0.20	16.47±0.28	17.3±6.0	
LMC02	5	05:39:46.08	–69:38:36.9	14.27±0.03	13.42±0.07	48±1	
LMC02	Avg					24.4±6.5	
LMC03	1	05:39:42.98	–69:38:54.6	14.99±0.03	14.52±0.06	7.3±1.2	
LMC03	2	05:39:42.98	–69:38:58.8	15.19±0.03	14.99±0.08	3.0±1.5	
LMC03	3	05:39:43.03	–69:38:53.6	13.48±0.08	12.64±0.04	13.7±1.6	
LMC03	Avg					7.8±3.2	
LMC04	1	05:32:52.51	–69:46:26.4	12.91±0.04	12.51±0.03	6.1±0.9	
LMC04	2	05:32:52.53	–69:46:21.3	14.67±0.02	14.06±0.03	9.7±0.6	<12
LMC04	3	05:32:52.57	–69:46:27.4	16.42±0.06	15.97±0.07	6.9±1.6	<16
LMC04	4	05:32:52.17	–69:46:22.1	16.92±0.08	16.09±0.09	13.5±2.1	<6
LMC04	5	05:32:52.47	–69:46:22.4	16.31±0.07	15.54±0.06	12.5±1.6	6±4
LMC04	6	05:32:52.18	–69:46:28.4	16.73±0.26	16.25±0.59	7±11	35±14
LMC04	Avg					9.3±1.3	
LMC05	1	05:39:41.58	–69:46:11.5	15.16±0.02	12.70±0.03	41.7±0.6	23±9
LMC05	2	05:39:41.61	–69:46:11.1	14.30±0.02	12.37±0.03	32.5±0.6	14±7
LMC05	3	05:39:41.32	–69:46:15.4	15.51±0.04	14.83±0.11	10.9±2.0	
LMC05	4	05:39:41.66	–69:46:9.4	15.23±0.03	14.87±0.04	5.4±0.9	16±4
LMC05	6	05:39:41.50	–69:46:12.5	15.90±0.03	15.38±0.06	8.1±1.2	9±7
LMC05	7	05:39:41.35	–69:46:11.1	15.46±0.04	15.08±0.14	5.7±2.5	
LMC05	Avg					17.4±6.4	

Sh2–157 from Chen et al. (2009b). The expected main sequence is also plotted for stars of spectral types from B0V to O3V (Cox, 2000) as well as a main sequence which has been reddened according to the median extinction measured towards sources in the two 30 Doradus regions (6.6 mag).

It appears that the majority of the detected sources exhibit colours consistent with reddened main sequence stars and Herbig AeBe stars. Many of the sources appear to lie at the expected colours for reddened main sequence but appear brighter than expected. Given the high incidence of binary systems amongst massive stars, it is likely that many of these sources are systems consisting of multiple massive stars which would account for some of the excess emission.

16 of the continuum point sources fall within the colour range of the Galactic massive YSO sample of Cooper et al. (2013) with $H-K > 0.6$ mag. These sources probably represent the most embedded in the sample and are therefore likely to be in the earliest evolutionary phases including massive YSOs, UCHIIs and compact H II regions. This colour cut of $H-K > 0.6$ mag will therefore be imposed, rejecting the sources which do not meet this criterion and leaving the 16 massive YSO candidates.

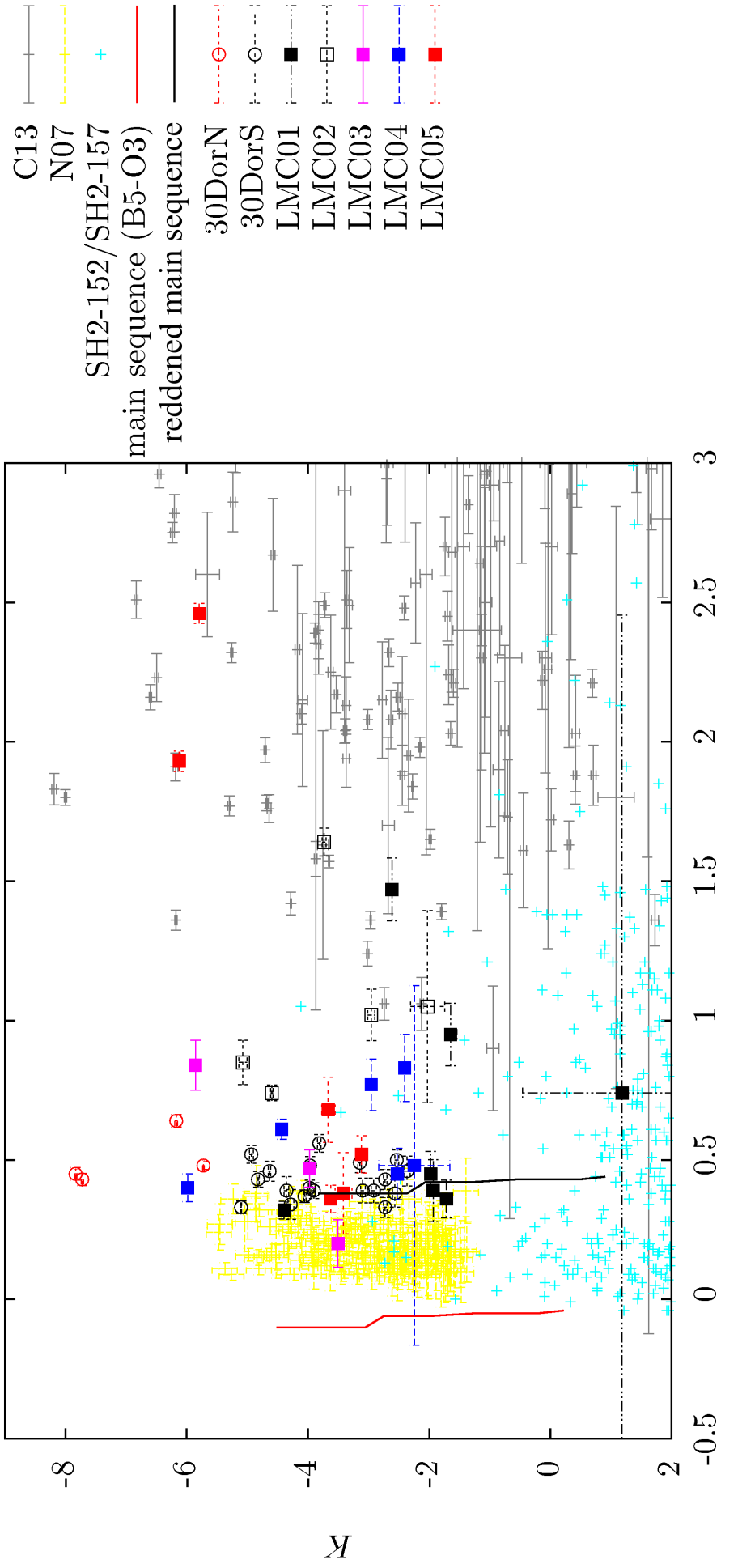

Figure 6.3: Colour-magnitude diagram for all sources from the SINFONI archival data. Also shown are sample data for comparison. C13 – massive YSOs from Cooper et al. (2013). N07 – Herbig AeBe candidates in the Magellanic bridge from Nishiyama et al. (2007). SH2-152/SH2-157 – pre-main sequence stars and YSOs from Chen et al. (2009b). Also shown are the main sequence from B5 to O3 spectral types colours/magnitudes from spectral type O9.5 to O3 (red line) and the main sequence reddened by the median extinction towards the 30 Doradus fields: $A_V = 6.6$ mag (black line).

6.2.4 Spectral features

The emission lines examined in this section are marked on the $H+K$ spectra for all continuum sources in Fig. D.8 and the measured emission line fluxes are shown in Table E.4 (Brackett series), E.5 (H_2 emission) and E.6 (He I and Fe II emisson).

H I emission

Brγ is the most frequently detected emission feature in this sample. As described in previous chapters, Brγ emission is one of the most commonly used tracers of accretion towards massive YSOs. It is worth re-iterating that Brγ emission is not unique to accreting objects and can be sourced in stellar and disc winds as well as from the direct photo-excitation of gas by stellar photons.

The extinction corrected Brγ emission line luminosity is plotted versus the absolute K-band magnitude for all of the $H-K$ colour selected YSO candidates in Fig 6.4 along side the N113 data from Chapter 3, the SMC data from Chapter 4 and the Galactic data from Cooper et al. (2013). As in Chapter 4 the CENKEN function of the R NADA library was used to fit a line to the LMC data of the form $y = 10^{mx+c}$ yielding the following relation:

$$\log(L^{LMC}_{Br\gamma}) = (-0.40 \pm 0.02)K - (2.01 \pm 0.15) \tag{6.3}$$

These can be compared to the previously obtained fits for the Galactic an SMC samples:

$$\log(L^{MW}_{Br\gamma}) = (-0.37 \pm 0.01)K - (2.69 \pm 0.03) \tag{6.4}$$

$$\log(L^{SMC}_{Br\gamma}) = (-0.39 \pm 0.05)K - (2.5 \pm 0.3) \tag{6.5}$$

In Brγ vs K. the LMC sample appears to fall above the Galactic massive YSO sample and within the scatter of the SMC sample but certainly tends towards the high end of the SMC range. The ATS regression fitted to the LMC sample falls higher than that fitted to the SMC sample, with a similar gradient but higher y-intercept.

Although there are no massive YSO candidates selected in the 30DorS region, for completeness the integrated flux maps and line centroid velocity maps of all seven regions will be analysed. In the 30 Doradus fields there appears to be two components of the Brγ emission: a narrow, ambient emission line component common to the region (although with spatially varying flux) and a much broader component which is only present towards some of the con-

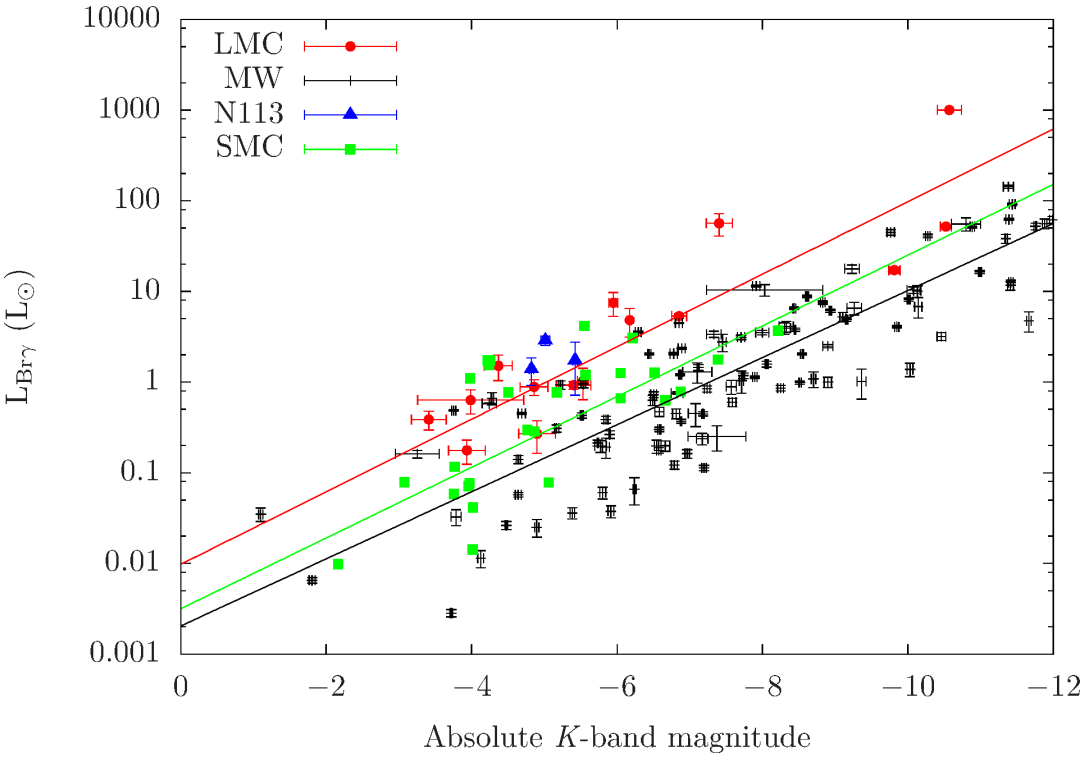

Figure 6.4: Brγ emission versus absolute K-band magnitude. The solid lines represent the ATS regressions fitted to the respective data of the same colour.

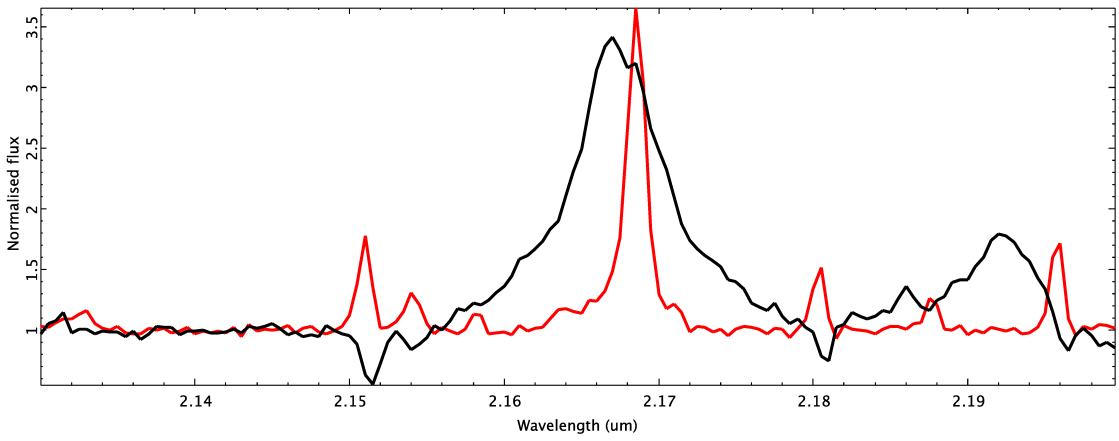

Figure 6.5: The Brγ emission line profiles for source #01 (black) in the 30 Doradus North field and that that extracted from a region away from any continuum source in the same field (red). The nebulous emission was normalised to the background level and the continuum source was divided by the continuum level and then exaggerated by a factor of 6 (i.e. multiplied by 6 and then subtracted 5).

tinuum sources. For comparison two normalised spectra are plotted together in Fig. 6.5, one of which is for 30DorN-1 (black) and the other is extracted from a region in 30DorN with no continuum source (red). Measurements of the emission detected towards the continuum sources minus the measured ambient narrow emission reveal that the narrow component typically contributes less than 10% of the total combined line fluxes. This is the case for the *H*-band Brackett series emission as well.

The widths of the Gaussian functions fitted to the line profiles are 3.5±0.1 nm (480±10 km s^{-1}) and 0.68±0.06 nm (94±8 km s^{-1}) for the on–source and nebulous emission respectively. The emission line centroids are offset, with the narrow line emission red-shifted with respect to the broader emission with velocities of 180±10 km s^{-1} and 340±8 km s^{-1} for the on-source emission and nebulous emission, respectively. Mean velocities towards massive stars in the 30 Doradus region have been previously determined to be in the region of ∼270 km s^{-1} (e.g. Bressert et al. 2012 and Kalari et al. 2014) but a very massive star in 30 Doradus has been found to have a radial velocity of up to 315±15 km s^{-1} (Bestenlehner et al. 2011). It is therefore possible that both the stars and the background emission in these fields are associated with 30 Doradus but that they are significantly displaced with respect to one another along the line of sight.

The integrated line flux maps for the 30DorN and 30DorS fields are shown in Fig. 6.6 with the broad and narrow emission line components separated. Whilst the broad Brγ emission appears to be relatively compact, the narrow emission spans the entirety of the fields and exhibits relatively complex filamentary structure in 30DorS although the peak emission fluxes appear to be outside our FOV in both cases. It is also clear from these flux maps that the narrow component is consistently weaker than the broad component by around an order of magnitude. It is likely that the observed stars lie in front of the narrow component of the emission whilst the broad component represents a smaller spatial scale, more turbulent region of gas excited by the stars themselves. If the stars are actively expelling excited gas then that could also explain the blue-shift of the broad component with respect to the mean stellar velocity in 30 Doradus.

The Brγ integrated flux maps for the remaining five fields are shown in Fig. 6.7. LMC01 exhibits an elongated Brγ morphology with two almost parallel strongly emitting linear structures amidst a more extended region of weaker emission. Sources LMC02, LMC03 and LMC04 all exhibit morphologies consistent with compact H II regions. Finally LMC05 exhibits compact Brγ emission centred on the continuum sources and a large extended emission region

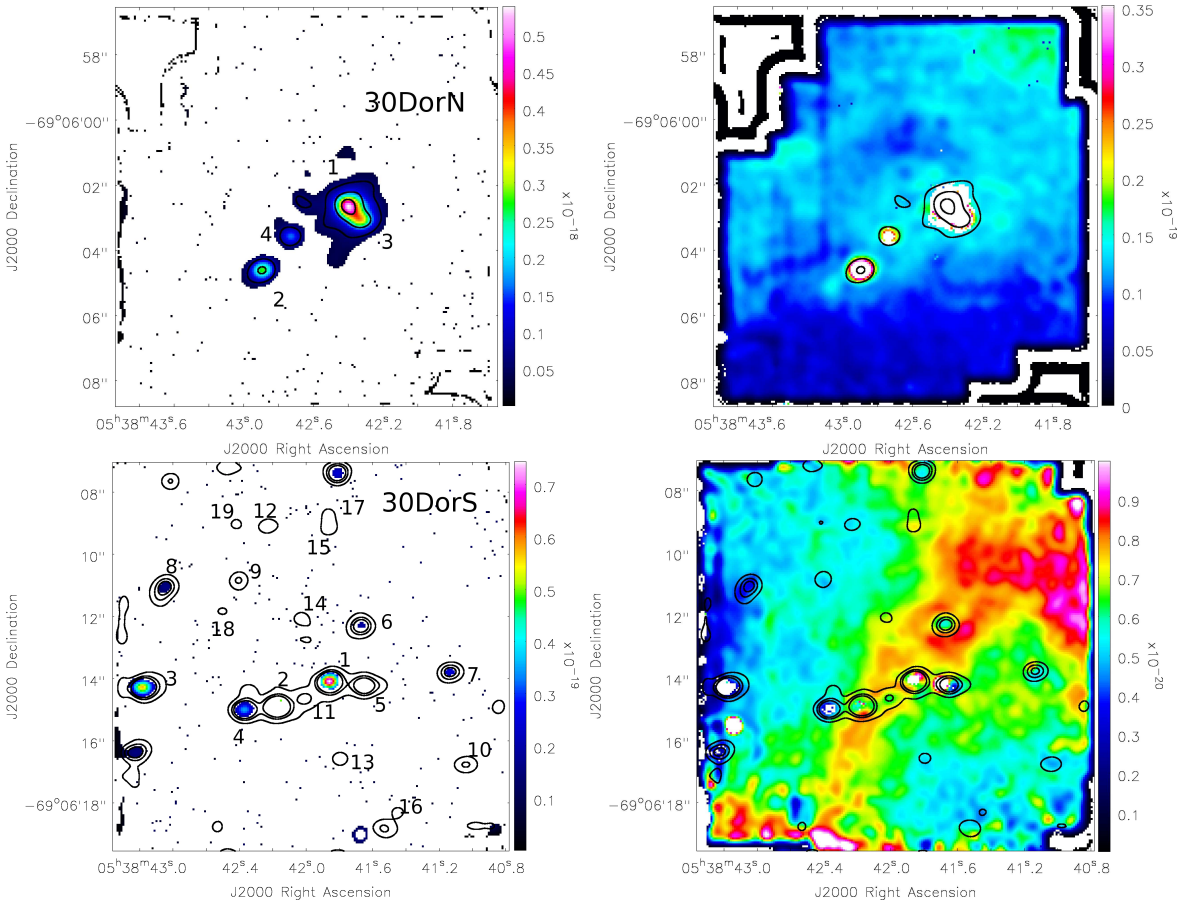

Figure 6.6: Brγ emission line integrated flux maps for the 30 Doradus fields. Left: broad component, right: narrow component (see text for details). Black contours: continuum emission.

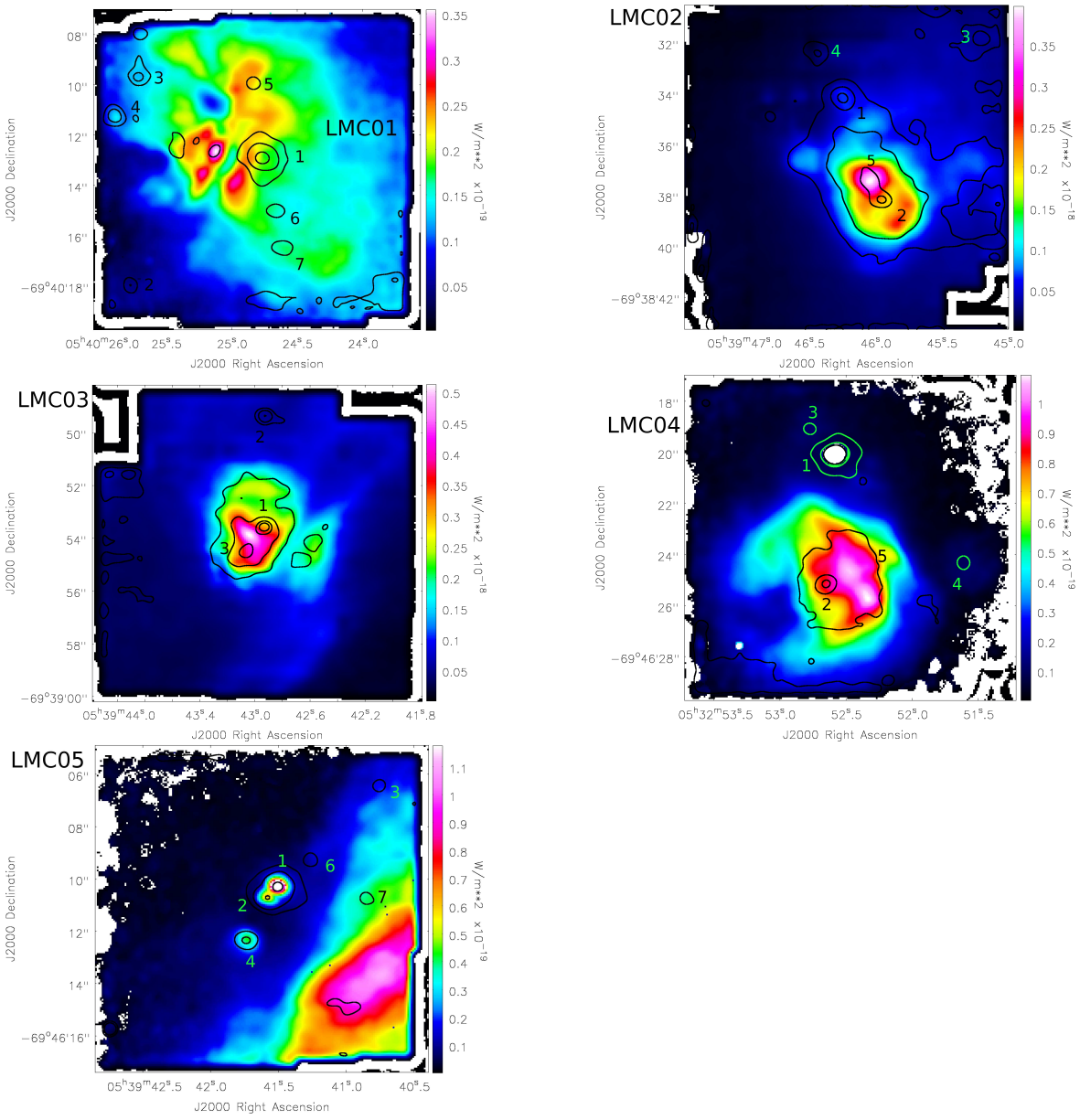

Figure 6.7: Brγ emission line integrated flux maps. Black contours: continuum emission ([0.25,0.5,0.75]$\times$ peak).

towards the south-west in which the peak flux is apparently outside the FOV.

The Brγ emission line velocity maps are shown in Fig. 6.8. For the 30 Doradus regions these maps are for the spatially extended narrow component rather than the broad compact component. These maps are directly analogous to those shown in Chapters 3 and 4 although the FOVs are significantly larger and the lower spectral resolution means that the uncertainties in the line centroid velocities are typically 8–9 km s^{-1} rather than $\sim$4 km s^{-1}. Clear velocity gradients are observed across the regions of the highest Brγ flux in sources LMC01 and LMC04 which are likely to be symptomatic of an expanding ionised medium surrounding young massive stars. Both of the 30 Doradus regions appear to exhibit slightly red-shifted emission in the brightest regions of the H I emission. Sources LMC02 and LMC03 exhibit rel-

atively clumpy velocity structures, possibly indicative of a turbulent clumpy medium. There appears to be little if any significant variation in the line centroid velocity across the LMC05.

Figure 6.9 shows the distance corrected Br10 emission line luminosity against the distance corrected Brγ emission line luminosity for the $H-K$ colour-selected YSO candidates and the Milky Way sample of Cooper et al. (2013). Also shown is the expected emission line ratio for a massive YSO with a temperature of 7500 K and a density of $10^6\,\mathrm{cm}^{-3}$ (Storey & Hummer, 1995) and the ratio for completely optically thick emission (i.e. a blackbody distribution). The Br10 emission is strongly correlated with the Brγ emission as expected. The majority of the sources fall within the scatter observed in the Milky Way sample with the exception of some of the brightest LMC sources.

ATS regressions have also been fitted to the Br10 versus Brγ data using the form $y = mx + c$. For the most part the ATS regression fitted to the LMC sample is very similar to the Galactic sample:

$$L_{\mathrm{Br10}}^{\mathrm{MW}} = (0.96 \pm 0.01) L_{\mathrm{Br}\gamma} - (0.47 \pm 0.02) \tag{6.6}$$

$$L_{\mathrm{Br10}}^{\mathrm{LMC}} = (0.93 \pm 0.02) L_{\mathrm{Br}\gamma} - (0.34 \pm 0.02) \tag{6.7}$$

where $L_{\mathrm{Br10}}^{\mathrm{MW}}$ and $L_{\mathrm{Br10}}^{\mathrm{LMC}}$ represent the Br10 luminosity for the Galactic and LMC samples respectively. This suggests that the LMC sample of YSO candidates does contain comparable sources to those of the Galactic sample.

He I emission

As discussed in earlier chapters, He I emission tends to be associated with the later evolutionary stage massive YSOs and compact H II regions where the central star has become hot enough to drive strongly ionizing stellar winds. The plot of He I 2.059 μm emission line flux versus the K-band magnitude is shown in Fig. 6.10.

In stark contrast to the sample of SMC YSOs presented in Chapter 4, the embedded cluster candidate sources in the LMC tend to exhibit significantly higher He I emission line fluxes as well as an excess in Brγ emission. This result is discussed in Section 6.3.2.

Figures 6.11 and 6.12 show the He I 2.0587 μm emission integrated flux and relative velocity maps respectively. Due to the low S/N of He I emission in the LMC05 field, computing a relative velocity map with uncertainties less than $10\,\mathrm{km\,s}^{-1}$ for this region was not possible. The extended He I emission tends to trace the same morphological structures and large scale velocity gradients exhibited in the Brγ emission, indicative of a common source of excitation

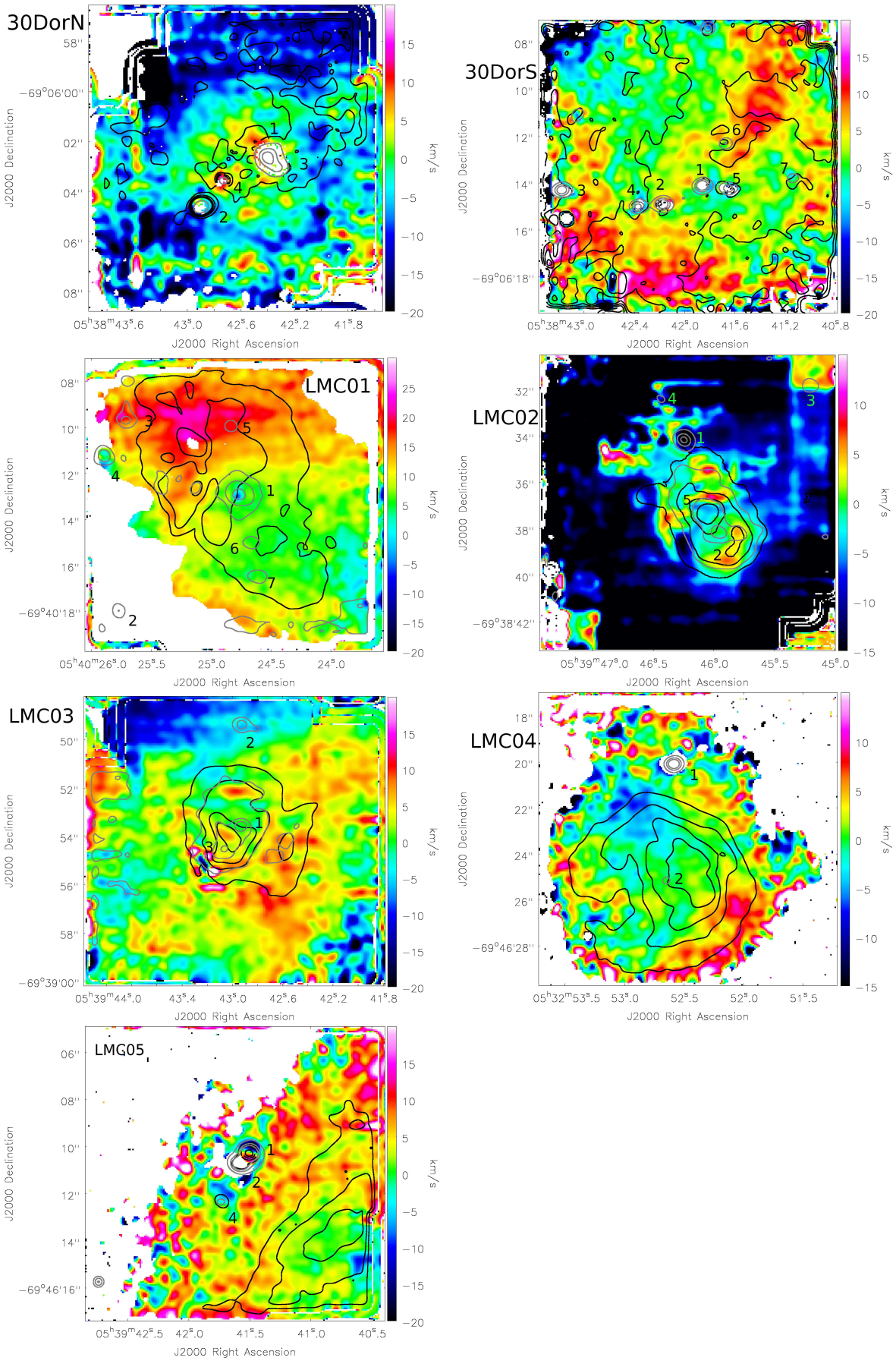

Figure 6.8: Velocity maps for all extended Brγ emission. All measured line centroid velocity uncertainties are in the range 5–10 km s^{-1}.

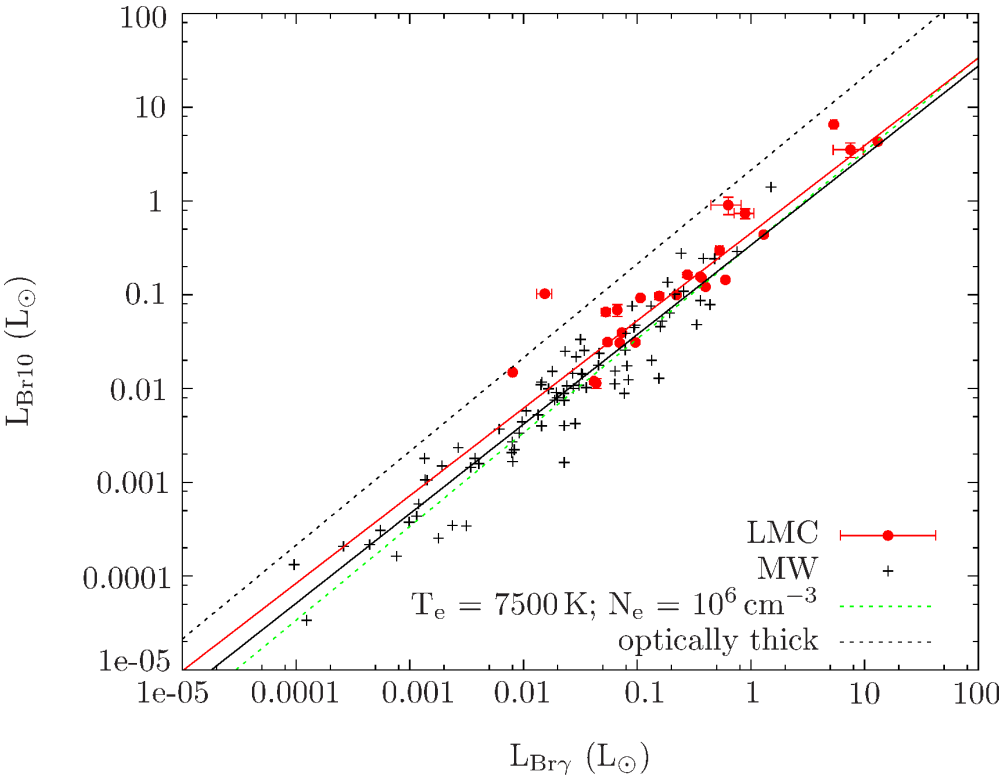

Figure 6.9: Br10 emission versus Brγ emission for the LMC sample (red) and the Galactic sources from Cooper et al. (2013, black). Also shown are the ATS regressions fitted to the data in red and black respectively as well as the optically thick emission line (black dashed line) and the expected ratio line for YSOs at with an effective temperature of 7500 K and electron density of $10^6\,cm^{-3}$ (green line, see text for details).

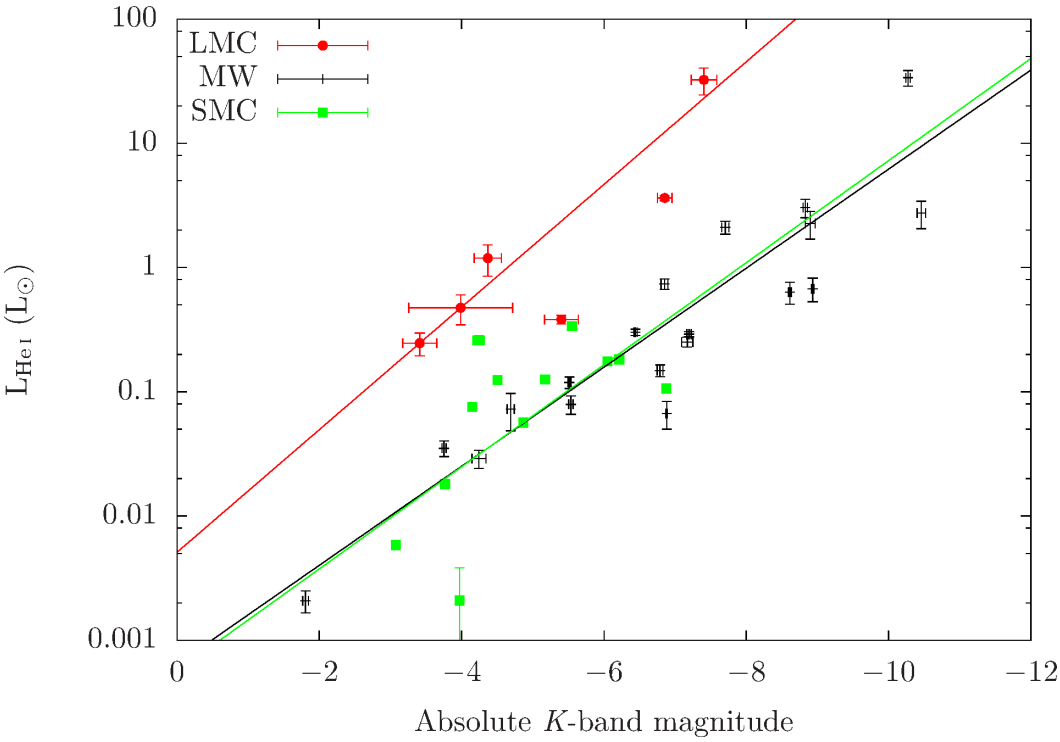

Figure 6.10: He I 2.0587 μm emission versus absolute K-band magnitude for the LMC (red), SMC (green) and Galactic (black) samples along with the respective ATS regressions fitted to each sample.

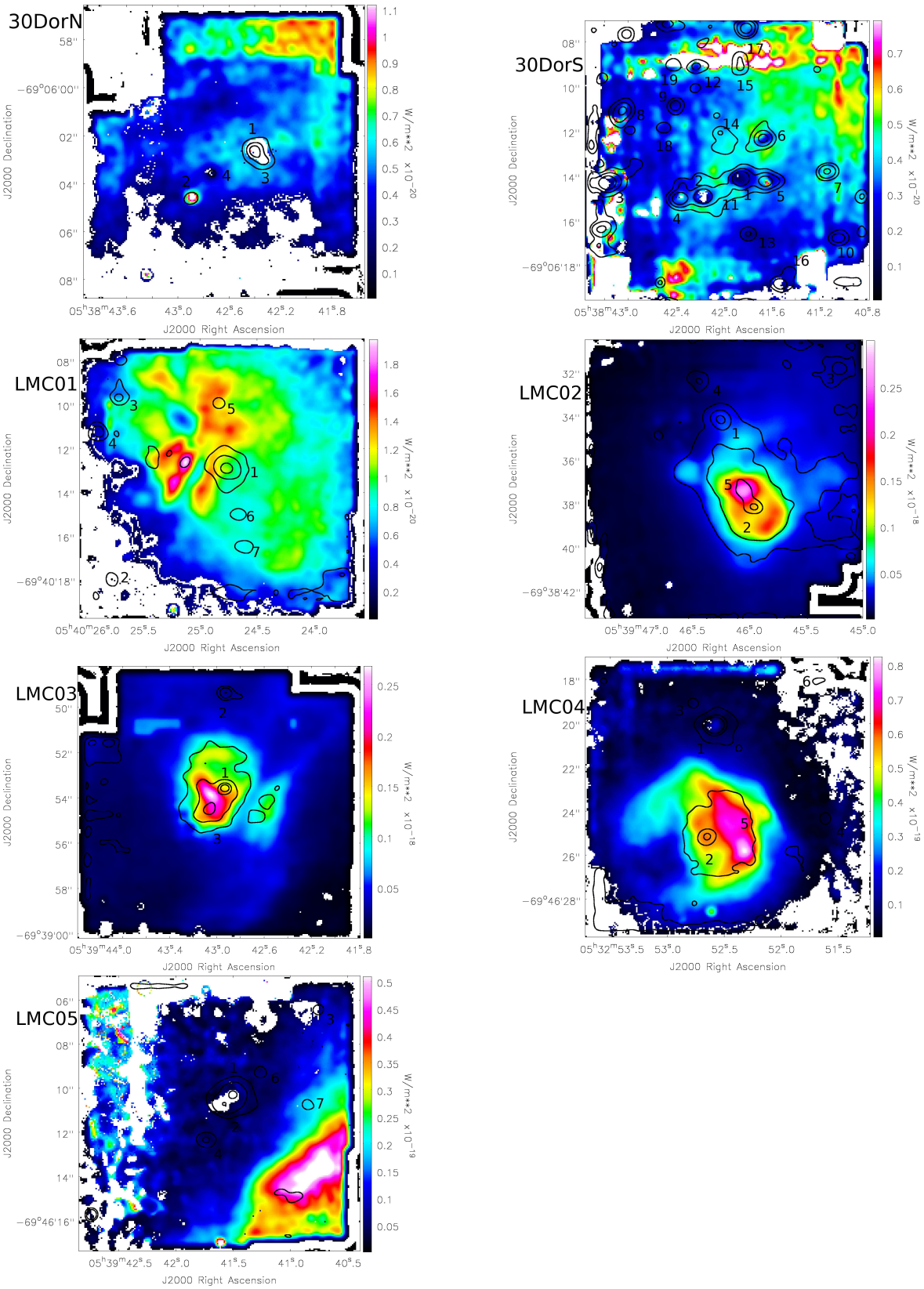

Figure 6.11: He I 2.0587 μm integrated flux maps. Black contours show [0.25,0.5,0.75]$\times$ maximum continuum emission.

for these sources.

H_2 and [Fe II] emission

H_2 emission lines and forbidden [Fe II] emission lines are both associated with shock fronts as a result of outflows (Lumsden, Puxley & Doherty, 1994; Porter, Drew & Lumsden, 1998; Cooper et al., 2013). As mentioned previously, the detection rate of H_2 emission is low and where present it is relatively weak. As in Chapters 3 and 4 it is expected that any massive YSO spectrum in which the H_2 2.1218 μm emission line is dominant over the Brγ emission line is likely to be a relatively young source. Hence H_2 1-0S(1) emission versus Brγ emission is plotted in Fig. 6.13, analogous to Figs. 3.8 and 4.8. As Fig. 6.13 shows, none of the colour selected YSO candidates in this sample with both H_2 and Brγ emission lines exhibit an H_2 flux greater than the Brγ flux.

The observed H_2 emission line ratios can be compared to those expected from photo-excitation and shocked emission models. As discussed in previous chapters, this cannot definitively give the nature of the emission but may provide a useful indication of a likely source of the emission. In general the H_2 emission lines measured towards the LMC targets are relatively faint so only the brightest emission lines (excluding the Q-branch) are used in this analysis. Table 6.3 shows the 1–0S(0) / 1–0S(1) and the 2–1S(1) / 1–0S(1) emission line ratios for all sources in which they are detected. Also shown are the expected H_2 emission line ratios for photo-excitation and shocked excitation mechanisms at a range of temperatures. The final column indicates whether the emission is more consistent with photo-excited or shocked emission where this can be determined from the H_2 line ratios. LMC02-2 exhibits H_2 emission line ratios which appear to be fully consistent with shocked excitation. Sources LMC02-4, LMC03-3 and LMC05-1 exhibit H_2 emission which is consistent with photo-excitation whilst the measurements towards the remaining sources are inconclusive.

The integrated flux maps for the H_2 1–0S(1) emission line in all seven fields are shown in Fig 6.14. In 30DorN the H_2 emission appears to be largely ambient and unlikely to be directly excited by the point sources which all appear to be foreground with respect to the H_2 emission. In the LMC03 region, the strongest H_2 emission at the north-eastern edge of the field could be an artefact caused by the stacking of multiple dithered positions or it could be a real feature which peaks outside the observed region. Towards the west a curved structure is traced by H_2 emission, possibly indicative of the edge of a bubble but it also appears slightly forked so it could be a slightly edge-on forked filamentary structure. LMC01

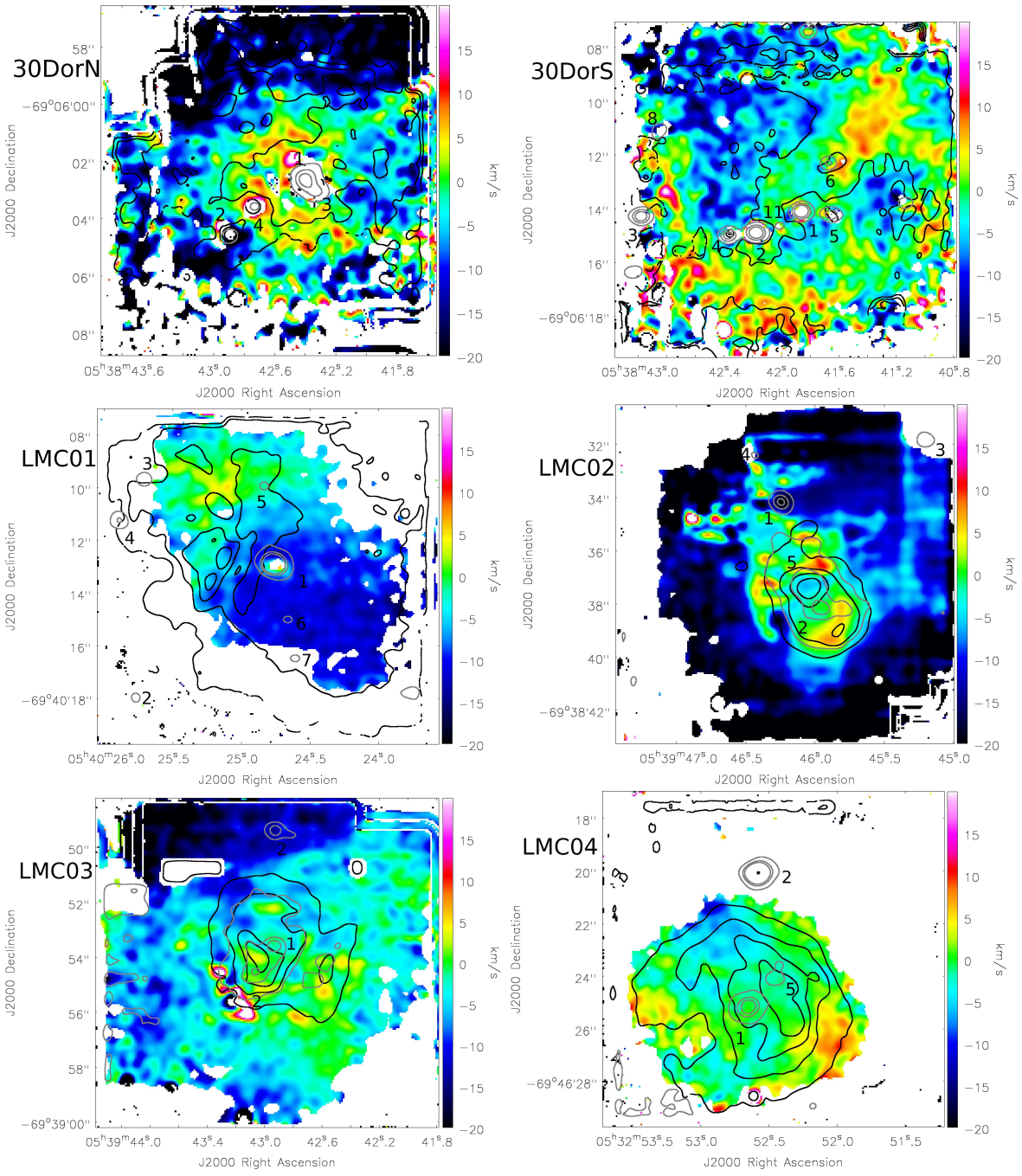

Figure 6.12: He I 2.059 μm relative velocity maps. Black contours show [0.2,0.4,0.6,0.8]$\times$ maximum He I line flux. Grey contours show [0.25,0.5,0.75]$\times$ maximum continuum emission.

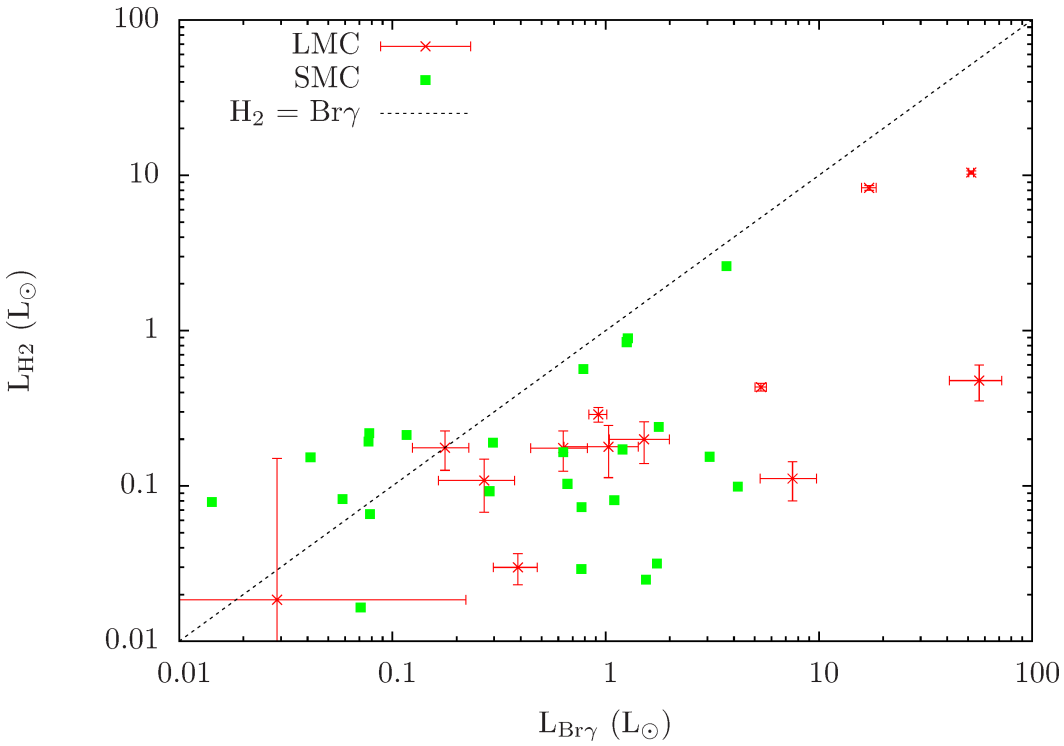

Figure 6.13: H_2 2.1218 μm emission versus Brγ emission for SMC and LMC sources. The dotted line indicates H_2 =Brγ.

Table 6.3: Extinction corrected H_2 1–0S(0) and 2–1S(1) emission line ratios with respect to the 2.1218μm 1-0S(1) emission line. The final column gives the nature of the emission as determined from these line ratios where applicable. Also shown are the model emission line ratios from Black & van Dishoeck (1987) and Shull & Hollenbach (1978) as in Chapters 3 and 4.

Field	Source	1-0S(0) 2.2235 μm	2-1S(1) 2.2477 μm	origin
LMC01	2	<0.41	$0.46^{+0.27}_{-0.34}$	
LMC01	4	$0.33^{+0.08}_{-0.06}$		
LMC01	7	$0.90^{+0.33}_{-0.35}$		
LMC02	1		0.37±0.05	
LMC02	2	$0.29^{+0.10}_{-0.14}$	$0.24^{+0.06}_{-0.11}$	shocked
LMC02	4	$0.63^{+0.28}_{-0.30}$		photo-excited
LMC02	5	0.3±0.2		
LMC03	3	$0.62^{+0.20}_{-0.27}$		photo-excited
LMC04	2	$0.44^{+0.10}_{-0.25}$	$0.29^{+0.07}_{-0.16}$	
LMC04	4	$0.54^{+0.11}_{-0.25}$	$0.38^{+0.12}_{-0.18}$	
LMC04	5	$0.43^{+0.10}_{-0.21}$	$0.34^{+0.07}_{-0.17}$	
LMC05	1	0.55±0.07		photo-excited
LMC05	2	0.32±0.03	$0.26^{+0.03}_{-0.02}$	
Photoexcitation		0.4–0.7	0.5–0.6	
1000 K shock		0.27	0.005	
2000 K shock		0.21	0.083	
3000 K shock		0.19	0.21	
4000 K shock		0.19	0.33	

exhibits a filamentary H_2 emission line morphology which coincides with the Brγ filament to the east of LMC01-1 whilst in LMC05 and 30DorS the H_2 emission appears to be filamentary in structure but unrelated to the Brγ emission. The remaining fields (LMC02 and LMC04) exhibit clumpy filamentary structures with typical widths of 0.1–0.2 pc (0.4–0.8 arcsec), many of which appear to trace the edges of Brγ and He I emission structures. Some of the clumps appear to be coincident with continuum sources (e.g. LMC04-2) whilst other sources (e.g. LMC04-1) appear to be located in a gap in the H_2 emission structure.

Figure 6.15 shows the line centroid relative velocity maps for the H_2 2.1218 μm emission shown in Fig. 6.14. This was only possible for four of the seven fields due to poor S/N in the H_2 emission and because of the low resolution line centroid velocities could only be determined with uncertainties in the range 8–10 km s^{-1}. As in the previous section spaxels for which the velocity uncertainty is greater than 10 km s^{-1} have been masked. For the large scale structures relatively little can be constrained from the velocity fields. In the LMC01 field the H_2 emission to the West of the central source appears to be significantly red-shifted with respect to the emission to the east, suggesting that these two structures may not be directly related to one another.

Given the low probability of photo-excited forbidden [Fe II] transitions, where it is detected it is more than likely indicative of a shocked excitation mechanism such as the boundary of outflows, strong stellar winds or H II regions and the surrounding ISM. If it is indeed associated with outflows, then it may well be an indication of relatively early stage massive YSOs which produce collimated bipolar outflows. [Fe II] emission is definitely detected towards six sources (LMC02-1, LMC02-2, LMC02-5, LMC05-1, LMC05-2 and LMC05-4) and tentatively detected towards a further six sources (see Table 6.4).

The [Fe II] integrated flux maps are shown for the two fields which show significant [Fe II] 1.644 μm emission in Fig. 6.16. In the LMC05 field the [Fe II] emission is largely confined to a region surrounding LMC05-4. In LMC03 the forbidden [Fe II] emission is extended and appears to have a significant peak in the West, near but not coincident with the H_2 region in the west of the field. There also appears to be a peak at LMC03-3. Due to the weak nature of the [Fe II] lines it was not possible to compute any centroid velocity maps.

CO bandhead and Fe II emission

The CO bandhead in emission, associated with discs in massive YSOs (as discussed in Chapters 3 and 4) is not found towards any of the sources in this sample. There are however four

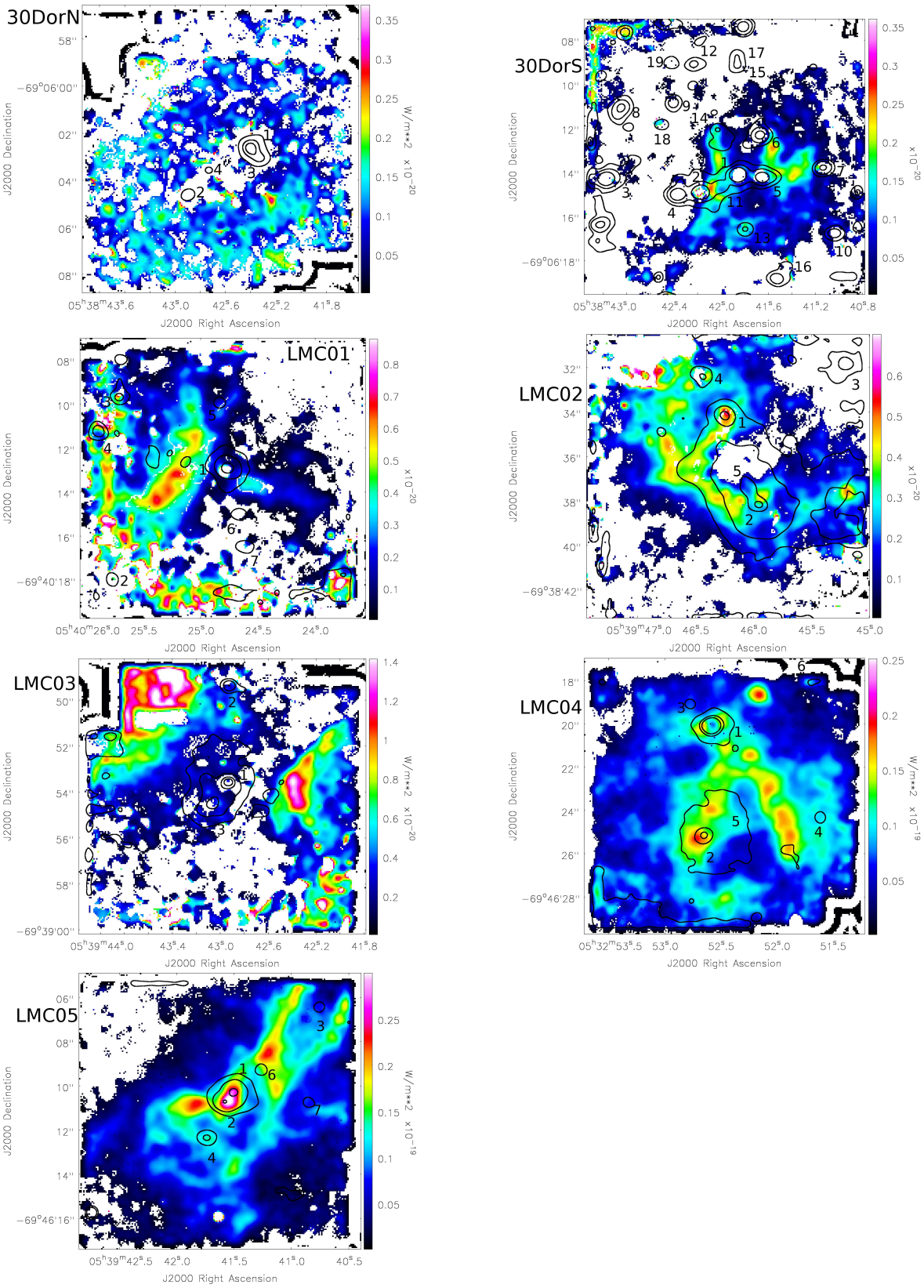

Figure 6.14: H_2 2.1218 μm integrated flux maps. Black contours show [0.25,0.5,0.75]× maximum continuum emission.

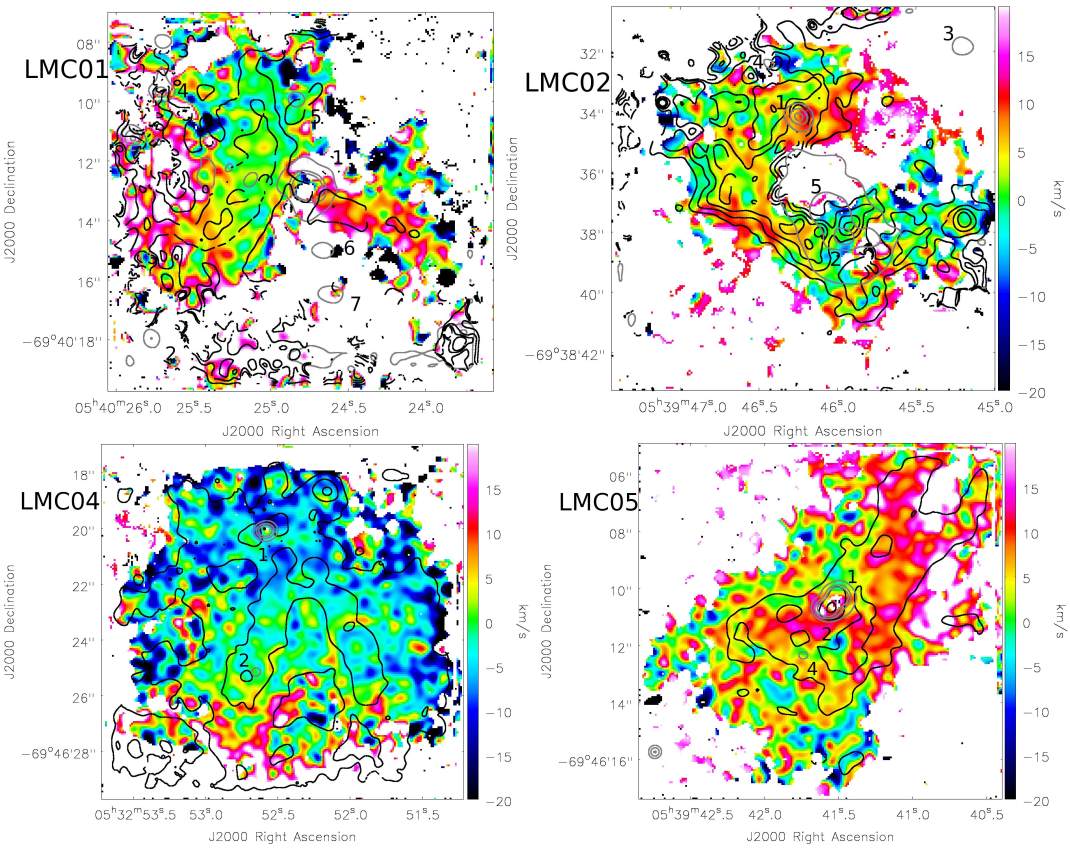

Figure 6.15: H_2 relative velocity maps. The S/N ratios in the 30 Doradus fields and LMC03 are insufficient to accurately measure centroid velocities. Black contours show [0.2,0.4,0.6,0.8]× maximum H_2 line flux. Grey contours show [0.25,0.5,0.75]× maximum continuum emission.

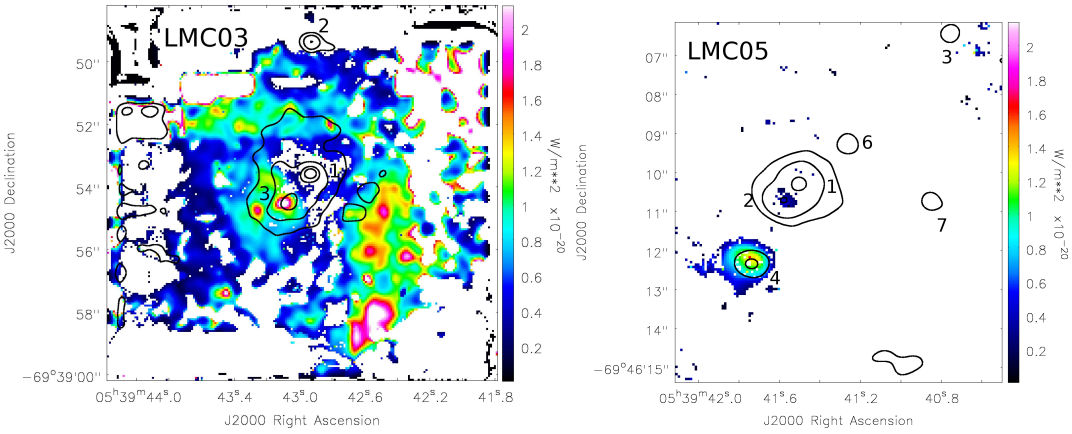

Figure 6.16: [Fe II] 1.64 μm emission line maps for sources LMC03 and LMC05. Black contours show [0.25,0.5,0.75]× maximum continuum emission.

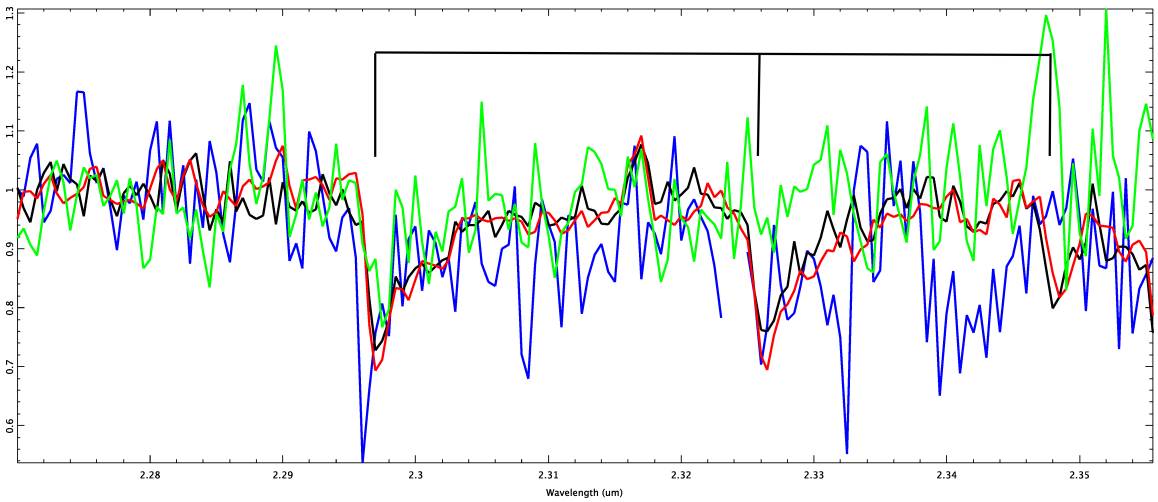

Figure 6.17: Normalised and continuum subtracted spectra for the region surrounding the CO bandhead feature for all sources which exhibit CO absorption.

sources which exhibit CO absorption. Although unusual in massive YSOs (Cooper et al., 2013), CO absorption is common in a number of astronomical objects as discussed for source #02 B in the SMC (see Chapter 4). The normalised and continuum subtracted spectra of these sources for the region around the CO bandhead (2.27–2.36 μm) are shown in Fig. 6.17. The equivalent widths of sources 30DorS-4 (black), LMC04-1 (red) LMC05-3 (blue) and LMC05-6 (green) are given in Table D.5.

As well as the CO bandhead in the K-band, fluorescent Fe II emission at 1.687 μm and 1.741 μm is found in the H-band and is also believed to be associated with accretion discs in massive YSOs (Porter, Drew & Lumsden 1998 and Cooper et al. 2013). Fluorescent Fe II emission lines are commonly associated with accretion discs in AGN (Baldwin et al., 2004) and in Be stars (Zorec et al., 2007). Fe II emission lines are detected towards 11 of the whole LMC sample of 50 continuum sources, 7 of which fall into the colour selected sample of massive YSO candidates. Only one of the Fe II detections is associated with a CO bandhead absorption source (LMC05-6) whilst the remaining CO absorption sources do not exhibit any fluorescent Fe II emission.

6.3 Discussion

All 50 continuum sources detected and analysed in this chapter are summarised in Table 6.4 showing the spectral features present as well as a morphological classification based on the integrated flux maps presented in Figs. 6.7, 6.11 and 6.14.

Table 6.4: Emission lines present for all sources with SINFONI H+K data. ? indicates that it is uncertain whether the line is present, abs indicates that the feature is in absorption rather than emission, A indicates that the emission is ambient and E indicates that the emission is extended. The morphological types determined from the emission line morphologies are given in the final column. Compact sources are indicated with C, H II denotes an H II region, Cl indicates a possible unresolved cluster and O is indicative of extended outflow sources. The final column indicates whether the source exhibits a colour of $H - K > 0$.

Target	Source #	H2 emission	[Fe II] emission	Brγ emission	Br10 emission	He I emission	Fe II emission	CO bandhead	morphological type	$H-K$ > 0.6?
30DorN	1			✓	✓				C	
30DorN	2			✓	✓	?			C	✓
30DorN	3			✓	✓	?	?		C	
30DorN	4			✓	✓	?	?		C	
30DorS	1		✓?	✓	✓	✓A			C	
30DorS	2			✓	✓	✓A			C	
30DorS	3			✓	✓	✓A			C	
30DorS	4			✓	✓	✓A		abs	C	
30DorS	5			✓	✓	✓A			C	
30DorS	6			✓	✓	✓A			C	
30DorS	7			✓	✓	✓A			C	
30DorS	8			✓	✓	✓A			C	
30DorS	9			✓A	✓A	✓A			C	
30DorS	10			✓A	✓A	✓A			C	
30DorS	11	✓	✓?	✓	✓	✓A			C	
30DorS	12			✓A	✓A	✓A			C	
30DorS	13	✓		✓A	✓A	✓A			C	
30DorS	14	✓		✓A	✓A	✓A			C	
30DorS	15			✓A	✓A	✓A			C	
30DorS	16	✓A		✓A		✓A			C	
30DorS	17			✓	✓	✓A			C	
30DorS	18			✓A	✓A	✓A			C	
30DorS	19			✓A	✓A	✓A			C	
LMC01	1	✓A		✓	✓	✓			C/H II	
LMC01	2	✓A	✓?	✓	✓	✓	✓		C	✓
LMC01	3	✓A		✓	✓	✓	✓		C	
LMC01	4	✓A	✓?	✓	✓	✓	✓		C	✓
LMC01	5	✓A		✓	✓	✓			C	
LMC01	6	✓A		✓	✓	✓	✓		C	
LMC01	7	✓A	✓?	✓	✓	✓	✓		C	✓
LMC02	1	✓	✓	✓	✓	✓	✓		C	✓
LMC02	2	✓	✓	✓	✓	✓			H II	✓
LMC02	3			✓A	✓A	✓A			C	✓
LMC02	4	✓	✓?	✓A	✓A	✓A			C	✓
LMC02	5		✓	✓	✓	✓			H II	✓
LMC03	1			✓		✓	✓		C/H II	
LMC03	2			✓A		✓A			H II	
LMC03	3	✓		✓		✓	✓		C	✓
LMC04	1	✓		✓A	✓A	✓A		abs	O?	
LMC04	2	✓		✓	✓	✓			H II	✓
LMC04	3	✓A		✓A	✓A	✓A			C	
LMC04	4	✓A		✓A	✓A	✓A			C	✓
LMC04	5	✓		✓A?	✓A?	✓A?			C	✓
LMC04	6	✓?		✓?	✓?				C	
LMC05	1	✓	✓	✓	✓	✓A	✓		C	✓
LMC05	2	✓	✓	✓	✓	✓A	✓		C	✓
LMC05	3	✓A		✓A	✓?	✓A		abs	C	✓
LMC05	4	✓	✓	✓	✓	✓A			C	
LMC05	6	✓		✓	✓	✓A	✓	abs	C	
LMC05	7	✓A		✓A?	✓A?	✓A?			C	

Table 6.5: Formalisation of massive YSO type classification criteria, originally outlined in Cooper (2013) based on the presence and absence of certain emission line species.

Type	H_2	Brγ	Br10	*Fluor.* Fe II
I	Present	Absent	Absent	Absent
II	Present	Present	Absent	Absent
III	Present	Present	Present	Present
IV	Absent	Present	Present	Present

6.3.1 Selection of YSOs and compact H II regions

Of the 50 selected point sources, 16 have been selected as having a significant K-band excess ($H-K > 0.6$) and this sample represents those sources which are most likely to host massive protostars. Comparing the morphologies of these sources with those discussed in Chapter 4, the majority of these sources are compact but three are consistent with compact H II regions (LMC02-2, LMC02-5 and LMC04-2).

Imposing the criteria that massive YSOs exhibit an $H-K$ colour excess ($H-K > 0.6$) are compact (diameter < 0.2 pc) continuum sources and that they only exhibit outflow-like extended line emission morphologies, the three compact H II regions are rejected yielding 13 massive YSO candidates.

A near-infrared classification criteria set out in Cooper (2013) and Lumsden et al. (in prep) is then imposed on the remaining 13 red, compact sources. This classification scheme has previously been applied to Galactic $H+K$ spectra in Ward & Lumsden (2016) and is formalised in Table 6.5. The classifications are based on a proposed evolutionary sequence where the youngest sources exhibiting bipolar outflows exhibit only H_2 emission (type I), whilst the latest stage sources exhibit no H_2 emission but strong Brackett series emission and fluorescent Fe II emission (type IV). Two intermediary stage classifications are also defined: type II spectra exhibit Brγ emission and H_2 emission with no H-band Brackett series emission or fluorescent Fe II emission whilst type III spectra are the same as type IV spectra but with weak H_2 emission. The additional classifications 0 and Br indicate sources with no emission line features and sources with only Brackett series line emission respectively. UCHIIs would exhibit Brackett series emission and He I emission but as accretion has slowed considerably by this stage (see Chapter 1), they are unlikely to host discs and therefore are not expected to exhibit fluorescent Fe II emission.

The remaining 13 YSO candidates are classified following the above criteria with the classifications given in Table 6.6. LMC03-3 only exhibits Brγ and Br10 of the Brackett series

Table 6.6: Properties of sources which exhibit a near-infrared excess. The final two columns are the morphological types set out in Chapter 4, determined from the integrated line flux maps and the YSO type in line with the classifications set out in Table 6.5.

Region	Source #	$H-K$	K	morphological type	YSO type
30DorN	2	0.64±0.02	–6.17±0.02	C	Br
LMC01	2	0.7±1.7	1.2±1.6	C	IV
LMC01	4	1.5±0.1	–2.61±0.08	C	IV
LMC01	7	1.0±0.1	–1.6±0.1	C	IV
LMC02	1	1.64±0.05	–3.73±0.03	C	III
LMC02	2	0.74±0.03	–4.59±0.02	H II	
LMC02	3	1.02±0.09	–2.95±0.06	C	0
LMC02	4	1.1±0.3	–2.0±0.3	C	I
LMC02	5	0.85±0.08	–10.6±0.2	H II	
LMC03	3	0.84±0.09	–5.85±0.04	C	II/III
LMC04	2	0.61±0.04	–4.4±0.03	H II	
LMC04	4	0.8±0.1	–2.40±0.09	C	0
LMC04	5	0.77±0.09	–2.95±0.06	C	I
LMC05	1	2.46±0.04	–5.79±0.03	C	III
LMC05	2	1.93±0.04	–6.12±0.03	C	III
LMC05	3	0.7±0.1	–3.7±0.1	C	0

along with fluorescent Fe II emission so is strictly a type III source. However it has been classed as a type II/III as type III sources typically exhibit the whole Brackett series in the H-band (believed to be indicative of the early formation of an H II region) so this source is likely to be in a transitional state between types II and III. Through this process 2 type I, 1 type II/III, 3 type III and 3 type IV YSOs have been identified. These successfully classified sources therefore make up the sample of 9 definite massive YSOs. Also identified are three type 0 objects and one object exhibiting only Brackett series emission. It should be noted however, that the signal-to-noise in the type 0 source LMC02-3 is very low and the spectrum exhibits multiple sky line residuals, so weak emission lines may be present but not detected. If it is assumed that these types do indeed represent an evolutionary sequence then 2 early-stage (types I) YSOs and six later-stage (types III and IV) YSOs have been successfully identified.

6.3.2 Brγ emission, He I emission and accretion

Taking only the seven successfully classified YSOs which exhibit Brγ emission (type II/III, III and IV) a new ATS regression has been fitted with the form $y = 10^{mx+c}$:

$$\log(L_{Br\gamma}^{YSOs}) = (-0.30 \pm 0.01)K - (1.43 \pm 0.13) \tag{6.8}$$

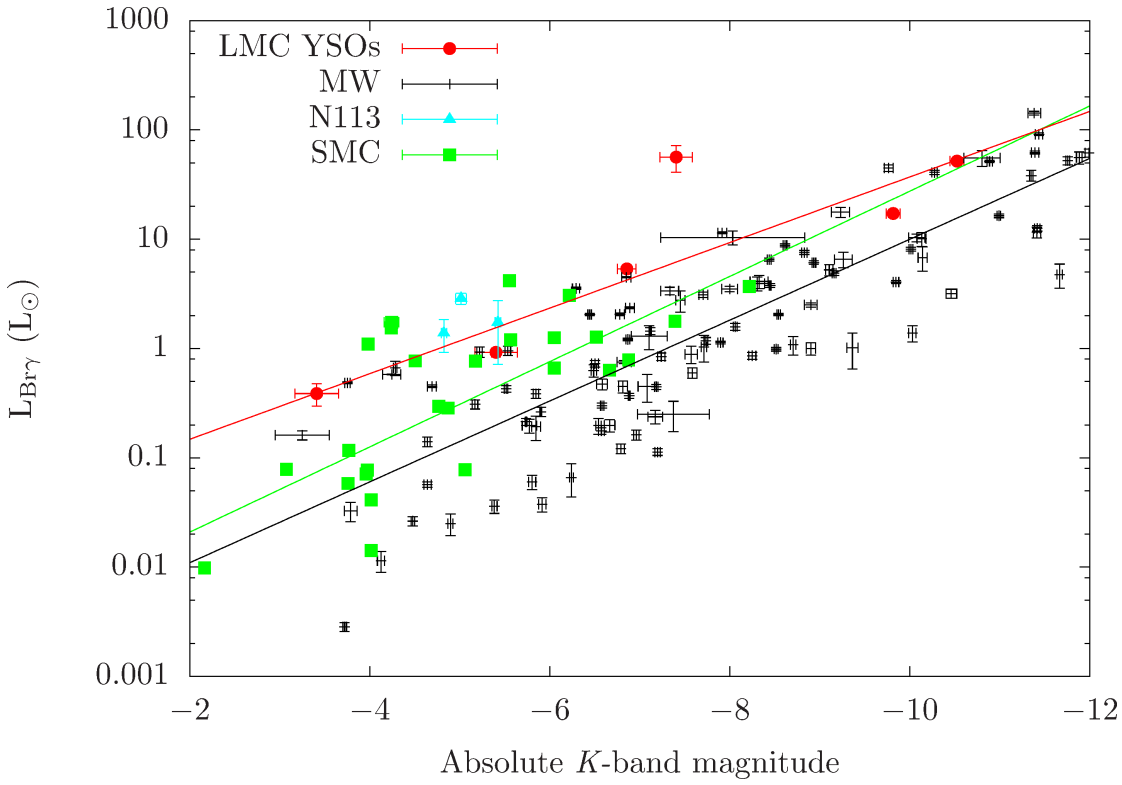

Figure 6.18: An updated plot of Brγ emission luminosity versus absolute K-band magnitude, showing only the LMC sources which fall into one of the YSO near-infrared spectral types defined in Table 6.5. The solid red line marks the ATS fitted regression to only the LMC YSOs classified in this chapter. All additional plotted data is as in Fig. 6.4.

with corresponding p and τ values of 0.06 and -0.73, respectively. Source LMC01-2 has been excluded from the ATS regression fitting due to the extremely large uncertainties in both the absolute K-band and the Brγ luminosity values.

These YSO sources are plotted alongside the new ATS regression in Fig. 6.18. All but one of the newly identified massive YSOs in the LMC sample fall within the scatter of sources of the Milky Way and the SMC and all but one appear to fall below the Brγ/K of the N113 sample. The ATS regression fitted to the LMC sample falls significantly higher than that fitted to the SMC sample. This may be interpreted as the massive YSO sources in the LMC (or at least in the region near 30 Doradus) exhibiting higher accretion rates than those in both the Galactic sample and the SMC sample. This interpretation leads to the conclusion that if there is a relationship between metallicity and accretion rates then it is unlikely to be a simple one.

An ATS regression has been fitted to the He I luminosities against absolute K-band magnitude, yielding a relation of $\log(L_{\mathrm{He\,I}}) = -0.5 \pm 0.1K - 2.3 \pm 0.6$ with τ and p values of -0.73 and 0.06, respectively. In contrast to the SMC sample, the LMC sample shows a significant enhancement in He I emission with respect to the Galactic sample of Cooper et al. (2013).

This is suggestive of a common excitation source for the Brγ emission and He I emission which would suggest that the observed enhancement in Brγ emission may not be caused only by an increase in accretion rates with respect to the SMC, and in fact has a significant contribution from stellar winds.

It should be noted that this LMC sample is small (six sources) and the sample is known to be biased towards PE type *Spitzer* targets and type III and IV near-infrared sources. This strongly suggests that the sample is made up primarily of later-stage YSOs as shown by our own infrared based spectral classifications. Additionally two sources, representing a third of the LMC sample fall well outside the K-band magnitude range of the SMC sample. Finally it should also be considered that all of the targets lie close together in the LMC and in one of the most active regions of star formation in the Local Group, implying that the sample may not be representative of the LMC as a whole. A more complete and representative sample of massive YSOs selected from regions across the LMC is therefore required to investigate the observed Brγ enhancement in the LMC further but the current results certainly point towards a relatively complex relationship between metallicity and accretion rates.

6.3.3 Outflows and H II regions

None of the extended H_2 emission towards the LMC embedded cluster fields appears to be consistent with large scale outflow structures similar to those observed in the SMC. It should be noted that the spatial resolution of the LMC data is $0\farcs25$ whilst that of the SMC data is $0\farcs1$. Furthermore only two sources exhibit H_2 emission line ratios which are fully consistent with shocked excitation (the compact H II region LMC02-2 and type III YSO LMC05-2). A relatively small outflow structure may be indicated by two small knots of emission to the east and west of LMC04-1. The remaining H_2 emission structures appear largely consistent with extended photo-excited structures. These structures are discussed in the next section.

One of the key benefits of obtaining H+K-band spectra in place of just the K-band is the inclusion of the 1.64 μm forbidden [Fe II] emission line associated with energetic shocked gas such as that at the boundaries of molecular outflows. This emission is detected in two of our fields, LMC03 and LMC05, and the integrated flux maps for [Fe II] emission are shown in Fig. 6.16. In LMC03 exhibits compact [Fe II] emission at the position of the massive YSO LMC03-3, possibly sourced at the shock front of an unresolved outflow. There is also additional off-source [Fe II] emission in the west of this field which could indicate further shocked emission. Some of the more diffuse [Fe II] emission to the north and west in this

field could however be the result of contamination from the nearby Br12 emission line. In LMC05-4 the [Fe II] emission appears to be compact, not extending beyond the continuum source, suggestive of the presence of an unresolved outflow. LMC05-4 does not exhibit a particularly red colour so it has not been included in the sample of selected massive YSO candidates but the source could be a lower mass YSO, pre-main sequence star or Herbig AeBe star. The type III YSOs LMC05-1 and LMC05-2 also exhibit [Fe II] emission, possibly indicative of unresolved outflows in these sources.

Four compact H II regions were detected in this work, apparently excited by the sources LMC01-1, LMC02-2, LMC02-5, LMC03-2 and LMC04-2 as described in 6.3.1. The compact source catalogue of Marx, Dickey & Mebold (1997) has been used to determine whether any of the point sources identified in the SINFONI $H+K$ data coincide with radio continuum sources. Two of the continuum sources identified in this work, LMC02-2 and LMC02-5, are clearly coincident with a compact source of radio emission. Another field (LMC04) also contains a 20 cm source although when compared to the continuum image (see Fig. 6.19), the centre of the radio emission appears to fall between sources LMC04-1, -2, -3 and -5. Assuming that the compact H II region structure traced in Brγ is the source of the radio continuum emission (see Chapter 1) then the most likely source of the Brγ emission is continuum source LMC04-2 as it falls in the centre of the Brγ emission and is relatively luminous compared with source LMC04-5. In both cases the Brγ emission morphology is highly suggestive of compact H II regions which are expected to exhibit free-free radio continuum emission. The identification of 20 cm radio continuum emission from the same sources therefore adds a significant weight of evidence to this classification.

The detected extended He I 2.059 μm emission appears to trace the extended Brγ emission almost exactly, reinforcing the assertion that LMC04-2, LMC02-2/LMC02-5 and LMC03-2 are the exciting sources of the compact H II regions. The detection of significant non-ambient He I emission towards continuum sources within four out of seven of our FOVs further indicates that these are extremely energetic regions, likely excited by massive stars.

Using the velocity maps and the angular size on the sky of the observed H II regions an estimate for their ages can be determined. This method assumes that the velocity of the gas in the outermost portions of the H II region is typical of its growth through the expansion of the Strömgren sphere. Taking source #02 in LMC04, the compact H II region appears to be approximately 3 arcsec across with a velocity gradient of $\sim$–10 to 10 km s^{-1}. At the distance of the LMC, this equates to a spatial distance of $\sim$0.73 pc = 2.25×10^{13} km. Using

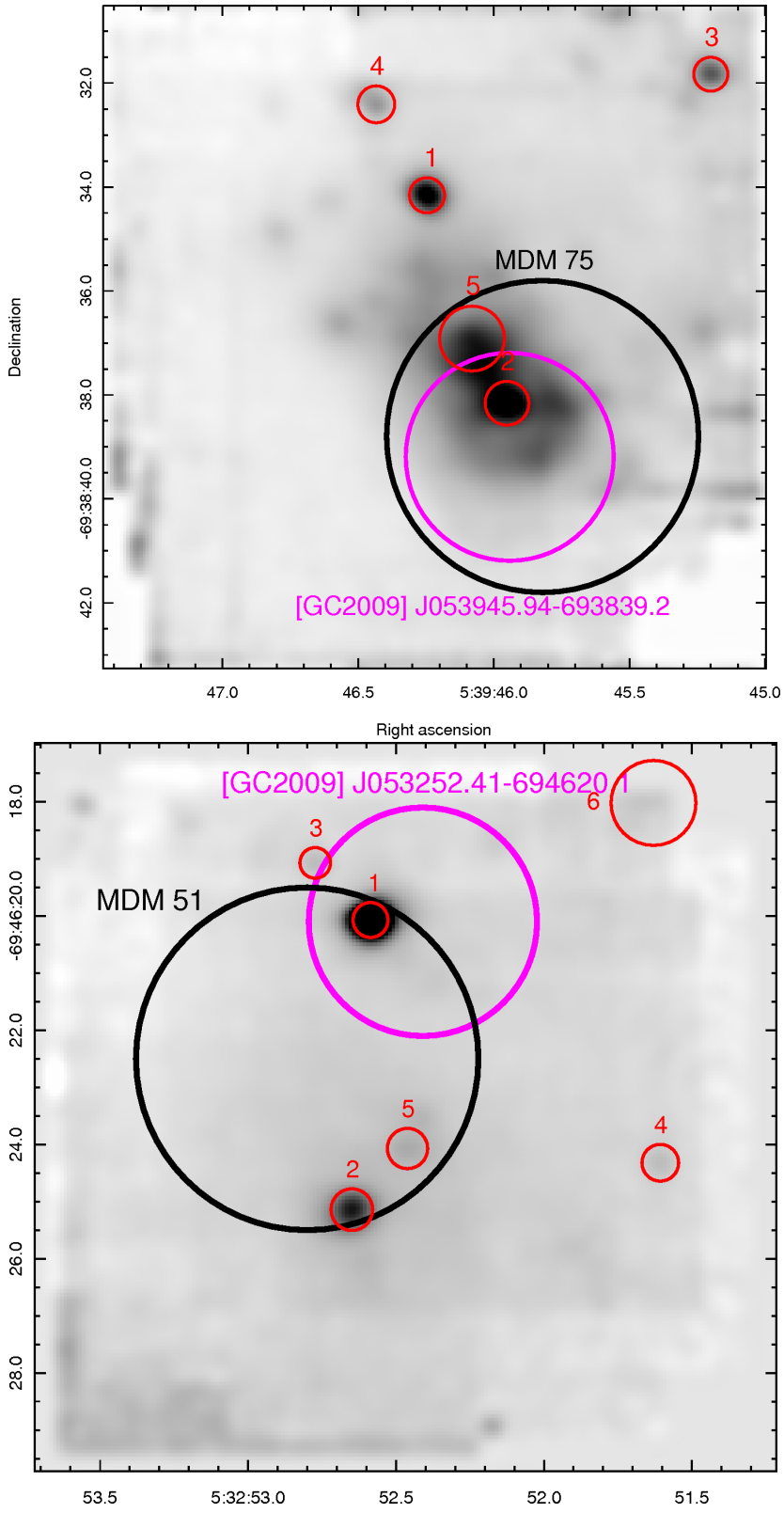

Figure 6.19: Positions of radio sources (black circles) relative to *Spitzer* sources (magenta circles) and newly resolved SINFONI sources (red circles) overlain on to the K-band continuum images for LMC02 (upper) and LMC04 (lower). The sizes of the circles for the *Spitzer* and radio sources are representative of the uncertainties in the positions whilst those of the SINFONI sources represent the area from which spectra was extracted.

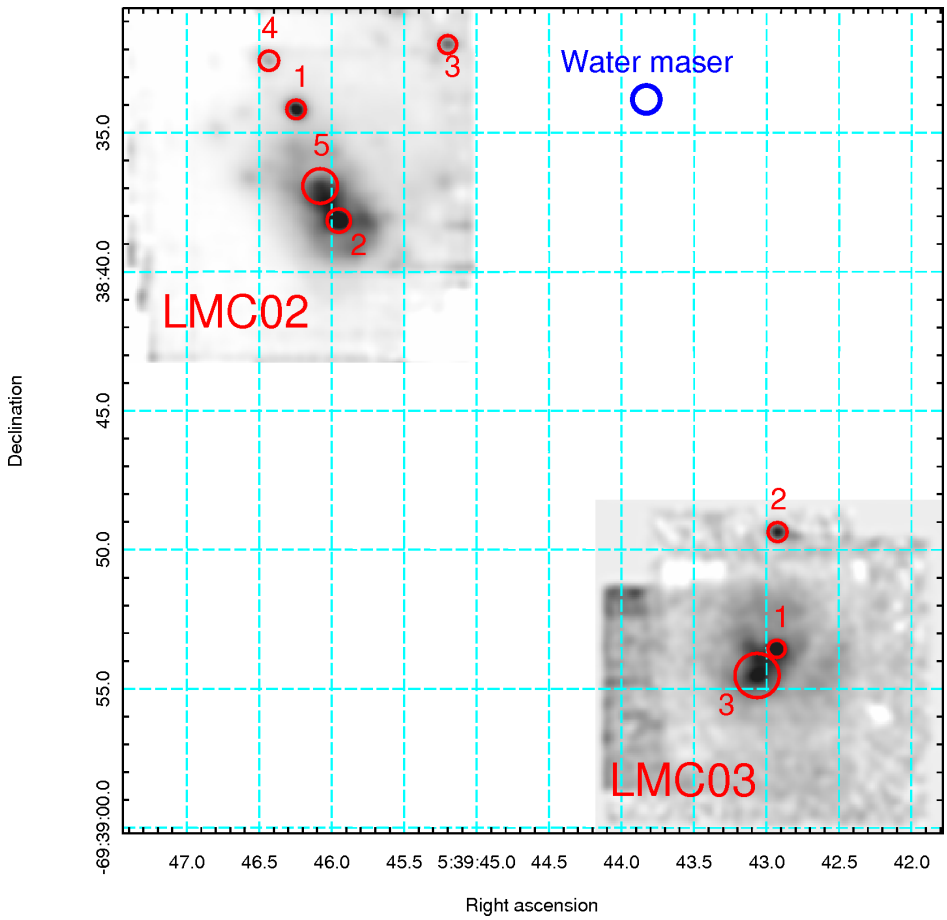

Figure 6.20: Position of the water maser emission described in Section 6.3.3 with respect to the two observed fields LMC02 and LMC03.

the measured projected size on the sky and velocity gradient across the region, an estimate of the age of the H II region can be determined as $\sim 10^{12}$ s ~ 32 kyr. This is consistent with expected lifetimes for cometary H II regions of a few 10^4 yr (Hoare et al., 2007). For the remaining compact H II regions deriving an upper limit on the age is not so straightforward, as they exhibit relatively clumpy morphologies and disordered velocity fields. Given that the morphology of LMC04-2 is the most extended however and that the relative velocities observed are similar between different regions, it seems that $\sim 10^{12}$ s ~ 32 kyr is a suitable upper limit on the ages of the compact H II regions observed towards LMC02 and LMC03.

The list of known H_2O masers in the LMC from Imai et al. (2013) was cross-referenced with the K-band continuum source positions established in this work. Continuum sources and masers were initially matched if the distance between them was less than 20 arcsec. This yielded a single match between LMC02-3 and a maser at 05:39:43.83–69:38:33.8. The position of this maser is shown in Fig. 6.20 along side the two nearby observed SINFONI fields LMC02 and LMC03. The water maser is coincident with another source from the Gruendl & Chu (2009) catalogue (GC J053943.83–693834.0) and it is therefore unlikely to be associated with

the sources detected in LMC02 and LMC03.

6.3.4 Photo-excited H_2 emission

The most striking features of the H_2 emission integrated flux maps are the filamentary structures present in five of the seven fields. The H_2 emission in to the east in LMC04 overlaps significantly with the Brγ emission but they share no similarities morphologically. This may be indicative of a complex 3-dimensional structure of a PDR. In LMC02 and LMC04 the H_2 emission appears at the edges of Brγ emission which suggests a similar scenario to that of N88 A (Chapter 4) of a PDR at the boundary of a compact H II region. As discussed in Chapter 1, PDRs are commonly observed in both H_2 and PAH emission so the photo-excited H_2 emission structures are consistent with the PE classifications in the Seale et al. (2009) catalogue.

6.3.5 Discs

The CO bandhead emission which is often associated with discs in Galactic massive YSOs has not been found towards any of the sources in the LMC sample. CO absorption has been found towards four sources but none of them appear in the final sample of massive YSOs. One source in this sample (LMC05-3) meets the colour cut $H - K > 0.6$ and exhibits CO bandhead absorption but exhibits no emission lines in its spectrum and has therefore been given the type 0 classification. The nature of the CO bandhead absorption sources remains unclear as many astronomical objects exhibit CO bandhead absorption including AGB stars, PMS stars and massive YSOs all of which are likely to exhibit red spectra.

On the other hand fluorescent Fe II emission, also arising in discs around massive protostars (Porter, Drew & Lumsden, 1998), has been detected towards seven of the final sample of nine massive YSOs (78% of the sample) which is about three times higher than the detection rate towards massive YSOs in the Milky Way (26%). Given the small size and biased nature of the sample, the most likely explanation is that this is due to a selection effect, rather than a physical difference between the Galaxy and the LMC. Both in this study and that of Cooper et al. (2013), the fluorescent Fe II emission has proven more common than the CO bandhead emission and therefore presents a suitable additional indicator of disc structures in YSOs in future studies towards the Magellanic Clouds.

Out of 76 Galactic sources exhibiting evidence of discs in Cooper et al. (2013), only six exhibit both the CO bandhead emission and Fe II emission. Furthermore, only type III/IV

objects (those with a full Brackett series and weak or no H_2 emission) exhibit Fe II emission. This suggests that the emission originating from accretion discs in massive YSOs is dependent on evolutionary state with the CO bandhead appearing earlier than the Fe II emission. The LMC sample of massive YSOs is heavily biased towards sources which exhibit spectral features associated with later-stage YSOs and therefore only fluorescent Fe II emission towards these sources and no CO bandhead emission is consistent with a scenario where the emission species observed is dependant on the evolutionary state of the YSO.

Four of the 50 detected point sources appear to exhibit fluorescent Fe II structures (LMC01-3, LMC01-6, LMC03-1 and LMC05-6) but do not exhibit the colour excess expected for massive YSOs. Given their presence in active regions of star formation sources are likely to be other lower mass young stars which feature discs such as Herbig AeBe stars or Be stars.

6.4 Chapter summary

In this chapter archival $H + K$ integral field spectroscopic observations towards embedded clusters have been analysed with the aim of identifying sites of current star formation and investigating the interactions between young clusters of stars and excited gas. The results of this work are summarised in six key points:

i Of the 50 newly resolved continuum sources in the seven embedded clusters analysed this chapter, 9 massive YSOs have been identified. Based on their colours and spectral properties the majority of these appear to be late-stage massive YSOs, which would explain the low detection rates of common outflow tracers towards these sources.

ii No sources appear to exhibit extended outflow structures such as those observed towards the SMC. Indeed, H_2 emission which is fully consistent with shocked emission is only detected towards one source and is likely due to a stellar wind or expanding H II region rather than a bipolar outflow. Forbidden [Fe II] emission was however detected towards a three massive YSOs, possibly indicating spatially unresolved outflow structures.

iii Five of the 50 continuum sources have been determined to be exciting sources of compact H II regions. Three of these sources also exhibit radio continuum emission as expected towards H II regions. Using gas velocities and measurements of the projected size on the sky of these H II regions, an age has been estimated as $\sim$32 kyr for one of the H II regions based on the available kinematic information.

iv Large scale and likely photo-excited structures are observed in H_2 emission towards the majority of fields, indicative of PDRs at the boundaries of compact H II regions. This is consistent with the *Spitzer* observations towards these sources and the observed PDRs are likely to be the source of the PAH emission.

v No CO bandhead emission is observed towards any of the detected sources although given the low number of YSOs, this is not unexpected (CO bandhead emission is very sensitive to geometrical effects). CO bandhead absorption is detected towards 4 sources but none of these are likely to be massive YSOs. Seven out of nine massive YSOs identified in this chapter exhibit fluorescent Fe II emission, indicative of discs in massive YSOs. This detection rate is significantly higher than that found towards the Galactic sample but this is probably a selection effect.

vi Brγ emission detected towards all of the massive YSOs identified in this chapter is high compared to the Galactic and SMC samples This may suggest higher accretion rates; however, the sample is small, heavily biased towards later stage YSOs and exhibits an excess in He I emission which is inconsistent with either the Galactic or SMC data sets. A more complete and representative sample of massive YSOs in the LMC is therefore required to investigate this further.

7 Fabry-Perot Interferometry with SALT/RSS

7.1 Introduction

As discussed in Section 2.3, Fabry-Perot interferometry provides a unique and novel technique for performing high spectral resolution, spatially resolved spectroscopy over a wide field of view. It is therefore ideal for observing single emission lines over large regions of interest such as the Hα and Hβ emission features originating in H II regions in the Magellanic Clouds. In this Chapter I present the results of using Fabry-Perot interferometry to map the ionized gas emission in two H II regions in the Magellanic Clouds: N113 in the LMC and N88 in the SMC which are discussed in detail in Chapters 3, 4 and 5.

Hα narrow band filter images exist of these regions with a high degree of sensitivity from the "Magellanic Cloud Emission Line Survey 2" (PI: You-Hua Chu, http://adsabs.harvard.edu/abs/2011noao.prop..537C) shown in Fig. 7.1. Whilst these images give an extremely deep view of the morphology and extent of the emission, little can be directly gained in terms of the emission line flux from these images alone and nothing can be learned of the gas kinematics of the region. Fabry-Perot interferometry allows the simultaneous mapping of the emission line flux and the kinematics of the excited gas. Additionally by using two lines of common origin such as the Balmer emission lines studied in this chapter, extinction maps can be made using their flux ratio.

Due to a series of technical issues with RSS at SALT, not all of the observations necessary to achieve the scientific goals of this work were carried out. Nonetheless the observations which were carried out have been of value in the development and verification of a data reduction pipeline for Fabry-Perot observations with SALT (as described in Section 2.3). Additionally a data treatment procedure has been developed based on the SINFONI data treatment procedure described in Section 2.1.

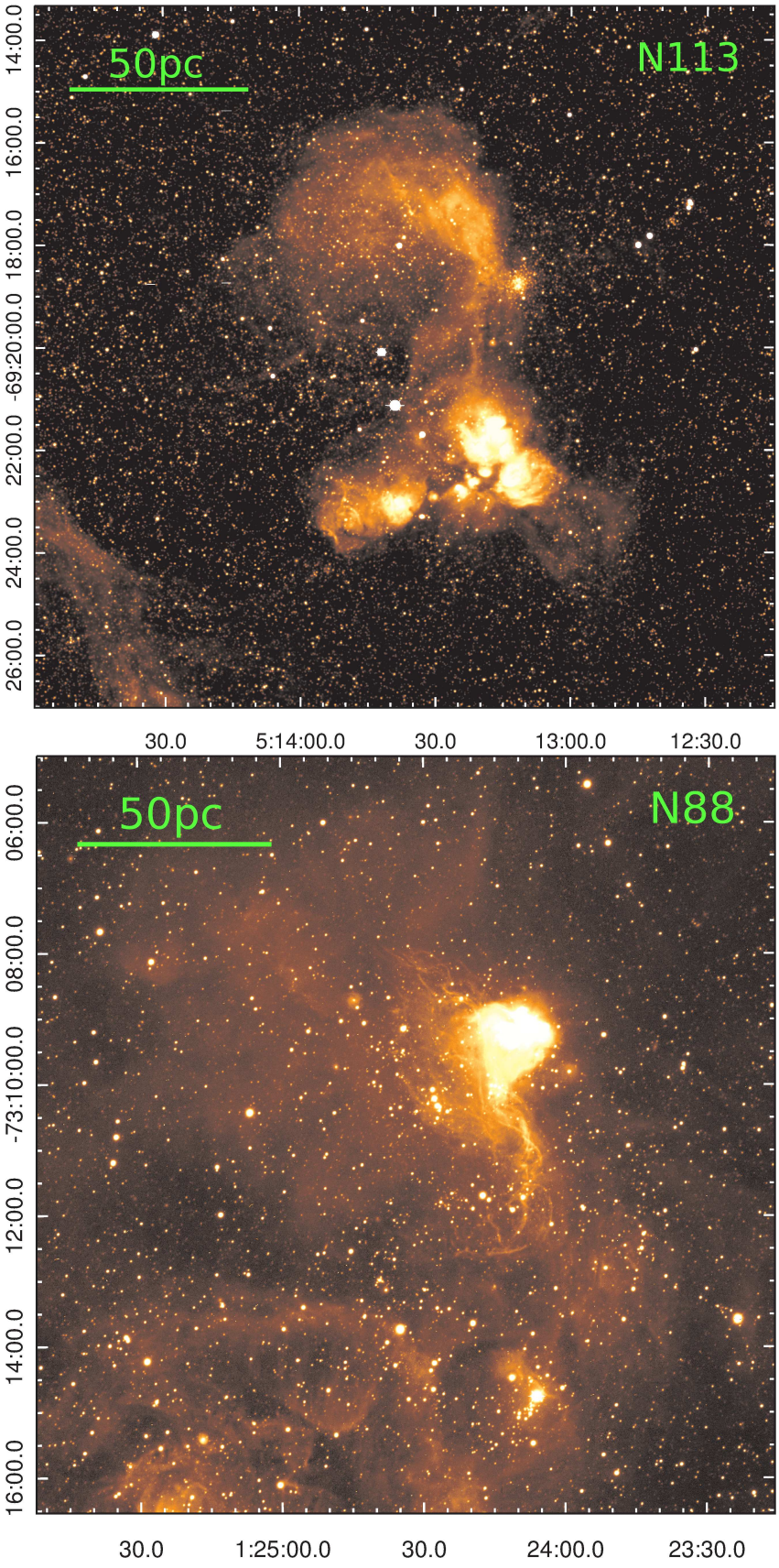

Figure 7.1: MCELS2 Hα narrow band filter images for N113 (upper) in the LMC and N88 (lower) in the SMC.

7.2 Results

7.2.1 Channel maps

Using the procedure outlined in Section 2.3 channel maps in velocity space have been produced by stacking and reordering the Fabry-Perot data cubes. Channel maps have been produced for the N88 Hα (MR) and Hβ (LR) observations shown in Figs. 7.2, and 7.3. The resolving powers of the LR, MR and HR modes at 6500 Å are ∼800, ∼1500 and ∼9000, respectively. The channel maps for the LR mode observations of Hβ emission in N113 are shown in Fig. 7.4. The spectral resolution of the low resolution mode is insufficient to gain any useful kinematic information for the regions. Comparing the observed morphologies from the channel maps with the images in Fig. 7.1 it is clear that much of the more diffuse emission is not detected in the Fabry-Perot observations. For the brighter regions however, the observed morphologies appear to be as expected. Note that the Fabry-Perot observations are rotated with respect to the images in Fig. 7.1 and each observation has a different position angle as setting the position angle is not supported in Fabry-Perot mode with RSS.

It can be seen that the N88 emission clearly peaks between 0 and 300 $\mathrm{km\,s^{-1}}$ from the N88 A Hβ channel maps which is in the range expected (∼160 $\mathrm{km\,s^{-1}}$) for sources in the SMC. The N113 Hβ flux appears to peak at a higher velocity than N88 A as expected for the LMC although it is difficult to place constraints on the velocity from the LR channel maps alone. Due to the relatively low S/N ratio of the MR mode Hα observations of N88, little can be determined from the channel maps but they do suggest the possibility that some of the more diffuse emission is blue-shifted with respect to the peak peak of the Hα emission (which contains the compact H II region discussed in Chapter 4) but it is just as likely that this is a systematic effect or foreground emission and thus no conclusion can be drawn.

7.2.2 Intensity maps

Integrated flux maps are created using the original images rather than the final velocity-space cubes to avoid any loss of data. The Hα and Hβ integrated flux maps for N88 are shown in Fig. 7.5. A small 'faint' mirrored image is visible in the lower left (south-east) of the MR Hα image whilst in LR mode this is effect not present.

From the LR Hβ flux image of N88, it is clear that the H II region has significant clumpy substructure with peaks around the masked foreground continuum sources as well as clumps to the north and east of the main HEB which do not appear to be associated with foreground

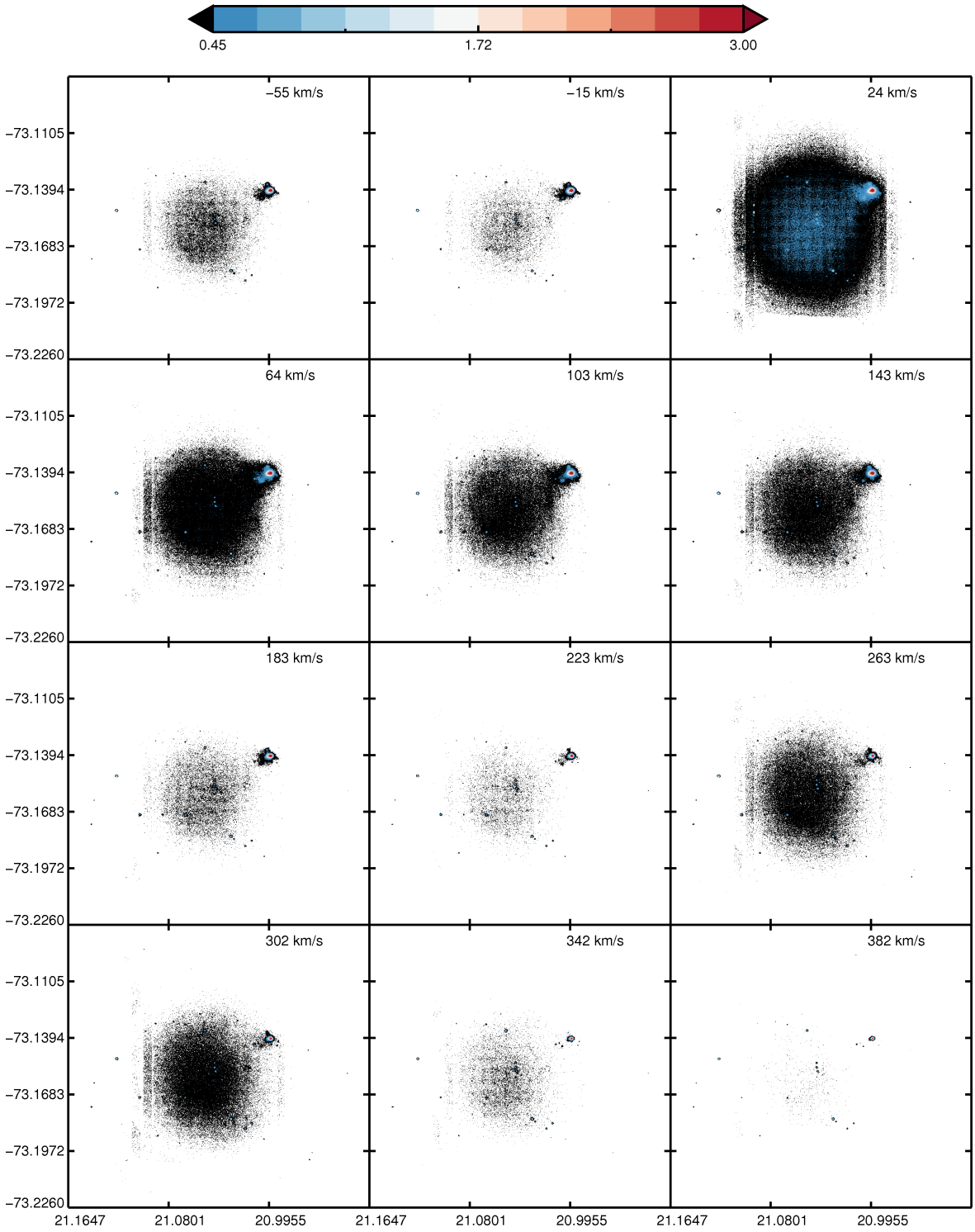

Figure 7.2: Medium resolution Hα channel maps of N88.

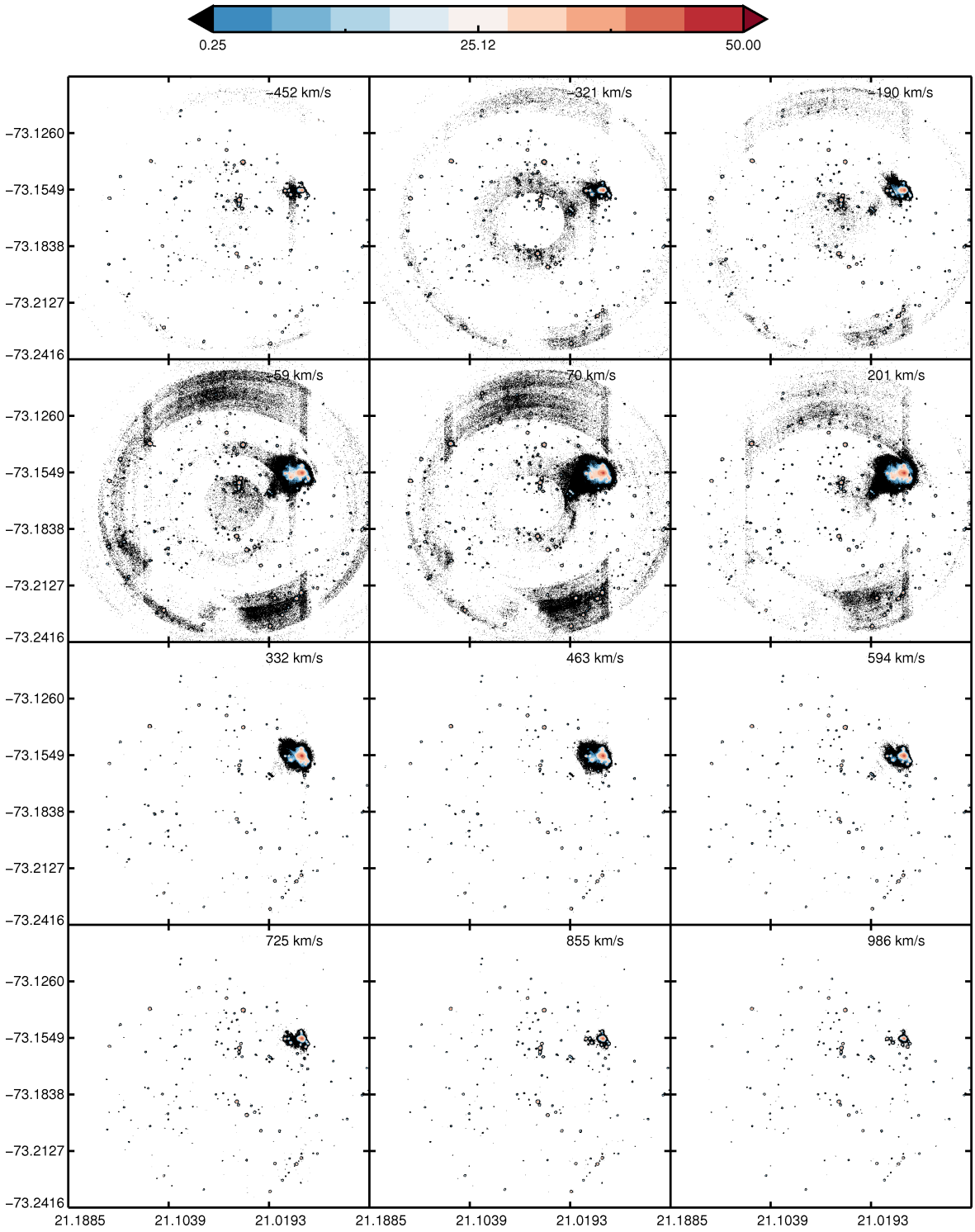

Figure 7.3: Low resolution Hβ channel maps of N88.

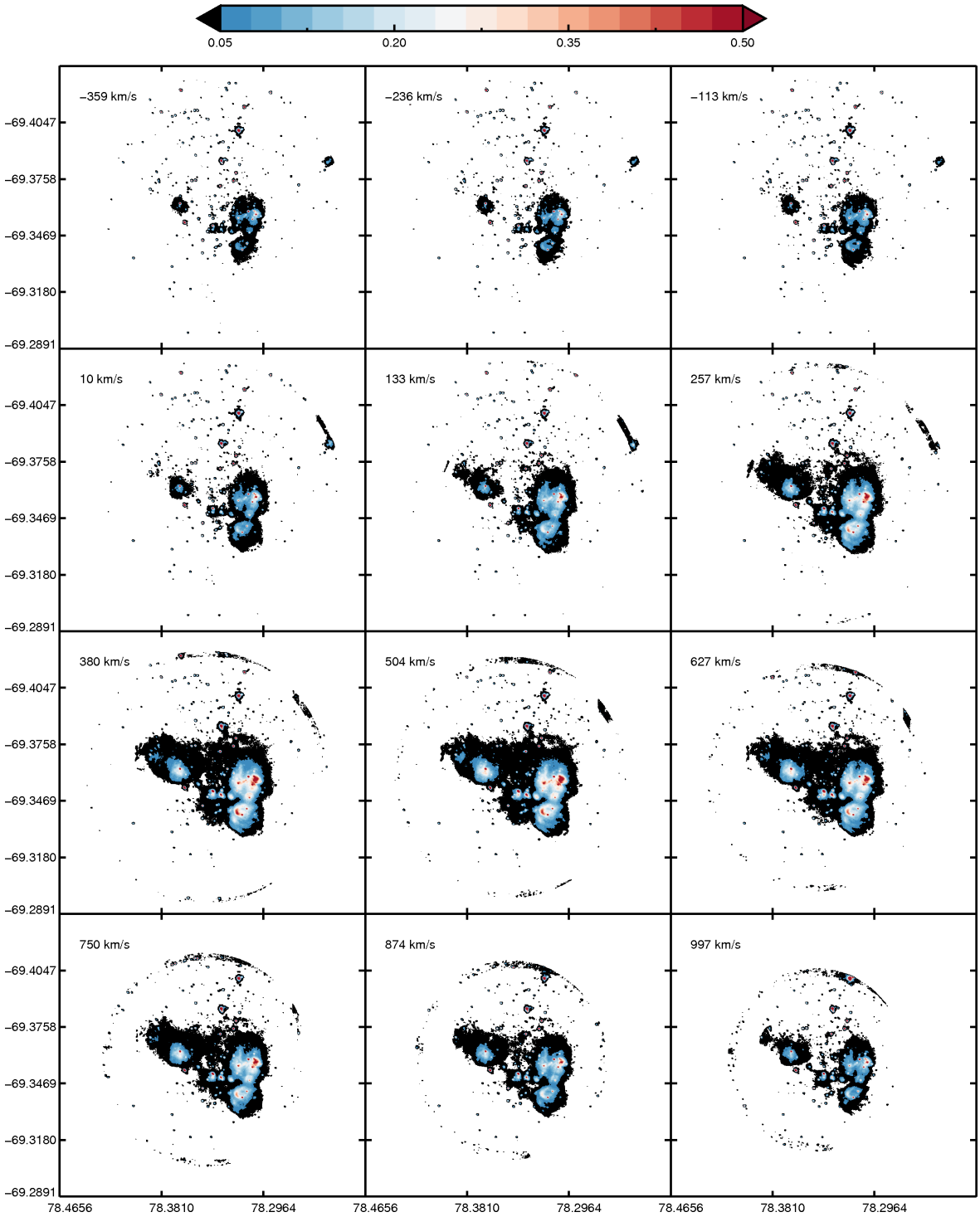

Figure 7.4: Low resolution Hβ channel maps of N113.

continuum sources. This hints at a complex and clumpy 3-dimensional structure. The 'tail' of N88 to the south of the HEB is detected in the LR Hβ observations but not in the MR Hα observations and even in the Hβ map the signal-to-noise is relatively low and the spatial resolution is insufficient to detect any of the filamentary sub-structure shown in Fig. 7.1.

The LR Hβ integrated flux map for N113 is shown in Fig. 7.6. The vast majority of the bright emission shown in Fig. 7.1 originates from the three main peaks in the central dusty lane (associated with the sources observed with SINFONI in Chapter 3) as well as a fourth, weaker peak to the east of the SINFONI fields and the three large bubble-like structures surrounding the star forming region. Some sub-structure is certainly observed in the large bubble features but not as much as previously observed with MCELS2. These sites would likely provide interesting results with higher spectral resolution Fabry-Perot observations to observe the velocity fields associated with this sub-structure in the bubbles.

7.2.3 Velocity maps

The emission line centroid velocity map for Hα emission in N88 is shown in Fig. 7.7. Due to the technical difficulties experienced with the Fabry-Perot mode of RSS over the last few years and because the spectral resolution of the LR mode observations is insufficient to create a velocity map, the MR cube is the only observation for which a velocity map can be obtained. The red contours in Fig. 7.7 show the peak Hα flux in the region, much of the information outside this small region exhibits high levels of noise so the velocity measurements are dubious. There is however a clear velocity gradient across the HEB from $\sim$140 km s^{-1} to $\sim$180 km s^{-1} which is on the same order of magnitude as the velocity field exhibited in the SINFONI data for N88 A (see Chapter 4) although the spatial scale of the Hα emission is significantly larger than that of the Brγ emission.

7.2.4 Extinction maps

The two H II regions examined in this chapter are active and complex sites of star formation. Extinction measurements can provide a proxy for the dust distribution across these regions where the highest extinctions are likely to be associated with the densest regions harbouring the earliest, most embedded YSOs. The same technique used in Chapter 5 to obtain an extinction estimate for a single spectrum using Hα and Hβ can be applied across a region assuming flux maps of both can be obtained.

Starting with just one of the Hβ integrated flux maps obtained from the low spectral

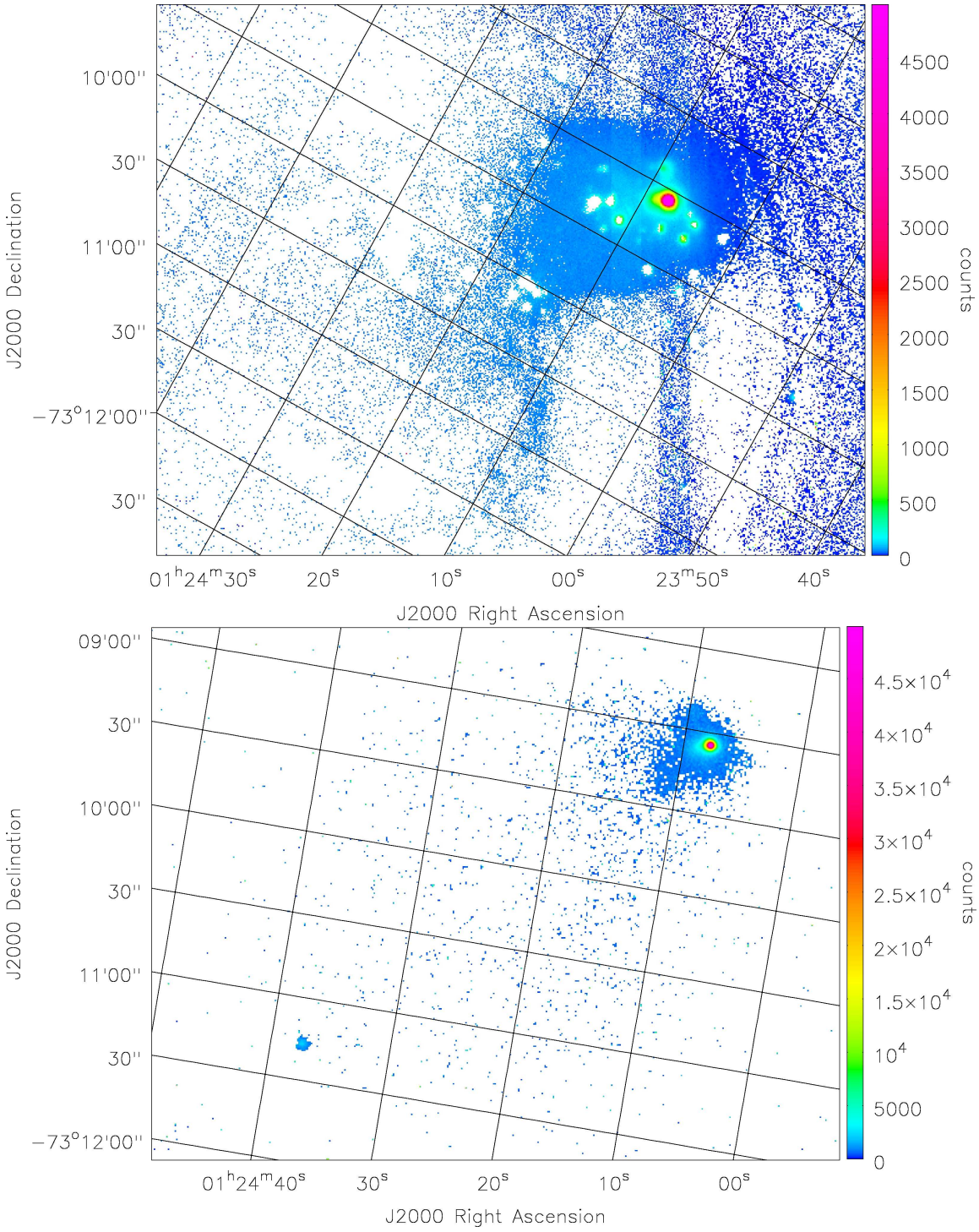

Figure 7.5: Upper: LR Hβ integrated flux map of N88 A. Lower: MR Hα integrated flux map of N88 A. The apparent object to the lower left is a mirrored ghost image of the N88 A. The Hα flux map is displayed with a bilinear sampling rather than a nearest pixel sampling for clarity. No flux calibration has been applied to these images.

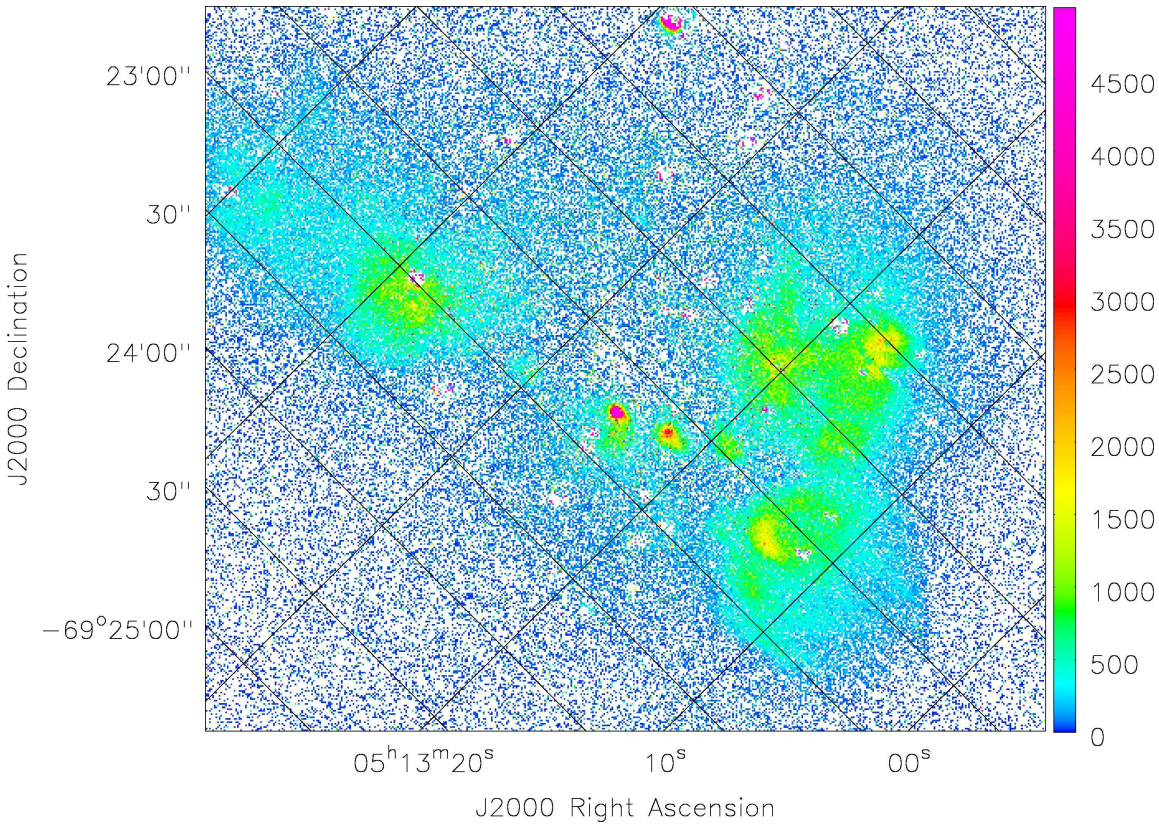

Figure 7.6: LR Hβ integrated flux map of N113. No flux calibration has been applied to this image.

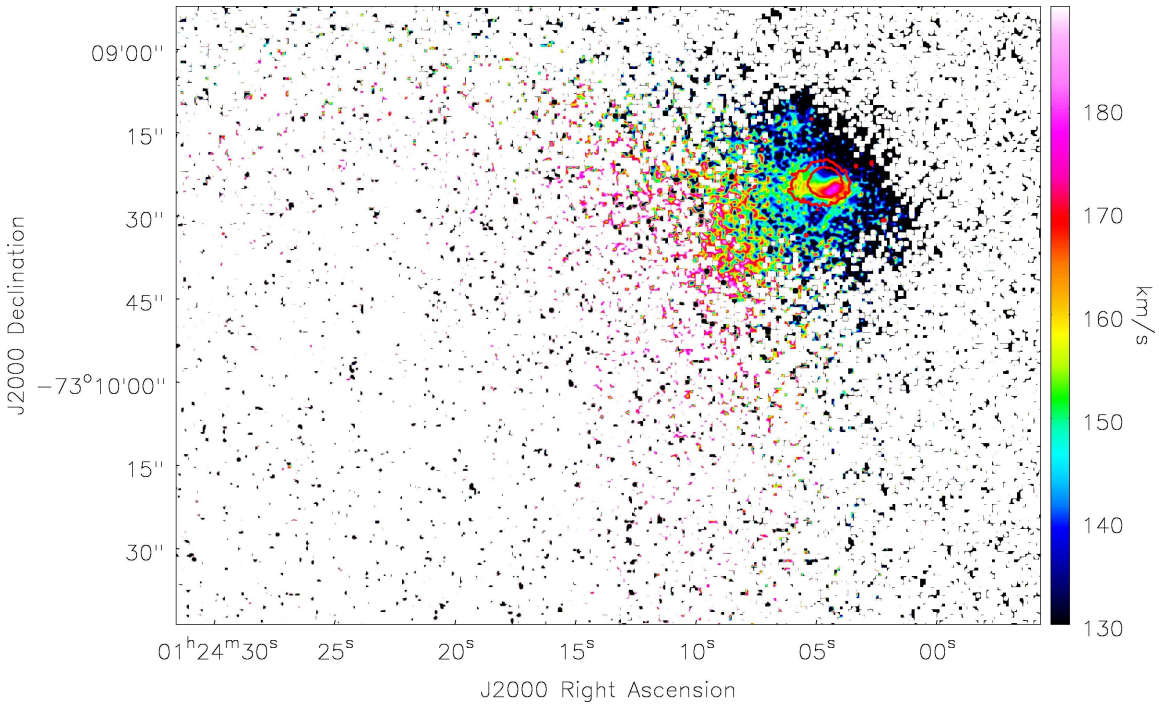

Figure 7.7: Hα velocity map of N88 A using bilinear sampling for clarity. Red contours show the position of the strongest Hα flux.

resolution Fabry-Perot observations it is possible to create an extinction map relative to a position in the map itself (much like the relative velocity maps of Chapters 3,4 and 6). Data was obtained from two additional sources: Hα images were obtained from the MCELS2 for both N113 and N88 and red filter images from the UK Schmidt Telescope at the Australian Astronomical Observatory obtained through the Digitised Sky Survey (DSS) image server[6]. The process of creating an extinction map from this data is described in the following steps:

1. The images must be shifted, rotated and scaled so that the coordinate systems are the same. This is carried out using the REMAP function of the WCStools package[7] which allows any image to be mapped to any WCS coordinate system. For the purposes of this work the Hα and Hβ images were both remapped to the coordinate system of the red filter image as this is the image with the lowest resolution.

2. The Hα and red filter images are then normalised to each other using a standard star which appears in both images. The star is selected using the criteria that it is relatively bright, free of bad pixels, appears in both images and is free of Hα emission.

3. The scaled red image is then subtracted from the Hα image to produce a map of the Hα emission line flux.

4. The Hα map is then divided by the Hβ map. The resulting [Hα / Hβ] map is then scaled using a region in the images for which the actual ratio is known.

5. Finally the ratio map is converted into an extinction map using Eqn. 5.1 with the assumptions that the intrinsic line ratio is 2.87 (see the discussion in section 5.1.1) and a value of $R = 3.1$ for the extinction curve, equal to that of the Milky Way.

The MCELS2 Hα images have the regions of brightest Hα emission masked. Unfortunately two of these regions are those for which high signal-to-noise spectra were presented in Chapter 5 and therefore the best constrained Hα / Hβ emission line ratios. An extinction map relative to the extinction at a single point in the image can be constructed by making the assumption that the region exhibits an Hα/Hβ flux ratio of $\sim$2.87, i.e. that the foreground extinction towards that region is negligible. This process has been applied to both the N88 and N113 observations with the resulting extinction maps shown in Fig. 7.8. There appears to be little discernible structure in these low resolution extinction maps, and it is immediately

[6] produced at the Space Telescope Science Institute through its Guide Star Survey group
[7] WCStools version 3.9.4 (http://tdc-www.harvard.edu/wcstools/), Mink (1997) and Mink (2002)

clear that there is little variation in extinction across the fields with the relative extinction values not exceeding $\delta A_V = 3.0$ in N113 and $\delta A_V = 1.8$ in N88.

7.3 A data treatment procedure for Fabry-Perot

The key advantage of Fabry-Perot observations is the ability to image relatively large fields for a series of very narrow spectral regions, allowing the construction of a high spectral resolution data cube. The downside to this is that the overhead times in Fabry-Perot observations are significant and therefore efficient use of the allotted observation times is crucial. This means that when using Fabry-Perot mode, it is more important than ever to be able to extract as much useful information as possible from the data whilst suppressing instrumental and noise effects. This therefore has formed the motivation to implement a data treatment procedure for RSS Fabry-Perot observations similar to that introduced by Menezes, Steiner & Ricci (2014) and Menezes et al. (2015) for the near-infrared IFUs NIFS and SINFONI.

The first step in developing this procedure is, as with the SINONI treatment, a 2×2 re-sampling in the spatial dimensions. A section of a single slice of the N113 LR Hβ observation is shown in the upper and middle panels of Fig 7.9 before and after re-sampling for comparison. It can be seen from this comparison that although the image has been successfully re-sampled, an additional high spatial-frequency (HSF) component has been introduced in the form of a granulation effect imposed across the image. Similarly as for the SINFONI data, Butterworth Spatial Filtering will be used to remove this new HSF component.

For the case of the Fabry-Perot data, a new filter is designed. Constraints on this new filter in Fourier space has been determined using a process of trial and error to minimise the difference between the Fourier Transform of the original image and that of the final image as shown in Fig. 7.10. Inspecting the difference between the upper and middle panels of Fig. 7.10, a squared filter as used with the SINFONI data may not be appropriate as the Fourier transform of the original image is not circular. Additionally in the centre of the horizontal axis of the image there is a strong vertical feature which cannot be fitted by a straightforward squared filter at the same time as the bulk of the data in the centre.

It was decided therefore to implement not one but two rectangular filters simultaneously with the form,

$$H(u,\nu) = \left\{ 1 + \left[\sqrt{\left(\frac{u-u_0}{a}\right)^2 + \left(\frac{\nu-\nu_0}{b}\right)^2} \right]^{2n} \right\}^{-2} \tag{7.1}$$

where in this case $a \neq b$ but it is otherwise identical to Eqn. 2.2. To produce the results

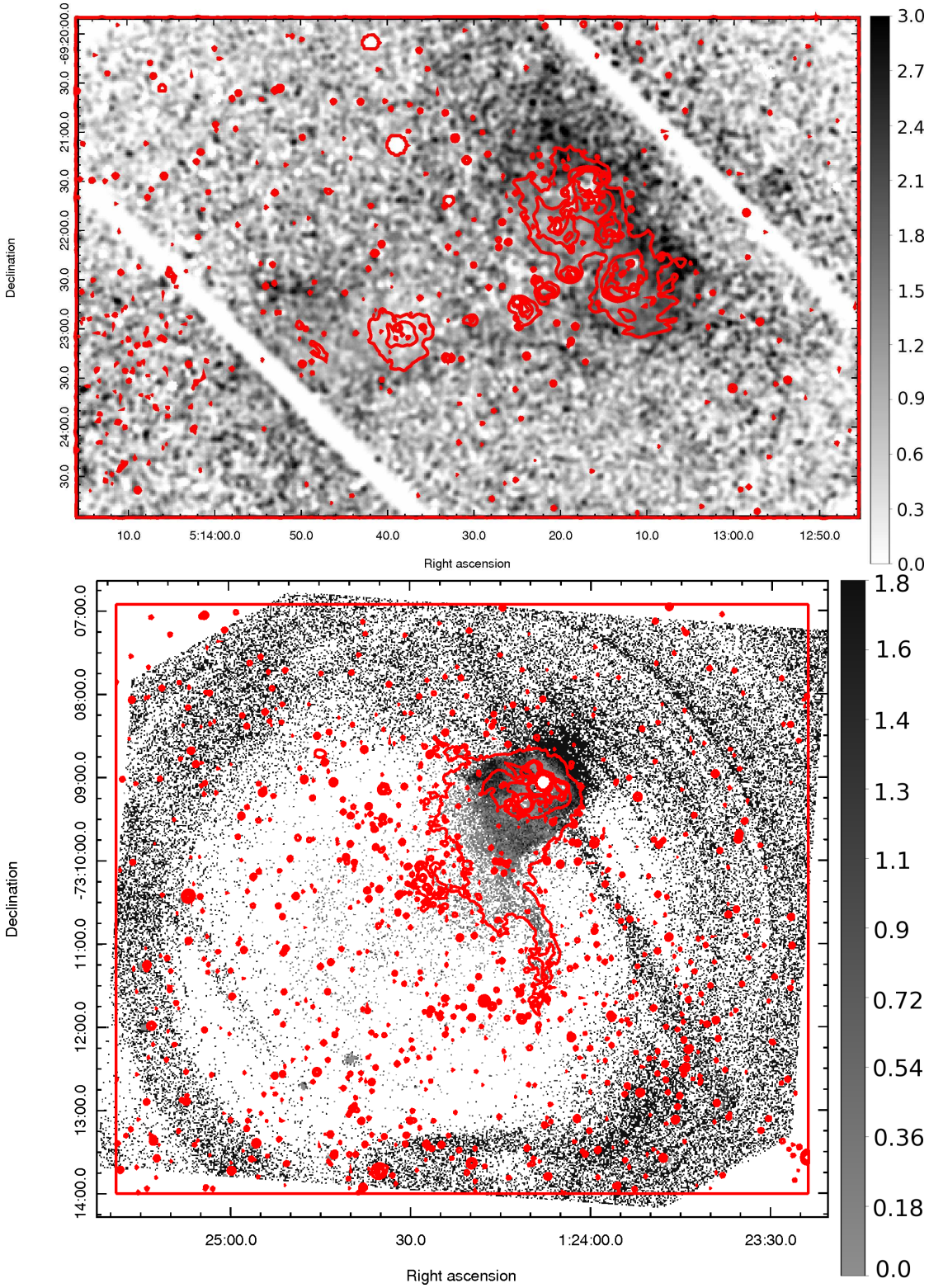

Figure 7.8: Relative extinction map for N113 in the LMC (upper) and N88 in the SMC (lower). The red contours show the distribution of Hα emission in the region. The images have been smoothed using a Gaussian function with a kernel radius of 3 pixels.

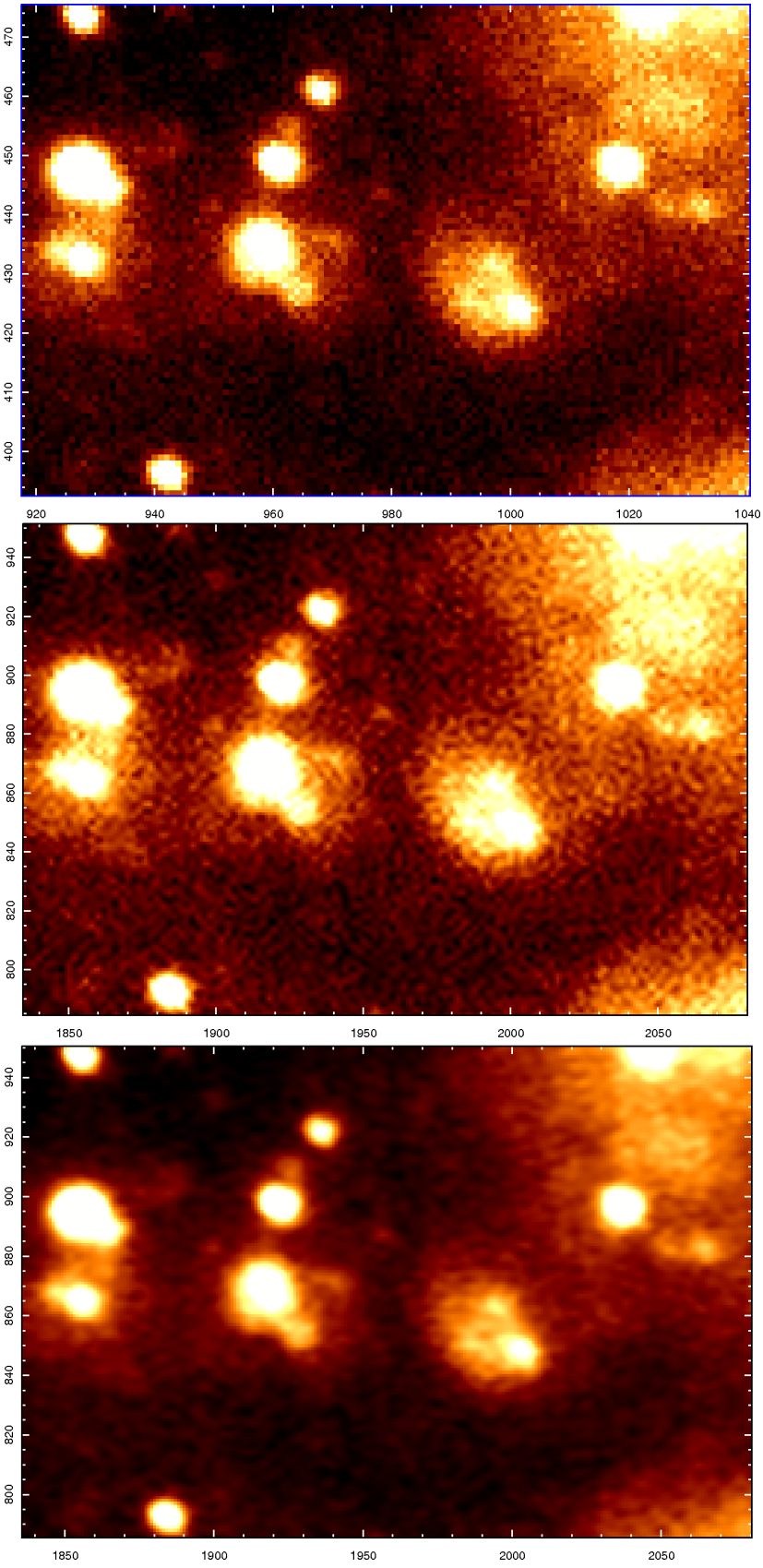

Figure 7.9: The Fabry-Perot images of N113 used to determine the parameters for the Butterworth Spatial Filter. From the upper panel to the lower panel: original image of N113, re-sampled image of N113 and filtered image of N113.

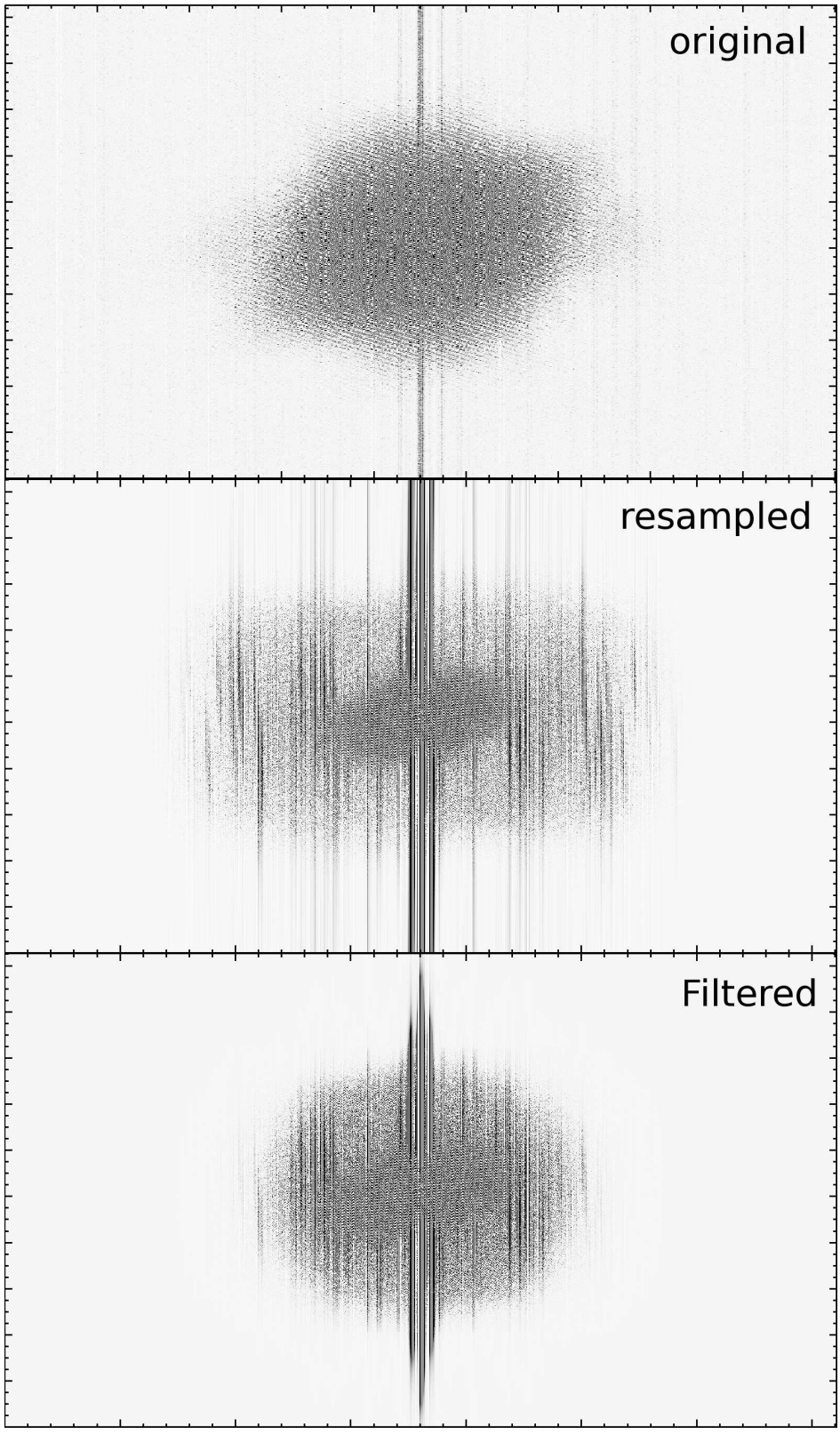

Figure 7.10: Fourier transforms of the original N113 Fabry-Perot image (upper), the resampled image (middle) and the filtered image (lower).

shown in the lower panels of Figs. 7.9 and 7.10 the filters H and H' were applied where $a = 0.35$, $b = 0.60$, $a' = 0.05$ and $b' = 0.80$. The resulting image using these filter and its corresponding Fourier transform are shown in the lower panels of Figs. 7.9 and 7.10 respectively. Note that the HSF component is significantly reduced with respect to the unfiltered image. This was then further improved following the same trial and error process with the LR mode observations of N88 resulting in changing the parameters of the first filter to $a = 0.25$ and $b = 0.30$. A section of the resulting application of the final filter to the N113 cube and its corresponding Fourier transform are shown in Fig. 7.11. Whilst this procedure is of limited use now, it will have a significant impact on the clarity of figures produced from the future high spectral resolution Fabry-Perot observations of H II regions using longer exposure times.

7.4 Discussion

It is unfortunate that not all of the desired data were acquired using the Fabry-Perot mode at SALT/RSS. However, the limited data that has been available has allowed the development of a Fabry-Perot data reduction pipeline for SALT/RSS where none existed before. It has also allowed the application of image enhancement techniques previously only applied to NIFS (Menezes, Steiner & Ricci, 2014) and SINFONI (Menezes et al., 2015) data with appreciable results.

The emission line intensity maps shown in Figs. 7.5 and 7.6 obtained with the LR mode, show that the majority of the interesting structures found in the MCELS2 maps of the same regions are detected. This bodes well for future observations using the HR mode at SALT/RSS to determine the velocity fields of these structures. The velocities measured towards N88 A are of the same order of magnitude as those detected in the near-infrared using SINFONI, indicating that they likely share a common source. The velocity structure observed bares little resemblance to that seen with SINFONI however, indicating that there is no smooth transition between the gas observed with SINFONI and that observed in the optical. Additionally, the spatial scales are different, this newly observed velocity gradient is across a region with a diameter of $\sim$10 arcsec whilst that in the SINONI observations is less than 3 arcsec. This could be indicative of a large gap between the two emitting regions or a turbulent environment.

Although wide field Hα Fabry-Perot data is still unavailable, it has been possible at least to generate relative extinction maps across the regions in question using previously obtained

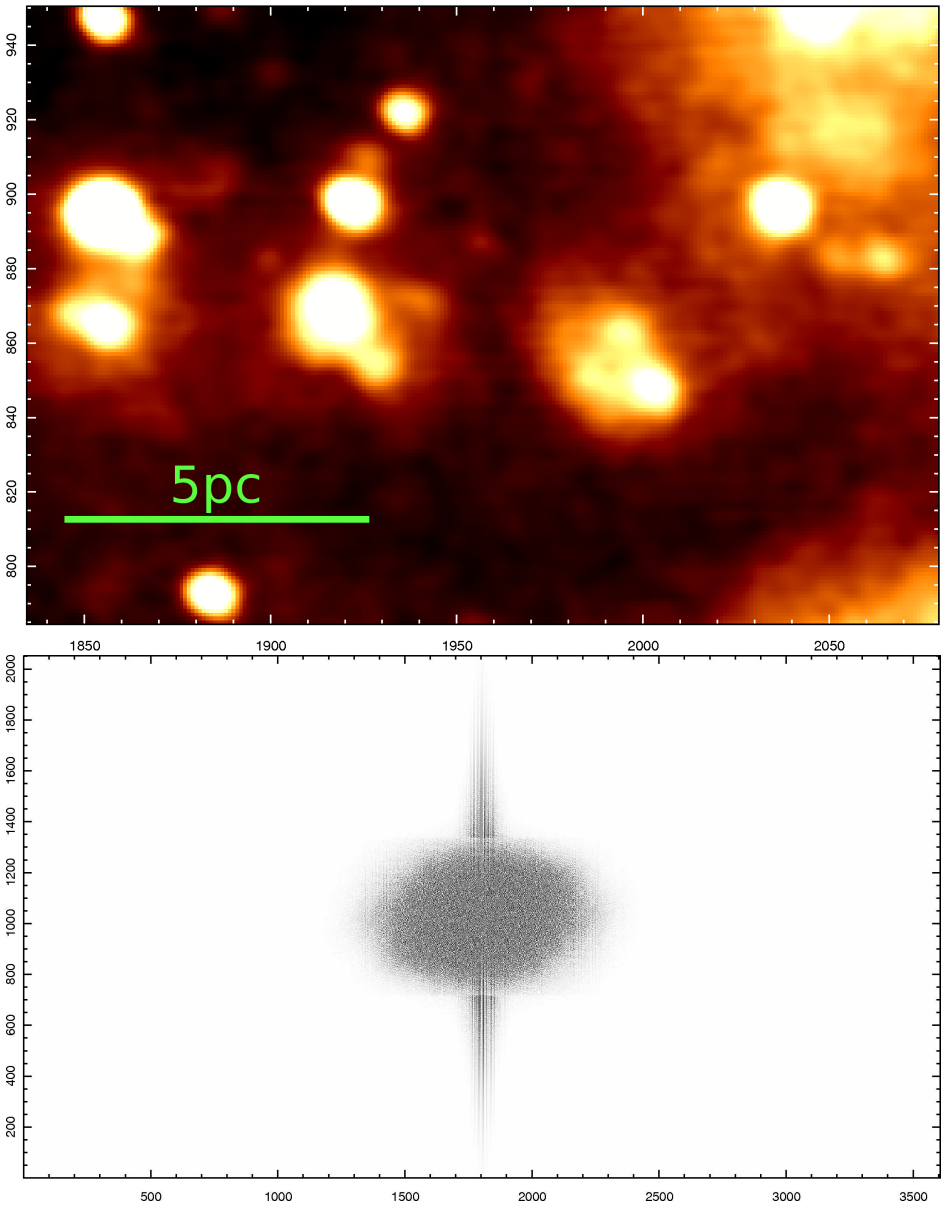

Figure 7.11: Upper: Example section of the re-sampled and filtered N113 velocity cube using a=0.25 and b=0.30, equivalent to figure 7.9. Lower: Fourier transform of the same slice shown in the upper panel.

data from MCELS2 and the DSS. Whilst these have a low spatial resolution and are produced through a relatively convoluted process, what is clear is that in both regions the extinction is approximately uniform and is consistent with the extinctions derived from the optical long-slit spectroscopy presented in Chapter 5. This indicates that none of the measured optical emission originates from an embedded source throughout both H II regions and must therefore originate from a relatively shallow region of the cloud. This implies a long mean-free path for UV photons in both cases assuming the emitting regions are caused by sources within H II regions as observed with SINFONI in Chapters 3 and 4 and that they are not significantly excited by external sources.

7.5 Chapter summary

Despite ongoing technical problems with the Fabry-Perot mode at SALT/RSS throughout this study, a number of interesting early results have been achieved:

i The data reduction procedure outlined in Section 2.3 has been successfully implemented on multiple Fabry-Perot observations. Additionally a data enhancement procedure has also been successfully developed based on a truncated version of the procedure outlined in Menezes, Steiner & Ricci (2014) and Menezes et al. (2015).

ii The low and medium spectral resolution modes have been successfully utilised to produce integrated flux maps of the H II regions LHA 120-N113 and LHA 115-N88 in the LMC and SMC respectively, without contributions from continuum emission.

iii The centroid velocity map of Hα emission in N88 has revealed excited gas velocities on the same order of magnitude as the small scale velocity fields observed in the near-infrared with SINFONI in N88 A, suggestive of a large scale expulsion of gas from the region.

iv Extinction maps have been generated for the two regions (although with large uncertainties) and show that the low levels of extinction towards optical emission in massive star forming regions found in Chapter 5 are ubiquitous across the entirety of the N88 and N113 H II regions.

It is clear that when the high spectral resolution Fabry-Perot data from SALT/RSS are available, these two regions are prime targets for investigations of the interplay between massive star formation and cloud scale gas dynamics in the Magellanic Clouds.

8 Discussion, conclusions and future work

In this thesis the first high spatial resolution spectroscopic study of a sample of massive YSOs in the Magellanic Clouds has been presented. 22 *Spitzer* selected massive YSO candidates were observed with SINFONI in the K-band (3 in LHA 120-N113 in the LMC and 19 in the SMC) described in Chapters 3 and 4. Both previously available and newly obtained spectra towards optical counterparts for 35 massive YSOs in the SMC as well as N113-YSO03 were analysed in Chapter 5. Additional SINFONI $H + K$ archival data towards seven embedded clusters in the LMC were analysed in Chapter 6, identifying 9 massive YSOs. Finally in Chapter 7 Fabry-Perot interferometric observations are presented towards two H II regions in the Magellanic Clouds, used to develop and verify data reduction and treatment procedures for Fabry-Perot interferometry at SALT.

In this final chapter, I will discuss the findings of this work as a whole, starting with a discussion regarding all of the previous chapters, followed by a note on future studies, and ending with a summary of the key conclusions of the work.

8.1 The interstellar medium of the Magellanic Clouds

The integral field spectroscopic observations towards massive YSOs in the SMC have revealed the presence of several large scale outflows, in some cases up to 1 pc in length (e.g. #22 A) with velocity gradients in the range of 5–30 $\mathrm{km\,s^{-1}}$. This includes three sources (#03, 28 A and 31) which appear to have left large low density, readily ionized cavities in the wake of outflows. In both the LMC and SMC compact H II regions have been observed up to $\sim$1 pc in diameter centred on massive stars with expansion velocities on the order of $\sim$10 $\mathrm{km\,s^{-1}}$. This indicates that massive YSOs are able to have a significant localised impact on the ISM of the Magellanic Clouds, creating large cavities and ionizing large volumes of interstellar gas.

The presence of large scale PDRs have been inferred towards massive star-forming regions in the LMC through observations of photo-excited H_2 emission (Chapter 6). These PDRs are likely to also be the primary sources of the PAH emission present in the *Spitzer* spectro-

scopic data for these regions analysed in Seale et al. (2009). Young massive stars and later stage massive YSOs therefore seem to actively drive much of the gas-phase chemistry in the surrounding ISM.

The median visual extinction estimates derived from the near-infrared observations towards massive YSOs in LHA 120-N113 (Chapter 3), the SMC (Chapter 4) and the LMC sample discussed in Chapter 6 are plotted against metallicity in Fig. 8.1, alongside the median extinction towards massive YSOs in the Galactic sample of Cooper et al. (2013). This figure assumes that metallicity is consistently 1, 0.5 and $0.2\,Z_{\odot}$ for the Milky Way, LMC and SMC respectively. Also shown in Fig. 8.1 is the median for the optical emission towards the SMC sample of massive YSOs. There is a clear reduction in median extinction towards massive YSOs in the lower metallicity environments with respect to the Galactic sample. The change in median extinction between the LMC and SMC is small compared to the change between the Galactic sample and the LMC. As discussed in Chapter 6, the LMC sample is likely to be biased towards later-stage and therefore less deeply embedded YSOs which could explain this finding. It is also worth noting that the extinction measurements towards sources in the Galactic sample also include a contribution resulting from the variable line-of-sight extinction through the plane of the Galaxy. In contrast, the line of sight extinction to the Magellanic Clouds is relatively small.

Optical emission line measurements presented in Chapter 5 indicate that the optical emission detected towards massive YSOs in the SMC is photo-excited and originates from a much shallower region of the molecular cloud than the YSOs detected with SINFONI. Making the assumption that the primary exciting source of the optical emission is indeed the same source observed in the near-infrared, this is indicative of a porous, possibly clumpy ISM allowing a large mean-free-path for UV photons. This finding is consistent with theoretical studies of the ISM which predict high porosity in low metallicity environments (Dimaratos et al., 2015) and with observational studies which find that the ISM does indeed tend to be more porous in low metallicity dwarf galaxies (Madden et al., 2006; Cormier et al., 2015; Chevance et al., 2016). In some cases where the targets reside in relatively crowded fields (e.g. LHA 120-N113 and LHA 115-N88) much of the optical emission may result from exciting sources other than the YSOs detected with SINFONI.

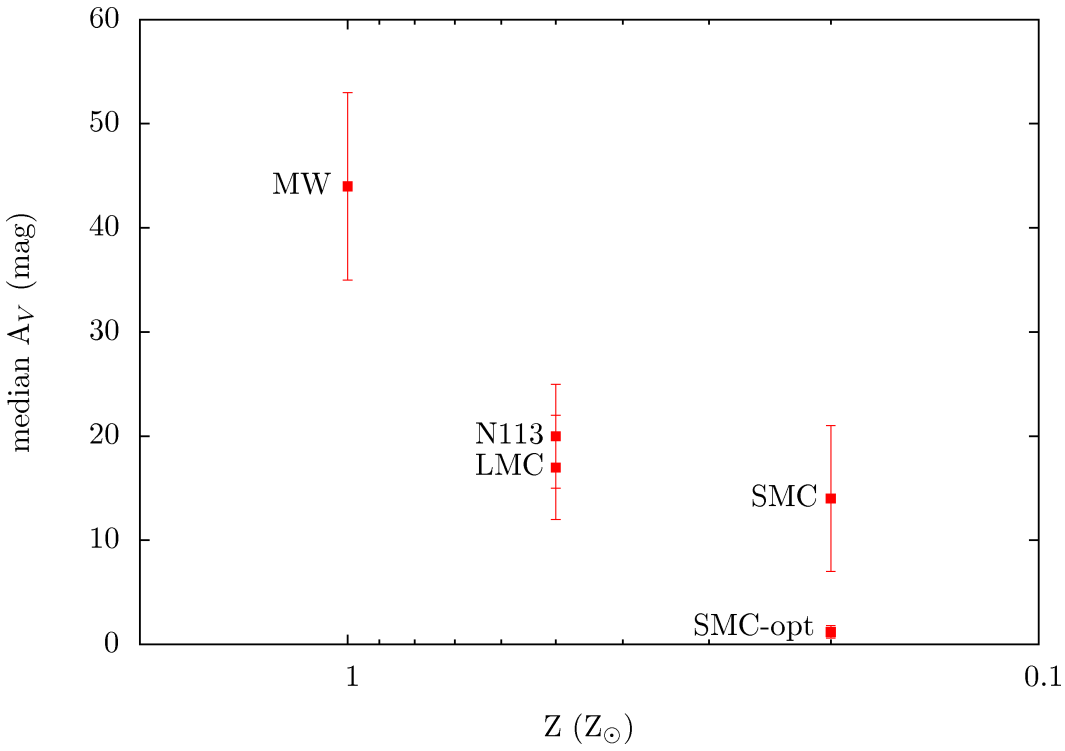

Figure 8.1: Median visual extinction against metallicity derived from near-infrared observations for the Milky Way, N113 (Chapter 3), the LMC YSOs (Chapter 6), and SMC (Chapter 4) and optical observations towards massive YSOs in the SMC (SMC-opt, Chapter 5). This plot assumes that the metallicities across the whole galaxies are 1, 0.5 and 0.2 $Z_\odot$ for the Milky Way, LMC and SMC respectively. The error bars are representative of the median absolute deviation for each sample.

8.2 Discs in the Magellanic Clouds

As discussed in Chapter 1, our current understanding of star formation requires dusty discs as a necessity for the formation of massive stars due to their role in overcoming the radiative pressure problem. The primary disc tracers used in this study are the CO bandhead emission in the *K*-band and fluorescent Fe II emission lines in the *H*-band.

The CO bandhead emission is highly dependant on disc geometry and therefore a low detection rate is not necessarily surprising, but the ∼5% detection rate in the SMC YSOs (Chapter 4) falls well below the rate detected towards Galactic YSOs (∼15 %, Cooper et al. 2013); in the one source where CO emission is present, it is weak. Furthermore no CO bandhead emission is detected towards the LMC samples in Chapters 3 and 6. One possible explanation is that the combination of lower carbon and oxygen abundances could lead to significantly lower levels of CO in discs. One should however be mindful of the relatively small sample sizes compared to the Galactic samples and possible selection effects present in the LMC sample (biased towards more evolved objects). Finally, the low detection rate of CO emission may be due to a change in physical conditions of the discs brought on by the difference in metallicity. This could take the form of higher temperatures and a harder radiation field in the discs leading to a higher rate of CO destruction, or it could be that the metallicity has a significant effect on the lifetimes of the CO emitting regions of protostellar discs.

Fluorescent Fe II emission appears to be present towards ∼78% of the massive YSOs identified in the LMC in Chapter 6, three times the rate of detection in the Galactic sample and only towards those which are classed as later-stage YSOs exhibiting a full Brackett series and little or no H_2 emission. This is probably a selection effect rather than representative of physical differences in discs in the Magellanic Clouds, since Fe II emission is usually found in sources which exhibit strong Brackett series emission (Cooper et al., 2013) which dominate the LMC sample. Furthermore in the Galactic sample only ∼8% of sources which show either disc indicator exhibit both CO bandhead emission and fluorescent Fe II emission. Nevertheless these observations are the most direct indications of discs around massive protostars in the LMC to date.

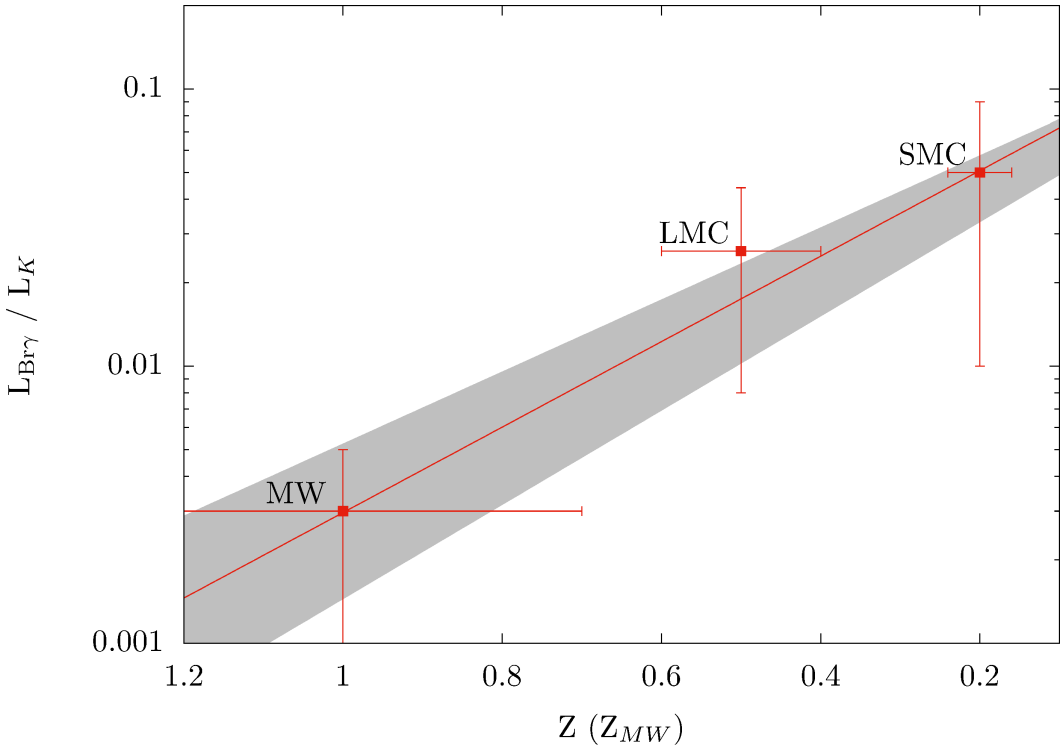

Figure 8.2: Plot of the ratio between Brγ and integrated K-band flux against metallicity for the Milky Way (MW), LMC and SMC assuming that the metallicities across the whole galaxies are 1, 0.5 and 0.2 $Z_\odot$. The N113 data from Chapter 3 is included in the LMC sample. The error bars in the y-axis are representative of the median absolute deviation for each sample, error bars on the x-axis are indicative of the standard deviation of H II region metallicities measured in each galaxy and red line shows the ATS regression fitted (see text). The filled grey area represents the uncertainty in the fitted ATS regression.

8.3 The effect of metallicity on accretion rates

The effects of metallicity on the accretion rates of protostars and PMS stars remains a contentious area of study. In this work Brγ emission in the K-band has been used as a tracer of accretion based on the assumption that Brγ emission towards massive YSOs scales with accretion luminosity in a similar manner to the empirically derived relationship for intermediate stars from Calvet et al. (2004).

There can be little doubt that a Brγ excess is observed towards the sample of YSOs in the SMC ($Z_{SMC} \sim 0.2\,Z_\odot$) compared to Galactic sources of the same K-band magnitude range as presented in Chapter 4. Assuming that this is an effect solely caused by the lower metallicity environment of the SMC, it is expected that the massive YSOs in the LMC will fall between the Galactic and SMC samples. However, the YSO candidates in the LMC sample (Chapter 6) tend to exhibit Brγ fluxes at the high end of the SMC sample distribution with a large scatter and the ATS regression fitted to these data falls much higher than that for the SMC

sample (see Fig. 6.18). This implies that although it apparently has some effect, metallicity may not in fact be a dominant factor in determining the accretion rates of massive YSOs. It should be noted that the LMC sample is small, highly biased towards later-stage YSOs and only four sources lie within the same K-band range sampled in the SMC. Furthermore, it is clear from Fig. 6.10 that the LMC sample deviates significantly from the SMC and Galactic samples in terms of He I emission, showing a similar excess to that seen in Brγ emission. This is likely indicative that a different production mechanism for both He I and Brγ is dominant in the LMC sample than in the Galactic and SMC samples, most likely strong stellar winds from the more evolved LMC sample.

In Fig. 8.2 the median ratio between Brγ integrated flux and the K-band continuum flux integrated in the range 2.028–2.295 μm is plotted against metallicity for the Galactic massive YSO data from Cooper et al. (2013), the LMC sample including N113 (Chapters 3 and 6) and the SMC sample (Chapter 4). In this figure it is assumed that the median metallicities of the Milky Way, LMC and SMC are 1.0, 0.5 and 0.2 $Z_{\odot}$, respectively. The apparent discrepancy between the position of the LMC median in Fig. 8.2 and the positions of the LMC YSOs in Fig. 6.19 can be explained by the two sources with $K < -8$ in the LMC sample which significantly reduce the median value of $L_{\mathrm{Br}\gamma}/L_K$ in such a small sample.

Despite the large levels of deviation from the median in each sample, Fig. 8.2 shows a clear correlation between the normalised Brγ flux and the metallicity of the galaxy in which the YSOs are found. The $L_{\mathrm{Br}\gamma}/L_K$ values for all three samples (Galactic, LMC and SMC) against metallicity (1.0, 0.5 and 0.2 $Z_{\odot}$, respectively) were fitted with an ATS regression. Uncertainties in the ATS regression were calculated as in previous chapters using the standard deviation of the metallicities of H II regions in each of the represented galaxies (Dufour, Shields & Talbot, 1982) for the randomly generated distributions in Z. The resulting fit is given in Eqn. 8.1 and has corresponding τ and p values of -0.32 and 5.7×10^{-15}, respectively indicating a definite, if relatively weak correlation.

$$\log(\mathrm{L}_{\mathrm{Br}\gamma}/\mathrm{L}_K) = (-1.5 \pm 0.2)\mathrm{Z} - (0.99 \pm 0.08). \tag{8.1}$$

This ATS regression and the Calvet et al. (2004) relation from Eqn. 4.3 can be used to establish that $\log(\mathrm{L}_{acc}) \propto -1.38\mathrm{Z}$. This is based on the assumptions that neither the K-band magnitude nor stellar radius vary significantly with metallicity and that the age and mass distributions of the samples are roughly the same. Therefore based on these assumptions,

the mass accretion rate ($\dot{M}$) seems to vary with metallicity as:

$$\dot{M} \propto 10^{(-1.4\pm0.2)\,\mathrm{Z/Z}_{MW}}. \tag{8.2}$$

The results of the Brγ emission analysis certainly suggest a strong (but probably complex) relationship between metallicity and the accretion rates in massive YSOs. This is consistent with the conclusions for lower mass PMS stars in the Magellanic Clouds (De Marchi, Panagia & Romaniello, 2010; De Marchi et al., 2011; Spezzi et al., 2012; De Marchi, Beccari & Panagia, 2013). A much larger sample of spectroscopic observations towards massive YSOs in the LMC is required to confirm/constrain this relation. The large degree of scatter in the samples used to derive this relationship suggests that metallicity is only one of a number of factors which have significant effects on accretion rates.

To constrain the effects of metallicity on massive star formation a more complete theoretical picture of the accretion process in massive YSOs is required, producing models covering a wide range of chemical abundances, ages and masses. Further observations are required both in the near-infrared and at longer wavelengths to determine accurate masses and luminosities and to sample larger range of metallicities in order to derive the relationship between metallicity and accretion rates empirically. Additionally more accurate techniques of estimating the ages and/or evolutionary status of sources would allow more precise constraints on the effects of metallicity.

8.4 Future prospects

The advantages of obtaining *H*-band spectra in addition to the *K*-band observations were made clear in Chapter 6, including tracers of both discs and outflows through Fe II emission lines. Additionally, more precise extinction estimates can be obtained without relying of the Q-branch H_2 emission which lies in a spectral region of poor atmospheric transmission. This has therefore formed the motivation for a current ongoing programme of 5 nights using IRIS2 at the Anglo-Australian Telescope (programme ID:A/2016B/102, PI: Jacob Ward) to obtain *H*-band spectra towards all of the massive YSOs in the SMC presented in Chapter 4. Due to technical problems with the instrument in the first run and poor weather conditions in the second, spectra were not obtained for all targets and a second *H*-band spectroscopy run is scheduled using SOFI at ESO's New Technology Telescope to complete the required observations (programme ID: 099.C-0213, PI: Jacob Ward).

As suggested in Section 8.3, obtaining a statistically significant sample of massive YSOs in the LMC is a top priority in taking this work further. Through the use of the K-band Multi Object Spectrograph (KMOS) at the VLT, a large sample of IFU observations can be obtained in a relatively short amount of time with the 24 IFU arms operating simultaneously. In a three night run (the same length used to carry out 23 observations with SINFONI), a sample of massive YSOs in the LMC can be observed with KMOS which is an order of magnitude larger than the current SMC sample. The target selection for such a study would cover a much wider range of evolutionary states based on the Seale et al. (2009) catalogue as well as observing sources across the entire LMC (the majority of previous studies are focussed on very active star forming regions such as 30 Doradus). Using this large and relatively unbiased sample, the question of accretion rates in the LMC compared to those in the SMC and the Galaxy may be settled. With the $H + K$ grating on KMOS, a statistical analysis can be undertaken using the CO bandhead and fluorescent Fe II disc tracers in in an attempt to understand the effects of metallicity on disc lifetimes and conditions. A large dataset will also allow the measurement of potentially hundreds of outflow structures, allowing a comparison to Galactic data sets such as UWISH2 which will lead to a better understanding of the effects of metallicity on the interaction between massive YSOs and the ISM.

8.5 Beyond the Magellanic Clouds

With the advent of extreme adaptive optics systems and upcoming 30-metre class ground based observatories as well as the arrival of a new generation space based observatories, high resolution studies of massive star formation can be extended beyond the Milky Way and its satellite galaxies.

The Mid-Infrared Instrument (MIRI, Wright et al. 2004) on the James Webb Space Telescope (JWST) will allow a SAGE-like survey to be conducted towards more distant galaxies in the local group in the wavelength range 5–28 μm. The pixel scale of MIRI is $0\farcs11$ with diffraction limited resolutions of $0\farcs22$ to $1\farcs0$ (at 5.6 μm and 25.5 μm respectively), an improvement of almost an order of magnitude on *Spitzer*. This means that spatial scales comparable to those probed by SAGE can be obtained at a distance of $\sim$400 kpc, allowing the study of the vast majority of the Milky Way's satellite galaxies. Other than the Magellanic Clouds, this sample includes almost exclusively dwarf spheroidal galaxies with little or no star formation. With a sacrifice in spatial resolution (by a factor of 2–3), SAGE-like surveys can be conducted towards both other large spiral galaxies in the local group: Andromeda (M31) and

Triangulum (M33) as well as their satellites. Whilst JWST does not offer the wavelength range offered by MIPS on *Spitzer* (see Chapter 1) it is capable of carrying out near-infrared observations in imaging, spectroscopic and IFU modes. The optical design of JWST gives each instrument a unique optical path meaning that near-infrared and mid-infrared observations can be carried out simultaneously (limited by the data transfer rate), which has the potential to significantly increase the efficiency of large multi-wavelength surveys.

The new generation of thirty-metre class telescopes, the European Extremely Large Telescope (E-ELT), the Giant Magellan Telescope (GMT) and the Thirty Metre Telescope (TMT), will all eventually be equipped with visible and near-infrared IFUs which will offer improvements in spatial resolution of greater than an order of magnitude compared with SINFONI. This will allow high-resolution follow-up studies for surveys of more distant local group galaxies analogous to the work presented in this thesis. A wider range of environments and more of the metallicity parameter space will also be sampled (M31 and M33 exhibit significant abundance gradients, Rosolowsky & Simon 2008; Sanders et al. 2012), leading to considerable constraints being placed on the effect of different environments on the accretion rates of massive YSOs.

Whilst a great deal has been learnt from star formation studies of our own Galaxy and undoubtedly a vast amount can yet be gained from Galactic studies, they can only provide a relatively limited view of star formation. Additionally the effects and process of star formation on the scale of an entire galaxy can never be observed in the Milky Way due to obscuration of lines of sight through the Galactic Plane and in particular through the Galactic Centre. The nearby galaxies of the local group therefore offer insights into the effects of galactic interactions and morphologies on current and past star formation. In order to develop a more detailed understanding of massive star formation the effect of different environments (including but not limited to different elemental abundances) must be understood. Star formation studies towards other galaxies in the local group from Galactic scales to the formation of individual stars therefore represent an important step towards understanding massive star formation.

8.6 Conclusions

Although each chapter has revealed a number of interesting results, the key findings of this thesis taken as a whole can be summarised below in five key points:

i This work highlights the limitations of relying solely of low-resolution long-wavelength

data as the basis of classification schemes. Stark differences in morphological and spectroscopic properties of have been revealed for *Spitzer* sources which were previously thought to be almost identical.

ii Optical emission towards massive YSOs is not uncommon in the Magellanic Clouds; however, without exception it originates from a shallower region of the molecular cloud, possibly forming a shell of optical emission. This is most likely a result of the high porosity and clumpiness associated with the low metallicity ISM.

iii The large scale outflows, compact H II regions and PDRs observed towards massive YSOs in the Magellanic Clouds in Chapters 3, 4, 6 and 7 show that massive star formation has a profound effect on the local ISM.

iv The commonly used CO bandhead emission disc tracer is absent from all but one spectrum analysed in this work. It is unlikely that this indicates a low number of discs as these are believed to be necessary for continued accretion in massive YSOs. In Chapter 6 the fluorescent Fe II emission (also associated with discs) was found in 76 % of massive YSOs, indicating that the low detection rate of CO does not necessarily imply a low number of discs. Possible explanations for the low CO bandhead emission detection rate are a depletion of CO in the gas phase or the destruction of CO in lower-metallicity discs with less dust shielding.

v Based on Brγ emission flux measurements, the accretion rates in massive YSOs have been found to increase from the Milky Way, to the LMC, to the SMC. Assuming metallicities of 1.0, 0.5 and 0.2 $Z_{\odot}$ for the Milky Way, LMC and SMC a correlation between Brγ emission and metallicity is found, suggestive of a significant relationship between accretion rates and metallicity.

Through the use of high-spatial-resolution integral field spectroscopy, in combination with optical spectroscopy and Fabry-Perot interferometry, a deeper understanding of a sample of massive YSOs in the Magellanic Clouds has been achieved than was previously possible with existing data. The environment in which massive stars form clearly has a significant impact on key aspects of the star formation process including accretion and the interaction between massive protostars and the ISM. Conditions within protostellar discs are also likely to be affected by low metallicities although this remains largely unconstrained. Further observations of larger samples of massive YSOs in the Magellanic Clouds and more distant galaxies will allow the effects of metallicity on star forming regions to be constrained further

whilst providing valuable insights into the massive star formation mechanism, the details of which remain highly uncertain.

Bibliography

Acke B., van den Ancker M. E., 2004, A&A, 426, 151

Akritas M. G., Murphy S. A., Lavalley M. P., 1995, Journal of the American Statistical Association, 90, 170

Alexander R. D., Clarke C. J., Pringle J. E., 2006a, MNRAS, 369, 216

Alexander R. D., Clarke C. J., Pringle J. E., 2006b, MNRAS, 369, 229

Allen M. G., Groves B. A., Dopita M. A., Sutherland R. S., Kewley L. J., 2008, ApJS, 178, 20

Allison R. J., Goodwin S. P., Parker R. J., de Grijs R., Portegies Zwart S. F., Kouwenhoven M. B. N., 2009, ApJL, 700, L99

Arfken G. B., 1985, Mathematical Methods for Physicists

Baba J., Morokuma-Matsui K., Saitoh T. R., 2017, MNRAS, 464, 246

Baldwin J. A., Ferland G. J., Korista K. T., Hamann F., LaCluyzé A., 2004, ApJ, 615, 610

Balfour S. K., Whitworth A. P., Hubber D. A., Jaffa S. E., 2015, MNRAS, 453, 2471

Bally J., O'Dell C. R., McCaughrean M. J., 2000, AJ, 119, 2919

Barbosa C. L., Damineli A., Blum R. D., Conti P. S., 2003, AJ, 126, 2411

Bate M. R., 2011, MNRAS, 417, 2036

Beltrán M. T., Cesaroni R., Zhang Q., Galván-Madrid R., Beuther H., Fallscheer C., Neri R., Codella C., 2011, A&A, 532, A91

Benjamin R. A. et al., 2003, PASP, 115, 953

Bernard J.-P. et al., 2008, AJ, 136, 919

Bestenlehner J. M. et al., 2011, A&A, 530, L14

Beuther H., Linz H., Bik A., Goto M., Henning T., 2010, A&A, 512, A29

Black J. H., van Dishoeck E. F., 1987, ApJ, 322, 412

Bolatto A. D. et al., 2007, ApJ, 655, 212

Bonnell I. A., Bate M. R., 2005, MNRAS, 362, 915

Bonnell I. A., Bate M. R., 2006, MNRAS, 370, 488

Bonnell I. A., Bate M. R., Clarke C. J., Pringle J. E., 2001, MNRAS, 323, 785

Bonnet H. et al., 2003, in Society of Photo-Optical Instrumentation Engineers (SPIE) Conference Series, Vol. 4839, Adaptive Optical System Technologies II, Wizinowich P. L., Bonaccini D., eds., pp. 329–343

Breen S. L., Lovell J. E. J., Ellingsen S. P., Horiuchi S., Beasley A. J., Marvel K., 2013, MNRAS, 432, 1382

Bressert E. et al., 2012, A&A, 542, A49

Brooks K. J., Whiteoak J. B., 1997, MNRAS, 291, 395

Buckley D. A. H., Swart G. P., Meiring J. G., 2006, in Society of Photo-Optical Instrumentation Engineers (SPIE) Conference Series, Vol. 6267, Society of Photo-Optical Instrumentation Engineers (SPIE) Conference Series

Calvet N., Muzerolle J., Briceño C., Hernández J., Hartmann L., Saucedo J. L., Gordon K. D., 2004, AJ, 128, 1294

Calzetti D., 2001, PASP, 113, 1449

Calzetti D. et al., 2007, ApJ, 666, 870

Cardelli J. A., Clayton G. C., Mathis J. S., 1989, ApJ, 345, 245

Carlson L. R., Sewiło M., Meixner M., Romita K. A., Lawton B., 2012, A&A, 542, A66

Casali M. M., Eiroa C., 1996, A&A, 306, 427

Charmandaris V., Heydari-Malayeri M., Chatzopoulos E., 2008, A&A, 487, 567

Chen C.-H. R., Chu Y.-H., Gruendl R. A., Gordon K. D., Heitsch F., 2009a, ApJ, 695, 511

Chen C.-H. R. et al., 2014, ApJ, 785, 162

Chen H.-R. V., Keto E., Zhang Q., Sridharan T. K., Liu S.-Y., Su Y.-N., 2016, ApJ, 823, 125

Chen Y., Yao Y., Yang J., Zeng Q., Sato S., 2009b, ApJ, 693, 430

Chevance M. et al., 2016, A&A, 590, A36

Churchwell E., 1990, ARA&A, 2, 79

Churchwell E., 2002, ARA&A, 40, 27

Churchwell E. et al., 2009, PASP, 121, 213

Ciardi D. R., Telesco C. M., Packham C., Gómez Martin C., Radomski J. T., De Buizer J. M., Phillips C. J., Harker D. E., 2005, ApJ, 629, 897

Connelley M. S., Greene T. P., 2014, AJ, 147, 125

Cooper H. D. B., 2013, PhD thesis, University of Leeds

Cooper H. D. B. et al., 2013, MNRAS, 430, 1125

Cormier D. et al., 2015, A&A, 578, A53

Cox A. N., 2000, Allen's astrophysical quantities. Springer-Verlag

Crawford E. J., Filipović M. D., de Horta A. Y., Wong G. F., Tothill N. F. H., Drašković D., Collier J. D., Galvin T. J., 2011, Serbian Astron. J., 183, 95

Crutcher R. M., Hakobian N., Troland T. H., 2009, ApJ, 692, 844

Cyganowski C. J. et al., 2008, AJ, 136, 2391

Davies B., Hoare M. G., Lumsden S. L., Hosokawa T., Oudmaijer R. D., Urquhart J. S., Mottram J. C., Stead J., 2011, MNRAS, 416, 972

Davies B., Lumsden S. L., Hoare M. G., Oudmaijer R. D., de Wit W.-J., 2010, MNRAS, 402, 1504

Davis C. J. et al., 2011, A&A, 528, A3

De Marchi G., Beccari G., Panagia N., 2013, ApJ, 775, 68

De Marchi G., Panagia N., Romaniello M., 2010, ApJ, 715, 1

De Marchi G., Panagia N., Romaniello M., Sabbi E., Sirianni M., Prada Moroni P. G., Degl'Innocenti S., 2011, ApJ, 740, 11

Devereux N. A., Scowen P. A., 1994, AJ, 108, 1244

Dimaratos A., Cormier D., Bigiel F., Madden S. C., 2015, A&A, 580, A135

Dobbs C. L. et al., 2014, Protostars and Planets VI, 3

Donehew B., Brittain S., 2011, AJ, 141, 46

Draine B. T., Lee H. M., 1984, ApJ, 285, 89

Dufour R. J., 1984, in IAU Symposium, Vol. 108, Structure and Evolution of the Magellanic Clouds, van den Bergh S., de Boer K. S. D., eds., pp. 353–360

Dufour R. J., Shields G. A., Talbot, Jr. R. J., 1982, ApJ, 252, 461

Durisen R. H., Boss A. P., Mayer L., Nelson A. F., Quinn T., Rice W. K. M., 2007, Protostars and Planets V, 607

Egan M. P. et al., 2003, The Midcourse Space Experiment Point Source Catalog Version 2.3 Explanatory Guide, Air Force Research Laboratory Technical Report AFRL-VS-TR-2003-1589

Eisenhauer F. et al., 2003, in Society of Photo-Optical Instrumentation Engineers (SPIE) Conference Series, Vol. 4841, Instrument Design and Performance for Optical/Infrared Ground-based Telescopes, Iye M., Moorwood A. F. M., eds., p. 1548

Eisenhauer F., Tecza M., Mengel S., Thatte N. A., Roehrle C., Bickert K., Schreiber J., 2000, in Society of Photo-Optical Instrumentation Engineers (SPIE) Conference Series, Vol. 4008, Optical and IR Telescope Instrumentation and Detectors, Iye M., Moorwood A. F., eds., pp. 289–297

Ellingsen S. P., 2006, ApJ, 638, 241

Engelbracht C. W., Gordon K. D., Rieke G. H., Werner M. W., Dale D. A., Latter W. B., 2005, ApJ, 628, L29

Ercolano B., Clarke C. J., 2010, MNRAS, 402, 2735

Fairlamb J. R., Oudmaijer R. D., Mendigutía I., Ilee J. D., van den Ancker M. E., 2015, MNRAS, 453, 976

Fallscheer C., Beuther H., Zhang Q., Keto E., Sridharan T. K., 2009, A&A, 504, 127

Fazio G. G. et al., 2004, ApJS, 154, 10

Feast M. W., Thackeray A. D., Wesselink A. J., 1961, MNRAS, 122, 433

Fish V. L., 2007, in IAU Symposium, Vol. 242, Astrophysical Masers and their Environments, Chapman J. M., Baan W. A., eds., pp. 71–80

Forbrich J., Stanke T., Klein R., Henning T., Menten K. M., Schreyer K., Posselt B., 2009, A&A, 493, 547

Froebrich D. et al., 2011, MNRAS, 413, 480

Fukui Y. et al., 2016, ApJ, 820, 26

Galliano F., Madden S. C., Jones A. P., Wilson C. D., Bernard J.-P., Le Peintre F., 2003, A&A, 407, 159

Gallimore J. F., Cool R. J., Thornley M. D., McMullin J., 2003, ApJ, 586, 306

Gennaro M., Brandner W., Stolte A., Henning T., 2011, MNRAS, 412, 2469

Gibb A. G., Davis C. J., Moore T. J. T., 2007, MNRAS, 382, 1213

Glover S. C. O., Clark P. C., 2012, MNRAS, 426, 377

Goldreich P., Kwan J., 1974, ApJ, 189, 441

Gonidakis I., Livanou E., Kontizas E., Klein U., Kontizas M., Belcheva M., Tsalmantza P., Karampelas A., 2009, A&A, 496, 375

Gonzalez R. C., Woods R. E., 2002, Digital image processing. Prentice-Hall

Gordon K. D., Clayton G. C., Misselt K. A., Landolt A. U., Wolff M. J., 2003, ApJ, 594, 279

Gordon K. D. et al., 2011, AJ, 142, 102

Gordon K. D. et al., 2014, ApJ, 797, 85

Gorjian V. et al., 2004, ApJS, 154, 275

Groenewegen M. A. T., 2000, A&A, 363, 901

Gruendl R. A., Chu Y.-H., 2009, ApJS, 184, 172

Hanner M. S., Brooke T. Y., Tokunaga A. T., 1998, ApJ, 502, 871

Hanson M. M., Howarth I. D., Conti P. S., 1997, ApJ, 489, 698

Harries T. J., Hilditch R. W., Howarth I. D., 2003, MNRAS, 339, 157

Harris J., Zaritsky D., 2004, AJ, 127, 1531

Hau G., Kaufer A., 2015, Very Large Telescope SINFONI User Manual P97, VLT-MAN-ESO-14700-3517

Haworth T. J. et al., 2015, MNRAS, 450, 10

Helsel D. R., 2005, Nondectects and Data Analysis; Statistics for censored environmental data. John Wiley and Sons

Henize K. G., 1956, ApJS, 2, 315

Hennebelle P., Falgarone E., 2012, ARA&A, 20, 55

Heydari-Malayeri M., Charmandaris V., Deharveng L., Rosa M. R., Zinnecker H., 1999, A&A, 347, 841

Heydari-Malayeri M., Le Bertre T., Magain P., 1988, A&A, 195, 230

Heydari-Malayeri M., Meynadier F., Charmandaris V., Deharveng L., Le Bertre T., Rosa M. R., Schaerer D., 2003, A&A, 411, 427

Heydari-Malayeri M., Rosa M. R., Schaerer D., Martins F., Charmandaris V., 2002, A&A, 381, 951

Hilditch R. W., Howarth I. D., Harries T. J., 2005, MNRAS, 357, 304

Hill T., Burton M. G., Minier V., Thompson M. A., Walsh A. J., Hunt-Cunningham M., Garay G., 2005, MNRAS, 363, 405

Hoare M. G., 2005, AP&SS, 295, 203

Hoare M. G., Kurtz S. E., Lizano S., Keto E., Hofner P., 2007, Protostars and Planets V, 181

Hoare M. G. et al., 2012, PASP, 124, 939

Hollenbach D. J., Tielens A. G. G. M., 1997, ARA&A, 35, 179

Hollenbach D. J., Tielens A. G. G. M., 1999, Reviews of Modern Physics, 71, 173

Hollenbach D. J., Yorke H. W., Johnstone D., 2000, Protostars and Planets IV, 401

Hosokawa T., Omukai K., 2009, ApJ, 691, 823

Houck J. R. et al., 2004, ApJS, 154, 18

Ilee J. D., Cyganowski C. J., Nazari P., Hunter T. R., Brogan C. L., Forgan D. H., Zhang Q., 2016, MNRAS, 462, 4386

Ilee J. D. et al., 2013, MNRAS, 429, 2960

Imai H., Katayama Y., Ellingsen S. P., Hagiwara Y., 2013, MNRAS, 432, L16

Indebetouw R. et al., 2013, ApJ, 774, 73

Ioannidis G., Froebrich D., 2012, MNRAS, 425, 1380

Israel F. P. et al., 2003, A&A, 406, 817

Ita Y. et al., 2008, PASJ, 60, S435

Jaehnig K. O., Da Rio N., Tan J. C., 2015, ApJ, 798, 126

Jeans J. H., 1902, Philosophical Transactions of the Royal Society of London Series A, 199, 1

Jenkins E. B., 2009, ApJ, 700, 1299

Kahn F. D., 1974, A&A, 37, 149

Kalari V. M., Vink J. S., 2015, ApJ, 800, 113

Kalari V. M. et al., 2014, A&A, 564, L7

Kato D. et al., 2007, PASJ, 59, 615

Keller S. C., Wood P. R., 2006, ApJ, 642, 834

Kendall M. G., 1938, Biometrika, 30, 81

Kennicutt, Jr. R. C., 1984, ApJ, 287, 116

Kewley L. J., Dopita M. A., Sutherland R. S., Heisler C. A., Trevena J., 2001, ApJ, 556, 121

Kim W.-T., Ostriker E. C., Stone J. M., 2002, ApJ, 581, 1080

Kitchin C. R., 2003, Astrophysical techniques. Taylor & Francis Group

Klessen R. S., 2011, in EAS Publications Series, Vol. 51, EAS Publications Series, Charbonnel C., Montmerle T., eds., pp. 133–167

Klessen R. S., Glover S. C. O., 2014, ArXiv e-print: 1412.5182

Kobulnicky H. A., Nordsieck K. H., Burgh E. B., Smith M. P., Percival J. W., Williams T. B., O'Donoghue D., 2003, in Society of Photo-Optical Instrumentation Engineers (SPIE) Conference Series, Vol. 4841, Instrument Design and Performance for Optical/Infrared Ground-based Telescopes, Iye M., Moorwood A. F. M., eds., p. 1634

Kong S., Tan J. C., Caselli P., Fontani F., Liu M., Butler M. J., 2017, ApJ, 834, 193

Koornneef J., 1983, A&A, 128, 84

Koornneef J., Israel F. P., 1985, ApJ, 291, 156

Kraus M., Krügel E., Thum C., Geballe T. R., 2000, A&A, 362, 158

Krtička J., 2006, MNRAS, 367, 1282

Krumholz M. R., 2015, ArXiv e-print: 1511.03457

Krumholz M. R., Klein R. I., McKee C. F., 2012, ApJ, 754, 71

Krumholz M. R., McKee C. F., 2005, ApJ, 630, 250

Kudritzki R. P., 2002, ApJ, 577, 389

Kuiper R., Klahr H., Beuther H., Henning T., 2010, ApJ, 722, 1556

Kuiper R., Yorke H. W., 2013, ApJ, 763, 104

Kuiper R., Yorke H. W., Turner N. J., 2015, ApJ, 800, 86

Kurt C. M., Dufour R. J., Garnett D. R., Skillman E. D., Mathis J. S., Peimbert M., Torres-Peimbert S., Ruiz M.-T., 1999, ApJ, 518, 246

Lada C. J., Shu F. H., 1990, Science, 248, 564

Laney C. D., Joner M. D., Pietrzyński G., 2012, MNRAS, 419, 1637

Lanz T., Hubeny I., 2003, ApJS, 146, 417

Lanz T., Hubeny I., 2007, ApJS, 169, 83

Lazendic J. S., Whiteoak J. B., Klamer I., Harbison P. D., Kuiper T. B. H., 2002, MNRAS, 331, 969

Leisy P., Dennefeld M., Alard C., Guibert J., 1997, A&AS, 121

Leroy A., Bolatto A., Stanimirovic S., Mizuno N., Israel F., Bot C., 2007, ApJ, 658, 1027

Lindsay E. M., 1961, AJ, 66, 169

Luhman M. L., Jaffe D. T., 1996, ApJ, 463, 191

Luhman M. L., Jaffe D. T., Keller L. D., Pak S., 1994, ApJL, 436, L185

Lumsden S. L., Hoare M. G., Oudmaijer R. D., Richards D., 2002, MNRAS, 336, 621

Lumsden S. L., Hoare M. G., Urquhart J. S., Oudmaijer R. D., Davies B., Mottram J. C., Cooper H. D. B., Moore T. J. T., 2013, ApJS, 208, 11

Lumsden S. L., Puxley P. J., Doherty R. M., 1994, MNRAS, 268, 821

Lumsden S. L., Puxley P. J., Hoare M. G., 2001, MNRAS, 328, 419

Lumsden S. L., Wheelwright H. E., Hoare M. G., Oudmaijer R. D., Drew J. E., 2012, MNRAS, 424, 1088

Madden S. C., Galliano F., Jones A. P., Sauvage M., 2006, A&A, 446, 877

Martín-Hernández N. L., Peeters E., Tielens A. G. G. M., 2008, A&A, 489, 1189

Martins F., Schaerer D., Hillier D. J., 2005, A&A, 436, 1049

Marx M., Dickey J. M., Mebold U., 1997, A&AS, 126

Massey P., Meyer M., 2001, Stellar Masses, Murdin P., ed.

McGee R. X., Newton L. M., 1981, Proc. Astron. Soc. Aust., 4, 189

McKee C. F., Tan J. C., 2003, ApJ, 585, 850

McKee C. F., Zweibel E. G., 1992, ApJ, 399, 551

Megeath S. T., Wilson T. L., Corbin M. R., 2005, ApJ, 622, L141

Meixner M. et al., 2010, A&A, 518, L71

Meixner M. et al., 2006, AJ, 132, 2268

Meixner M. et al., 2013, AJ, 146, 62

Mendigutía I., Calvet N., Montesinos B., Mora A., Muzerolle J., Eiroa C., Oudmaijer R. D., Merín B., 2011, A&A, 535, A99

Menezes R. B., da Silva P., Ricci T. V., Steiner J. E., May D., Borges B. W., 2015, MNRAS, 450, 369

Menezes R. B., Steiner J. E., Ricci T. V., 2014, MNRAS, 438, 2597

Menten K. M., 1991, ApJL, 380, L75

Mercer E. P. et al., 2007, ApJ, 656, 242

Mink D. J., 1997, in Astronomical Society of the Pacific Conference Series, Vol. 125, Astronomical Data Analysis Software and Systems VI, Hunt G., Payne H., eds., p. 249

Mink D. J., 2002, in Astronomical Society of the Pacific Conference Series, Vol. 281, Astronomical Data Analysis Software and Systems XI, Bohlender D. A., Durand D., Handley T. H., eds., p. 169

Moneti A., Pipher J. L., Helfer H. L., McMillan R. S., Perry M. L., 1984, ApJ, 282, 508

Mottram J. C. et al., 2011a, ApJL, 730, L33

Mottram J. C., Hoare M. G., Lumsden S. L., Oudmaijer R. D., Urquhart J. S., Meade M. R., Moore T. J. T., Stead J. J., 2010, A&A, 510, A89

Mottram J. C. et al., 2011b, A&A, 525, A149

Mouschovias T. C., 1976, ApJ, 207, 141

Mouschovias T. C., Spitzer, Jr. L., 1976, ApJ, 210, 326

Murakawa K., Lumsden S. L., Oudmaijer R. D., Davies B., Wheelwright H. E., Hoare M. G., Ilee J. D., 2013, MNRAS, 436, 511

Murphy T. et al., 2010, MNRAS, 402, 2403

Nishiyama S. et al., 2007, ApJ, 658, 358

North P., Gauderon R., Barblan F., Royer F., 2010, A&A, 520, A74

Oliveira J. M. et al., 2009, ApJ, 707, 1269

Oliveira J. M. et al., 2011, MNRAS, 411, L36

Oliveira J. M. et al., 2013, MNRAS, 428, 3001

Oliveira J. M., van Loon J. T., Stanimirović S., Zijlstra A. A., 2006, MNRAS, 372, 1509

Olsen K. A. G., 1999, AJ, 117, 2244

Osterbrock D. E., Ferland G. J., 2006, Astrophysics of gaseous nebulae and active galactic nuclei. University Science Books

Owen J. E., Ercolano B., Clarke C. J., Alexander R. D., 2010, MNRAS, 401, 1415

Panagia N., 1973, AJ, 78, 929

Panagia N., Romaniello M., Scuderi S., Kirshner R. P., 2000, ApJ, 539, 197

Patel N. A. et al., 2005, Nature, 437, 109

Pilbratt G. L. et al., 2010, A&A, 518, L1

Porter J. M., Drew J. E., Lumsden S. L., 1998, A&A, 332, 999

Prato L., Greene T. P., Simon M., 2003, ApJ, 584, 853

Puls J., Springmann U., Lennon M., 2000, A&AS, 141, 23

Purcell C. R. et al., 2013, ApJS, 205, 1

Rangwala N., Williams T. B., Pietraszewski C., Joseph C. L., 2008, AJ, 135, 1825

Ridge N. A., Moore T. J. T., 2001, A&A, 378, 495

Rieke G. H. et al., 2004, ApJS, 154, 25

Rigaut F., 2015, PASP, 127, 1197

Robitaille T. P., Whitney B. A., Indebetouw R., Wood K., 2007, ApJS, 169, 328

Robitaille T. P., Whitney B. A., Indebetouw R., Wood K., Denzmore P., 2006, ApJS, 167, 256

Roche P. F., Aitken D. K., Smith C. H., 1987, MNRAS, 228, 269

Roddier F., Roddier C., 1988, in European Southern Observatory Conference and Workshop Proceedings, Vol. 30, European Southern Observatory Conference and Workshop Proceedings, Ulrich M.-H., ed., p. 667

Roman-Duval J. et al., 2014, ApJ, 797, 86

Rosolowsky E., Simon J. D., 2008, ApJ, 675, 1213

Rousseeuw P. J., M. L. A., 1987, Robust Regression and Outlier Detection. Wiley

Ruiz-Velasco A. E., Felli D., Migenes V., Wiggins B. K., 2016, ApJ, 822, 101

Sanders N. E., Caldwell N., McDowell J., Harding P., 2012, ApJ, 758, 133

Sandstrom K. M., Bolatto A. D., Draine B. T., Bot C., Stanimirović S., 2010, ApJ, 715, 701

Scalise, Jr. E., Braz M. A., 1982, AJ, 87, 528

Schleuning D. A., Vaillancourt J. E., Hildebrand R. H., Dowell C. D., Novak G., Dotson J. L., Davidson J. A., 2000, ApJ, 535, 913

Schulz N. S., 2005, The Formation and Early Evolution of Stars, Second Edition. Springer-Verlag

Seale J. P., Looney L. W., Chu Y.-H., Gruendl R. A., Brandl B., Chen C.-H. R., Brandner W., Blake G. A., 2009, ApJ, 699, 150

Seale J. P., Looney L. W., Wong T., Ott J., Klein U., Pineda J. L., 2012, ApJ, 751, 42

Seale J. P. et al., 2014, AJ, 148, 124

Sen P. K., 1968, Journal of the American Statistical Association, 63, 1379

Seth A. C., Greenhill L. J., Holder B. P., 2002, ApJ, 581, 325

Sewiło M. et al., 2013, ApJ, 778, 15

Sewiło M. et al., 2010, A&A, 518, L73

Shepherd D. S., Kurtz S. E., 1999, ApJ, 523, 690

Shields J. C., 1993, ApJ, 419, 181

Shimonishi T., Onaka T., Kato D., Sakon I., Ita Y., Kawamura A., Kaneda H., 2008, ApJ, 686, L99

Shimonishi T., Onaka T., Kato D., Sakon I., Ita Y., Kawamura A., Kaneda H., 2010, A&A, 514, A12

Shu F. H., Adams F. C., Lizano S., 1987, ARA&A, 25, 23

Shull J. M., Hollenbach D. J., 1978, ApJ, 220, 525

Siebenmorgen R., Prusti T., Natta A., Müller T. G., 2000, A&A, 361, 258

Smecker-Hane T. A., Cole A. A., Gallagher, III J. S., Stetson P. B., 2002, ApJ, 566, 239

Smith N. et al., 2010, MNRAS, 406, 952

Spera M., Mapelli M., Jeffries R. D., 2016, MNRAS, 460, 317

Spezzi L., de Marchi G., Panagia N., Sicilia-Aguilar A., Ercolano B., 2012, MNRAS, 421, 78

Spiegel M. R., Lipschutz S., Spellman D., 2009, Vector Analysis (2nd ed.). McGraw-Hill Education

Stahler S. W., Palla F., 2004, The Formation of Stars. WILEY-VCH

Stanimirovic S., Staveley-Smith L., Dickey J. M., Sault R. J., Snowden S. L., 1999, MNRAS, 302, 417

Steiner J. E., Menezes R. B., Ricci T. V., Oliveira A. S., 2009, MNRAS, 395, 64

Storey P. J., Hummer D. G., 1995, MNRAS, 272, 41

Sugitani K. et al., 2010, ApJ, 716, 299

Tan J. C., Beltran M. T., Caselli P., Fontani F., Fuente A., Krumholz M. R., McKee C. F., Stolte A., 2014, in Accepted for publication as a chapter in Protostars and Planets VI, University of Arizona Press (2014)

Tanaka K. E. I., Tan J. C., Zhang Y., 2016, ApJ, 818, 52

Testor G., Lemaire J. L., Field D., 2003, A&A, 407, 905

Testor G., Lemaire J. L., Field D., Callejo G., 2005, A&A, 434, 497

Testor G., Lemaire J. L., Heydari-Malayeri M., Kristensen L. E., Diana S., Field D., 2010, A&A, 510, A95

Testor G., Pakull M., 1985, A&A, 145, 170

Theil H., 1950, Proceedings of the Royal Netherlands Academy of Sciences, 53, 386

Tielens A. G. G. M., 2005, The Physics and Chemistry of the Interstellar Medium. Cambridge University Press

Tielens A. G. G. M., Meixner M. M., van der Werf P. P., Bregman J., Tauber J. A., Stutzki J., Rank D., 1993, Science, 262, 86

Urquhart J. S., Busfield A. L., Hoare M. G., Lumsden S. L., Clarke A. J., Moore T. J. T., Mottram J. C., Oudmaijer R. D., 2007a, A&A, 461, 11

Urquhart J. S. et al., 2007b, A&A, 474, 891

Urquhart J. S. et al., 2008, A&A, 487, 253

Urquhart J. S. et al., 2009, A&A, 501, 539

Vaisanen P., 2015, Proposal Information for SALT Call for Proposals: 2016 Semester 1

van Loon J. T., 2012, ArXiv e-prints, 1210.0983

van Loon J. T., Cohen M., Oliveira J. M., Matsuura M., McDonald I., Sloan G. C., Wood P. R., Zijlstra A. A., 2008, A&A, 487, 1055

van Loon J. T. et al., 2010a, AJ, 139, 68

van Loon J. T., Oliveira J. M., Gordon K. D., Sloan G. C., Engelbracht C. W., 2010b, AJ, 139, 1553

Varricatt W. P., 2011, A&A, 527, A97

Varricatt W. P., Davis C. J., Ramsay S., Todd S. P., 2010, MNRAS, 404, 661

Vijh U. P. et al., 2009, AJ, 137, 3139

Vink J. S., de Koter A., Lamers H. J. G. L. M., 1999, A&A, 350, 181

Vink J. S., de Koter A., Lamers H. J. G. L. M., 2001, A&A, 369, 574

Vrba F. J., Strom S. E., Strom K. M., 1976, AJ, 81, 958

Walborn N. R., Barbá R. H., Brandner W., Rubio M., Grebel E. K., Probst R. G., 1999, AJ, 117, 225

Walsh A. J., Burton M. G., Hyland A. R., Robinson G., 1998, MNRAS, 301, 640

Wang Y. et al., 2011, A&A, 527, A32

Ward J. L., 2013, MSc thesis, University of Leeds

Ward J. L., Lumsden S. L., 2016, MNRAS, 461, 2250

Ward J. L., Oliveira J. M., van Loon J. T., Sewiło M., 2016, MNRAS, 455, 2345

Ward J. L., Oliveira J. M., van Loon J. T., Sewiło M., 2017, MNRAS, 464, 1512

Ward-Thompson D., Whitworth A. P., 2011, An Introduction to Star Formation. Cambridge University Press

Weaver H., Williams D. R. W., Dieter N. H., Lum W. T., 1965, Nature, 208, 29

Welty D. E., Xue R., Wong T., 2012, ApJ, 745, 173

Werner M. W. et al., 2004, ApJS, 154, 1

Wheelwright H. E., Oudmaijer R. D., de Wit W. J., Hoare M. G., Lumsden S. L., Urquhart J. S., 2010, MNRAS, 408, 1840

Whitney B. A. et al., 2008, AJ, 136, 18

Williams D. A., Viti S., 2013, Observational Molecular Astronomy. Cambridge University Press

Wolniewicz L., Simbotin I., Dalgarno A., 1998, ApJS, 115, 293

Wong G. F. et al., 2012, Serbian Astron. J., 184, 93

Wong G. F., Filipović M. D., Crawford E. J., de Horta A. Y., Galvin T., Drašković D., Payne J. L., 2011a, Serbian Astron. J., 182, 43

Wong G. F. et al., 2011b, Serbian Astron. J., 183, 103

Wood D. O. S., Churchwell E., 1989, ApJ, 340, 265

Woods P. M. et al., 2011, MNRAS, 411, 1597

Wright G. S. et al., 2004, in Society of Photo-Optical Instrumentation Engineers (SPIE) Conference Series, Vol. 5487, Optical, Infrared, and Millimeter Space Telescopes, Mather J. C., ed., pp. 653–663

Wright N. J., Bouy H., Drew J. E., Sarro L. M., Bertin E., Cuillandre J.-C., Barrado D., 2016, MNRAS, 460, 2593

Wright N. J., Parker R. J., Goodwin S. P., Drake J. J., 2014, MNRAS, 438, 639

Yamaguchi R. et al., 2001, PASJ, 53, 985

Zaritsky D., Harris J., Thompson I., 1997, AJ, 114, 1002

Zhang Q., 2005, in IAU Symposium, Vol. 227, Massive Star Birth: A Crossroads of Astrophysics, Cesaroni R., Felli M., Churchwell E., Walmsley M., eds., pp. 135–144

Zinnecker H., Yorke H. W., 2007, ARA&A, 45, 481

Zorec J., Arias M. L., Cidale L., Ringuelet A. E., 2007, A&A, 470, 239

Zubovas K., Sabulis K., Naujalis R., 2014, MNRAS, 442, 2837

Appendix A Notes on the virial theorem derivation

In this appendix, additional notes are provided for the virial theorem derivation presented in Section 1.1.

A.1 The tensors $\mathbf{\Pi}$ and $\mathbf{T_M}$:

The tensors $\mathbf{\Pi}$ and $\mathbf{T_M}$ are written in tensor notation as

$$(\mathbf{\Pi})_{ij} = \rho v_i v_j + P\delta_{ij} \tag{A.1}$$

$$(\mathbf{T_M})_{ij} = \frac{1}{4\pi}\left(B_i B_j - \frac{1}{2}B_k B_k \delta_{ij}\right) \tag{A.2}$$

The substitution of Eqn. 1.5 into Eqn. 1.2 is presented here explicitly following that presented in (Krumholz, 2015).

$$(\nabla \times \mathbf{B}) \times \mathbf{B} = \eta_{ijk}\eta jmn \left(\frac{\partial}{\partial x_m}B_n\right) B_k \tag{A.3}$$

$$(\nabla \times \mathbf{B}) \times \mathbf{B} = -\eta_{ijk}\eta jmn \left(\frac{\partial}{\partial x_m}B_n\right) B_k \tag{A.4}$$

$$(\nabla \times \mathbf{B}) \times \mathbf{B} = (\delta_{in}\delta_{km} - \delta_{im}\delta_{kn}) \left(\frac{\partial}{\partial x_m}B_n\right) B_k \tag{A.5}$$

$$(\nabla \times \mathbf{B}) \times \mathbf{B} = B_k \frac{\partial}{\partial x_k}B_i - B_k \frac{\partial}{\partial x_i}B_k \tag{A.6}$$

$$(\nabla \times \mathbf{B}) \times \mathbf{B} = \left(B_k \frac{\partial}{\partial x_k}B_i + B_i \frac{\partial}{\partial x_k}B_k\right) - B_k \frac{\partial}{\partial x_i}B_k \tag{A.7}$$

$$(\nabla \times \mathbf{B}) \times \mathbf{B} = \frac{\partial}{\partial x_k}(B_i B_k) - \frac{1}{2}\frac{\partial}{\partial x_i}(B_k^2) \tag{A.8}$$

$$(\nabla \times \mathbf{B}) \times \mathbf{B} = \nabla \cdot \left(\mathbf{BB} - \frac{B^2}{2}\right) \tag{A.9}$$

A.2 Divergence theorem

The divergence theorem (or Gauss-Ostrogradsky theorem) establishes that without the creation or destruction of matter the only way to change the density of a region is for matter to cross the boundary of the region. It states that the divergence of $\mathbf{F}$ ($\nabla \cdot \mathbf{F}$) over V and the surface integral of $\mathbf{F}$ over the bounday ∂V of V are related by (Arfken , 1985):

$$\int_V (\nabla \cdot \mathbf{F}) dV = \int_{\partial V} \mathbf{F} da \tag{A.10}$$

A.3 Identity for volume integral of tensor T:

The identity from Krumholz (2015) for the volume integral of an arbitrary tensor (Eqn. 1.13) is set out here.

$$\int_V \mathbf{r} \cdot \nabla \cdot \mathbf{T} = \int_V x_i \frac{\partial}{\partial x_j} T_{ij} dV \tag{A.11}$$

$$\int_V \mathbf{r} \cdot \nabla \cdot \mathbf{T} = \int_V \frac{\partial}{\partial x_j}(x_i T_{ij}) dV - \int_V T_{ij} \frac{\partial}{\partial x_j} x_i dV \tag{A.12}$$

$$\int_V \mathbf{r} \cdot \nabla \cdot \mathbf{T} = \int_S x_i T_{ij} dS_j - \int_V S_{ij} T_{ij} dV \tag{A.13}$$

$$\int_V \mathbf{r} \cdot \nabla \cdot \mathbf{T} = \int_S \mathbf{r} \cdot \mathbf{T} \cdot dS - \int_V Tr\mathbf{T} dV \tag{A.14}$$

A.4 The virial theorem in full:

The full result of the derivation in Section 1.1 is shown below.

$$\frac{d^2 I}{dt^2} = 2\left[\int_V (\rho v^2 + 3P) dV - 2\int_S \mathbf{r} \cdot \mathbf{\Pi} \cdot dS\right] + 2\left[\frac{1}{8\pi}\int_V B^2 dV + \int_S \mathbf{r} \cdot \mathbf{T_M} \cdot dS\right] - 2\left[\int_V \rho \cdot \nabla\phi dV\right] - \frac{d}{dt}\int_S (\rho v r^2) dS \tag{A.15}$$

Multiplying this equation by 1/2 then gives the virial theorem. In equation 1.16 the final term ($\frac{d}{dt}\int_S (\rho v r^2) dS$) is set to zero.

Appendix B Original SINFONI images for N113

Here I present the original images presented in Ward et al. (2016a) in order to demonstrate that the results of Chapter 3 remain unaffected by the application of the SINFONI data treatment described in Section 2.1.4.

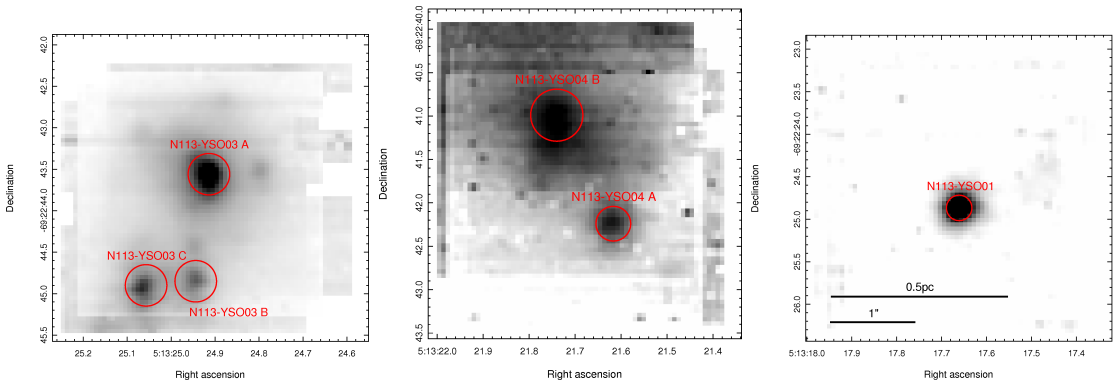

Figure B.1: SINFONI K-band Continuum emission maps. Left to right: N113-YSO03, N113-YSO04, N113-YSO01. Marked regions show the identified continuum sources and the regions from which spectra were extracted.

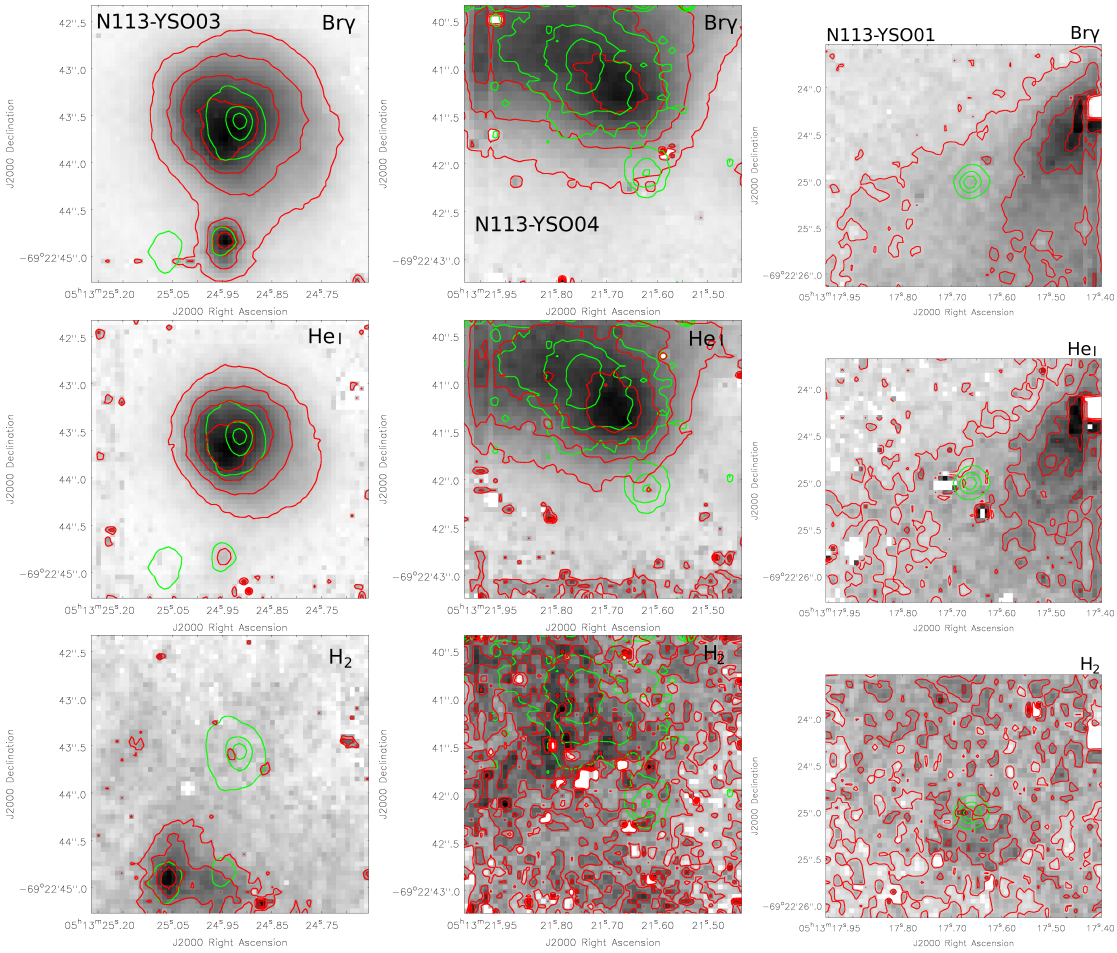

Figure B.2: Emission line maps with contours overlaid. Red contours - line emission [0.2, 0.4, 0.6, 0.8]×peak, green contours - continuum emission [0.25, 0.5, 0.75]×peak. Left to right - N113-YSO03, N113-YSO04, N113-YSO01. Top to bottom - Brγ, He I, H_2 1-0(S1).

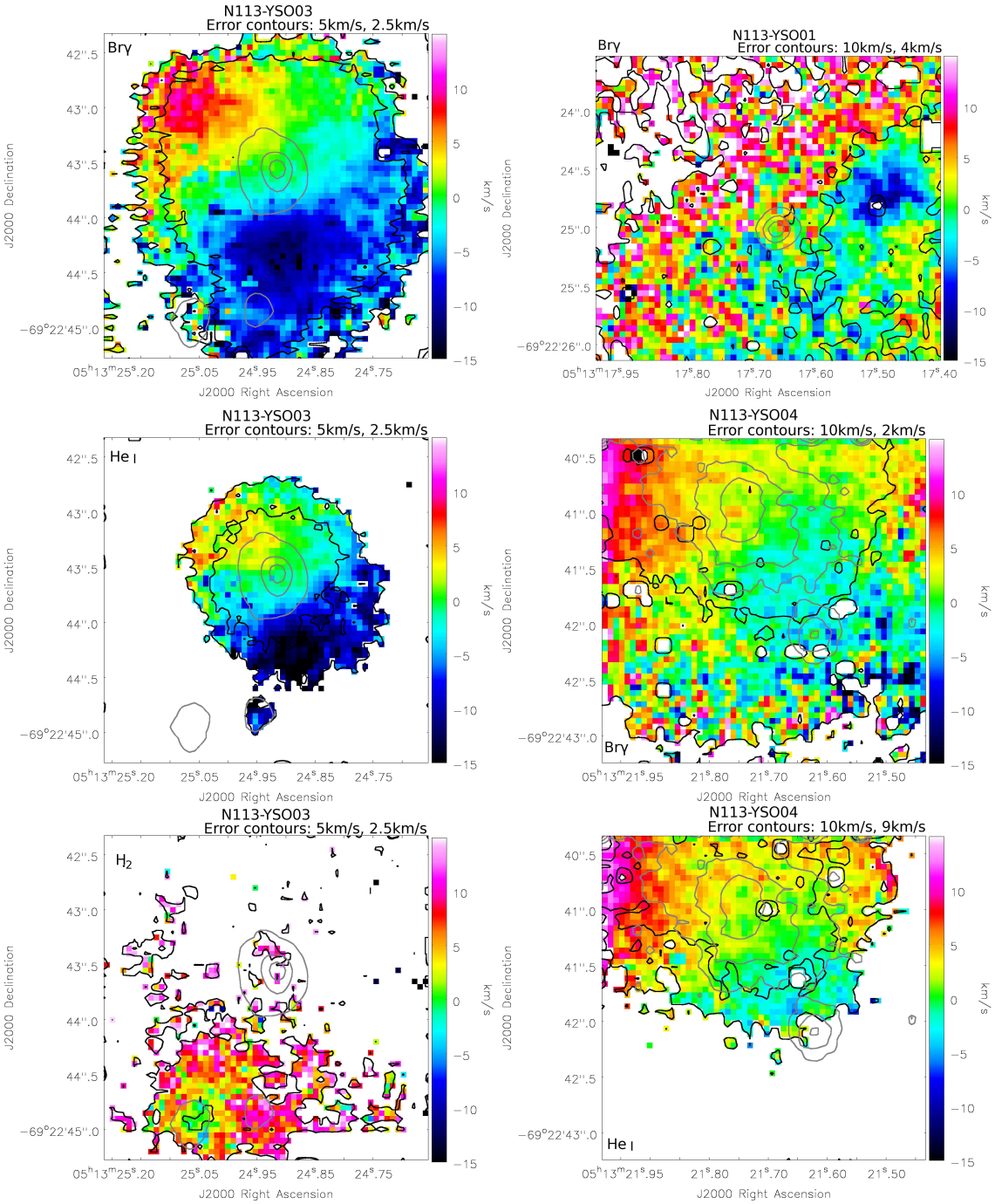

Figure B.3: Left: Brγ, He I and H_2 2.1218μm centroid velocity maps for N113-YSO03. Right: Brγ centroid velocity map for N113-YSO01 (top) and Brγ and He I velocity maps for N113-YSO04 (middle and bottom). Black contours represent the uncertainties; the outer (left) and inner (right) contour values are indicated in each image. The continuum contour levels are [0.25, 0.5, 0.75]×peak (grey).

Appendix C Flux and velocity maps

This appendix contains additional sky line centroid velocity maps and continuum maps. Figure C.1 shows the relative centroid velocity maps for three sky emission lines from the sky cube corresponding to N113-YSO03, showing that there is no systematic velocity gradient across the SINFONI fields. The continuum images from Chapter 4 are presented in Fig. C.2 with the positions of all detected continuum sources marked.

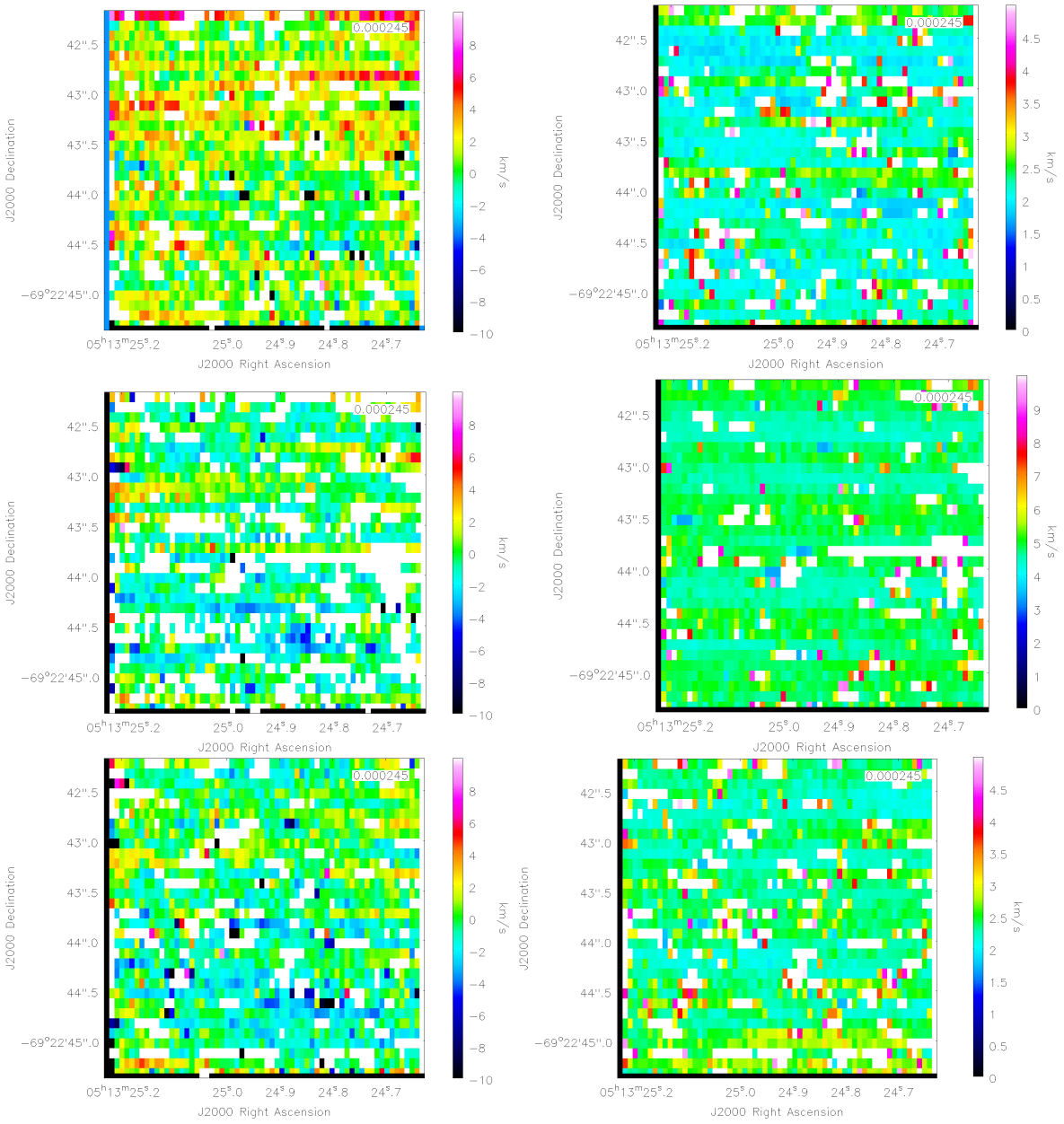

Figure C.1: Relative velocity (left) and error maps (right) for sky emission lines in the N113-YSO03 sky cube. Top: 2.0567μm; middle: 2.1511μm; bottom: 2.1806μm.

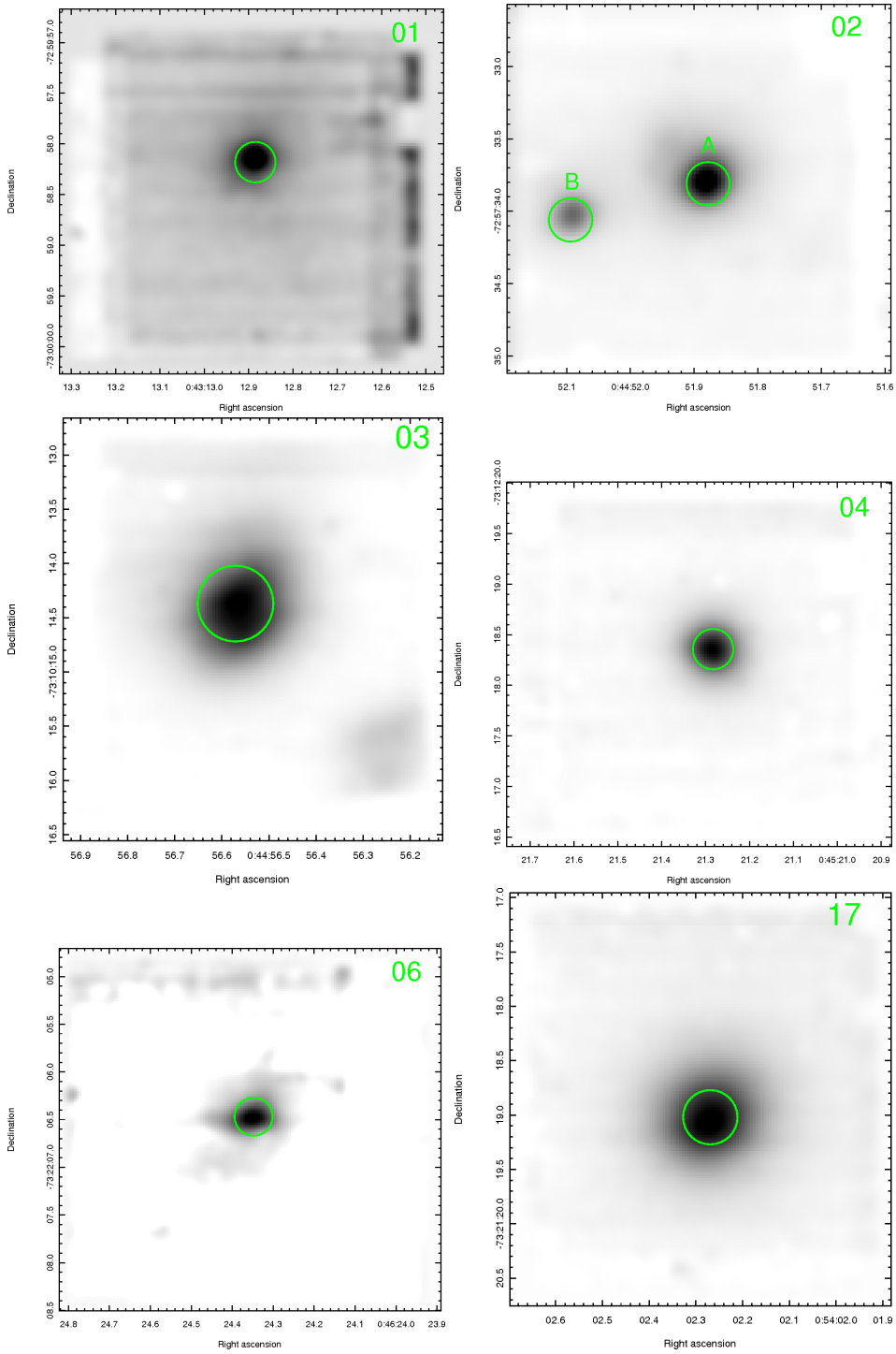

Figure C.2: SINFONI K-band continuum images for all observed FOVs.

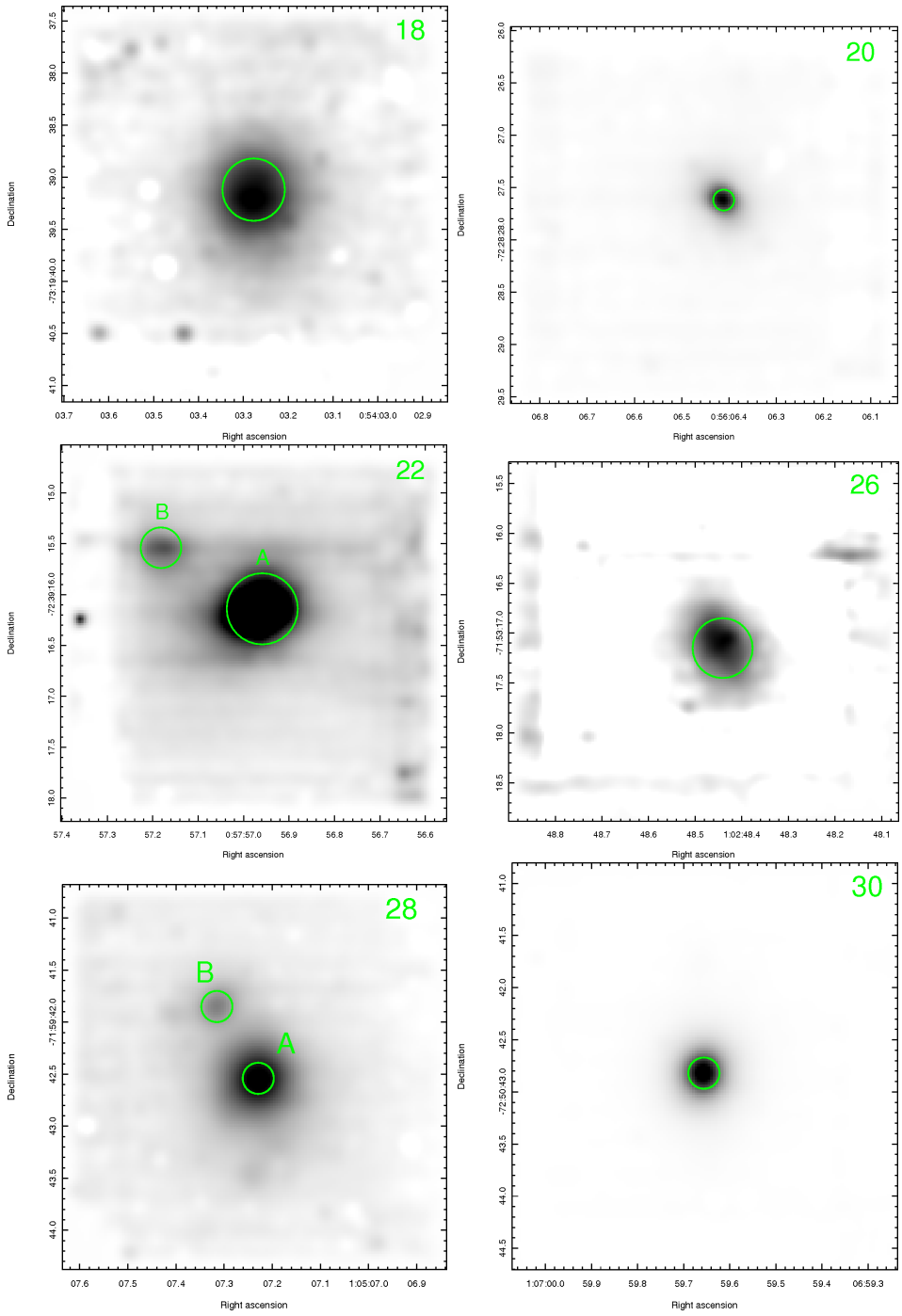

Fig. C.2 cont. SINFONI K-band continuum images for all observed FOVs.

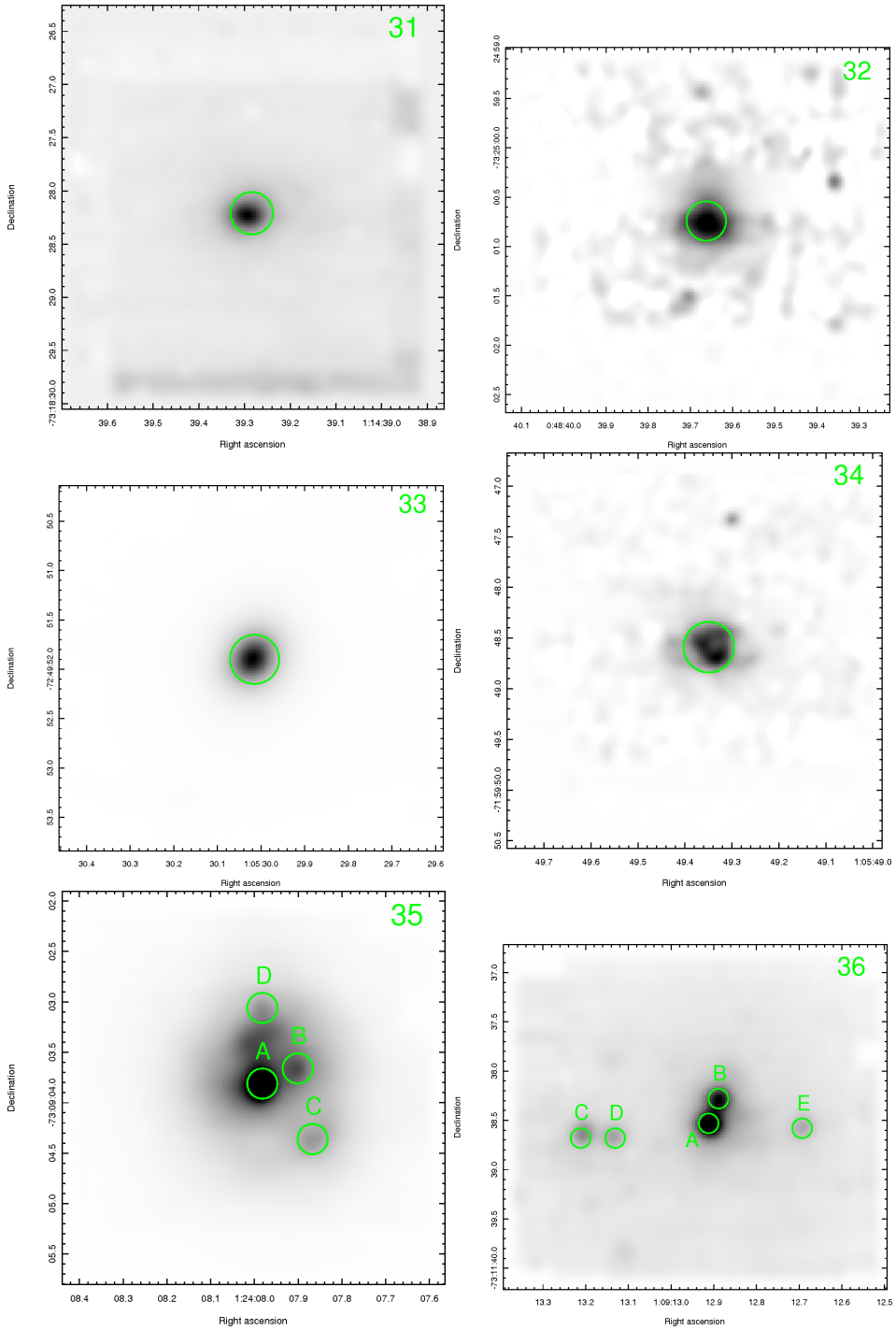

Fig. C.2 cont. SINFONI K-band continuum images for all observed FOVs.

Appendix D Extracted spectra

In this appendix the extracted spectra from all chapters are presented. K-band spectra for all continuum sources in the N113 fields from chapter 3 are presented in Fig. D.1, followed by spectra showing the positions of sky residuals and the H I Pfund series emission in Figs. D.2 and D.3. Figure D.4 shows normalised K-band spectra for all continuum sources detected in the SMC from Chapter 4. The optical spectra obtained with SALT/RSS discussed in Chapter 5 are given in Figs. D.5, D.6 and D.7. Finally the $H + K$ spectra towards all continuum sources detected in the LMC embedded clusters sample from Chapter 6 are shown in Fig. D.8.

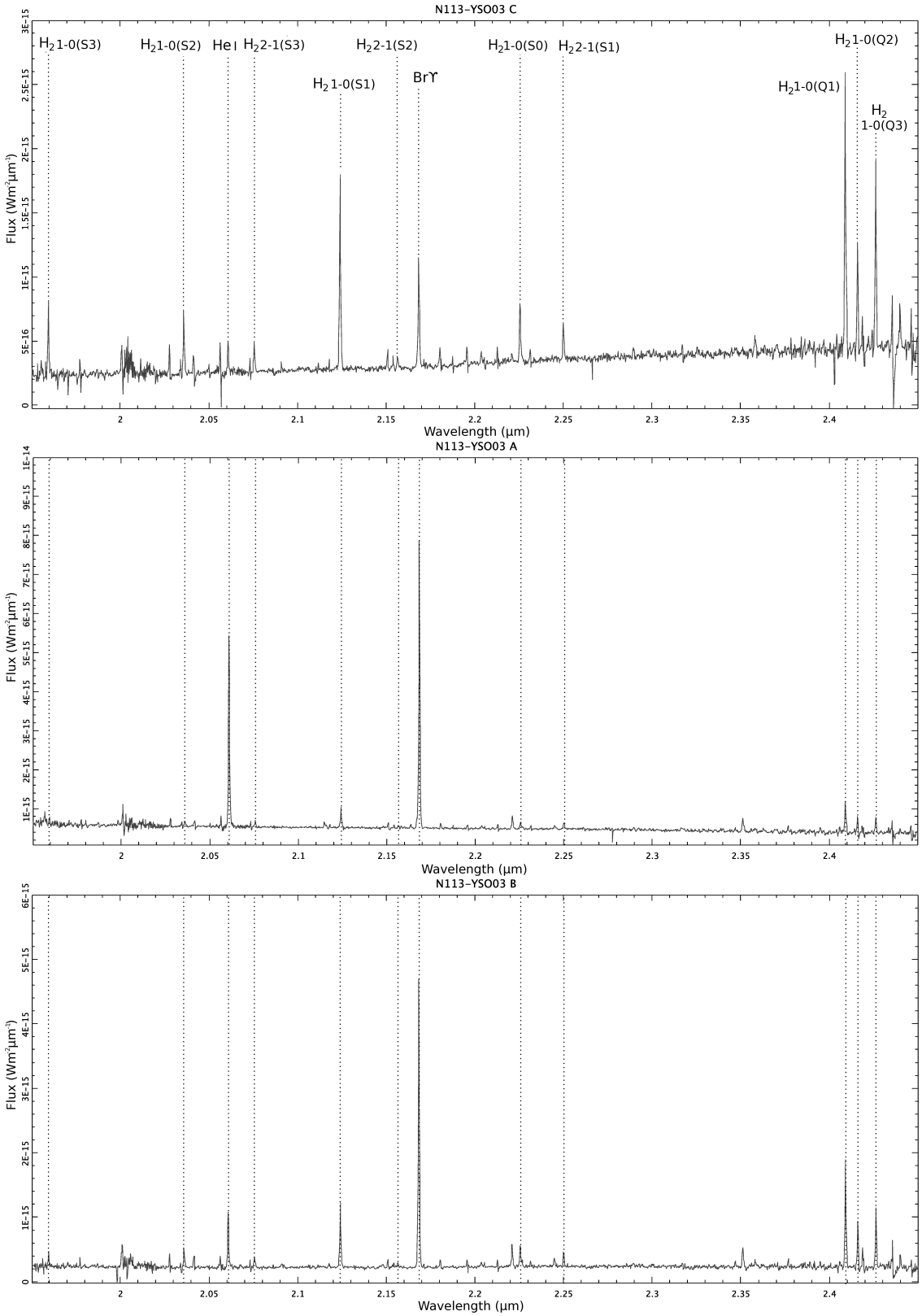

Figure D.1: Spectra of all N113 continuum sources extracted from the regions shown in Fig. 2. The spectrum of N113-YSO03 C (shown first) is marked with the positions of all of the measured spectral lines.

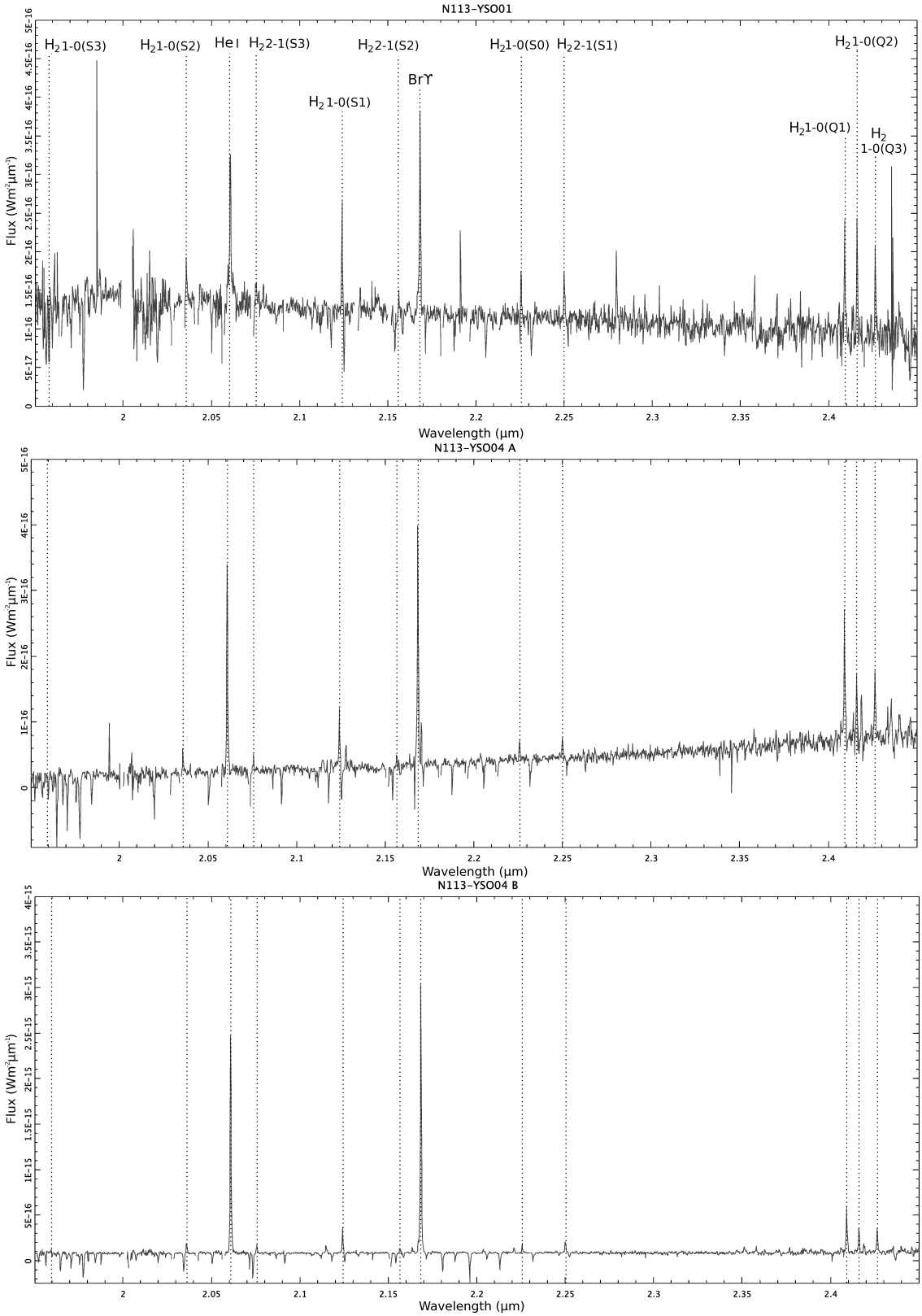

Figure D.1 cont. The spectrum of N113-YSO01 shows line identifications.

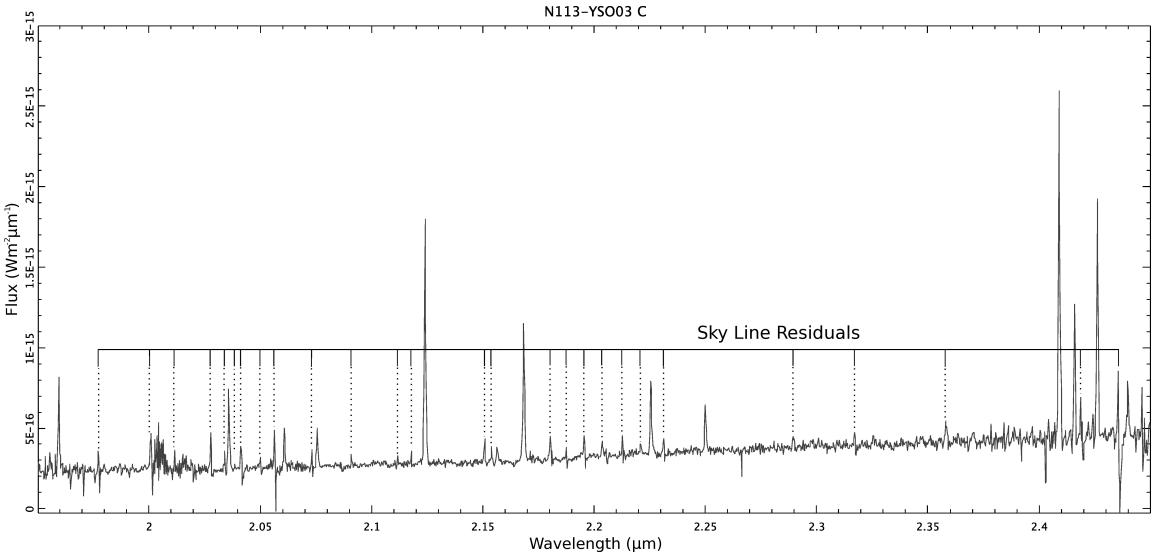

Figure D.2: Spectrum of N113-YSO03 C showing the positions of all of the sky line residuals.

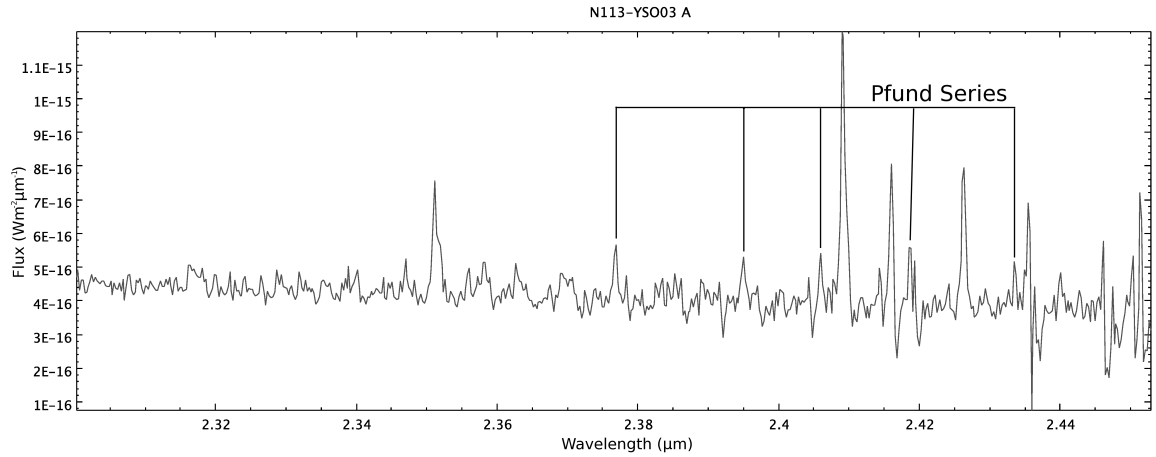

Figure D.3: Spectrum of N113-YSO03 A showing the positions of the Pfund series emission lines.

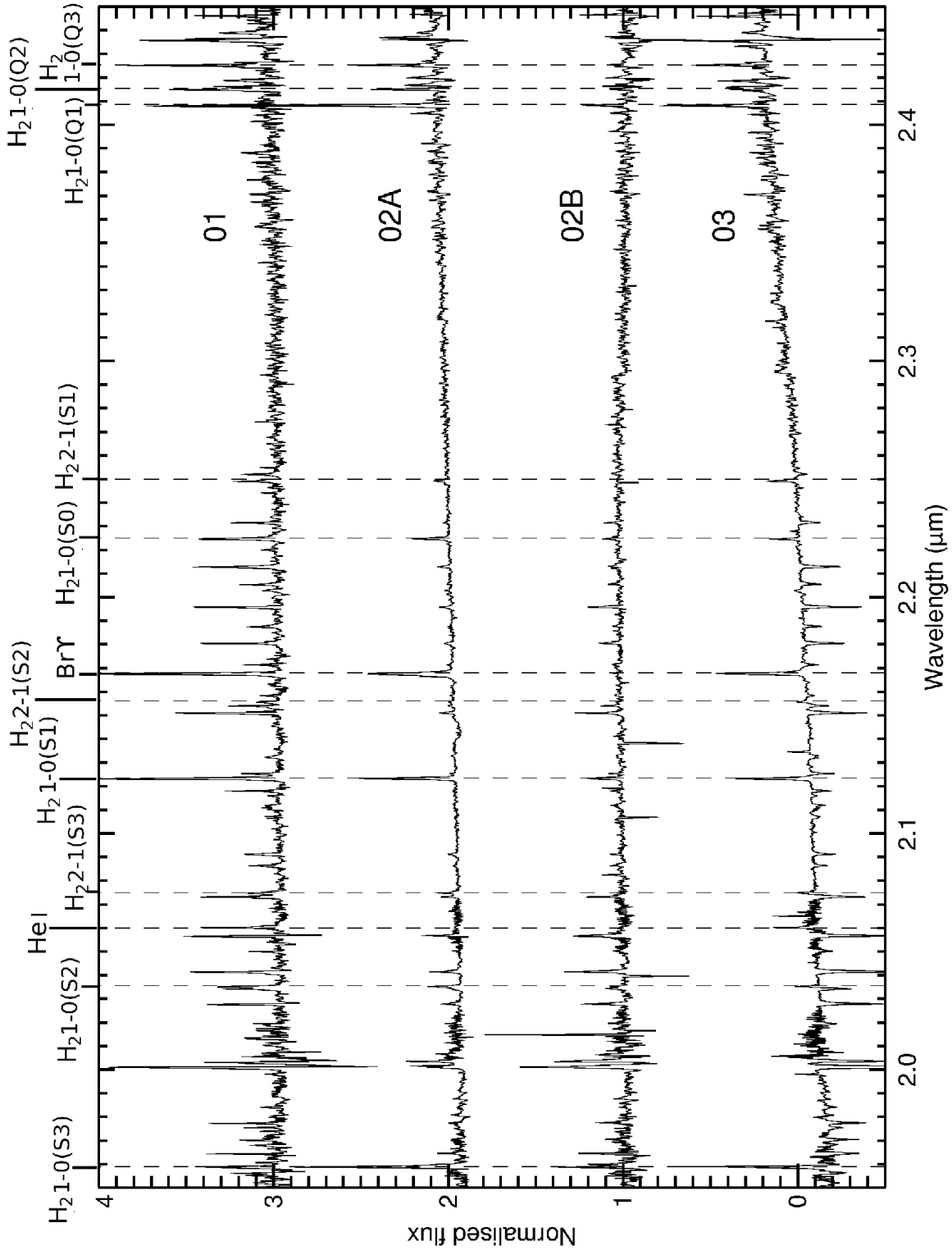

Figure D.4: Continuum normalised extracted spectra towards all K-band continuum sources detected. Positions of the emission lines studied in this work are marked.

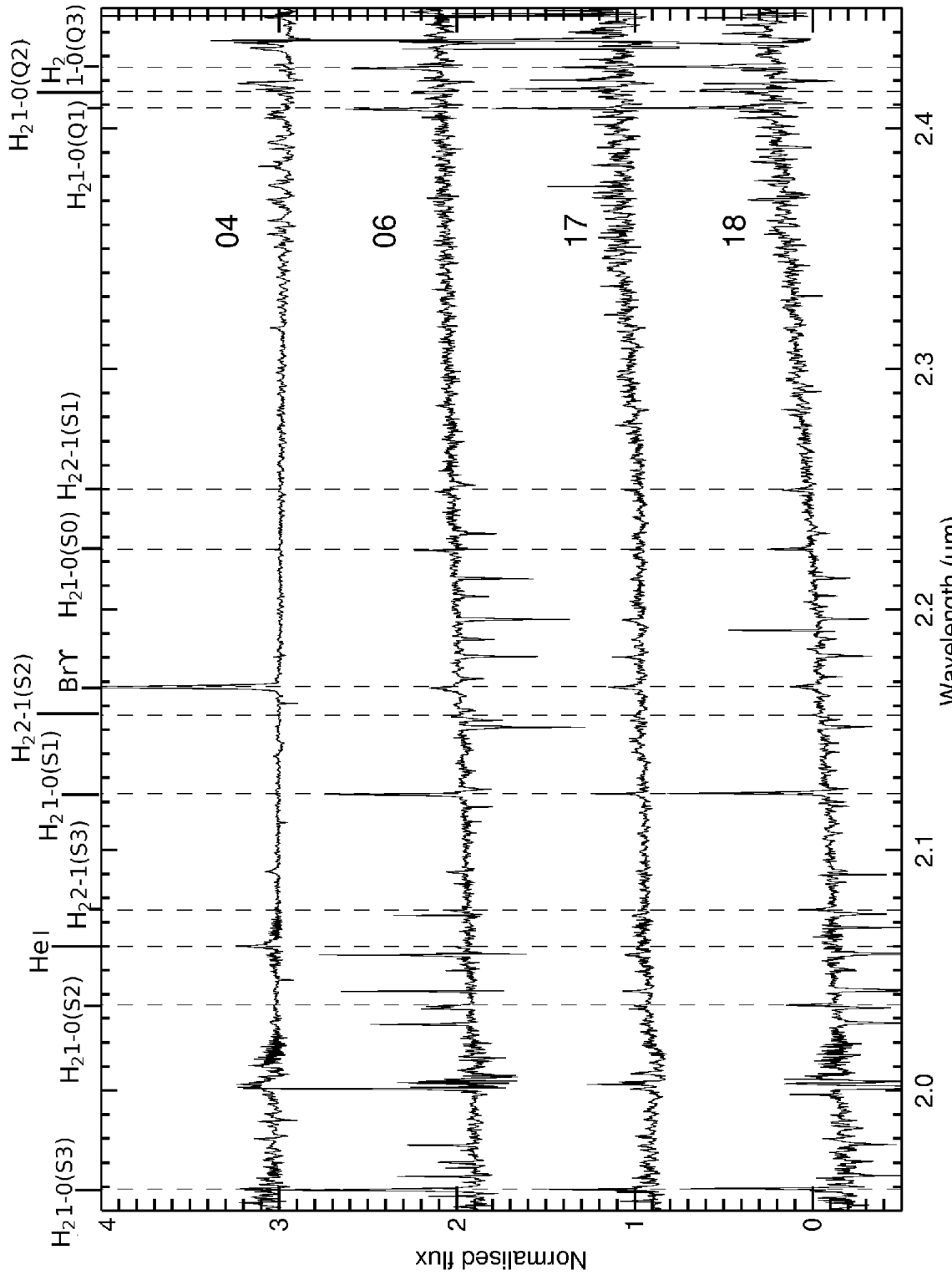

Fig. D.4 cont. Extracted K-band spectra.

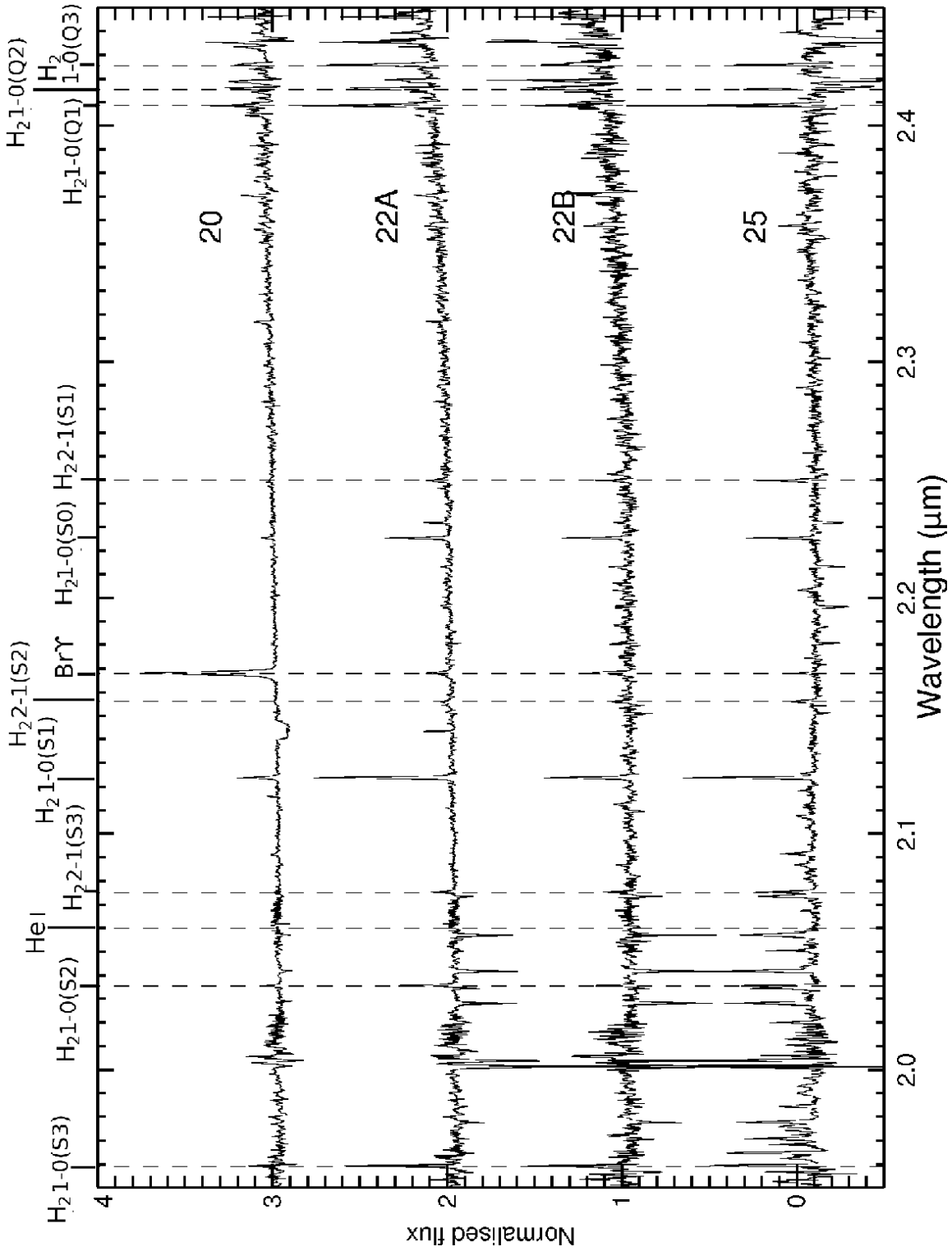

Fig. D.4 cont. Extracted K-band spectra.

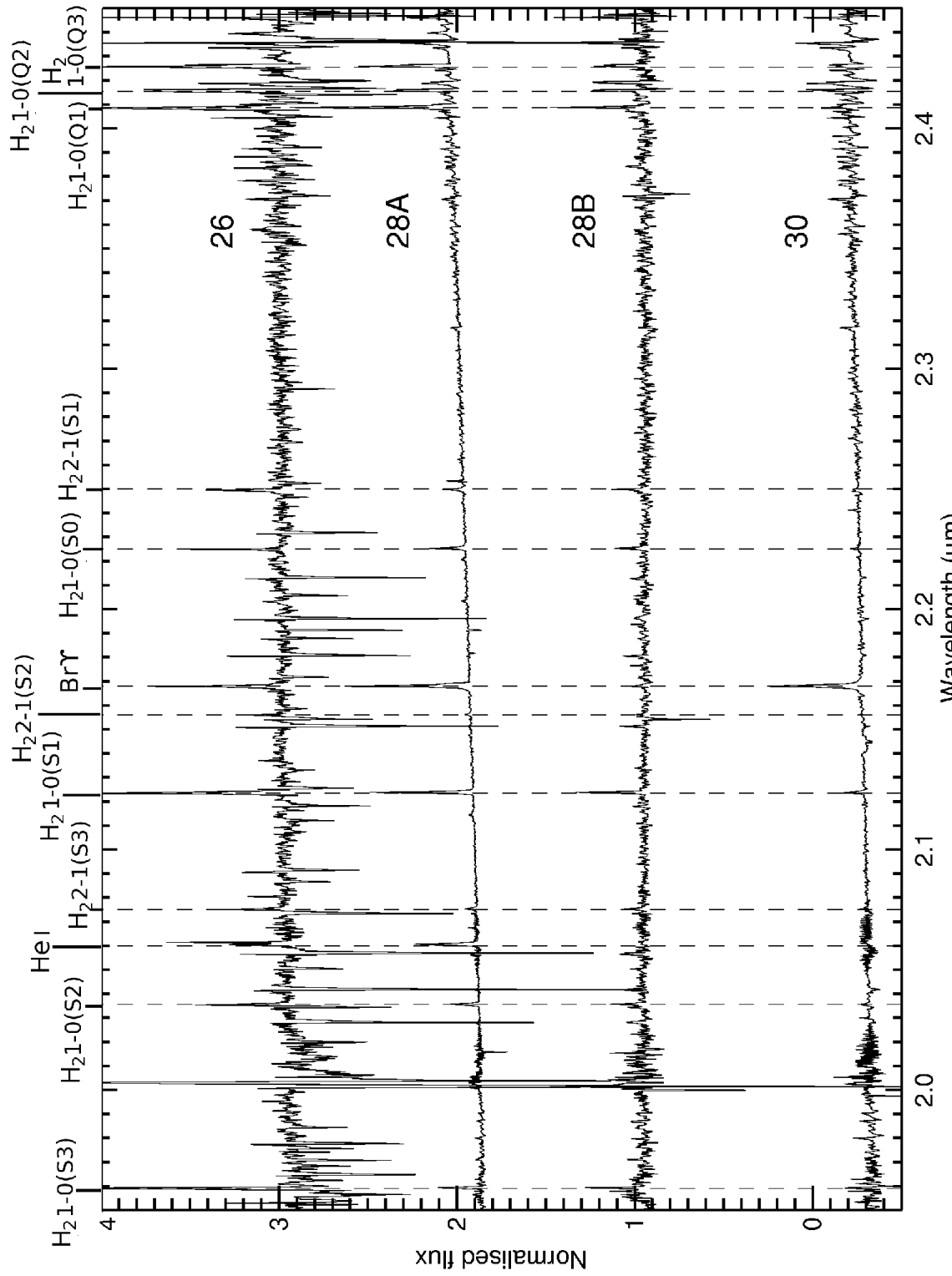

Fig. D.4 cont. Extracted K-band spectra.

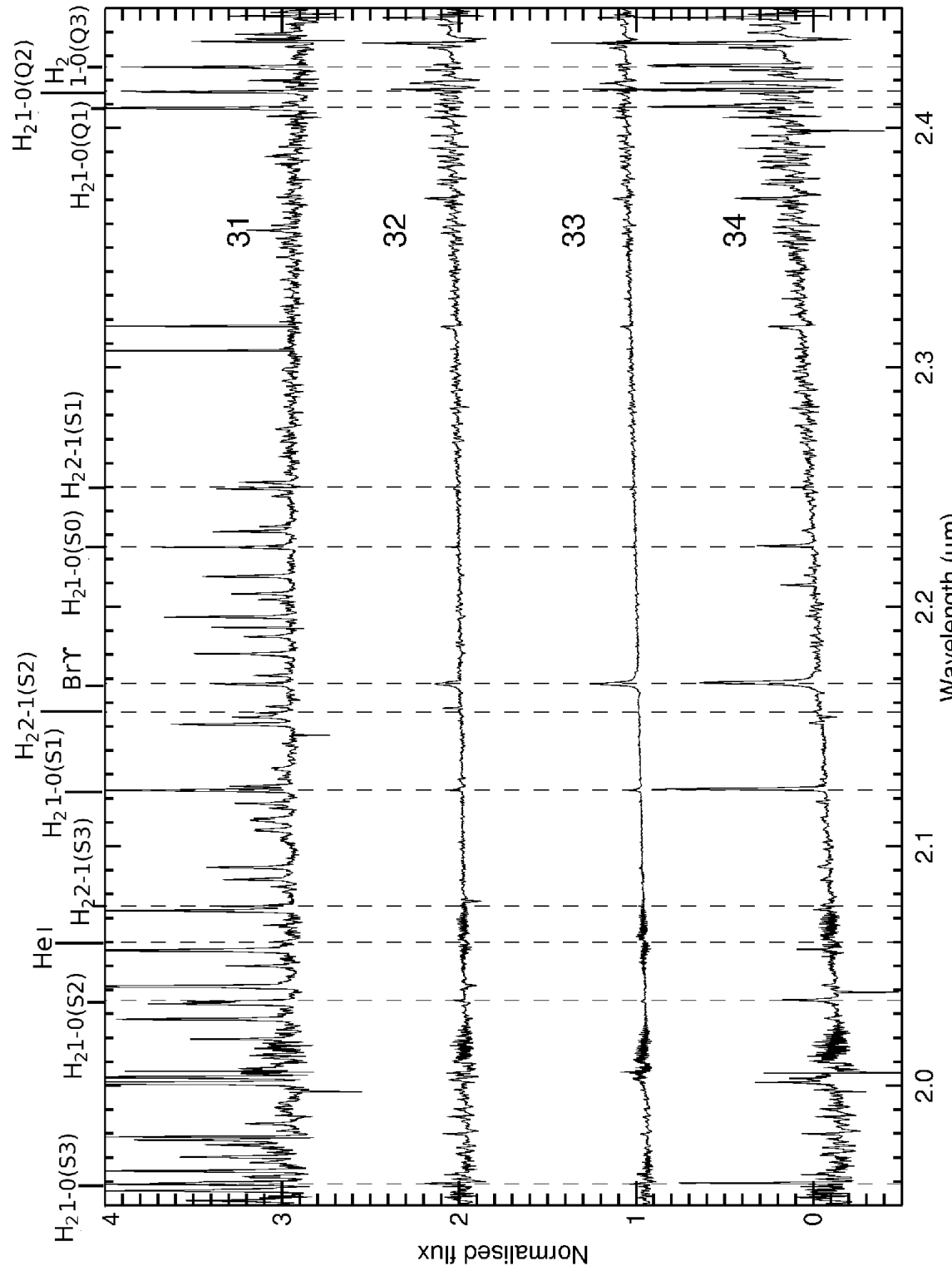

Fig. D.4 cont. Extracted K-band spectra.

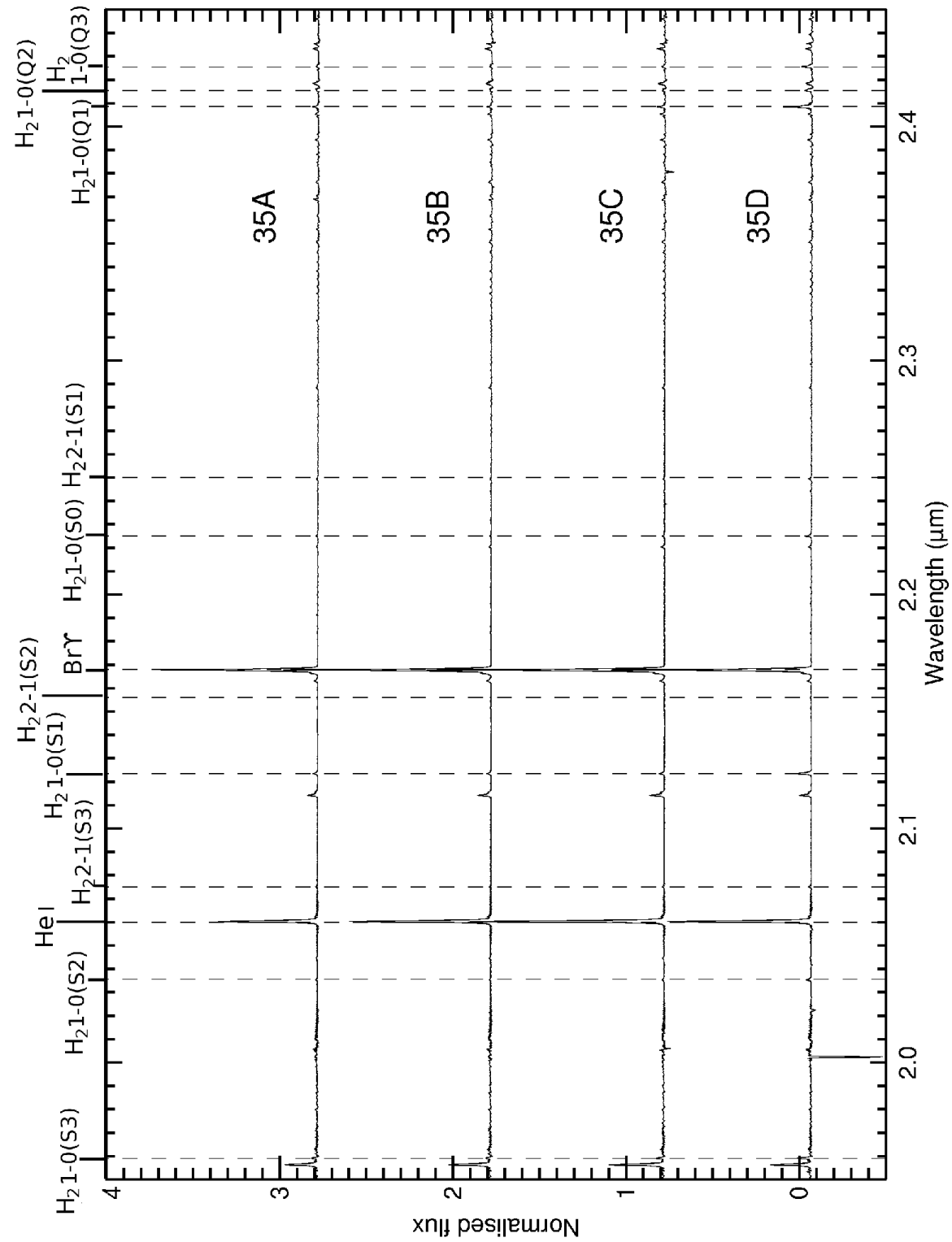

Fig. D.4 cont. Extracted K-band spectra.

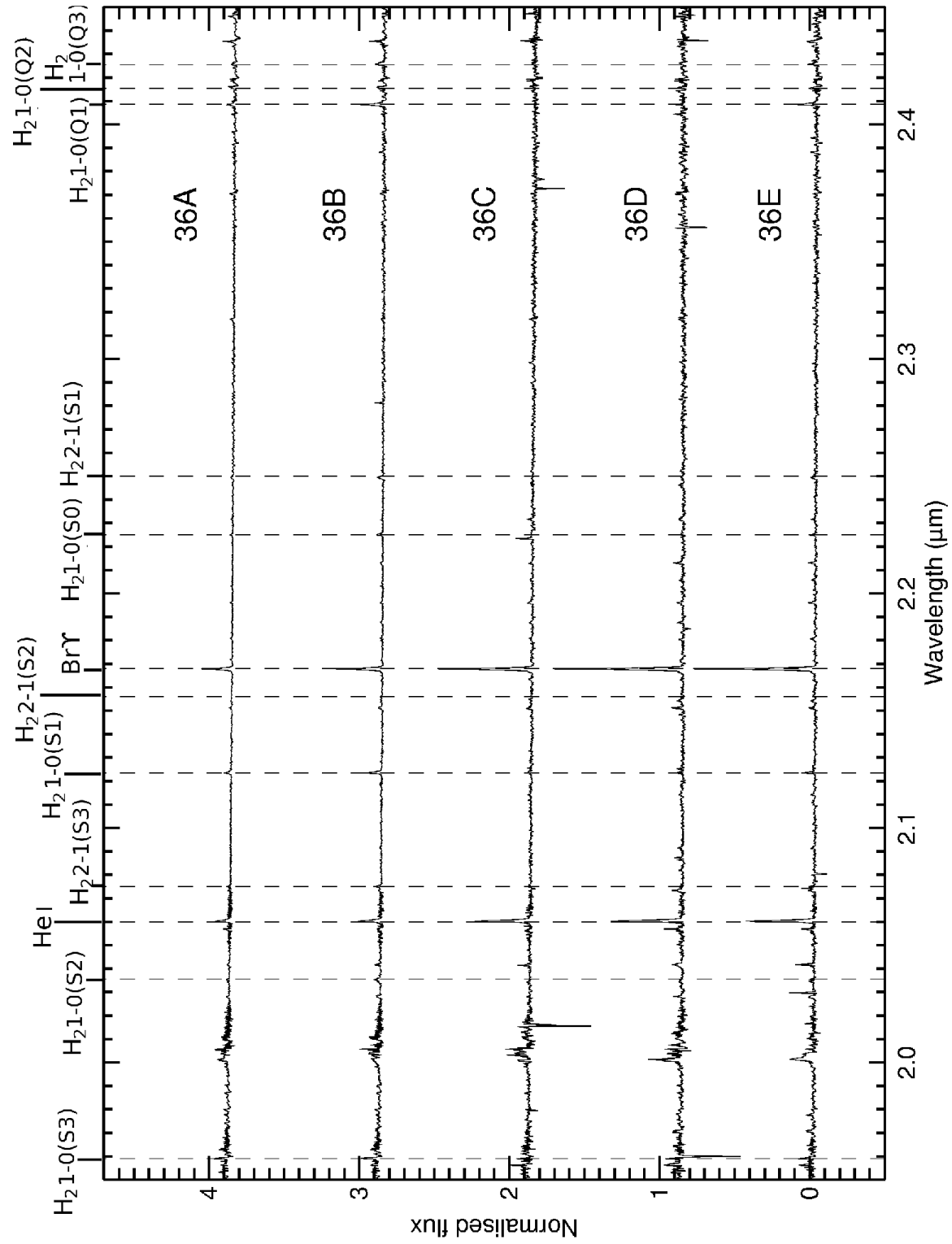

Fig. D.4 cont. Extracted K-band spectra.

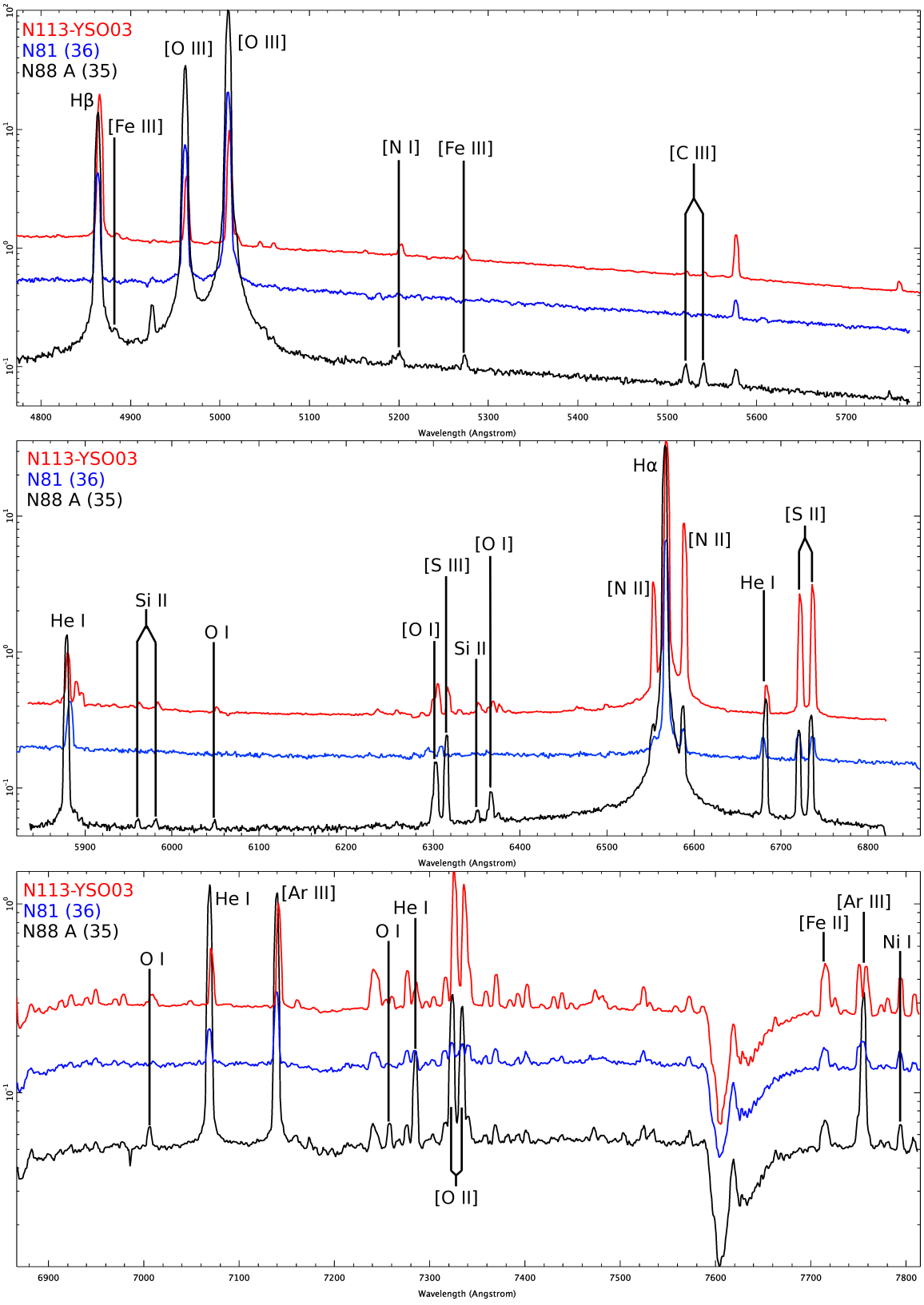

Figure D.5: Low resolution optical spectra of sources 35 and 36 in the SMC (N88A and N81, respectively) and N113-YSO03 in the LMC obtained with SALT/RSS (Chapter 5).

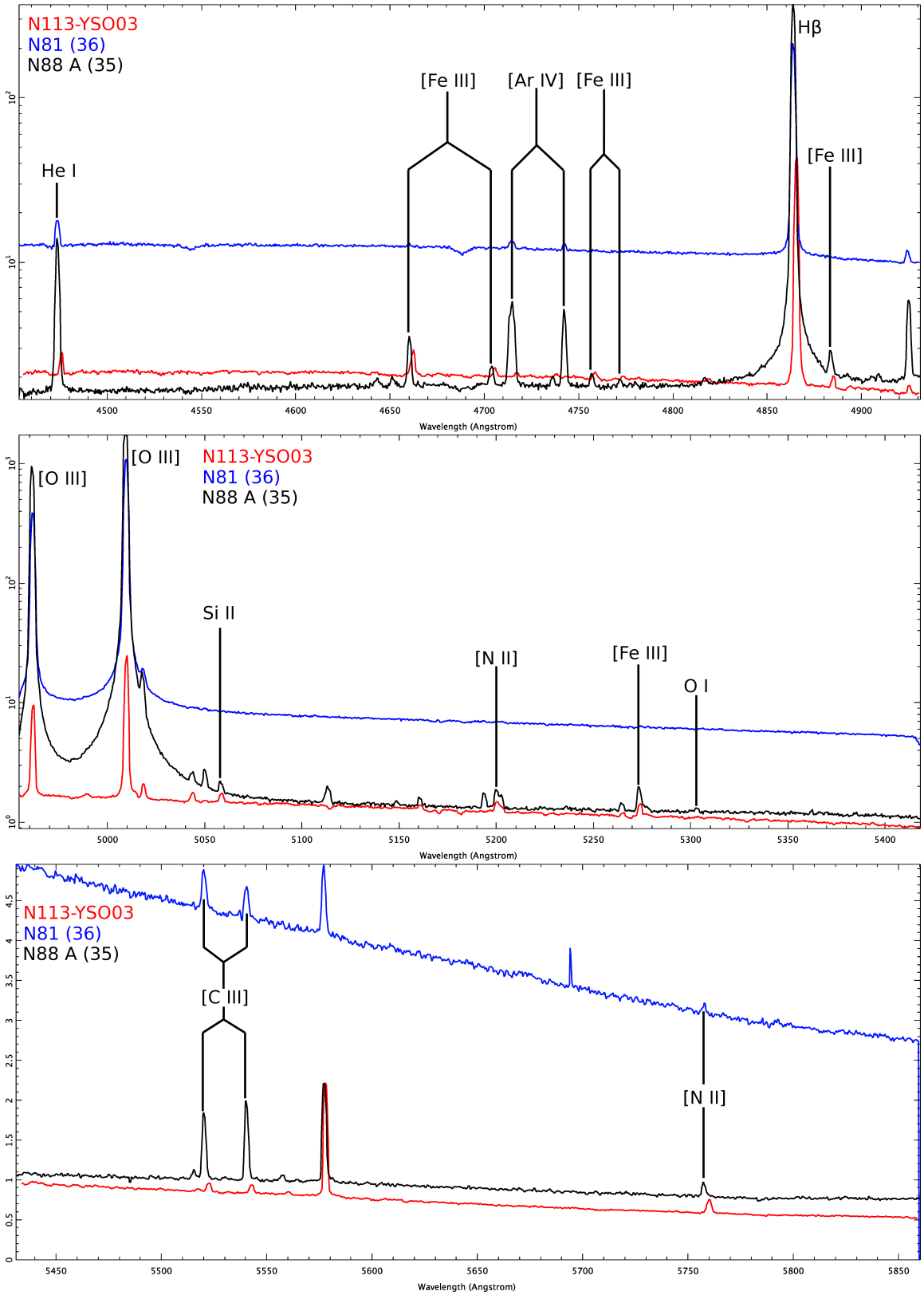

Figure D.6: Medium resolution blue optical spectra towards sources 35 and 36 in the SMC (N88A and N81, respectively) and N113-YSO03 in the LMC obtained with SALT/RSS (Chapter 5).

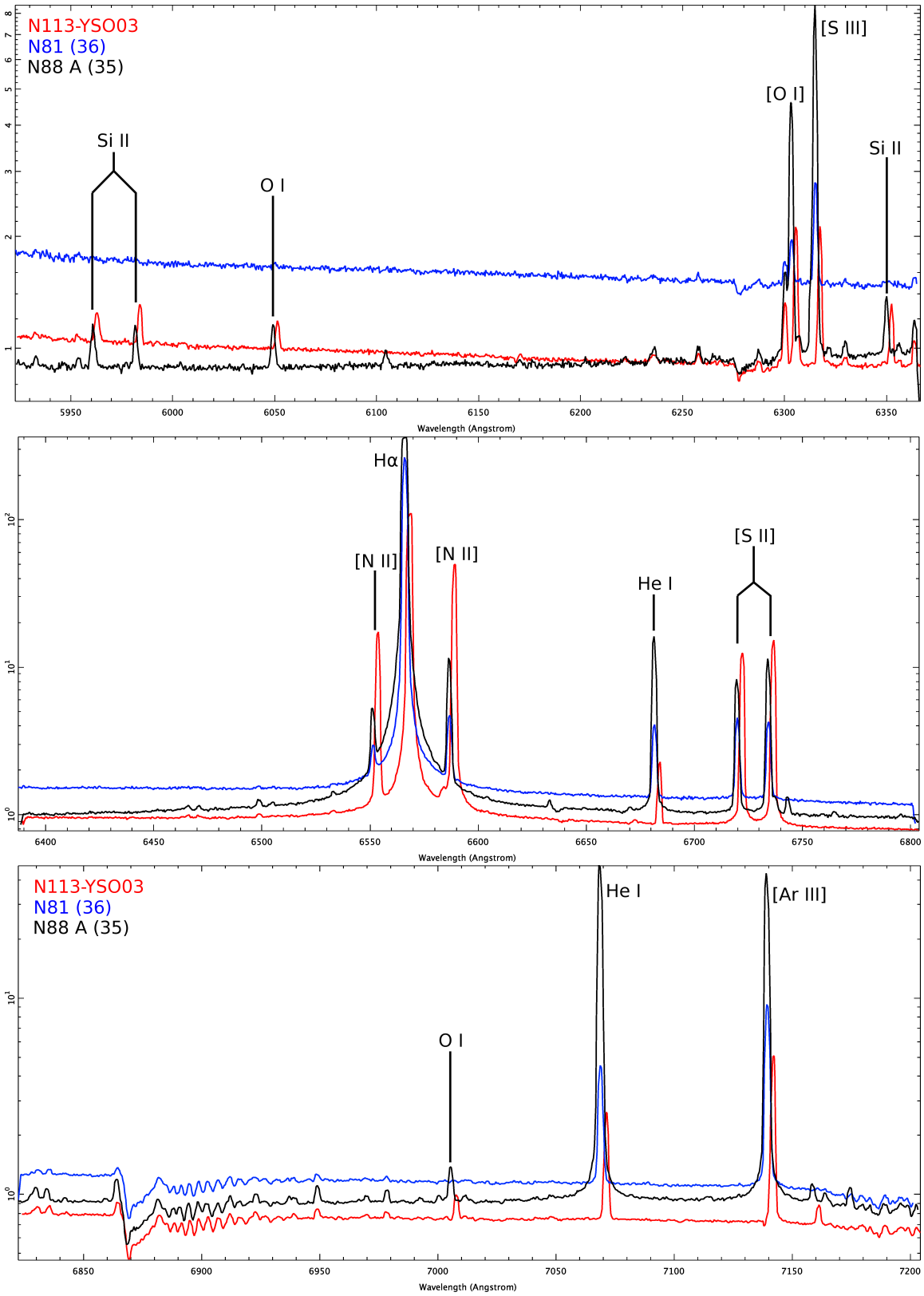

Figure D.7: Medium resolution red optical spectra towards sources 35 and 36 in the SMC (N88A and N81, respectively) and N113-YSO03 in the LMC obtained with SALT/RSS (Chapter 5).

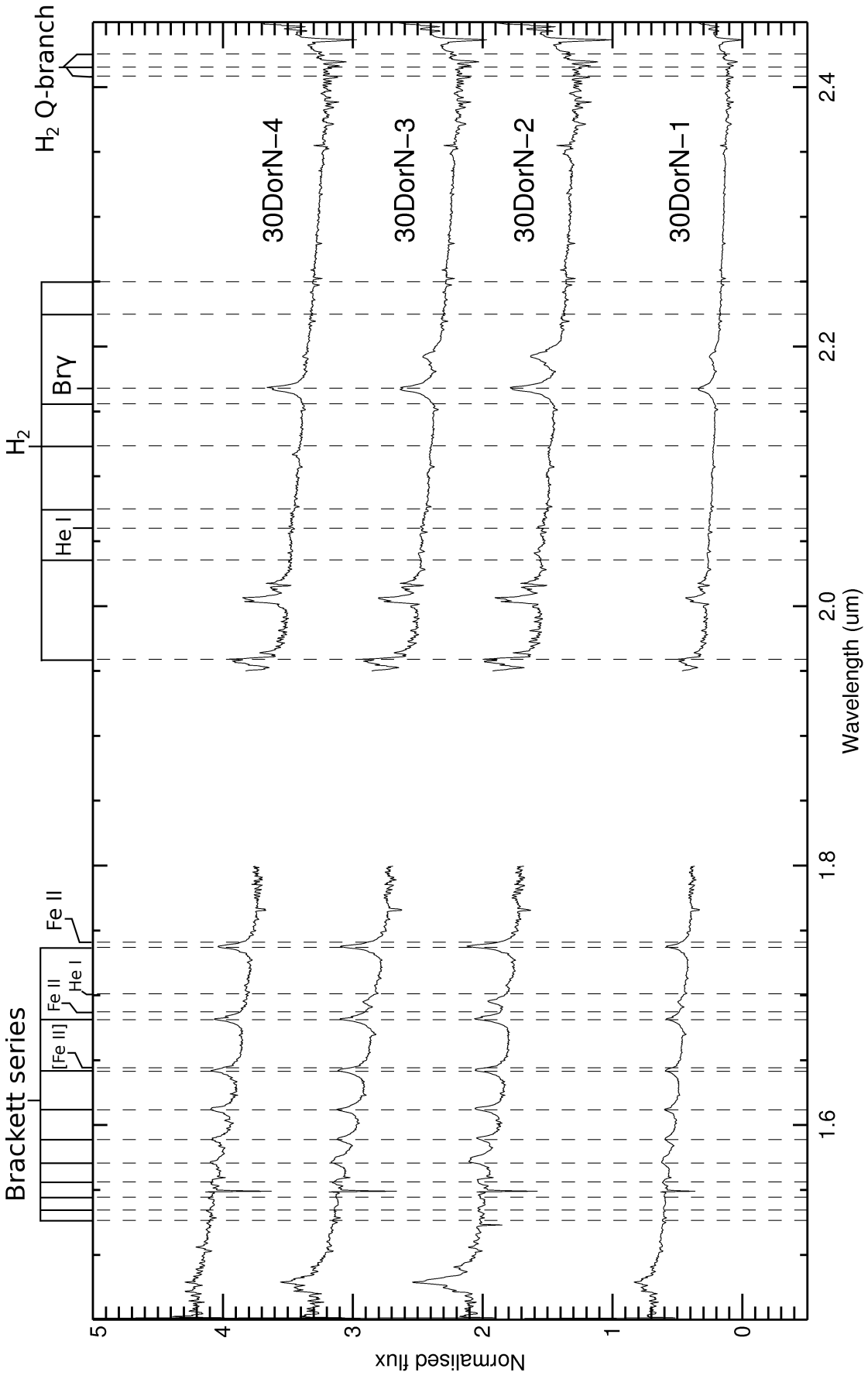

Figure D.8: $H + K$ spectra towards sources 1–4 in 30DorN (Chapter 6). The Brackett series emission is marked only up to Br19.

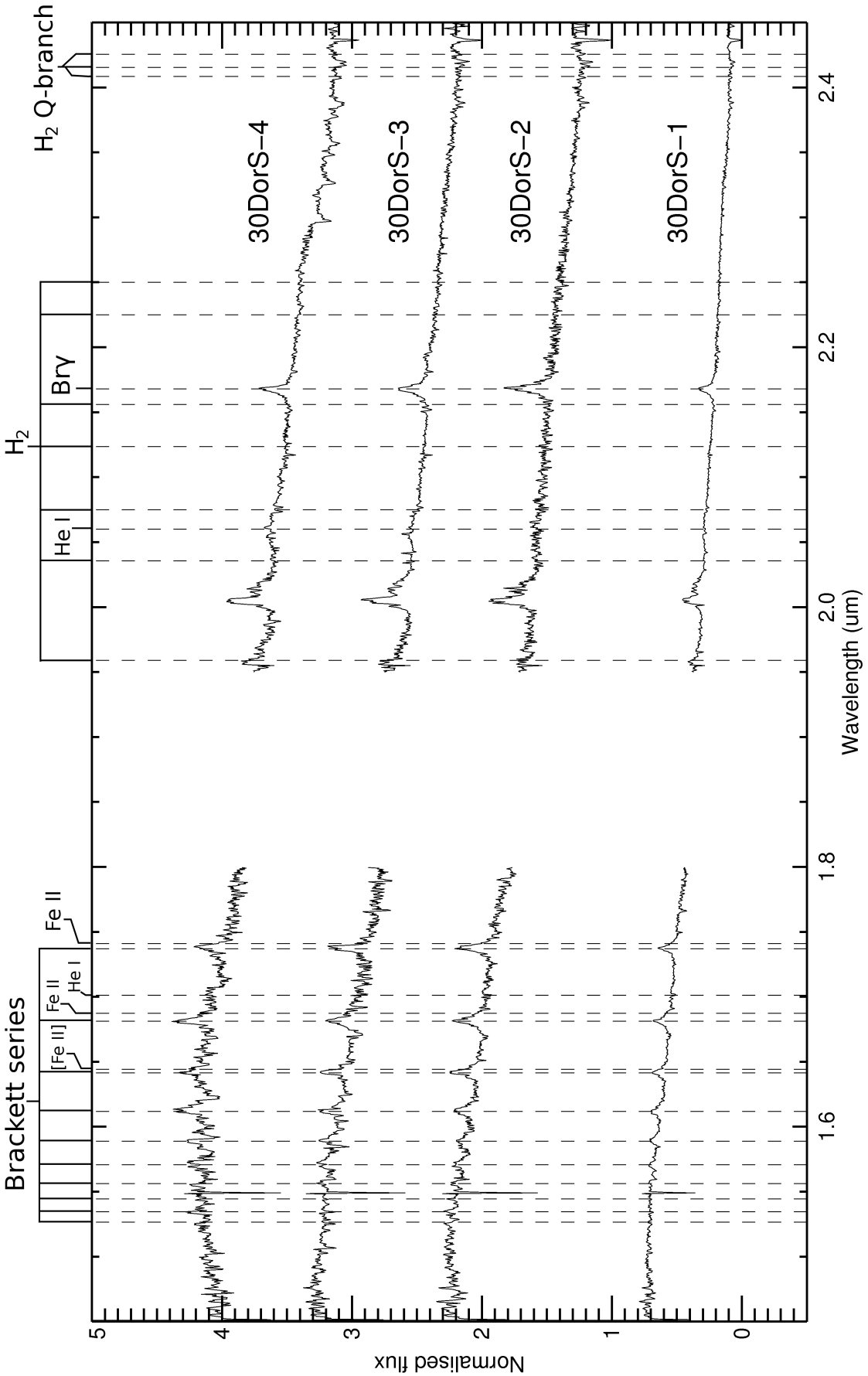

Fig. D.8 cont. $H + K$ spectra towards sources 1–4 in 30DorS (Chapter 6). The Brackett series emission is marked only up to Br19.

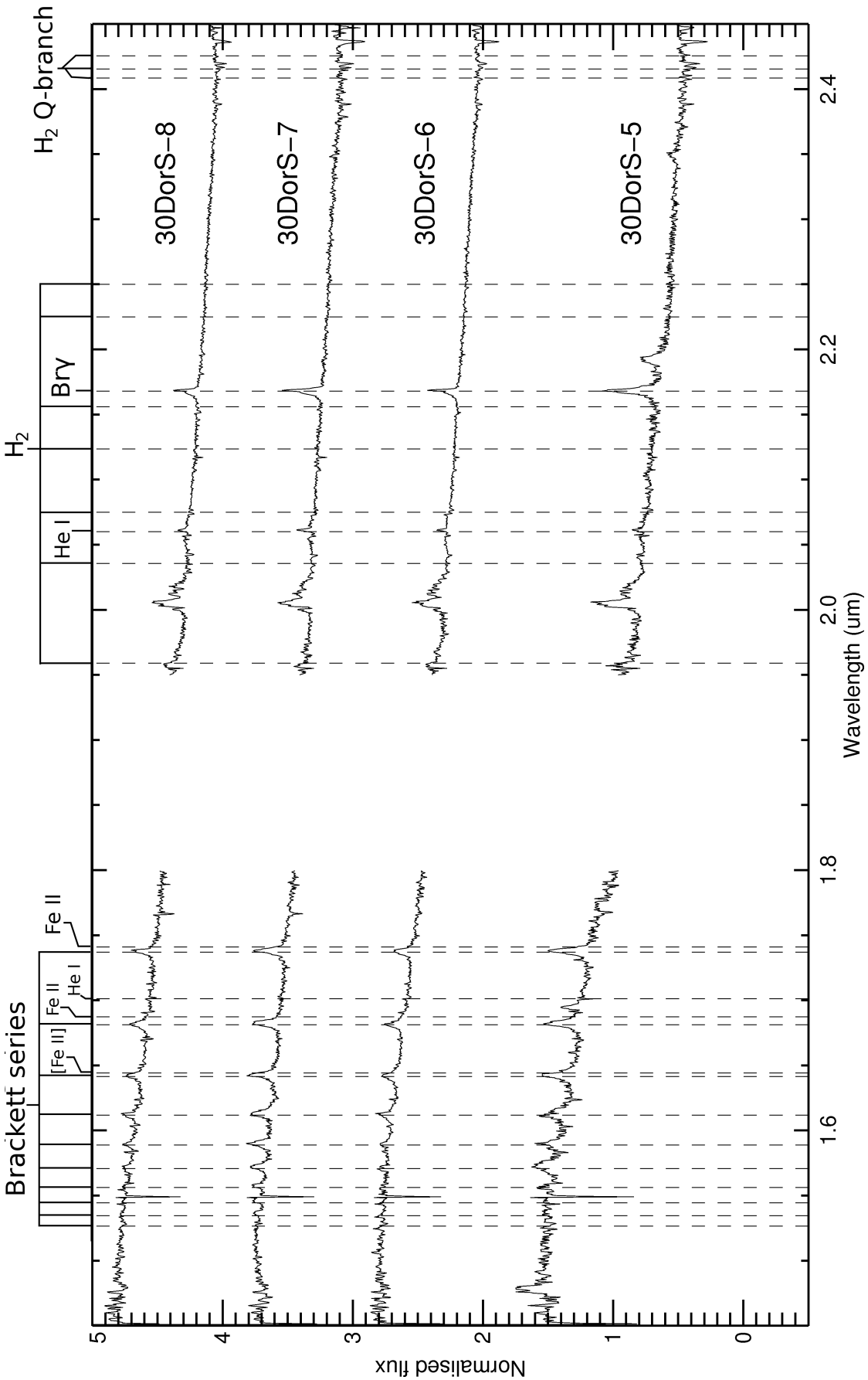

Fig. D.8 cont. $H + K$ spectra towards sources 5–8 in 30DorS (Chapter 6). The Brackett series emission is marked only up to Br19.

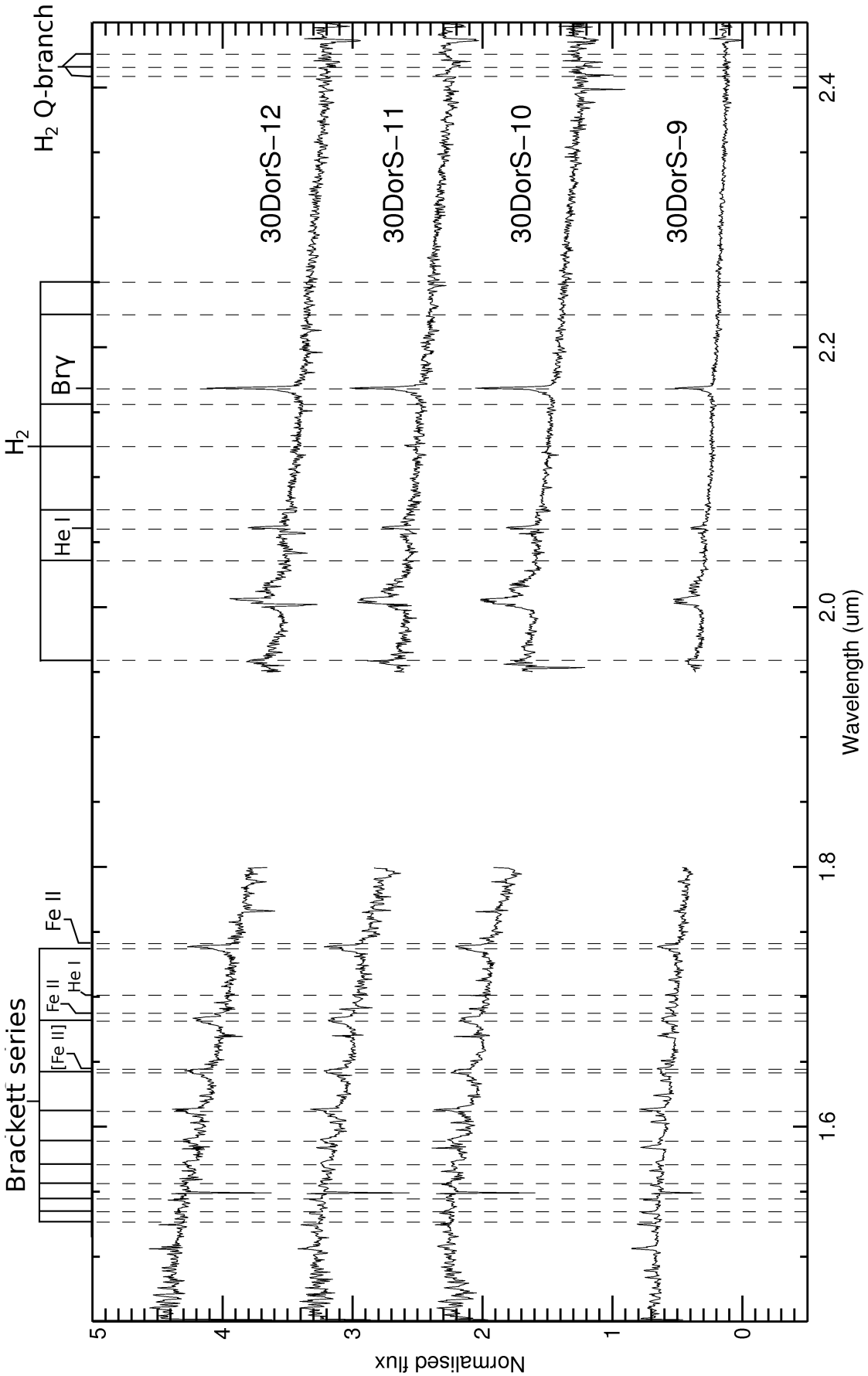

Fig. D.8 cont. $H + K$ spectra towards sources 9–12 in 30DorS (Chapter 6). The Brackett series emission is marked only up to Br19.

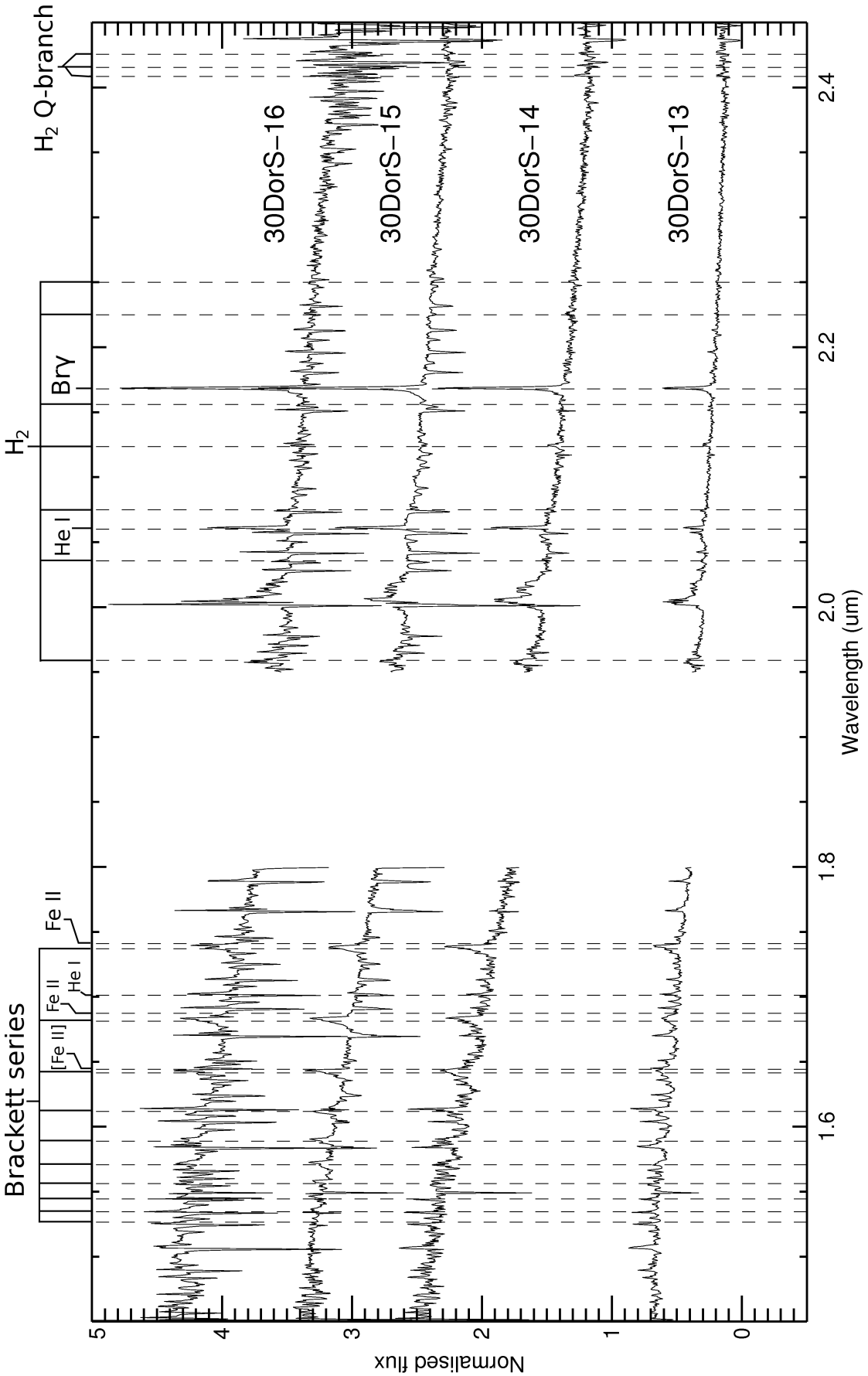

Fig. D.8 cont. $H + K$ spectra towards sources 13–16 in 30DorS (Chapter 6). The Brackett series emission is marked only up to Br19.

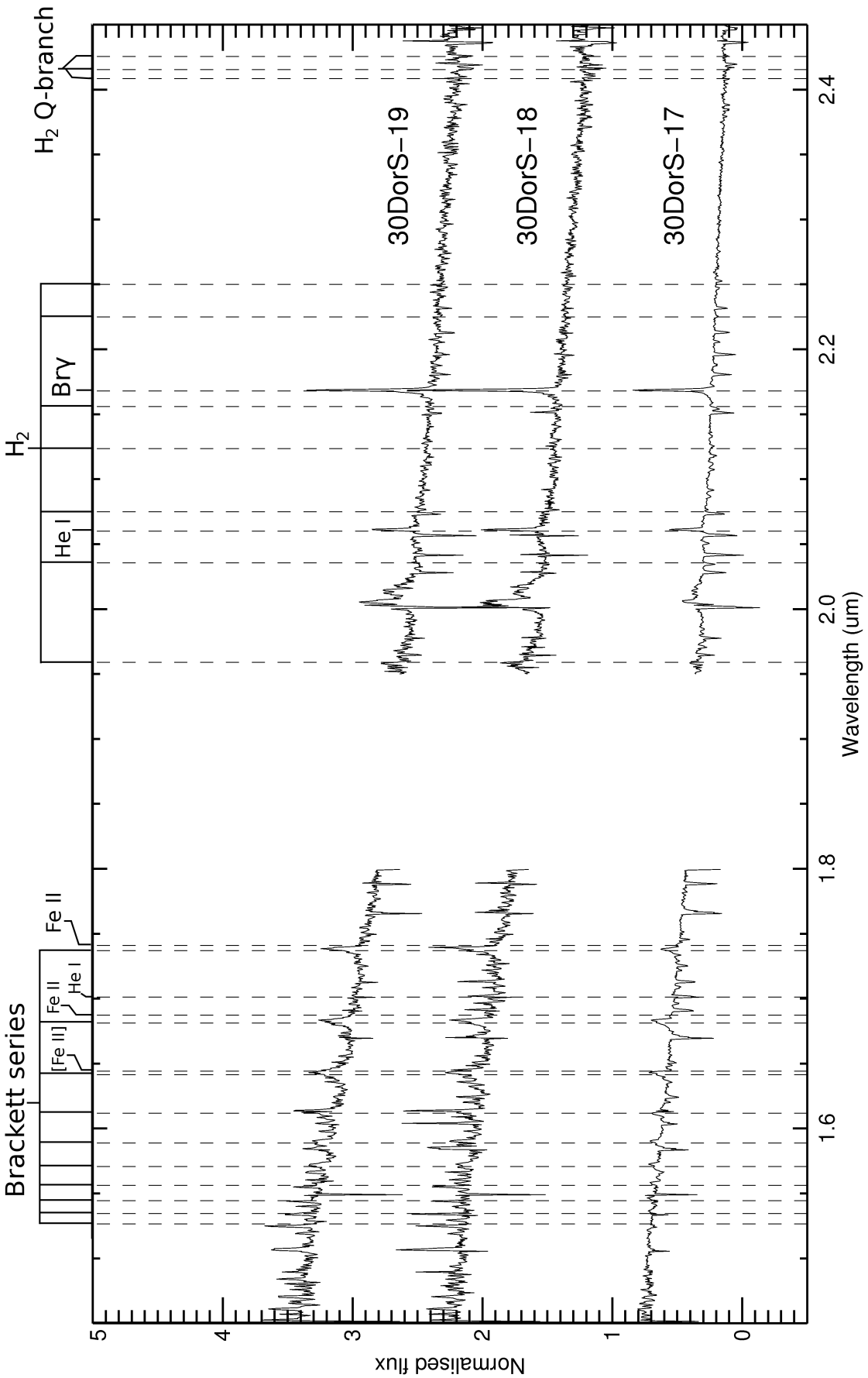

Fig. D.8 cont. $H + K$ spectra towards sources 17–19 in 30DorS (Chapter 6). The Brackett series emission is marked only up to Br19.

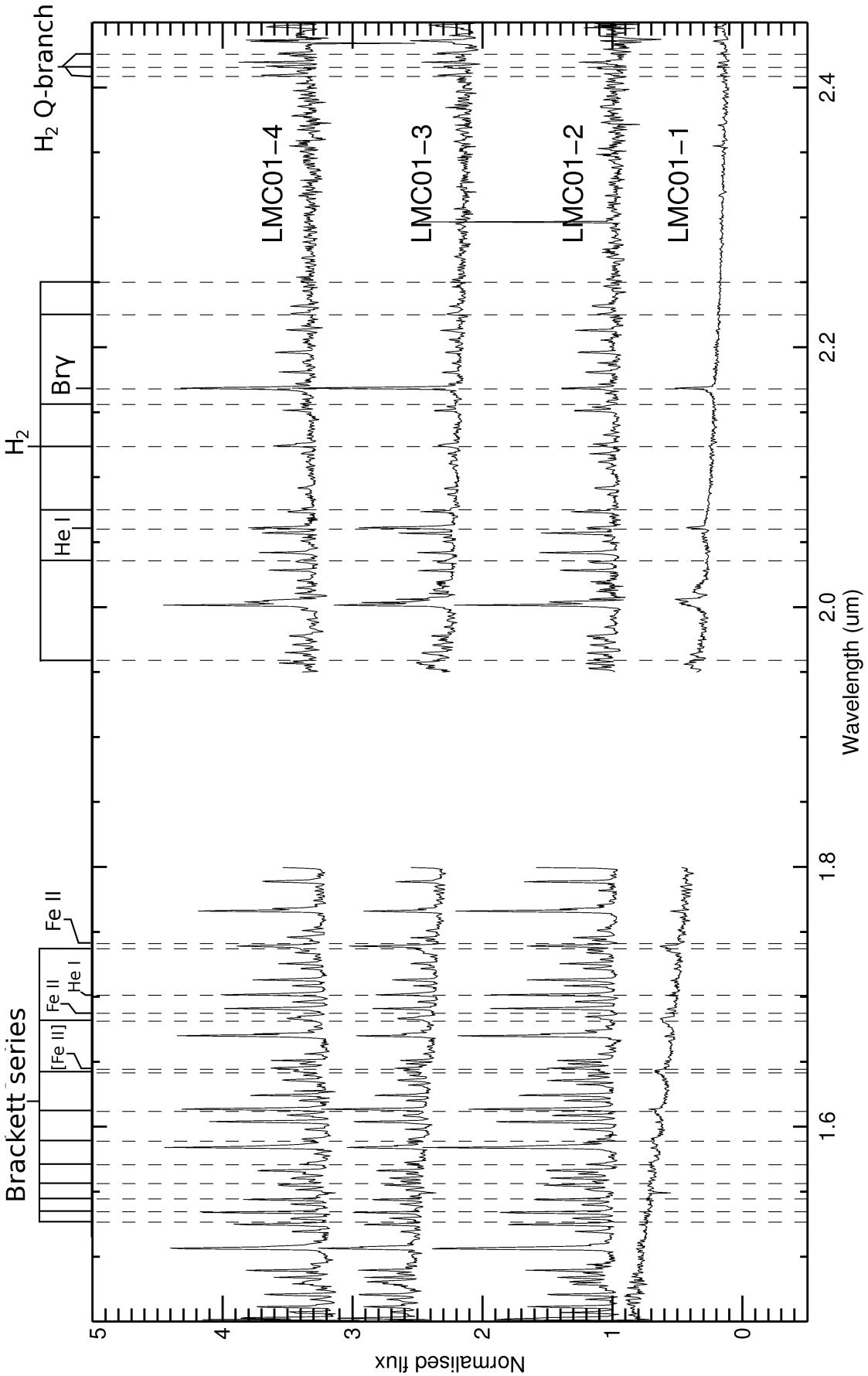

Fig. D.8 cont. $H + K$ spectra towards sources 1–4 in LMC01 (Chapter 6). The Brackett series emission is marked only up to Br19.

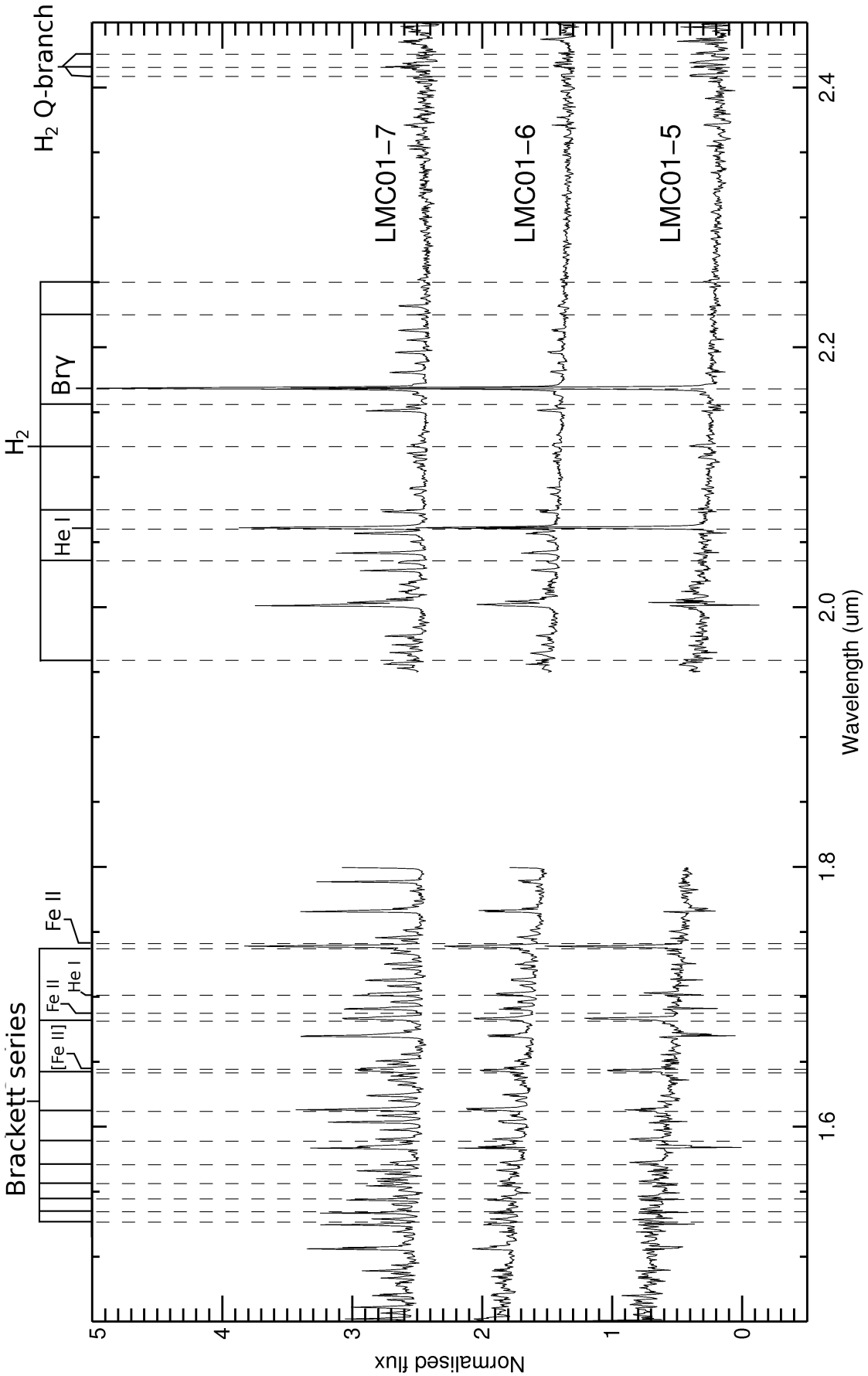

Fig. D.8 cont. $H + K$ spectra towards sources 5–7 in LMC01 (Chapter 6). The Brackett series emission is marked only up to Br19.

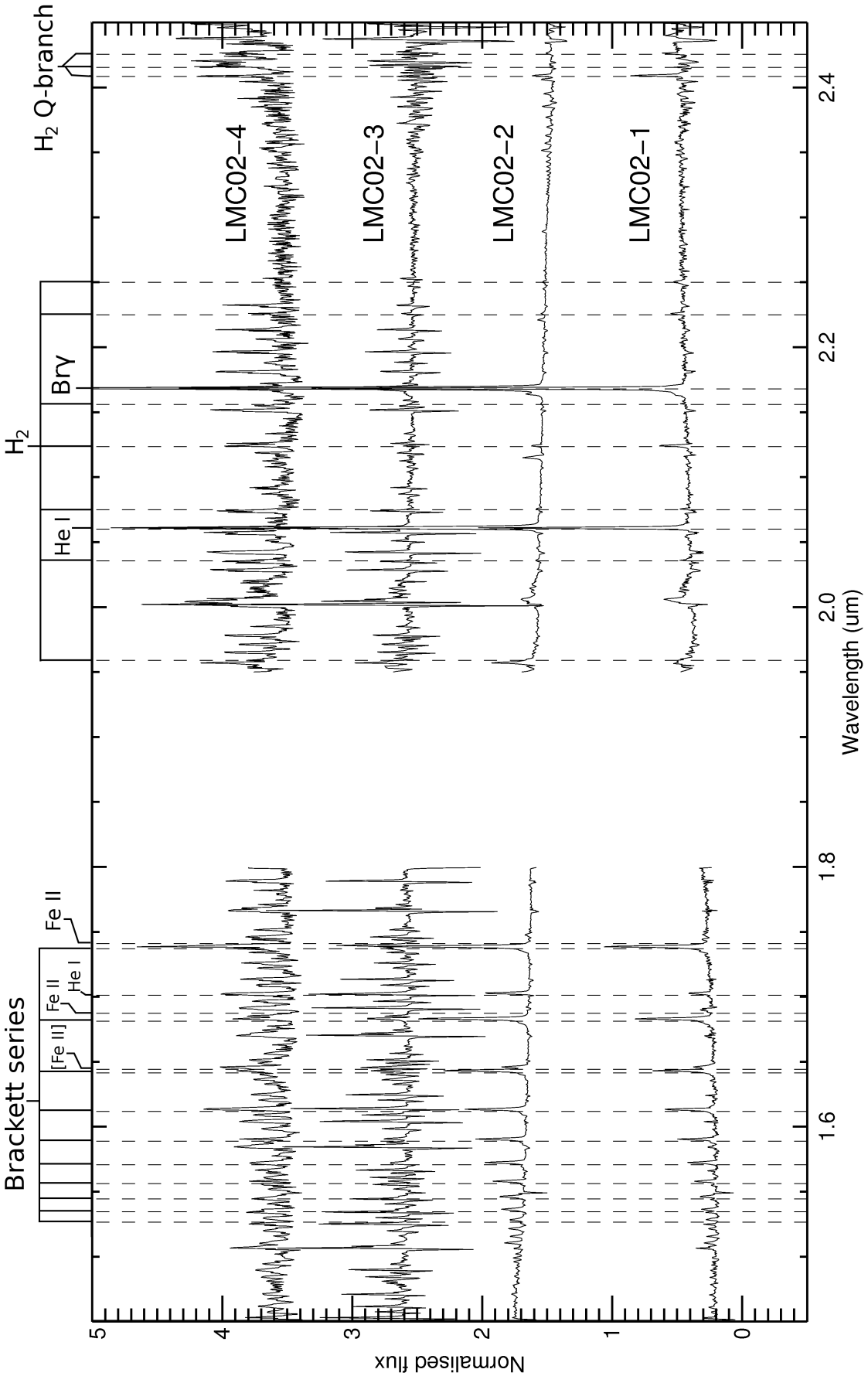

Fig. D.8 cont. $H + K$ spectra towards sources 1–4 in LMC02 (Chapter 6). The Brackett series emission is marked only up to Br19.

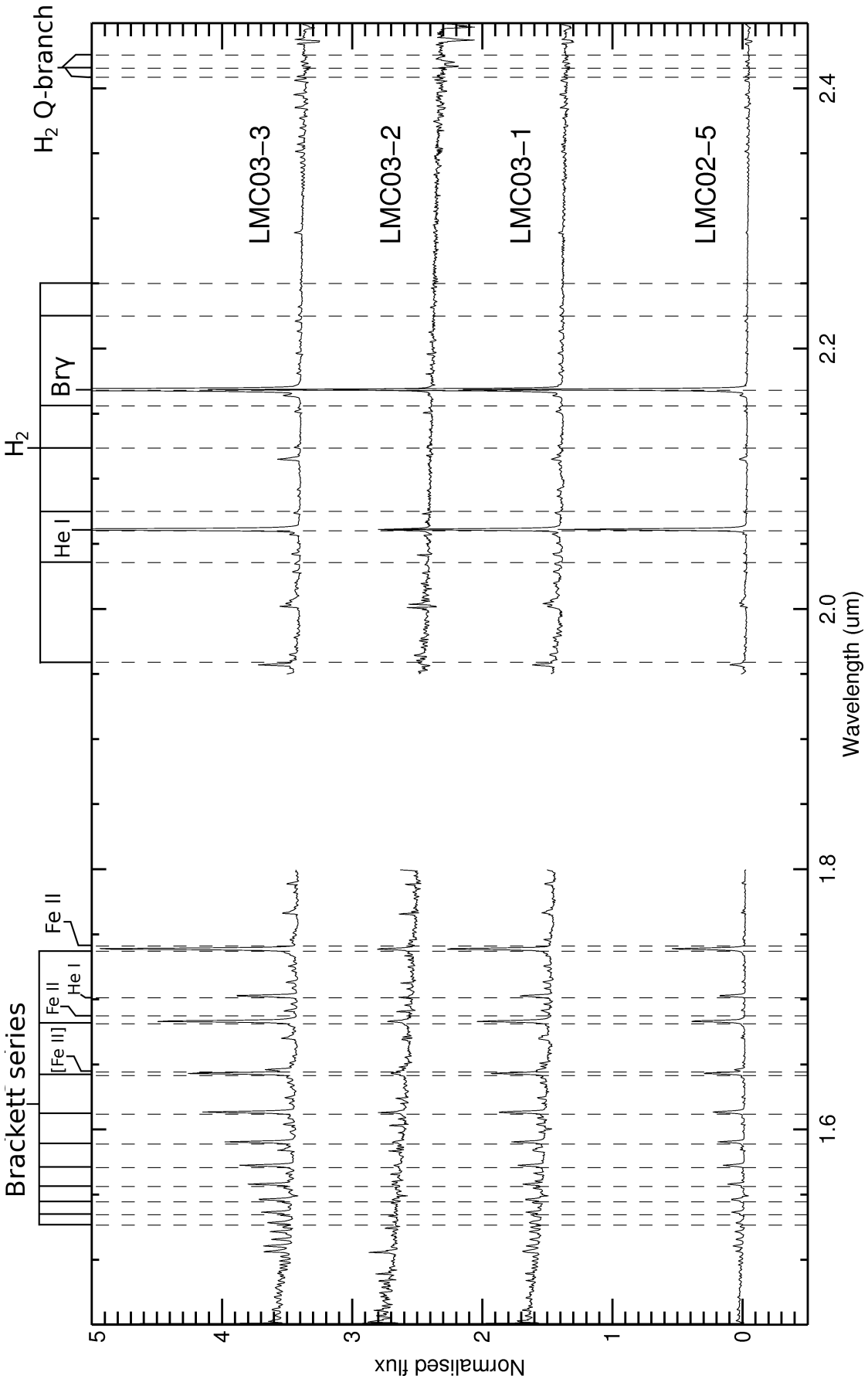

Fig. D.8 cont. $H + K$ spectra towards source 5 in LMC02 and sources 1–3 in LMC03 (Chapter 6). The Brackett series emission is marked only up to Br19.

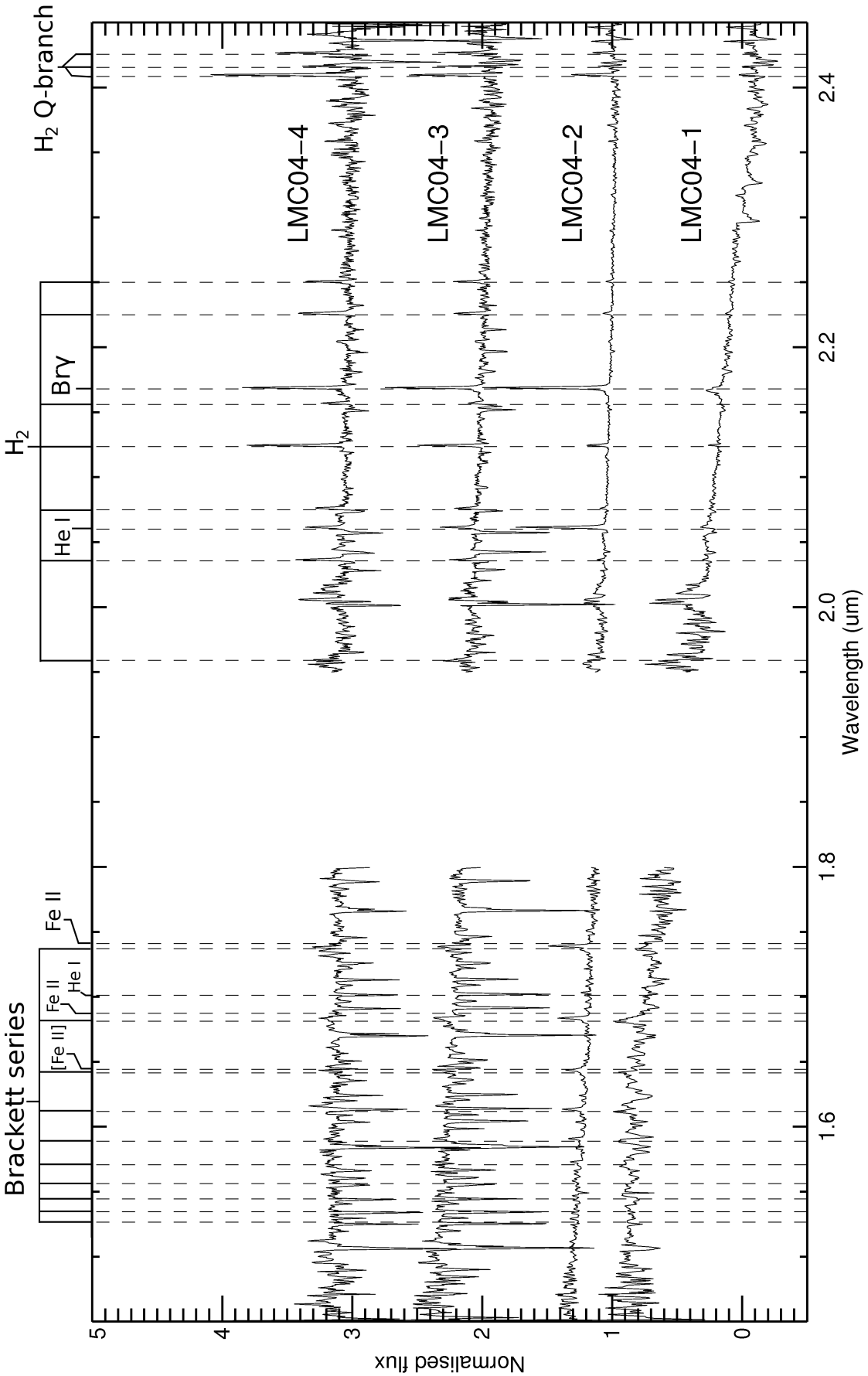

Fig. D.8 cont. $H + K$ spectra towards sources 1–4 in LMC04 (Chapter 6). The Brackett series emission is marked only up to Br19.

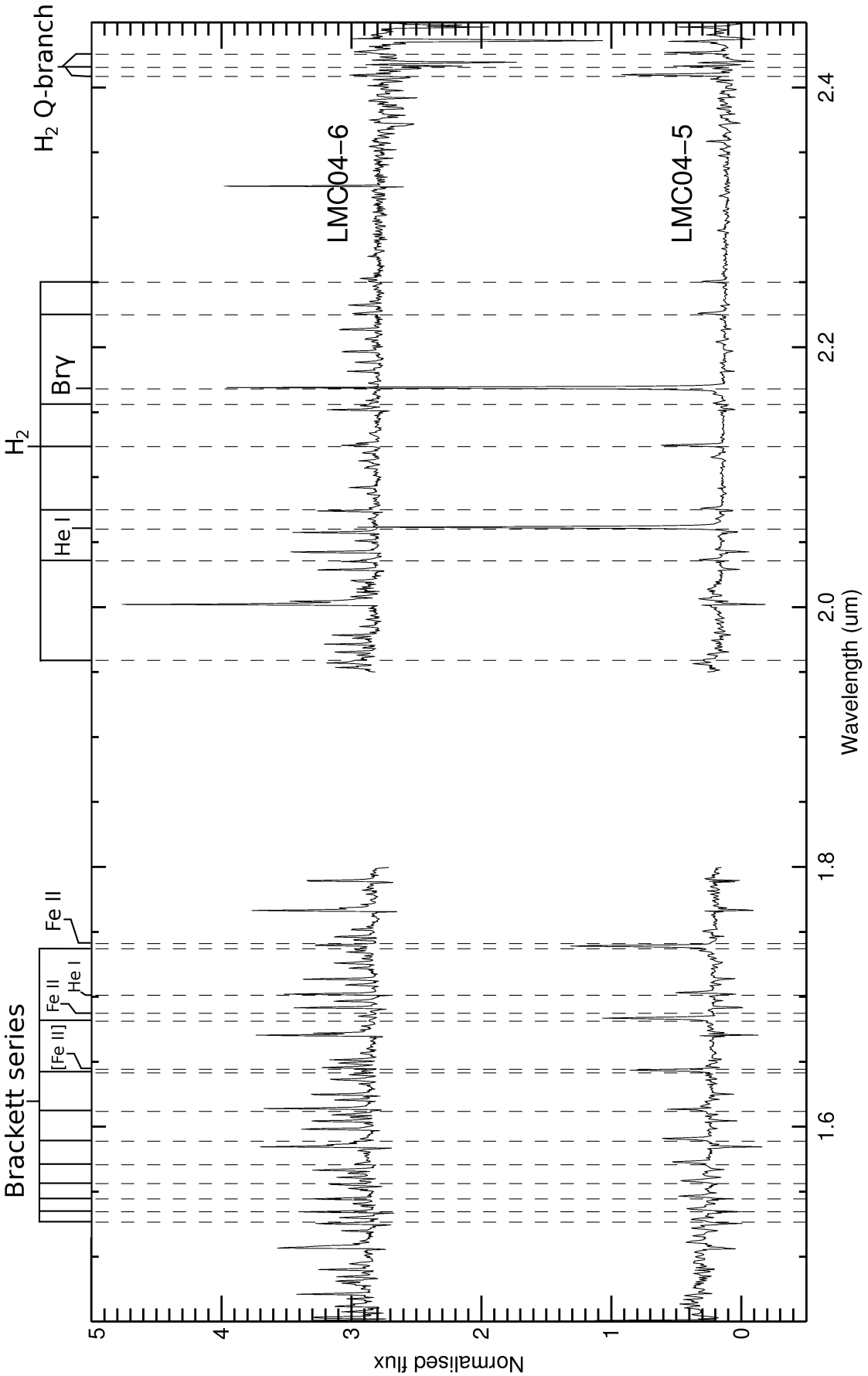

Fig. D.8 cont. $H + K$ spectra towards sources 5 and 6 in LMC04 (Chapter 6). The Brackett series emission is marked only up to Br19.

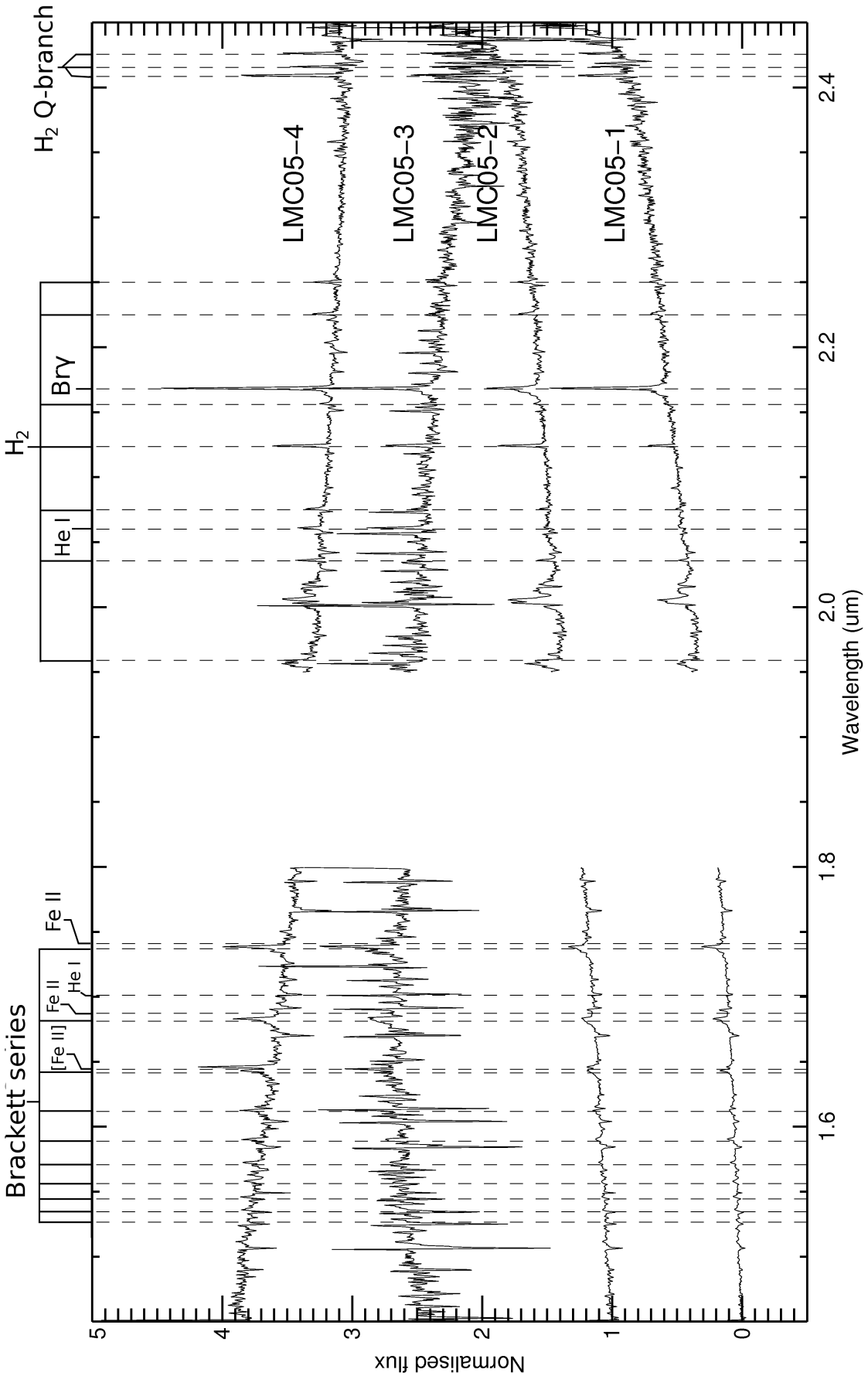

Fig. D.8 cont. $H + K$ spectra towards sources 1–4 in LMC05 (Chapter 6). The Brackett series emission is marked only up to Br19.

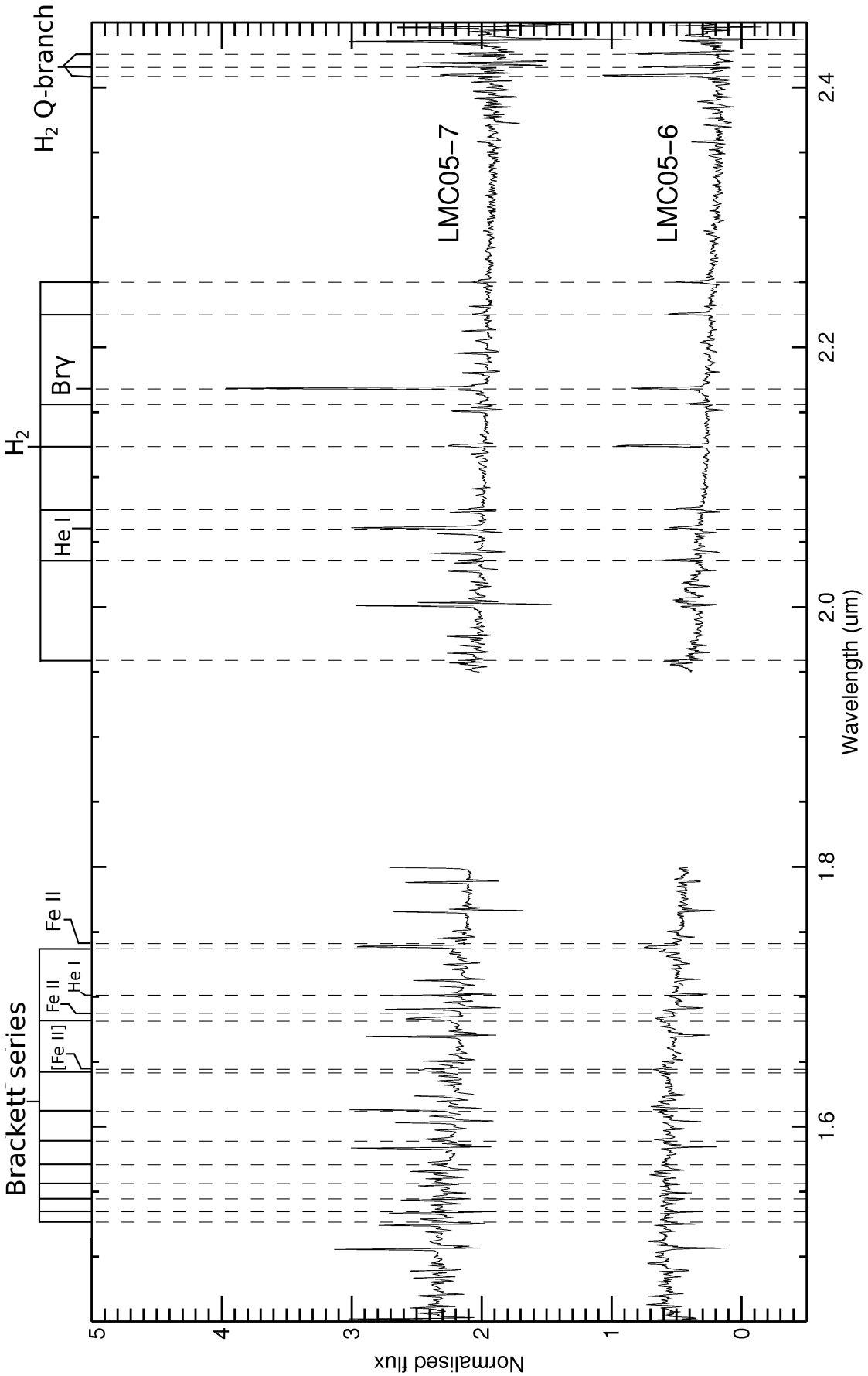

Fig. D.8 cont. $H + K$ spectra towards sources 6 and 7 in LMC05 (Chapter 6). The Brackett series emission is marked only up to Br19.

Appendix E Emission line fluxes

Here I present the fluxes for all measured emission lines in the spectra from Chapters 3, 4, 5 and 6. The K-band emission lines measured towards all continuum sources detected in N113 (Chapter 3) are shown in Table. E.1, followed by those measured towards the SMC sources (Chapter 4) in Table. E.2 and the optical emission lines for the SMC sources (Chapter 5) in Table E.3. Table E.4 shows the H I Brackett series emission from Brγ to Br14 measured from the SINFONI $H + K$ spectra (Chapter 6) followed by the H_2 emission features in Table E.5 and the He I and Fe II features in Table E.6. Finally, the measured equivalent widths of the CO absorption features observed in Chapter 6 are given in Table E.7.

Table E.1: Emission line fluxes towards all resolved sources in N113 (Chapter 3). No extinction correction has been applied. Where p appears in place of a flux this denotes that the line is present but the flux cannot be measured.

Object	He I (2.058 μm) 10^{-19}Wm^{-2}	Brγ 10^{-19}Wm^{-2}	H_2 1-0(S0) 10^{-19}Wm^{-2}	H_2 1-0(S1) 10^{-19}Wm^{-2}	H_2 1-0(S2) 10^{-19}Wm^{-2}	$H_2$1-0(S3) 10^{-19}Wm^{-2}
N113-YSO01	1.92±0.25	2.00±0.13	0.27±0.26	0.73±0.18	0.41±0.30	
N113-YSO03 A	37.4±2.2	53.8±2.4	1.67±0.30	3.66±0.50	1.19±0.20	1.30±0.41
N113-YSO03 B	6.56±0.35	33.8±1.4	3.02±0.49	7.18±0.49	1.92±0.34	1.37±0.34
N113-YSO03 C	1.53±0.20	7.70±0.38	3.64±0.30	11.7±6.1	3.47±0.36	4.09±0.50
N113-YSO04 A	2.22±0.15	2.66±0.19	0.20±0.03	0.56±0.08	0.19±0.05	
N113-YSO04 B	17.1±1.0	21.1±1.4	0.56±0.12	1.74±0.17	0.75±0.24	
Object	H_2 2-1(S1) 10^{-19}Wm^{-2}	H_2 2-1(S2) 10^{-20}Wm^{-2}	H_2 2-1(S3) 10^{-19}Wm^{-2}	1-0Q(1) 10^{-19}Wm^{-2}	1-0Q(2) 10^{-19}Wm^{-2}	1-0Q(3) 10^{-19}Wm^{-2}
N113-YSO01	0.36±0.08	1.36±0.63		0.94±0.18	1.09±0.10	0.83±0.13
N113-YSO03 A	1.25±0.18	5.53±1.29	1.18±0.22	7.47±0.87	3.14±0.57	3.39±0.27
N113-YSO03 B	1.38±0.14	4.65±0.97	1.42±0.16	12.2±1.0	5.34±0.44	6.93±0.54
N113-YSO03 C	2.04±0.21	6.67±0.85	1.85±0.14	16.5±1.4	6.33±0.56	11.3±0.6
N113-YSO04 A	0.16±0.02	0.93±0.27	0.11±0.03	1.47±0.19	0.69±0.15	0.85±0.07
N113-YSO04 B	0.78±0.11	3.46±1.00	0.62±0.09	3.72±0.45	2.07±0.19	2.11±0.16
Object	He I (2.113 μm) 10^{-20}Wm^{-2}	Pf 20-5 10^{-20}Wm^{-2}	Pf 21-5 10^{-20}Wm^{-2}	Pf 22-5 10^{-20}Wm^{-2}	Pf 23-5 10^{-20}Wm^{-2}	Pf 25-5 10^{-20}Wm^{-2}
N113-YSO01						
N113-YSO03 A	9.1±1.6	22.1±8.5	p	9.4±2.0	9.3±1.7	10.1±1.3
N113-YSO03 B			13.9±4.3		4.8±1.2	6.7±1.0
N113-YSO03 C						
N113-YSO04 A	2.4±0.5					
N113-YSO04 B	5.8±1.1		8.1±2.4	5.3±1.3	5.2±1.9	3.6±0.9

Table E.2: K-band emission line fluxes measured towards all sources. The fluxes have not been corrected for extinction.

Source	He I (2.058μm) 10^{-19} W/m^2	Brγ 10^{-19} W/m^2	H_2 1–0(S0) 10^{-19} W/m^2	H_2 1–0(S1) 10^{-19} W/m^2	H_2 1–0(S2) 10^{-19} W/m^2	$H_2$1–0(S3) 10^{-19} W/m^2
01	1.6±0.2	5.3±0.3	2.2±0.2	4.4±0.3	1.9±0.3	2.4±0.4
02 A		9.8±0.6	2.3±0.2	6.1±0.4	2.2±0.4	11±1
02 B			0.7±0.2	1.18±0.07	0.4±0.1	1.8±0.4
03	5.5±1.3	16.2±1.2	2.8±0.3	11.1±0.9	2.5±0.8	20±3
04	6.3±1.0	36.2±0.8				
06		0.41±0.06	0.14±0.04	0.92±0.06	0.32±0.08	1.4±0.1
17		2.0±0.1		1.2±0.2	0.4±0.2	2.4±0.4
18		0.93±0.09	0.71±0.05	2.4±0.2	0.8±0.2	2.0±0.4
20		8.1±0.2	3.0±0.4	1.1±0.1	0.40±0.08	0.8±0.3
22 A		1.3±0.1	1.86±0.09	4.5±0.2	1.7±0.2	2.9±0.2
22 B		0.46±0.05	0.43±0.04	0.60±0.04	0.19±0.05	0.8±0.1
25		0.33±0.06	1.05±0.09	2.4±0.2		
26	0.9±0.2	2.3±0.2	1.0±0.1	3.9±0.4	1.1±0.5	3.6±0.6
28 A	6.4±0.4	13.8±1.0	3.0±0.3	8.6±0.7	2.6±0.2	3.6±0.4
28 B		0.09±0.03	0.25±0.03	0.43±0.03	0.19±0.07	0.3±0.1
30		15.3±0.7	0.77±0.09	2.3±0.3	0.8±0.2	2.3±1.1
31	1.0±0.4	5.9±0.4	7.4±0.6	15±1	7±1	16±4
32		5.2±0.4	0.44±0.06	1.3±0.2	0.68±0.05	3.6±0.9
33		158±9	6.5±0.9	21±2	5±1	p?
34		20±1	4.2±0.3	13.6±0.8	4.4±0.5	9±1
35 A	197±9	326±18	2.9±0.3	7.7±0.8	2.3±0.2	7±3
35 B	91±5	138±10	0.7±0.2	2.2±0.4	0.5±0.1	2.0±0.7
35 C	100±6	127±10	0.9±0.2	2.3±0.3	1.0±0.3	2.8±0.8
35 D	68±4	98±9	2.7±0.3	7.2±0.8	2.0±0.2	5.4±1.0
36 A	3.1±0.5	6.3±0.3	0.4±0.1	1.5±0.2	0.55±0.06	1.7±0.9
36 B	3.0±0.3	6.1±0.3	0.85±0.07	1.9±0.2	0.27±0.07	1.6±0.4
36 C	4.1±0.4	6.8±0.4				p
36 D	3.6±0.3	6.2±0.4		0.27±0.04		0.39±0.09
36 E	4.4±0.4	8.2±0.7	0.32±0.06	0.72±0.07		0.6±0.2
Source	H_2 2–1(S1) 10^{-19} W/m^2	H_2 2–1(S2) 10^{-19} W/m^2	H_2 2–1(S3) 10^{-19} W/m^2	1–0Q(1) 10^{-19} W/m^2	1–0Q(2) 10^{-19} W/m^2	1–0Q(3) 10^{-19} W/m^2
01	0.9±0.2	0.7±0.1	1.5±0.6	2.7±0.5	2.2±0.4	3.3±0.6
02 A	0.8±0.1	p	1.1±0.4	14±1	2.7±0.4	5.2±0.8
02 B		0.2±0.1		1.5±0.3		0.9±0.3
03	3.1±0.4	1.2±0.3	2.4±0.6	15±2		10±2
04						
06	0.11±0.05	<1.0	0.08±0.03	0.76±0.09	0.23±0.06	0.75±0.08
17	p?			3.0±0.5	2.2±0.6	2.2±0.3
18	0.52±0.09	0.18±0.03	0.4±0.1	2.6±0.5	2.2±0.6	2.5±0.4
20				1.7±0.3	?	1.2±0.3
22 A	0.91±0.09	0.6±0.1	0.51±0.08	4.7±0.6	3.8±0.7	3.9±0.4
22 B	0.21±0.03	0.17±0.03	0.12±0.04	0.6±0.1	1.0±0.2	0.7±0.2
25	1.1±0.1	?	?	?	?	1.3±0.3
26	1.1±0.2	0.42±0.05	0.7±0.1	4.7±0.8	3.6±1.5	3.7±1.0
28 A	1.6±0.2	0.44±0.05	1.0±0.2	14±2	7±1	9±1
28 B	0.21±0.05		0.12±0.02	0.7±0.2	0.5±0.1	0.5±0.1
30				3.0±0.9	4±2	2±1
31	3.6±0.4	2.0±0.5	4.3±0.8	16±1	9.4±0.8	11±1
32						1.4±0.5
33	p?			14±4	p	13±2
34	1.8±0.4	1.4±0.4		13±3	14±3	13±2
35 A	2.6±0.3	0.9±0.3	1.5±0.5	11±2	7±3	6±2
35 B	0.70±0.09	0.18±0.08	p?	2.8±0.5	2.1±0.8	1.4±0.5
35 C	0.8±0.1	0.22±0.06	0.7±0.2	3.8±0.5	2.0±0.8	1.7±0.4
35 D	1.2±0.1	0.43±0.06	0.9±0.2	?	?	5.0±0.7
36 A	0.6±0.1		p?	1.9±0.4	1.3±0.6	0.9±0.5
36 B	0.8±0.1	0.27±0.07	0.6±0.1	3.2±0.5	1.5±0.5	1.7±0.4
36 C	0.29±0.06	p?	0.14±0.03	?	?	0.26±0.09
36 D				0.5±0.1	?	0.4±0.1
36 E				1.4±0.2	0.6±0.3	0.8±0.3
Source	Pf 20–5 10^{-19} W/m^2	Pf 21–5 10^{-19} W/m^2	Pf 22–5 10^{-19} W/m^2	Pf 23–5 10^{-19} W/m^2	Pf 24–5 10^{-19} W/m^2	Pf 25–5 10^{-19} W/m^2
35 A	9.7±0.6	?	5.5±0.7	5.6±0.9	3.5±1.8	6.3±0.7
35 B	4.1±0.4	5.2±1.0	2.6±0.3	2.6±0.4	1.4±0.4	2.5±0.3
35 C	3.8±0.3	4.2±0.4	2.4±0.4	2.3±0.4	1.4±0.3	2.0±0.4
35 D	3.1±0.3	4.3±1.1	1.7±0.4	1.9±0.2	7.3±0.7	1.7±0.2

Table E.3: Optical emission line fluxes. Fluxes have not been corrected for extinction.

Source	H_α	H_β	H_γ	H_δ	H_η	He I 3888 Å	He I 4464 Å
			10^{-13} erg s^{-1} cm^{-2}				
01	1.77±0.03	0.382±0.003	0.160±0.005	0.084±0.005	0.044±0.004		
02	0.072±0.003						
03	7.8±0.2	2.0±0.1	0.73±0.05	0.32±0.02	0.18±0.03	0.16±0.03	
04	1.86±0.1	0.241±0.001	0.0732±0.0008	0.030±0.003			
07	0.21±0.01	0.040±0.006					
08	0.62±0.02	0.149±0.008	0.057±0.008	0.033±0.005			
09	4.3±0.1	1.26±0.04	0.53±0.04	0.24±0.01			
10	0.050±0.009			0.02±0.01			
11	0.06±0.02						
12	0.14±0.01	0.037±0.009					
13	1.05±0.08	0.157±0.007	0.054±0.009	0.011±0.006			
14	0.28±0.04						
15	0.90±0.05	0.237±0.007	0.102±0.008	0.05±0.01	0.029±0.006	0.037±0.006	
16	0.21±0.02						
17	0.038±0.005						
18	0.07±0.02						
20	1.8±0.3	0.28±0.07		p?			
21	0.43±0.02	0.060±0.006	0.018±0.004				
22	0.54±0.04	0.19±0.01	0.07±0.01	0.024±0.004			
23	0.055±0.006						
25	1.18±0.02	0.35±0.02	0.12±0.02				
26	6.1±0.3	2.6±0.2	0.82±0.04	0.41±0.07	0.27±0.03	0.33±0.06	
27	0.07±0.01						
28	0.90±0.05	0.24±0.02	0.081±0.006	0.03±0.01			
30	0.36±0.02	0.054±0.005	0.013± 0.005				
32	0.21±0.04						
33	0.20±0.07						
34	0.082±0.007			p?			
35	97±6	44±4					
36	19±1	11.9±0.3					

Source	He I 5876 Å	He I 6679 Å	He I 7066 Å	[N II] 6548 Å	[N II] 6584 Å	[S II] 6717 Å	[S II] 6731 Å
			10^{-13} erg s^{-1} cm^{-2}				
01				0.049±0.003	0.160±0.004	0.12±0.07	0.119±0.003
02							
03	1.14±0.02	0.033±0.004		0.19±0.02	0.62±0.01	0.4±0.1	0.38±0.03
04						0.04±0.01	0.028±0.002
07					0.023±0.009	0.021±0.004	0.020±0.001
08	0.02±0.01	0.009±0.003	0.005±0.002	0.009±0.004	0.036±0.005	0.03±0.02	0.025±0.002
09				0.13±0.02	0.43±0.03	0.35±0.09	0.30±0.02
12					0.018±0.003	0.024±0.003	0.016±0.003
13				0.014±0.005	0.065±0.008	0.04±0.01	0.044±0.006
15		0.005±0.003		0.014±0.007	0.062±0.006	0.063±0.009	0.05±0.01
16						0.009±0.003	
21					0.033±0.006	0.012±0.003	0.017±0.002
22						0.04±0.01	0.033±0.009
23							0.002±0.001
25				0.036±0.006	0.097±0.007	0.14±0.01	0.105±0.008
26	0.31±0.01	0.073±0.009	0.063±0.007		0.159±0.008	0.20±0.01	0.16±0.02
27				0.006±0.003	0.007±0.003	0.019±0.002	0.015±0.003
28	0.015±0.005	0.0027±0.0009		0.025±0.006	0.060±0.007	0.07±0.01	0.07±0.01
34							0.002±0.001
35	3.8±0.4		3.5±0.4	0.42±0.03	1.11±0.06	0.68±0.04	0.94±0.06
36			0.23±0.01	0.32±0.05	0.35±0.03	0.27±0.03	0.27±0.03

Source	[O II] 7319/7319 Å	[O II] 7330/7331 Å	[O III] 4959 Å	[O III] 5007 Å	[Ne III] 3869 Å	[Ar III] 7136 Å	[Ar III] 7751 Å
			10^{-13} erg s^{-1} cm^{-2}				
01	0.031±0.006						
03	0.16±0.06		0.45±0.01	1.28±0.06		0.095±0.001	0.028±0.005
08	0.021±0.004		0.054±0.008	0.19±0.01		0.010±0.003	
09	0.07±0.02						
12				0.027±0.005			
13	0.030±0.003		0.014±0.006	0.018±0.005	0.03±0.02		
35	0.95±0.05	0.79±0.03	110±10	330±20		3.3±0.4	9.3±0.1
36	0.14±0.01	0.21±0.06	22.4±0.5	65±1		0.61±0.03	0.32±0.02

Table E.4: *H*+*K*-band H I emission line fluxes towards all continuum sources identified in Chapter 6.

Field	src#	Brγ	Br10	Br11	Br12	Br13	Br14
				$\times 10^{-19}$ W m^{-2}			
30DorN	1	790±40	650±40	550±40	390±20	270±20	200±10
30DorN	2	210±10	146±8	112±4	89±5	67±3	52±3
30DorN	3	910±40	670±40	620±40	450±20	300±20	220±10
30DorN	4	90±4	79±5	66±4	56±3	42±2	32±3
30DorS	1	35±2					
30DorS	2	42±3	33±2	27±2	20±2	19±1	10±1
30DorS	3	36±2	34±5	29±2	16±1	12±3	6.5±0.4
30DorS	4	20±2	15±1	20±1	15±3	16±5	
30DorS	5	28±2	26±1	20±1	15±1	14±2	10±1
30DorS	6	10±2	12±1	10.6±0.8	10.4±0.6	9±1	4.4±0.5
30DorS	7	11±1	12±1	11.7±0.6	10.2±0.6	9.5±0.6	7.6±0.6
30DorS	8	9±1	10±1	9.6±0.6	7.5±0.5	6.5±0.8	3.9±0.3
30DorS	9	5±1	8±1				
30DorS	10	4.0±0.3	5.9±0.7	3.7±0.4	3.0±0.2	2.8±0.6	2.6±0.3
30DorS	11	2.7±0.6	3.6±0.6	2.8±0.2	1.9±0.1	1.4±0.4	1.0±0.2
30DorS	12	4.4±0.7	4.6±0.8	5.1±0.5	3.3±0.5	3.2±0.8	1.8±0.4
30DorS	13	4.3±0.6	4.2±0.8				
30DorS	14	4.9±0.6	7±2	3.5±0.9	5.1±0.6	2.7±0.9	
30DorS	15	17±1	9±1	9±2	7±2	1.3±0.2	3.6±0.5
30DorS	16	30±3	10±1				
30DorS	17	18±2	8±1	16±3	8±3	4.7±0.5	4.2±0.6
30DorS	18	4.0±0.4	1.7±0.9	1.7±0.3	2.2±0.2		
30DorS	19	4.1±0.5	3.1±0.9	3.5±0.4	3.6±0.4	2.3±0.1	
LMC01	1	14±2	12±2	17±2	15±2	13±2	10±2
LMC01	2	10±1	1.9±0.1	0.8±0.2	1.8±0.6 b	3.3±0.1	0.26±0.07
LMC01	3	7.2±0.5	4.1±0.8	2.7±0.5	3.8±0.8	4.4±0.3	1.00±0.06
LMC01	4	9±1	9±3	3.4±0.7	2.4±0.4	8.4±0.3	1.9±0.4
LMC01	5	12.6±0.6	4.1±0.4	3.5±0.4	2.6±0.2		1.3±0.1
LMC01	6	9.2±0.5	4.0±0.3	2.9±0.4	2.7±0.3	3.0±0.6	1.2±0.3
LMC01	7	9.6±0.5	5.2±0.3	3.4±0.4	4.4±0.6	3.3±0.6	
LMC02	1	37±2	13±1	9.0±0.1	7.4±0.1	6.4±0.7	3.9±0.4
LMC02	2	270±10	75±5	53±5	40±5	31±3	23±2
LMC02	3	19±1	7±2	8±3			2.2±0.3
LMC02	4	13.0±0.9	8±3	6±2		6.3±0.5	
LMC02	5	770±40	150±15	160±16	124±9	109±5	74±5
LMC03	1	170±8	57±4	38±2	29±2	28±2	17±2
LMC03	2	29±2	13±2	11±2	9±2	7±1	
LMC03	3	1710±70	560±30	380±30	320±40	260±20	180±10
LMC04	1						
LMC04	2	48±3	20±2	16±3	17±3	13±1	7±2
LMC04	3	5.7±0.5	1.5±0.5				
LMC04	4	5.5±0.4	1.6±0.3				
LMC04	5	52±3	1.6±0.1	12.3±0.8	9.0±0.7		5.7±0.4
LMC04	6	2.0±0.7	13±2				
LMC05	1	78±5	19±3	20±9	11±2		5.2±0.2
LMC05	2	70±20	39±9	33±4	32±4		9±1
LMC05	3	11±2					
LMC05	4	20±1	13±3	9±3	9±7		3±1
LMC05	6	69±9	9±2	4±3	2.3±0.8		0.7±0.4
LMC05	7	47±3	20±2	14±2	14±2		5.1±0.3

Table E.5: *H+K*-band H_2 emission line fluxes towards all continuum sources identified in Chapter 6.

Field	src#	1–0S(0)	1–0S(1)	1–0S(2)	1–0S(3)	2–1S(1)	2–1S(2)
				$\times 10^{-19}$ W m^{-2}			
30DorS	13		0.38±0.03				
30DorS	14		0.60±0.09				
LMC01	1		1.8±0.7				
LMC01	2	0.29±0.07	0.6±0.2				
LMC01	3	0.8±0.1	1.44±0.09				
LMC01	4	1.0±0.1	2.5±0.6	1.5±0.3			
LMC01	5		0.7±0.1			0.3±0.2	
LMC01	6		0.6±0.1				
LMC01	7		0.7±0.1				
LMC02	1		2.7±0.2			1.3±0.1	
LMC02	2	1.2±0.2	3.9±0.3	1.2±0.5		1.0±0.6	
LMC02	4		3.4±0.7				
LMC02	5	2±1	4±2				
LMC03	3	9±2	13.8±0.6	12±4			
LMC04	2	3.8±0.5	8.0±0.3			2.5±0.3	1.8±0.2
LMC04	3	1.8±0.2	3.3±0.4	1.2±0.4		2.0±0.3	0.7±0.2
LMC04	4	3.1±0.2	5.2±0.3	2.5±0.4		2.3±0.3	1.2±0.2
LMC04	5	3.2±0.3	6.6±0.3	1.9±0.4		2.5±0.1	1.1±0.3
LMC04	6	6±1	7.4±0.4	9±2		3.5±0.1	
LMC05	1	10±3	14±5	3.1±0.9			
LMC05	2	12±2	30±1	9.0±0.9		11±2	7±1
LMC05	3		4.3±0.5				
LMC05	4	2.9±0.2	6.6±0.2	2.5±0.6		3.0±0.3	1.2±0.2
LMC05	6	3.8±0.2	7.7±0.2	3.5±0.4		3.3±0.4	
LMC05	7	3.1±0.4	9±1	2±1		4±1	

Field	src#	2–1S(2)	1–0Q(1)	1–0Q(2)	1–0Q(3)
			$\times 10^{-19}$ W m^{-2}		
30DorS	11		0.4±0.2		0.3±0.1
30DorS	13		0.34±0.02		
30DorS	14		0.5±0.1		<0.4
LMC01	1				1.0±0.4
LMC01	3				1.3±0.2
LMC01	4		2.2±0.3	3±1	1.2±0.4
LMC01	5		1.3±0.2		0.8±0.2
LMC02	1	0.6±0.1			1.0±0.6
LMC02	2				2.2±0.6
LMC04	2	1.6±0.2	14.0±0.6		6±1
LMC04	3	1.1±0.2	5.1±0.6		2.4±0.4
LMC04	4	1.8±0.5	7.6±0.7	2±1	3.6±0.2
LMC04	5	1.9±0.8	11.0±0.4		5.2±0.2
LMC04	6				11±2
LMC05	1		23±5		15±2
LMC05	2	5±1	47±5		28±3
LMC05	4	2.1±0.3	13±1	5±1	6.3±0.3
LMC05	6	2.4±0.2	10.9±0.7	4.3±0.5	6.7±0.7
LMC05	7		10±3		

Table E.6: *H+K*-band He I and Fe II emission line fluxes towards all continuum sources identified in Chapter 6. ? denotes that the line identification is uncertain.

Field	src#	He I 1.7011 μm	He I 2.059 μm	He I 2.113 μm	[Fe II] 1.644 μm	Fe II 1.687 μm	Fe II 1.741 μm
				$\times 10^{-19}$ W m^{-2}			
30DorN	2		9±2				
30DorN	3		21±3				
30DorS	1			4±1			
30DorS	4		5.2±0.5				
30DorS	5		2.7±0.8				
30DorS	6		2.6±0.3				
30DorS	7		2.8±0.2				
30DorS	8		2.7±0.3				
30DorS	9		1.5±0.3				
30DorS	10		1.9±0.2				
30DorS	11		1.02±0.08		2±1 ?		
30DorS	12		1.7±0.2				
30DorS	13		1.7±0.2				
30DorS	14		2.2±0.2				
30DorS	15		7.4±0.4				
30DorS	16		15±3				
30DorS	17		7.8±0.5				
30DorS	18		1.8±0.3				
30DorS	19		1.7±0.2				
LMC01	2		0.62±0.09	3.8±0.8		2.3±0.1	0.83±0.06
LMC01	3		4.4±0.3			2.2±0.2	
LMC01	4		2.9±0.3		3.9±0.5		2.4±0.5 ?
LMC01	5		6.8±0.5	0.4±0.2			
LMC01	6		4.9±0.3			1.6±0.6	1.0±0.3
LMC01	7		5.3±0.3		7.3±0.6 ?	2.3±0.4	1.4±0.3
LMC02	1	2.5±0.2	1.9±0.1		3.0±0.3	2.0±0.8	0.7±0.2
LMC02	2	19.5±0.9	172±7	9.8±0.8	11.9±0.9		
LMC02	3		11.2±0.9				
LMC02	4		8±1		5.0±0.7		
LMC02	5	78±2	500±30	30±3	32±1		
LMC03	1	17±1	81±3	7.0±0.8	8.7±0.5 ?	3.7±0.9	3.1±0.9
LMC03	2		14.8±0.7				
LMC03	3	180±10	870±30	73±8	88.3±0.5	28±6	
LMC04	1		10±3				
LMC04	2		31±1				
LMC04	3		20±2				
LMC04	4		2.2±0.2				
LMC04	5	3±1	37±2	1.8±0.3			
LMC05	1				3.2±0.7	6±2	4±1
LMC05	2				9±1	7±2	
LMC05	3		3.9±0.5				
LMC05	4		3.1±0.4				
LMC05	6		3.0±0.4			2.5±0.3	
LMC05	7		23±1				

Table E.7: Measured equivalent widths for all four sources with CO bandhead absorption features in the LMC (see Chapter 6).

Source	2.295 μm (μm)	cont ($\mathrm{W\,m^{-2}\,\mu m^{-1}}$)	2.324 μm (μm)	cont ($\mathrm{W\,m^{-2}\,\mu m^{-1}}$)	2.354 μm (μm)	cont ($\mathrm{W\,m^{-2}\,\mu m^{-1}}$)
30DorS-4	0.0016	8.21E-16	0.0014	7.54E-16	0.0013	6.75E-16
LMC04-1	0.0016	2.96E-15	0.0015	2.78E-15	0.0015	2.49E-15
LMC05-3	0.0011	3.57E-16	0.0021	3.42E-16	0.0013	3.23E-16
LMC05-6	0.0006	2.29E-16				